Vrije Universiteit Brussel

Doctoral Thesis

From Cosmic Crashes to High-Energy Neutrinos

Investigating high-energy neutrino emission from luminous and ultraluminous infrared galaxies in the Great Observatories All-Sky LIRG Survey

---

Author:
Yarno Merckx

Promotor:
Prof. Dr. Krijn D. de Vries

Co-promotor:
Prof. Dr. Nick van Eijndhoven

A thesis submitted in fulfillment of the requirements for the degree of Doctor of Philosophy

in the

Sciences & Bio-Engineering Sciences
Department of Physics and Astronomy
Interuniversity Institute for High Energies

June 24, 2025

Doctoral Examination Commission

Chair
Prof. Dr. Stijn Buitink
Interuniversity Institute for High Energies – Vrije Universiteit Brussel

Promotors
Prof. Dr. Krijn D. de Vries
Interuniversity Institute for High Energies – Vrije Universiteit Brussel

Prof. Dr. Nick van Eijndhoven
Interuniversity Institute for High Energies – Vrije Universiteit Brussel

Jury members
Prof. Dr. Alberto Mariotti
Interuniversity Institute for High Energies – Vrije Universiteit Brussel

Prof. Dr. Vincent Ginis
Data Analytics Lab – Vrije Universiteit Brussel

Prof. Dr. Simona Toscano
Interuniversity Institute for High Energies – Université Libre de Bruxelles

Prof. Dr. Juliana Stachurska
Department of Physics and Astronomy – Universiteit Gent

Acknowledgements

To be done.

Summary

The origin of the diffuse high-energy neutrino flux observed in the TeV–PeV range by the IceCube Neutrino Observatory at the South Pole remains a central unresolved question in high-energy astrophysics. This thesis investigates (ultra)luminous infrared galaxies (U/LIRGs) as potential sources of this flux. U/LIRGs exhibit infrared luminosities exceeding 10^{11} solar luminosities, powered by intense star formation ($\sim$ 10–100 solar masses per year) and accreting supermassive black holes ($\gtrsim 10^6$ solar masses), commonly identified as active galactic nuclei (AGN). These energetic environments provide promising conditions for hadronic acceleration, potentially leading to high-energy neutrino production through interactions with dense matter and radiation fields within the source region.

Leveraging multi-wavelength data from NASA's Great Observatories All-Sky LIRG Survey (GOALS), which includes over 200 local U/LIRGs (redshift $z < 0.09$), we develop a novel phenomenological framework for steady-state, starburst-driven high-energy neutrino production via proton-proton interactions.

The model connects a galaxy's infrared luminosity to its expected high-energy neutrino flux, with its parameters constrained by electromagnetic observations. As a case study, we first apply the model to one of the brightest LIRGs in the GOALS sample, NGC 3690. We then extend the analysis to the full GOALS sample and compare the resulting neutrino flux predictions to the per-source sensitivities of IceCube and its planned extension, IceCube-Gen2. The results indicate that a high-energy neutrino signal originating from steady-state starburst activity in individual GOALS U/LIRGs—among the most intensely star-forming systems in the local Universe—is unlikely to be detectable by IceCube. However, IceCube-Gen2 is expected to be sensitive to more optimistic emission scenarios, potentially offering new insights into the mechanisms of high-energy neutrino production.

We further show that the neutrino signal from the LIRG NGC 1068—the first steady IceCube point source reported with statistical evidence—cannot be explained by starburst activity alone. This points to additional high-energy neutrino-production mechanisms, likely linked to its obscured AGN.

Beyond individual galaxies, we estimate the diffuse, starburst-driven high-energy neutrino flux from U/LIRGs across cosmic time using analytic methods. While our projections indicate that ULIRGs likely contribute only a subdominant fraction, consistent with existing upper limits, the results suggest that LIRGs may account for a significant portion of the diffuse astrophysical neutrino flux. This contribution is, however, constrained by the extragalactic gamma-ray background.

These modeling efforts culminate in foundational work in which we integrate the neutrino-production framework into cosmological hydrodynamic simulations. Once finalized, this novel approach will enable a redshift-dependent study of starburst-driven neutrino production across cosmic time, going beyond the simplified population models used in analytic methods. This will enable a more realistic estimation of the high-energy neutrino emission from starburst activity, as well as tighter constraints on the physical parameters governing high-energy neutrino production in these regions.

Complementing our modeling efforts, we perform a correlation analysis using 13 years of up-going muon-track data from IceCube to search for high-energy neutrino emission from 113 GOALS U/LIRGs located in the Northern Sky, specifically those with declinations $\delta > -3^\circ$. This analysis includes both individual source investigations and a search for a cumulative signal from a subset of extremely compact, energetic, and

heavily obscured U/LIRGs. The 113 sources—excluding NGC 1068, for which independent evidence of neutrino emission was already reported in a previous analysis—consist primarily of starburst-dominated systems, but also include AGN-dominated and composite (starburst+AGN) systems.

We adopt a model-agnostic approach in our searches, assuming a generic power-law neutrino spectrum. Although no significant signals are detected in any of the searches, we establish the most stringent upper limits to date on steady high-energy neutrino emission from nearby U/LIRGs. When combined with electromagnetic data from GOALS, this yields a valuable multi-messenger dataset for future modeling of high-energy processes in the nearby Universe. Furthermore, the null results from the numerous starburst-dominated systems in the sample provide important context for the growing body of evidence linking high-energy neutrino emission to AGN-dominated sources (e.g., NGC 1068).

Notably, while not statistically significant, we observe a 2.3σ excess from the direction of NGC 7469—a nearby LIRG hosting both a luminous AGN and vigorous starburst activity. Intriguingly, this excess is spatially coincident with two ~ 100 TeV IceCube alert events, highlighting NGC 7469 as a novel compelling candidate neutrino source.

Samenvatting

Het IceCube Neutrino Observatorium op de Zuidpool detecteert een diffuse flux van hoogenergetische neutrino's in het TeV–PeV-bereik. De oorsprong van deze flux vormt echter nog altijd een open vraag binnen de hoogenergetische astrofysica. Deze thesis onderzoekt (ultra)luminieuze infraroodstelsels (U/LIRGs) als mogelijke bronnen van deze neutrino's. U/LIRGs zijn sterrenstelsels met een infraroodhelderheid van meer dan 10^{11} keer de lichtkracht van de zon, voornamelijk veroorzaakt door het opwarmen van stof in compacte regio's van intense stervorming (10–100 zonsmassa's per jaar) en accretie van materie op supermassieve zwarte gaten ($\gtrsim 10^6$ zonsmassa's), ook wel actieve galactische kernen (AGN) genoemd. Deze energetische omgevingen bieden gunstige omstandigheden voor de versnelling van hadronische deeltjes tot hoge energieën, wat kan leiden tot de productie van hoogenergetische neutrino's via interacties met materie- en stralingsvelden in de bronregio.

Op basis van NASA's Great Observatories All-Sky LIRG Survey (GOALS), een studie die meer dan 200 nabije U/LIRGs beschrijft (roodverschuiving $z < 0.09$), ontwikkelen we een nieuw model om de productie van hoog-energetische neutrino's in deze stelsels te kwantificeren. De focus ligt op neutrino's die ontstaan door interactie van sterexplosies met hun omgeving. Dit is gemotiveerd door GOALS-data die aantonen dat de infraroodemissie van de meeste U/LIRGs voornamelijk aangedreven wordt door stervorming. Het model legt een kwantitatief verband tussen de infraroodhelderheid van een U/LIRG en de verwachte neutrino-flux, waarbij de modelparameters worden afgeleid uit de rijke GOALS-dataset.

Als casestudy passen we dit model toe op de krachtige LIRG NGC 3690, waarna het wordt uitgebreid naar de volledige GOALS-catalogus. De resulterende voorspellingen voor de neutrino-flux worden vergeleken met de gevoeligheid van IceCube en diens geplande uitbreiding, IceCube-Gen2. Onze resultaten tonen aan dat IceCube naar verwachting geen detecteerbaar signaal zal opvangen van dit specifieke emissieproces, terwijl IceCube-Gen2 wél gevoelig kan zijn om optimistische scenario's te testen.

Daarnaast tonen we aan dat het neutrinosignaal van NGC 1068—de eerste continu gedetecteerde puntbron van hoog-energetische neutrino's—niet kan worden verklaard door activiteit die uitsluitend verband houdt met sterexplosies. Dit wijst op een bijkomende, dominante productiecomponent, mogelijks gerelateerd aan het sterk verduisterde supermassieve zwarte gat in dit stelsel.

Naast individuele schattingen ramen we met analytische methoden de geaccumuleerde diffuse neutrino-flux afkomstig van sterexplosies binnen de bredere U/LIRG-populatie doorheen de kosmische geschiedenis. Hoewel ULIRGs slechts een beperkte bijdrage leveren, in overeenstemming met bestaande limieten voor deze bronklasse, suggereren onze resultaten dat LIRGs een substantieel deel van de diffuse astrofysische neutrino-flux kunnen verklaren. Hun bijdrage wordt echter begrensd door de cumulatieve extragalactische gammastralingsachtergrond.

Tot slot zijn de eerste substantiële stappen gezet om het model te integreren in een bestaande hydrodynamische simulatie van de kosmos. Deze integratie maakt het, eenmaal voltooid, mogelijk om de neutrino-emissie uit steruitbarstingsregio's doelgericht te bestuderen doorheen de kosmische tijd, zonder terug te vallen op de veralgemeniseringen die kenmerkend zijn voor analytische methoden. Een belangrijk voorbeeld daarvan is de aanname dat lokale omstandigheden representatief zijn voor gelijkaardige bronnen in het volledige kosmische verleden—een veronderstelling die, zoals aangetoond voor U/LIRGs, niet volledig opgaat. Dit vernieuwende kader biedt

uitzicht op robuustere voorspellingen van de diffuse astrofysische neutrino-flux en diens oorsprong, evenals op strengere beperkingen van modelparameters dan haalbaar is met analytische benaderingen.

Als aanvulling op onze modellering voeren we een correlatieanalyse uit met behulp van 13 jaar aan interne IceCube-data, waarbij we nagaan of er een ruimtelijke correlatie bestaat tussen de richtingen van gedetecteerde neutrino's en de posities van 113 GOALS-U/LIRGs op het noordelijk halfrond, specifiek met declinaties $\delta > -3^\circ$. De geselecteerde bronnen omvatten voornamelijk steruitbarstingsstelsels, aangevuld met AGN-gedomineerde en hybride systemen, die allemaal beschikken over rijke multigolflengtegegevens dankzij hun opname in GOALS.

Onze model onafhankelijke benadering vertrekt van een generiek neutrinospectrum dat afvalt volgens een machtswet, in contrast met het fysisch gemotiveerde model gebruikt in het eerste deel van deze studie. Hoewel geen statistisch significant signaal werd gevonden, stellen we de tot dusver strengste bovengrenzen vast op continue neutrino-emissie door deze 113 nabije U/LIRGs. In combinatie met de elektromagnetische gegevens uit GOALS vormt dit een waardevolle dataset voor toekomstig onderzoek naar de meest energetische processen in het nabije heelal. De nulresultaten voor de steruitbarstingsgedomineerde U/LIRGs bieden bovendien belangrijke context bij de groeiende consensus dat hoog-energetische neutrino's voornamelijk afkomstig zijn van AGN-gedomineerde puntbronnen op vergelijkbare afstanden.

Opmerkelijk is dat we, hoewel de statistische significantie beperkt is, een clustering van hoog-energetische neutrino's waarnemen die de afwezigheid van een puntbron van neutrinos met een betrouwbaarheid van 2.3σ tegenspreekt. Deze clustering bevindt zich in de richting van de nabije LIRG NGC 7469, een sterrenstelsel met zowel een lumineuze AGN als intense stervorming. Intrigerend genoeg valt deze overschrijding samen met twee ~ 100 TeV-neutrino's die eerder en onafhankelijk werden gedetecteerd door het waarschuwingssysteem van IceCube voor astrofysisch interessante gebeurtenissen die snelle opvolging vereisen. Dit maakt NGC 7469 tot een nieuwe veelbelovende kandidaat voor een neutrinobron.

Contents

List of Abbreviations

Acronym	Full name
AGN	**A**ctive **G**alactic **N**ucleus
BDT	**B**oosted **D**ecision **T**ree
CC	**C**harged **C**urrent
CMB	**C**osmic **M**icrowave **B**ackground
CL	**C**onfidence **L**evel
CON	**C**ompact **O**bscured **N**ucleus
CR	**C**osmic **R**ay
DAQ	**D**ata **AQ**uisition
DIS	**D**eep **I**nelastic **S**cattering
DOM	**D**igital **O**ptical **M**odule
EBL	**E**xtragalactic **B**ackground **L**ight
EGB	**E**xtragalactic **G**amma-ray **B**ackground
ELIRG	**E**xtremely **L**uminous **I**nfrared **G**alaxy
GCN	**G**eneral **C**oordinates **N**etwork
GRB	**G**amma-**R**ay **B**urst
GZK	**G**reisen **Z**atsepin **K**uzmin
HAGS	**H**Adronically-powered **G**amma-ray **G**alaxie**S**
HCN	**H**ydrogen **C**ya**N**ide
HESE	**H**igh-**E**nergy **S**tarting **E**vents
HLC	**H**ard **L**ocal **C**oincidence
HyLIRG	**Hy**per **L**uminous **I**nfrared **G**alaxy
ICL	**IceC**ube **L**ab
IGRB	**I**sotropic **G**amma-**R**ay **B**ackground
IMF	**I**nitial **M**ass **F**unction
IR	**I**nfra**R**ed
LED	**L**ight **E**mitting **D**iode
LIRG	**L**uminous **I**nfra**R**ed **G**alaxy
MAD	**M**agnetically **A**rrested **D**isk
MC	**M**onte **C**arlo
MPE	**M**ultiple **P**hoto**E**lectron
NC	**N**eutral **C**urrent
PDF	**P**robability **D**ensity **F**unction
PMT	**P**hoton **M**ultiplier **T**ube
PnF	**P**rocessing a**n**d **F**iltering
SBR	**S**tar**B**urst **R**egion
SED	**S**pectral **E**nergy **D**istribution
SFH	**S**tar **F**ormation **H**istory
SFR	**S**tar **F**ormation **R**ate
SLC	**S**oft **L**ocal **C**oincidence
SMBH	**S**uper**M**assive **B**lack **H**ole
SMT	**S**imple **M**ultiplicity **T**rigger

continued on next page

Acronym	Full name
SN	**S**uper**N**ova
SPE	**S**ingle **P**hoto**E**lectron
sps	**s**amplings **p**er **s**econd
TDE	**T**idal **D**isruption **E**vent
TS	**T**est **S**tatistic
UHECR	**U**ltra-**H**igh-**E**nergy **C**osmic **R**ay
ULIRG	**U**ltra-**L**uminous **I**nfra**R**ed **G**alaxy
UV	**U**ltra**V**iolet
VHE	**V**ery-**H**igh **E**nergy

Introduction

Until the early 20^{th} century, the study of outer space relied solely on electromagnetic radiation. However, an unexpected discovery in 1912 transformed our understanding of the cosmos and opened up a new field of astronomy. That year, Victor Hess demonstrated, using a hot air balloon, that the Earth is bombarded by charged atomic nuclei of extraordinary high energy, now known as cosmic rays [1]. These particles, reaching energies of about 10^{20} electronvolts (eV), equivalent to a macroscopic energy of ~ 16 joules, are the most energetic subatomic particles ever detected. Identifying the sources of cosmic rays is of great interest, as they are associated with the most powerful particle accelerators in the Universe, capable of achieving energies far beyond the reach of terrestrial accelerators. Despite more than a century of research, however, their origin remains largely unknown.

Tracing cosmic rays back to their sources presents a significant challenge due to the distortion of their trajectories by interactions with galactic and intergalactic magnetic fields. Consequently, the reconstructed arrival directions of cosmic rays do not reliably indicate their origin. However, a fraction of cosmic rays could interact with matter or radiation within the source environment before escaping. These interactions produce predominantly charged and neutral pions. The neutral pions decay into gamma rays (high-energy photons), while the charged pions decay, among other particles, into high-energy neutrinos.

Gamma rays, being electrically neutral, are unaffected by magnetic fields, making them valuable potential tracers of cosmic-ray sources. However, the Universe is opaque to high-energy photons due to their interactions with dust and background radiation fields, which limit their propagation range. Additionally, gamma rays can be efficiently produced by leptonic processes, such as inverse Compton scattering, making them ambiguous indicators of hadronic acceleration. In contrast, high-energy neutrinos offer a unique advantage. As electrically neutral, fundamental particles that interact solely via the weak force and gravity, neutrinos can travel vast cosmological distances without deflection or significant attenuation. Moreover, high-energy neutrinos are produced uniquely through hadronic interactions involving cosmic rays. These characteristics position high-energy neutrinos as ideal cosmic messengers for identifying hadronic accelerators in the Universe, particularly when analyzed in conjunction with gamma-ray observations.

In recent years, gravitational waves have emerged as a powerful new probe in astrophysics [2, 3]. However, their study and connection to other messengers are beyond the scope of this work, which focuses exclusively on high-energy neutrinos and their relation to cosmic-ray acceleration and gamma-ray emission.

The interconnection between cosmic rays, gamma rays, neutrinos, and gravitational waves originating from a common astrophysical source is illustrated in Figure 1.

In 2013, the IceCube Neutrino Observatory at the South Pole discovered for the first time a diffuse and isotropic flux of high-energy neutrinos from astrophysical origin [4, 5], nearly a century after the first detection of cosmic rays. Over a decade later, this diffuse flux has been confirmed through multiple independent analyses spanning a broad energy range, from approximately 10^{12} eV (TeV) to 10^{15} eV (PeV) [6–11]. Identifying the astrophysical accelerators responsible for these neutrinos has been a

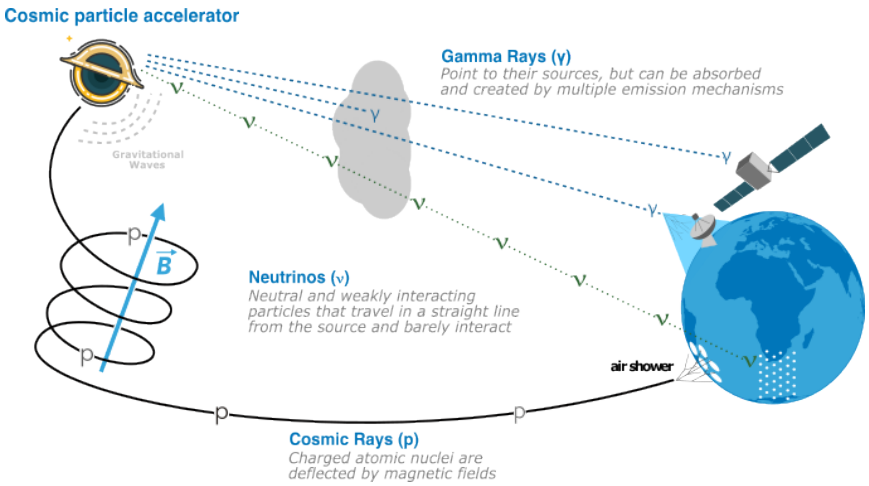

FIGURE 1: Visualisation of the propagation of different subatomic particles from the same source. Unlike cosmic rays, which are deflected by magnetic fields, gamma rays and neutrinos travel in a straight line towards the Earth. However, gamma rays may interact with matter or radiation on their way to the Earth, while neutrinos reach the Earth nearly unaffected. Gravitational waves, also shown for completeness, are not discussed in this work. *Edited with courtesy of J. A. Aguilar.*

major focus of high-energy astrophysics. As such, numerous studies have investigated correlations between IceCube data and potential (extra)galactic sources. While many of these searches have returned null results, they have placed significant constraints on various astrophysical processes (e.g. [12]).

Recently, however, the IceCube Collaboration reported compelling evidence of high-energy neutrino emission from the Galactic plane [13]. Despite its relative proximity, the Galactic plane accounts for only about 10% of the observed diffuse neutrino flux, implying that the majority of this flux originates from extragalactic sources.

Currently, the IceCube data have identified only two extragalactic active galaxies, TXS 0506+056 [14, 15] and NGC 1068 [16], that show tentative evidence of high-energy neutrino emission. However, neither has reached the statistical threshold required to claim a discovery. Even if these sources are confirmed as genuine neutrino emitters, they would collectively contribute less than about 1% of the diffuse neutrino flux within their respective sensitive energy ranges. This leaves the vast majority of the diffuse high-energy neutrino flux unaccounted for, as well as the identity of the corresponding hadronic accelerators.

In addition to correlation studies, multi-wavelength modeling using the results of these studies has provided important insights into the characteristics of potential neutrino sources. For example, studies of NGC 1068 suggest that high-energy neutrinos are likely produced near the galaxy's central supermassive black hole, where simultaneously produced gamma rays are significantly attenuated. These findings align with diffuse neutrino and gamma-ray observations, which indicate that at least a portion of bright neutrino sources must appear dim in gamma rays [17, 18].

This thesis explores **(ultra)luminous infrared galaxies** (U/LIRGs) as candidate sources of high-energy neutrinos. U/LIRGs are distinguished by their extraordinary infrared (IR) luminosities, defined as $L_{\mathrm{IR}} \equiv L_{\mathrm{IR}[8-1000\mu\mathrm{m}]}$, with values exceeding 10^{11} solar luminosities. Such luminosities surpass the total electromagnetic output of the Milky Way by more than an order of magnitude.

The bright IR emission originates primarily from compact regions harboring intense star formation ($\sim$ 10–100 solar masses per year) and actively accreting supermassive black holes ($\gtrsim 10^6$ solar masses), both obscured by dense dust and gas. Such energetic and dynamic environments are promising sites for hadronic particle acceleration, where abundant target material can facilitate the production of secondary particles such as high-energy neutrinos and gamma rays. Additionally, the dense baryonic matter and radiation fields within U/LIRGs can significantly attenuate the gamma rays, making these galaxies promising gamma-ray dim neutrino sources.

In this thesis we focus specifically on characterizing high-energy neutrino emission from local U/LIRGs ($z < 0.09$) in NASA's Great Observatories All-Sky LIRG Survey (GOALS [19]). This is done by developing, in close collaboration with the GOALS team, a phenomenological framework for high-energy neutrino production at the source. Furthermore, we perform a correlation study between experimental high-energy neutrino data from the IceCube Neutrino Observatory at the South Pole and GOALS U/LIGRs in the Northern Hemisphere.

Overview of Chapters

The following provides an overview of the chapters of this thesis, highlighting the key contributions and main findings of each. This research was conducted under a personal PhD Fellowship awarded by the Research Foundation – Flanders (FWO).

Chapter 1

We outline the current understanding of the high-energy Universe through observations of cosmic rays, gamma rays, and high-energy neutrinos. This chapter motivates the search for high-energy neutrino sources to help resolve the standing mystery of cosmic-ray origins.

Contributions & Achievements:

- Co-supervised two bachelor theses focused on high-energy neutrino source identification [20] and modeling [21].

Chapter 2

We explore the properties of U/LIRGs, including their IR luminosities, morphologies, nuclear activity, and redshift evolution. These characteristics are examined to establish U/LIRGs as promising sources of high-energy neutrinos. Additionally, the Great Observatories All-Sky LIRG Survey (GOALS) is introduced, along with the subpopulations of GOALS that will be used for source modeling in Chapter 3 and a correlation study using IceCube data in Chapters 5 and 6.

Contributions & Achievements:

- Further developed a collaborative partnership with the GOALS team, originally established during my master's research.

- Led the compilation of relevant archival electromagnetic data required to characterize the high-energy neutrino production in individual U/LIRGs. I combined this information into a comprehensive table, provided in Table D, alongside the corresponding source-specific neutrino flux predictions obtained in Chapter 3.

Chapter 3

We present a novel framework, developed in this thesis, for modeling steady high-energy neutrino production in starburst regions, using multi-wavelength observations from GOALS. As a case study, we first apply the framework to NGC 3690—the most luminous LIRG within 50 megaparsecs (Mpc). We then extend the analysis to the GOALS sample, providing the first high-energy neutrino flux predictions for the majority of these galaxies. These predictions are compared with the current sensitivity of IceCube and future neutrino observatories. By extrapolating local fluxes across cosmic history, we derive a diffuse high-energy neutrino flux from the global LIRG and ULIRG populations. For LIRGs in particular, this represents the first extrapolation to a large sample based on local multi-wavelength data. Finally, we explore the integration of this model into cosmological hydrodynamical simulations to assess the contribution of starburst activity to the diffuse astrophysical neutrino flux over cosmic time.

Contributions & Achievements:

- This chapter (excluding the framework on cosmological hydrodynamical simulations) is largely based on my first-author publication: *Investigating Starburst-Driven Neutrino Emission from Galaxies in the Great Observatories All-Sky LIRG Survey* [22], published in *Physical Review D*.
- I presented this work orally at the 2023 International Cosmic Ray Conference (ICRC 2023) in Nagoya, Japan [23], the premier conference in astroparticle physics. Additionally, I showcased a poster on this topic at the Netherlands Astronomy Conference (2022), the Belgian Physical Society General Scientific Meeting (2024), and the International School of Cosmic Ray Astrophysics (2024).
- Co-supervised a bachelor's thesis on supernova rate calculations and their impact on neutrino production in U/LIRGs [24], within the context of my model.
- Initiated a novel framework that integrates cosmological hydrodynamical simulations with the neutrino production model developed in this chapter. This was done in collaboration with Romeel Davé, maintainer of the SIMBA simulations [25] and Chair of Physics at the University of Edinburgh.
- Co-supervised a master's thesis that expanded on the framework combining hydrodynamical simulations and starburst-neutrino framework [26] and will be presented at ICRC 2025 in Geneva, Switserland.

Chapter 4

We provide an overview of the IceCube detector, including its detection principles, instrumentation, data acquisition, and event processing. Emphasis is placed on the selection of muon neutrinos coming form the Northern Hemisphere, which form the dataset used in the point-source searches of Chapters 5 and 6.

Chapter 5

This chapter introduces the statistical framework used by IceCube for time-integrated point-source and stacking searches, along with performance tests of the analysis. Using the event selection from Chapter 4 and source selection from Chapter 2, we examine biases, estimate backgrounds, and evaluate sensitivity and discovery potential.

Contributions & Achievements:

- Regularly presented the statistical framework, source selection criteria, dataset choices, and performance metrics for the IceCube Collaboration. I also authored internal documentation detailing this work on the IceCube Wiki[1].
- Developed and maintained reproducible analysis scripts hosted on GitHub[2], utilizing the internal IceCube software `i3SkyLLH` and the open-source `Python` framework `SkyLLH` [27, 28] that provide building blocks for point-source searches. My scripts include tools for background estimation, analysis-specific performance evaluations such as sensitivity and discovery potential calculations, as well as neutrino flux and significance computations. I optimized the scripts for execution on high-throughput computing systems.
- Through interaction with the software and in-depth data analysis, I identified software bugs. These issues were resolved through collaboration with the maintainers of `SkyLLH` and `i3SkyLLH`.

Chapter 6

We report on a search for high-energy neutrino emission from GOALS U/LIRGs in the Northern Hemisphere. While no statistically significant signal was found, an intriguing excess was observed from the nearby LIRG NGC 7469, driven by two events independently flagged by IceCube's realtime alert system. This excess is especially notable given the galaxy's energy output, close distance, and multiple potential neutrino production sites. Furthermore, our results underscore the non-detection of high-energy neutrino emission from a population of starburst-dominated galaxies in the nearby universe, contrasting with independent hints of such emission from AGN-driven sources.

Contributions & Achievements:

- The most stringent upper limits to date on high-energy neutrino emission from a population of powerful nearby sources ($z < 0.09$) in the Northern Hemisphere. The results are presented in Table F.1. Combined with GOALS data, this yields a multi-wavelength dataset that lays the groundwork for future studies of high-energy processes in the local Universe.
- First-time hints of high-energy neutrino emission from the LIRG NGC 7469.
- Recommendations for future targeted neutrino searches using current and next-generation observatories.

Chapter 7

We summarize our investigation of U/LIRGs as potential neutrino sources. Data-driven analyses disfavor nearby starburst-dominated galaxies as detectable point sources of high-energy neutrinos, while systems with combined starburst and AGN activity emerge as more plausible contributors. This supports the growing evidence for AGN–neutrino connections. We further suggest that starburst activity in dense environments over cosmic time may significantly contribute to the diffuse astrophysical neutrino flux. These findings motivate continued exploration of starburst and AGN processes through cosmological hydrodynamical simulations and targeted studies of local hybrid sources.

[1] wiki.icecube.wisc.edu/index.php/Search_for_neutrino_emission_from_LIRGs_and_ULIRGs
[2] github.com/icecube/wg-nu-sources/tree/main/2024_GOALS_Analysis

CHAPTER 1

The High-Energy Universe Seen Through Subatomic Particles

This chapter provides an overview of the high-energy Universe from the perspective of subatomic particles, focusing in particular on high-energy charged atomic nuclei (cosmic rays), gamma rays, and high-energy neutrinos. We discuss acceleration mechanisms, potential sources, and the interrelation between these different messengers. The chapter concludes by emphasizing that solving the century-old mystery of cosmic accelerators may hinge on identifying the sources of high-energy neutrinos, which, based on recent observations, appear to be (partially) dim in gamma rays.

Overview & Context Sections 1.1 and 1.2 review the current observational status of cosmic rays and how these particles can generate gamma rays and high-energy neutrinos at their sources. Sections 1.3 and 1.4 then discuss the diffuse observations of gamma rays and high-energy neutrinos, respectively. In Section 1.5, we combine the information from these different messengers to infer common source properties. Finally, in Section 1.6, we examine the current observational status of point sources of high-energy neutrinos, setting the stage for a focus on (ultra)luminous infrared galaxies as potential sources of high-energy neutrinos, which is the central theme of this work.

1.1 Cosmic Rays

1.1.1 Energy spectrum

Cosmic rays (CRs) are charged subatomic particles of extraterrestrial origin that permeate the Universe. At the lowest energies, below about 10^9 eV (GeV), CRs are primarily sourced from within the heliosphere, the region influenced by the Sun's magnetic field. In contrast, CRs with energies exceeding 10 GeV originate outside the Solar System and are observed by a variety of observatories across a broad energy range, from approximately 10 GeV to 300 EeV [29], where 1 $\mathrm{EeV} = 10^{18}$ eV. Over this range, the particle flux decreases by more than 30 orders of magnitude. The least energetic particles are detected at a rate of one particle per square meter per second, while the most energetic particles are observed at a rate of one particle per square kilometer per century. This vast variation in flux necessitates different detection techniques.

At the lower end of the CR spectrum, where the particle flux is high, CRs can be directly detected using balloon- and space-based experiments, such as the Alpha Magnetic Spectrometer (AMS) [30] aboard the International Space Station (ISS) and the Dark Matter Particle Explorer (DAMPE) [31]. However, such direct detection is practical only for energies below about 100 TeV. At higher energies, where the flux is extremely low, ground-based observatories with large detection areas are required. These observatories take advantage of the fact that CRs interact with the nucleons of molecules in the Earth's atmosphere, creating a hadronic particle cascade with a large

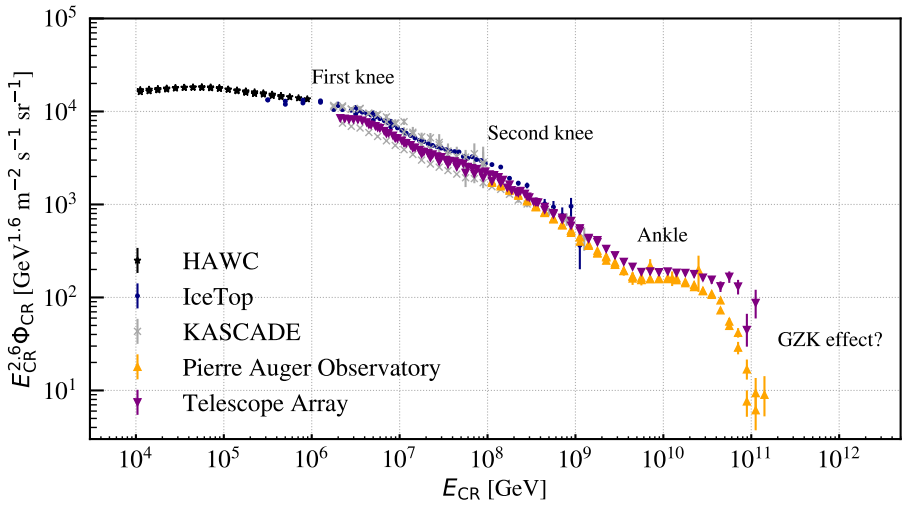

FIGURE 1.1: The all-particle CR energy spectrum above 10 TeV observed by a non-exhaustive list of CR observatories. The CR spectrum is scaled by a factor $E_{\mathrm{CR}}^{2.6}$, with E_{CR} the energy of the CR, to highlight the various features in the CR spectrum. Data for this plot was obtained from: `lpsc.in2p3.fr/crdb/`.

footprint (illustrated in Figure 1). By detecting the particles in this footprint at ground level it is possible to estimate the energy, direction, and composition of the primary CR.

Examples of such ground-based observatories include the High Altitude Water Cherenkov Observatory (HAWC) on the flanks of the Sierra Negra volcano in Mexico, IceTop at the South Pole [32], the Pierre Auger Observatory covering approximately 3000 km^2 in Argentina's Pampa Amarilla [33], and the Telescope Array (TA) in Utah's high desert [34]. The latter two use fluorescence detectors in conjunction with surface detectors to track the longitudinal development of the particle shower [33, 35], providing more accurate measurements of the primary CR's properties. Additionally, the properties of the primary CR can be studied through the radio emission generated as the shower progresses through air. This is done by observatories such as the Low-Frequency Array (LOFAR) [36].

1.1.2 Features of the spectrum

Figure 1.1 shows the all-particle CR energy spectrum (Φ_{CR}, see Appendix A for the implied notation) above 10 TeV as observed by a non-exhaustive list of ground-based CR observatories. A remarkable feature of the CR spectrum is the simplicity of its shape over many orders of magnitude. To emphasize the distinct features in the CR spectrum, the steeply falling flux has been scaled by a factor of $E_{\mathrm{CR}}^{2.6}$, where E_{CR} denotes the CR energy.

The CR particle flux above 10 TeV and up to a few PeV is well described by a single power law in energy, $\Phi(E_{\mathrm{CR}}) \propto E_{\mathrm{CR}}^{-\gamma}$, with $\gamma \approx 2.7$. Beyond this energy, the CR spectrum undergoes a first steepening ($\gamma \approx 3.1$), termed the *first knee*, followed by a second steepening at a few hundred PeV ($\gamma \approx 3.3$), known as the *second knee*. Interestingly, the spectrum hardens at a few EeV ($\gamma \approx 2.5$), forming the *ankle*, and then steeply declines at energies of several tens of EeV. CRs with energies exceeding 1

EeV are classified as **ultra-high energy cosmic rays** (UHECRs). To date, the highest-energy UHECR recorded is the so-called "Oh-My-God" particle, with an energy of about 320 EeV [37].

The broken power-law structure of the CR spectrum is incompatible with a black-body distribution, indicating that CRs are not produced by thermal processes but rather by non-thermal mechanisms in astrophysical sources. These sources are extraordinary accelerators, capable of achieving energies far beyond those reached by terrestrial particle accelerators. Unfortunately, tracing CRs back to their origins is hindered by deflections in magnetic fields due to their electromagnetic charge. Nevertheless, the features observed in the CR spectrum provide insights, as described below.

First knee, second knee, and ankle Due to their charge, CRs gyrate around magnetic field lines. When the gyroradius exceeds the Milky Way's size—approximated here by the scale height of the galactic disk—the CR escapes. The gyroradius ($r_{\rm g}$) is determined by balancing the Lorentz force with the centrifugal force

$$r_{\rm g} = \frac{p_\perp}{eZB},$$

where $p_\perp$ is the particle's momentum perpendicular to the field, e is the elementary charge, Z is the particle's atomic number, and B is the magnetic field strength. Note that for relativistic particles, which are of interest here, the energy of the particle scales with its momentum, $E \approx pc$.

Assuming a scale height of approximately $300\,\mathrm{pc}$ and a mean magnetic field strength of $\sim 3\,\mu\mathrm{G}$ (noting that these parameters remain uncertain), protons with energies exceeding $\sim 1\,\mathrm{EeV}$ cannot be confined within the Milky Way [38]. Consequently, the spectral hardening observed at a few EeV, referred to as the ankle of the CR spectrum, likely signifies the transition from galactic to extragalactic CR sources. Note that the extragalactic source class could become significant somewhat before the ankle, but the exact transition region remains under active debate [39].

In contrast, the first and second knees in the CR spectrum are generally interpreted as the result of galactic CRs reaching the maximum energies achievable by galactic accelerators. Since the maximum energy depends on the particle's charge Z, as discussed later in this chapter, the first knee is thought to correspond to protons ($Z = 1$) reaching their confinement limit, while the second knee is attributed to heavier nuclei, such as iron ($Z = 26$). This interpretation is supported by studies of the CR mass composition, which show a trend toward heavier elements between the first and second knees [40].

There is broad consensus that CRs up to the first knee could originate from non-thermal acceleration in supernova remnants (SNRs) within the Milky Way, which are expanding shells of exploded massive stars ($\gtrsim 8\ M_\odot$). Energy budget considerations suggest that the locally observed CR energy density can be explained if, on average, approximately 10% of the kinetic energy released in stellar explosions is converted into CR acceleration [41–43]. More sophisticated simulations of hadron acceleration in Galactic supernova remnants have demonstrated that the CR spectrum up to approximately 10^{16}–$10^{18}\,\mathrm{eV}$ can be reasonably well reproduced [44]. However, it has also been argued that a single galactic component—with energy cutoffs applied to the individual spectra of different elements—can adequately describe lower energy measurements below approximately 1 PeV, but fails to simultaneously account for both the knee and the second knee in the all-particle CR spectrum [45].

GZK effect During propagation, UHECRs with energies above ~ 60 EeV are expected to interact with the cosmic microwave background (CMB), the relic radiation from the Big Bang. Such interactions reduce the energy of the corresponding reaction products, suppressing the flux unless the UHECRs originate within a few tens of Mpc. This attenuation is known as the GZK effect, named after Greisen [46] and Zatsepin & Kuz'min [47]. However, it remains unclear whether the observed steep flux decline at the highest energies shown in Figure 1.1 is solely due to the GZK effect or also reflects a limit on the maximum energies attainable by cosmic accelerators.

1.1.3 Acceleration mechanisms

The exact acceleration mechanisms that give rise to the CRs remain unknown. In any case, the mechanism should be able to transform particles from a thermal population into a non-thermal distribution following a power-law spectrum (see Figure 1.1).

Direct acceleration by electric fields is largely ineffective in most astrophysical settings, because highly conductive, ionized plasmas quickly rearrange free charges to short out any large-scale electric fields. Instead, the electric fields required for particle acceleration arise from the bulk motions of magnetized plasmas [48]. In particular, when a shock front—a sharp discontinuity propagating faster than the local sound speed—forms in the interstellar medium, charged particles can scatter repeatedly across it and gain energy on each crossing. This process, known as diffusive shock acceleration (DSA), implements the first-order Fermi mechanism [49–51] and naturally produces the observed power-law spectrum of CRs. Although a full treatment of DSA's microphysics is beyond the scope of this work, we outline its key principles and highlight the features relevant for further discussions.

In DSA, particles gain energy by repeatedly crossing the shock front, interacting with moving magnetic fields. The relative energy gain per crossing is proportional to the shock velocity β, leading to $\Delta E/E \propto \beta$. Since the energy gain is independent of the particle's energy and the escape probability from the acceleration region remains constant, the system exhibits scale invariance[1], naturally producing a power-law energy spectrum [52]. For non-relativistic shocks ($\beta \ll 1$) this mechanism yields [53]

$$\frac{\mathrm{d}N}{\mathrm{d}E} \propto E^{-2}. \tag{1.1}$$

Interestingly, the predicted spectral index γ at strong, non-relativistic shocks ($\gamma \approx 2$) coincides with the injection spectrum required to explain galactic CRs up to the knee. After propagation through the Galaxy, diffusive losses soften the source spectrum to approximately $E^{-2.7}$ (see Figure 1.1) [54]. In practice, however, deviations from the idealized $\gamma \approx 2$ source spectrum can arise due to variations in the shock compression ratio, obliquity, and the underlying magnetic-turbulence spectrum.

UHECRs, believed to be of extragalactic origin, are likely accelerated in relativistic shocks ($\beta \approx 1$). In such environments, first-order Fermi acceleration remains viable, though the resulting spectral index may differ from $\gamma = 2$. Additionally, alternative acceleration mechanisms have been proposed for UHECRs, including unipolar induction, magnetic reconnection, wakefield acceleration, and shear or one-shot acceleration (see, e.g., [48] and references therein).

In conclusion, there are multiple possible mechanisms that could lead to particle acceleration. These mechanisms range from diffusive shock acceleration to entirely

[1] The system has no inherent energy scale to favor specific particle energies

different processes. Each mechanism is supported by observational evidence or theoretical modeling efforts.

1.1.4 Source candidates

Although CRs with energies up to the knee, around a few PeV, are generally attributed to galactic sources, the origins of UHECRs remain far less understood. The population of sources responsible for the observed UHECR flux must satisfy at least two key conditions. First, the sources must not only be capable of accelerating particles, but also confine them up to ultra-high energies (greater than 1 EeV). This requirement is commonly quantified by the Hillas criterion, which relates the maximum energy of accelerated particles to the size and magnetic field strength of the acceleration region. Second, the energy budget of the source population must be sufficiently large to account for the observed UHECR flux. In the following, we delve into these two conditions.

- **Hillas criterion:** To accelerate a CR, the magnetic field within an accelerator must confine the particle. For a uniform magnetic field B, the maximum CR energy ($E_{\mathrm{CR,max}}$) is reached when the gyroradius of the CR is comparable to the characteristic size of the accelerator. This relationship forms the basis of the Hillas criterion [55]. For a CR with charge $q = Ze$, where e is the elementary charge and Z is the atomic number, the maximum energy for a (relativistic) shock moving at velocity $\beta_{\mathrm{sh}}c$ is [48, 56]

$$E_{\mathrm{CR,max}} \approx \eta^{-1}\beta_{\mathrm{sh}} cqBR\Gamma, \tag{1.2}$$

  where R is the comoving size of the accelerator, and Γ is the bulk Lorentz factor accounting for relativistic flows.[2] The parameter $\eta \geq 1$ represents the acceleration efficiency, with $\eta = 1$ corresponding to the Bohm diffusion limit. Since $E_{\mathrm{CR,max}}$ depends on Z, heavier nuclei can achieve higher maximum energies than lighter ones within the same accelerator.

  It is important to note that the Hillas criterion provides an upper limit on the achievable energy, assuming acceleration is feasible. Additional constraints, such as the lifetime of the accelerator and energy losses due to interactions, further limit the maximum energy attainable by CRs.

  By applying Eq. (1.2) to (extra)galactic sources with known or estimated magnetic fields and sizes, one can evaluate their potential to accelerate UHECRs to particular energies. Figure 1.2 illustrates the capability of various astrophysical objects to confine CRs with energies up to 10^{20} eV. Objects located to the left of a given line cannot accelerate particles to such energies under the assumed conditions. For instance, Wolf-Rayet stars, despite their strong magnetized winds, are unlikely to be UHECR sources. In contrast, subclasses of gamma-ray bursts (GRBs), active galactic nuclei (AGN), and starburst galaxies satisfy the Hillas criterion, with AGN and starburst galaxies being particularly relevant for this work.

- **Required energy budget:** To contribute significantly to the observed UHECR flux, a source population must possess a sufficiently large cumulative energy budget. This energy budget can be derived from the observed UHECR flux but

[2] The original formulation by Hillas did not include the efficiency factor η and the bulk Lorentz factor Γ.

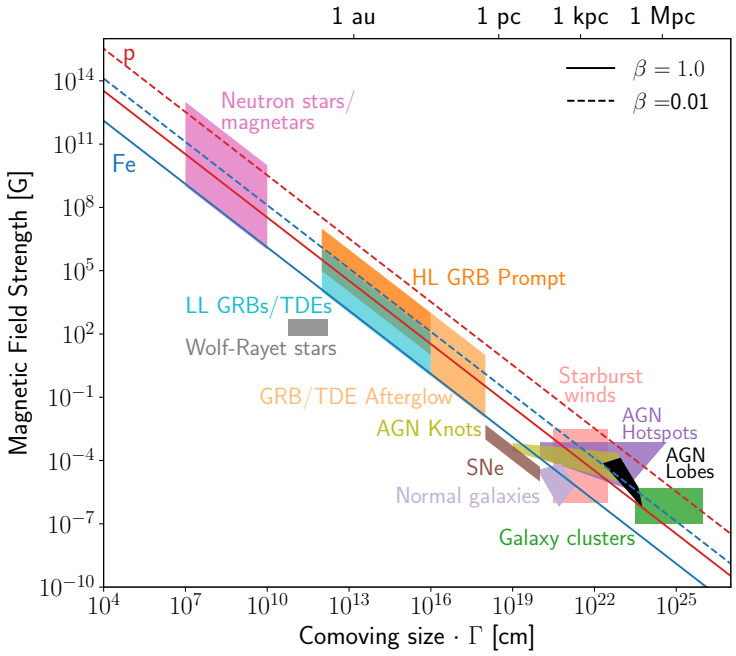

FIGURE 1.2: Hillas diagram presenting various known astrophysical objects, characterized by their magnetic field strength (B) and characteristic size (R) in the comoving frame. The extended regions represent uncertainties in these parameters. Solid diagonal lines indicate the minimum product of magnetic field strength (B) and accelerator radius (R) required to accelerate protons (red) and iron nuclei (blue) to an energy of 10^{20} eV, assuming an extreme shock velocity of $\beta_{\rm sh} = 1$ and maximum acceleration efficiency ($\eta = 1$). Dashed lines represent the same requirement for protons and iron but with a much slower shock velocity of $\beta_{\rm sh} = 0.01$. Source classes occupying parameter space to the left of the diagonal lines cannot satisfy the conditions necessary to accelerate particles to 10^{20} eV for the respective shock velocities and efficiency. The diagram demonstrates that slower shocks necessitate a higher $B \cdot R$ product to achieve the same particle energy. Figure taken from [56].

depends on several model-dependent factors, including the injected CR spectrum per source, the composition of the UHECRs, the efficiency of CR acceleration, and the evolution of the source populations over cosmic time. Despite these dependencies, estimates converge to $\gtrsim 5 \times 10^{43}$ erg Mpc^{-3} yr^{-1}, which corresponds to the energy generation rate of the sources required to sustain the observed UHECR flux at Earth [48, 56].

Below, we present an overview of promising candidate source classes that satisfy the Hillas criterion, although they may not meet the energy requirements necessary to account for the observed UHECR flux. The aim is not to offer a comprehensive review of each class in the context of UHECR production but to highlight their general characteristics and relevance as potential sources of high-energy radiation. For detailed discussions on these source classes as UHECR sources, see, for example, the reviews in [48, 56].

Gamma-ray bursts

Gamma-ray bursts (GRBs) are brief yet extraordinary luminous explosions, characterized by an isotropic bolometric luminosity of approximately $L_{\rm bol} \sim 10^{51}$ erg s^{-1}, and lasting anywhere from a few milliseconds to several minutes. GRBs are typically divided into two populations based on the duration of the flash [57]: short GRBs, which last less than two seconds, and long GRBs, which persist for more than two seconds. These categories are linked to distinct progenitor systems. Short GRBs are likely the result of the merger of compact objects, such as neutron stars or black holes, while long GRBs are thought to originate from the direct collapse of a massive star into a black hole.

GRBs have long been proposed as potential sources of UHECRs [58], supported by their ability to satisfy the Hillas criterion. In particular, low luminosity (LL) GRBs have been suggested as compelling candidates. This is due to their significant number density, which compensates for their lower relativistic outflow compared to the more classical high luminosity (HL) GRBs [48].

Starburst Galaxies

Starburst galaxies are characterized by elevated star formation rates, particularly inside their central kiloparsec (kpc) regions, reaching approximately 10–100 $M_\odot$ yr^{-1} [19, 59]. This contrasts with more quiescent star-forming galaxies, such as the Milky Way, where the star formation rate is only about 1–5 $M_\odot$ yr^{-1} [60]. The enhanced star formation in starburst galaxies leads to a higher rate of massive stars undergoing supernova explosions, which drive strong shock waves that serve as potential sites for particle acceleration (see Section 1.1.3). Although supernova remnants in starburst galaxies—where magnetic fields can far exceed those in the Milky Way—can accelerate particles to higher energies, they are unlikely to do so efficiently into the ultra-high-energy regime [61–64].

At the center of a supernova remnant, a dense, rapidly rotating neutron star often remains. Depending on their observable properties, neutron stars are classified into various types. Magnetars possess exceptionally strong magnetic fields, approximately three orders of magnitude stronger than typical neutron stars. Pulsars, on the other hand, are neutron stars that emit beams of electromagnetic radiation from their magnetic poles, observed as periodic signals. These neutron star varieties are considered promising candidates for UHECR acceleration [65].

The dense environments and strong magnetic fields in starburst galaxies pose significant challenges for CR escape. CRs may undergo interactions with the surrounding medium before escaping, resulting in substantial energy losses. Regions where interaction timescales are much shorter than the CR escape times are referred to as CR reservoirs or CR calorimeters (e.g. [66]; see also Chapter 3). Despite these constraints, starburst galaxies also produce powerful, magnetized galactic-scale winds with velocities ranging from hundreds to thousands of kilometers per second [67]. These winds, driven by the combined effects of supernova feedback, stellar winds, and intense radiation pressure, offer an alternative environment for particle acceleration, potentially allowing UHECRs to escape more efficiently (see e.g. [68]).

The term starburst galaxy encompasses a broad spectrum of physical conditions and classifications. Some notable subtypes include: Wolf-Rayet galaxies, characterized by a large fraction of their bright stars being Wolf-Rayet stars; blue compact galaxies, which are low in mass, metallicity, and dust content; and (ultra)luminous infrared galaxies (U/LIRGs), distinguished by their intense infrared emission, indicative of the most vigorous star-formation environments in the local Universe. However, not all galaxies exhibiting significant starburst activity fall neatly into these subtypes. For instance, prominent nearby starburst systems such as Messier 82 (M82) and NGC 253 do not belong to any of these specific categories.

In this thesis, our focus is specifically on U/LIRGs, which are formally introduced in Chapter 2.

Active Galactic Nuclei (AGN)

There is growing evidence that every massive galaxy contains a spinning supermassive black hole (SMBH) with a mass $\gtrsim 10^6\ M_\odot$ at its center [69]. When gas accretes onto the SMBH, it can create an enhanced state of activity known as an active galactic nucleus (AGN). This phenomenon is characterized by strong electromagnetic emission over twenty orders of magnitude in frequency, emanating from a compact region on the order of milliparsecs (see for example [70] for a review). Over the years, many observatories have targeted these fascinating astrophysical objects, and the rich observational history of AGN has led to a complex classification scheme. However, it is now clear that this classification is only partly due to intrinsic differences between AGN. Rather, the observed differences arise from variations in a few key parameters such as the orientation, accretion rate, and the presence/absence of particle jets [71]. Several components commonly found in AGN are listed below in order of their proximity to the central SMBH (for further details, see e.g., [70] and references therein). These components are also illustrated in Figure 1.3.

- A hot *accretion disk* surrounds SMBH at sub-pc scales, emitting radiation across a broad spectrum, from optical to X-ray wavelengths. The intense gravitational and dynamic interactions within the disk, combined with magnetic dissipation, can lead to the formation of a hot, turbulent, and magnetized plasma in the disk's vicinity known as the corona. This plasma interacts with photons emitted by the accretion disk. Through inverse Compton scattering, electrons in the plasma can transfer energy to these lower-energy photons, boosting their energies to the X-ray regime. This process contributes to the high-energy X-ray emission commonly observed from AGN.

- A *broad-line region* located at 0.1–1 pc, consisting of high-density clouds moving at approximately Keplerian velocities.

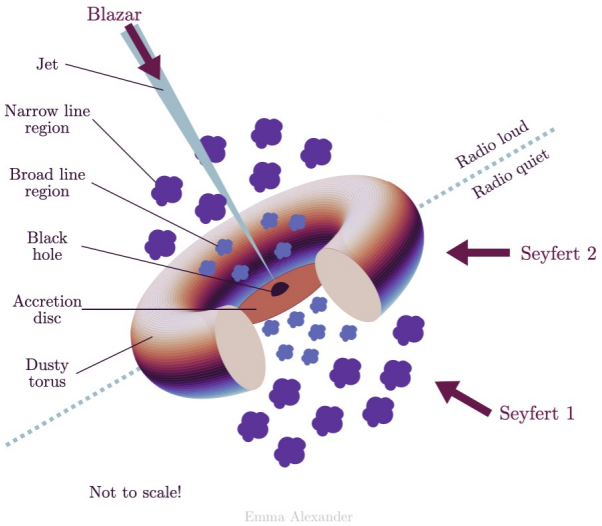

FIGURE 1.3: Illustration of various components found in active galactic nuclei as well as the types of AGN—blazar, Seyfert 1 and 2—that are relevant to this work. Credit to: *E. Alexander*

- A *dusty torus*-like structure extending from ~ 0.1–10 pc. This structure, heated by the accretion disk, is a source of infrared emission.
- A *narrow-line region*, consisting of ionized clouds with lower density and velocity than those in the broad-line region. This region extends from just outside the torus up to hundreds or thousands of pc along the opening of the torus.
- A *relativistic particle jet* perpendicular to the accretion disk *can* be present and can extend up to the $\sim$ Mpc scale, reflecting the immense power of these systems. These jets are known to emit powerful gamma rays.

Historically, AGN have been classified into two main groups: radio-loud and radio-quiet (each with multiple subclassifications). However, as these labels stem from observational differences rather than intrinsic physical distinctions, an alternative classification scheme has been proposed. The proposition is to replace radio-loud and radio-quiet with *jetted* and *non-jetted*, respectively [72]. Using this classification, we highlight some AGN types that are relevant to this work:

- **Jetted AGN:** When the relativistic jet of an AGN is closely aligned with the observer's line of sight, the AGN is classified as a **blazar**. If the jet is observed at an angle from the side, the AGN falls into the *Fanaroff-Riley* (FR) classification, with FR-I and FR-II types distinguished based on the morphology and brightness distribution of the jets. Specifically, FR-I AGN exhibit jets that gradually become fainter with increasing distance from the core, while FR-II AGN display bright terminal hotspots where the jets interact with the surrounding medium. Notably, only a minority of AGN, less than about 10%, exhibit prominent relativistic jets [73].

  These large-scale relativitsitc jets are considered prime candidates for accelerating hadrons to ultra-high energies. Despite their relatively low occurrence rate, they remain compelling candidates for contributing a (significant) fraction of the observed UHECR flux (see, e.g., [74] for a review).

- **Non-jetted AGN:** The most common subclass of AGN without prominent relativistic jets is comprised of **Seyfert galaxies**. These AGN were initially divided into Type I (or Seyfert I) and Type II (or Seyfert 2) based on differences in their optical spectra [75]. It is now understood that these spectral differences arise primarily from the observer's viewing angle, specifically whether or not the line of sight is obscured by the dusty torus surrounding the central region.

  A quantity relevant for this work related to the classification of Seyfert I and II galaxies is the **column density**, representing the amount of obscuring matter along the observer's line of sight when observing the galaxy. This parameter is typically expressed as the hydrogen column density (N_{H}), defined as the number of hydrogen atoms per unit area along the line of sight. A source is per definition classified as *Compton thick* if $N_{\mathrm{H}} \geq 1.5 \times 10^{24}\ \mathrm{cm}^{-2}$, corresponding to an optical depth of unity for Compton scattering [76].

  In contrast to jetted AGN, Seyfert galaxies are expected to reach comparatively lower maximum CR energies. It is unclear whether UHECR energies can be efficiently produced in such sources. However, their greater abundance makes them noteworthy in discussions of high-energy sources [56].

Tidal Disruption Events

When a star passes close to a SMBH, it can be disrupted if the tidal forces exceed the self-gravity of the star. This process, known as a tidal disruption event (TDE), leads to the disintegration of the star into debris. If the disruption occurs outside the event horizon of the SMBH, the stellar debris can be gravitationally bound to the black hole, forming an accretion disk. The accretion process results in a luminous flare of electromagnetic radiation, often observed across multiple wavelengths (see e.g. [77] for a review of TDEs).

In a fraction of these events, a relativistic jet of particles is expected to be formed, likely driven by the rapid accretion onto the SMBH and associated magnetic processes. These relativistic jets could accelerate particles to ultra-high energies, potentially making TDEs a source of UHECRs [78, 79]. Over time, as the SMBH gradually accretes the stellar debris, the emission fades, with typical timescales ranging from several months to a year.

TDEs are rare transient phenomena, with only about 10^{-4} per galaxy per year [80], and only about four confirmed to exhibit relativistic jets [77, 81]. This low occurrence rate limits their ability to supply a dominant fraction of the observed UHECR flux. However, TDEs remain compelling candidates for UHECR production due to their ability to reach the required ultra-high energies and the extreme physical conditions present during jet formation.

1.2 Neutrinos & Gamma Rays from Cosmic Rays

As discussed in Section 1.1, cosmic rays (CRs) are extensively observed; however, their origins remain largely unkown. Due to their electric charge, CRs are deflected by magnetic fields during propagation, which prevents them from pointing directly back to their sources. Nonetheless, not all CRs escape their sources unaltered. A fraction of CRs may undergo interactions either within the source environment or during their propagation through space. If the energy of a CR is sufficiently high, it can experience inelastic collisions with baryonic matter or ambient radiation fields through **hadronuclear** or **photohadronic** interactions, respectively.

These interactions produce, among others, charged and neutral pions. The decay products of these pions—electrons, positrons, gamma rays, and neutrinos—are related and provide a unique opportunity to identify and study cosmic accelerators.

In the following sections, we will explore photohadronic and hadronuclear interactions in greater detail, followed by a discussion of the relationships between the three cosmic messengers: CRs, gamma rays, and neutrinos.

1.2.1 Hadronic interactions

In the remainder of this work, we assume, for the sake of simplicity, that both CRs and the target material consist of protons (p).[3] Under this assumption, photohadronic interactions reduce to pγ interactions, and hadronuclear interactions to pp interactions.

Both pγ and pp-interactions are inelastic collisions that produce an avalanche of new particles, including baryons and mesons. Among the mesons, the charged pions ($\pi^{\pm}$) and neutral pions (π^0) are the most abundant.[4] Pion decay yields neutrinos and gamma rays which can leave the source environment with a fraction of the CR energy. However, both interactions are different in terms of energy threshold, cross section, and pion production.

pγ-interactions

- **Energy threshold:** The cross section for pγ-interactions peaks at the so-called Δ–resonance, which occurs when the CR energy surpasses the threshold required to produce a Δ^+–baryon. This threshold energy ($E_{\mathrm{p,thr}}$) can be derived using four-vector kinematics and is expressed as

$$E_{\mathrm{p,thr}} = \frac{m_\Delta^2 - m_p^2}{4E_\gamma} \ . \tag{1.3}$$

  Here, E_γ is the energy of the target radiation field, m_Δ is the mass of the Δ^+–baryon, and m_p is the mass of the proton [29]. This calculation assumes a head-on collision between the photon and the proton.

  For example, when considering the cosmic microwave background (CMB) as the target radiation field with $E_\gamma \sim 0.6$ meV, the threshold energy required for a pγ-interaction is $E_{\mathrm{p,thr}} \sim 6 \times 10^{19}$ eV. This is known as the GZK limit, as discussed in Section 1.1.2. For higher-energy target photons, such as ultraviolet photons with $E_\gamma \sim 10$ eV, the energy threshold decreases significantly to $E_{\mathrm{p,thr}} \sim 10^{16}$ eV.

[3] Extrapolation to heavier nuclei is relatively straightforward, as they undergo similar interactions at the energies of interest.

[4] In pp-interactions roughly 80% of the newly produced mesons are pions and the remaining mesons consist mostly of kaons [82]. However, for pγ-interactions, the kaons contribute about one or two orders of magnitude less to the total meson fluxes [83].

- **Total cross section:** The total cross section for pγ-interactions, illustrated in Figure 1.4, can be approximated as a two-step function. Near the Δ–resonance, the cross section reaches $\sigma_{\mathrm{p}\gamma} \approx 340$ μb, while at higher energies, it plateaus at $\sigma_{\mathrm{p}\gamma} \approx 120$ μb. However, a comprehensive model of pγ-interactions must also account for higher-order processes, such as multi-pion production, direct pion production, and contributions from additional baryon resonances [83].

- **Pion production:** At the Δ–resonance, pγ-interactions predominantly produce charged and neutral pions as

$$\mathrm{p} + \gamma \to \Delta^{+} \to \begin{cases} p + \pi^{0} & \text{(fraction } 2/3\text{)} \\ n + \pi^{+} & \text{(fraction } 1/3\text{)} \end{cases}, \tag{1.4}$$

  where the relative fractions are dictated by isospin conservation. This gives rise to a charged-to-neutral pion number ratio defined as

$$K_{\pi} \equiv \frac{N_{\pi^{\pm}}}{N_{\pi^{0}}}, \quad \text{where} \quad N_{\pi^{\pm}} \equiv N_{\pi^{+}} + N_{\pi^{-}}\,, \tag{1.5}$$

  with $N_{\pi^{\pm}}$ the number of $\pi^{\pm}$ mesons. At the the Δ–resonance, $K_{\pi} = 0.5$. However, when higher-order processes, such as multi-pion production, are taken into account, this ratio shifts to $1 \lesssim K_{\pi} \lesssim 3/2$ for pγ-interactions [83].

  Finally, numerical studies of the interaction phase space indicate that approximately 20% of the initial CR energy is transferred to the pion during a photohadronic interaction [84].

pp-interactions

- **Energy threshold:** Unlike pγ-interactions, the energy threshold for hadronuclear (pp) interactions is trivially satisfied in most astrophysical environments. A pp-interaction can occur whenever the center-of-mass energy is sufficient to produce a pion. Using four-vector kinematics, the threshold energy for the CR proton ($E_{\mathrm{p,thr}}$) in the rest frame of the target matter is given by

$$E_{\mathrm{p,thr}} = m_{\mathrm{p}}c^{2}\left(1 + \frac{m_{\pi}^{2} + 4m_{\pi}m_{p}}{2m_{\mathrm{p}}^{2}}\right)\,, \tag{1.6}$$

  which corresponds to $E_{\mathrm{p,thr}} \gtrsim 1.22$ GeV.

- **Total cross section:** The cross section for pp-interactions, σ_{pp}, shown in Figure 1.4, begins at $\sigma_{\mathrm{pp}} \approx 30$ mb near the interaction threshold and rises to $\sigma_{\mathrm{pp}} \approx 80$ mb at around 100 PeV. This makes the cross section of pp-interactions about two orders of magnitude larger than that of pγ-interactions. However, for pp-interactions to occur efficiently, the astrophysical environment must have sufficiently dense regions of target matter, which may not be trivial for all sources. This topic is discussed in detail in the context of starburst galaxies in Chapter 3, and is also relevant for active galactic nuclei (e.g., [85]).

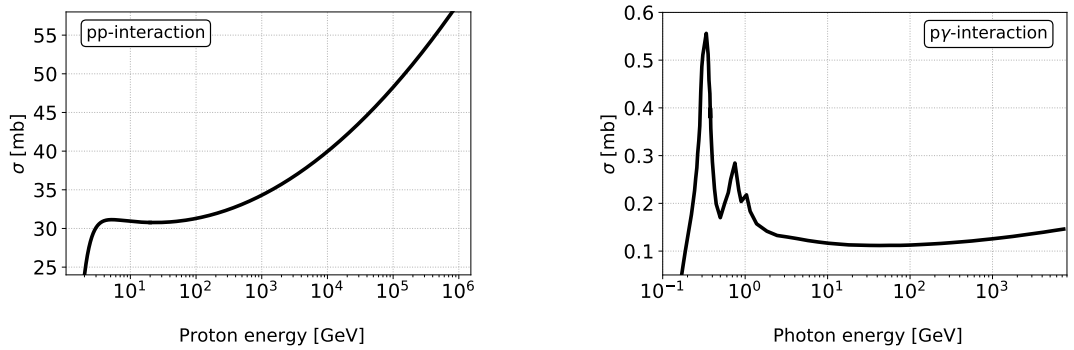

FIGURE 1.4: Left: Interaction cross section for inelastic pp-interactions as a function of proton energy in a fixed target frame. This plot uses the cross section parameterization in [87], constructed from accelerator and simulation data. Right: Total interaction cross section of pγ-interactions as a function of the required photon energy in the rest frame of the proton. Figure adapted from [84].

- **Pion production:** In the simplest case of single-pion production, pp-interactions produce charged and neutral pions as

$$\mathrm{p} + \mathrm{p} \rightarrow \begin{cases} \mathrm{p} + \mathrm{p} + \pi^0 & (\text{fraction } 2/3), \\ \mathrm{p} + n + \pi^+ & (\text{fraction } 1/3)\ , \end{cases} \tag{1.7}$$

  where the relative fractions are determined by isospin conservation. Unlike pγ-interactions, pp-interactions do not have a significant energy threshold, meaning that protons of virtually all energies can interact. This is expected in astrophysical environments where CR acceleration is possible. Thus, for increasing proton energy, multi-pion production becomes more significant. Due to isospin conservation, an approximately equal number of charged and neutral pions is expected, resulting in a charged-to-neutral pion ratio, defined in Eq. (1.5), of $K_\pi \approx 2$ for pp-interactions [86].

  Finally, numerical simulations indicate that approximately 17% of the initial kinetic energy of the CR proton is transferred to each pion [87].

1.2.2 A powerful connection

The pions produced in pγ and pp interactions are unstable, decaying rapidly with lifetimes of 8.4×10^{-17} s for neutral pions and 2.6×10^{-8} s for charged pions [29].[5] Regardless of the hadronic interaction that produced them, the pions decay as

$$\begin{aligned} \pi^+ &\rightarrow \mu^+ + \nu_\mu \rightarrow e^+ + \overline{\nu}_\mu + \nu_e + \nu_\mu, \\ \pi^- &\rightarrow \mu^- + \overline{\nu}_\mu \rightarrow e^- + \nu_\mu + \overline{\nu}_e + \overline{\nu}_\mu, \\ \pi^0 &\rightarrow \gamma + \gamma\ , \end{aligned} \tag{1.8}$$

[5] Note that these decay timescales differ significantly, as the former proceeds via an electromagnetic decay, whereas the latter proceeds via a weak decay.

where the decay products consist of electrons, positrons, gamma rays, and high-energy neutrinos.[6]

As discussed in Section 1.2.1, approximately 20% of the parent CR energy is transferred to each pion in both pp and pγ interactions. Since the final pion-decay products are significantly lighter than the pions themselves, they share the pion energy approximately equally. From the decay chains in Eq. (1.8), it then follows that roughly 10% of the initial CR energy is transferred to each gamma ray, while about 5% is transferred to each lepton. This provides a direct connection between the average energies of CRs ($E_{\rm CR}$), gamma rays (E_γ), and high-energy neutrinos (E_ν), which can be expressed as (e.g., [88, 89])

$$E_\nu \sim \frac{E_\gamma}{2} \sim \frac{E_{\rm CR}}{20} \ . \tag{1.9}$$

Consequently, the energy generation rates of gamma rays and neutrinos at the source—each with dimensions of energy per unit volume per unit time—are related (e.g., [90]; see also Appendix A for notation):

$$E_\gamma \mathcal{Q}_{E_\gamma} \approx \frac{4}{3K_\pi} \left[E_\nu \mathcal{Q}_{E_\nu}\right]\big|_{E_\nu = E_\gamma/2} \ , \tag{1.10}$$

where K_π is the charged-to-neutral pion ratio defined in Eq. (1.5).

It is crucial to exercise caution when applying the relation in Eq. (1.10), as gamma rays are also efficiently produced via other processes that are not related to hadronic interactions (e.g. inverse Compton scattering). Moreover, gamma rays may be attenuated by dust and gas within the Universe.

The relationship between the decay products of pions provides a framework for identifying and studying cosmic accelerators through the secondary particles generated by CR interactions, rather than relying solely on direct observations of the CRs themselves.

Electrons and positrons, due to their rapid energy losses via mechanisms such as synchrotron radiation in magnetic fields and electromagnetic cascades in the surrounding medium, cannot escape their astrophysical environments. In contrast, gamma rays and neutrinos possess the critical property of being electrically neutral, allowing them to propagate in straight lines from their source to Earth, unaffected by magnetic fields. Gamma rays, however, face limitations as a fraction of gamma rays produced at the source may be absorbed by dust and gas in the Universe. Additionally, gamma-ray production is not unique to hadronic interactions, as leptonic processes can also contribute significantly. Despite these challenges, gamma rays remain valuable probes of cosmic accelerators, especially for those relatively close to the Earth.

High-energy neutrinos, in contrast, are uniquely[7] produced by CR interactions and interact only via the weak force and gravity, making them unique and powerful cosmic messengers. The shared origin of CRs, hadronic gamma rays, and neutrinos is illustrated in Figure 1. Coordinated observations of these messengers enable insights

[6] Neutrons produced in pγ and pp-interactions also contribute an additional flux of electron antineutrinos through beta decay, $n \to {\rm p} + e^- + \overline{\nu}_e$. Unlike the high-energy neutrinos from charged-pion decay, these electron antineutrinos are generally lower in energy.

[7] High-energy neutrino production via leptonic processes is possible but unlikely. For example, [91] investigated a leptonic scenario where di-muon production results from di-photon scattering and concluded it is unlikely to account for most of IceCube's diffuse flux, particularly at the highest energies. Similarly, [92] excluded this model for IceCube's most significant high-energy neutrino source (see Section 1.6.2).

into processes within the same astrophysical source, forming the foundation of **multi-messenger astronomy**.

Combining information from different messengers is crucial for advancing our understanding of the extraordinary cosmic accelerators that produce them. Before exploring some insights gained from multi-messenger astronomy, we first discuss the state-of-the-art of gamma-ray and high-energy neutrino astronomy individually.

1.3 Diffuse Gamma-Ray Astronomy

Gamma rays, the most energetic form of electromagnetic radiation, have energies (E_γ) exceeding 100 keV. The closest extraterrestrial gamma-ray source is the Sun, which typically emits gamma rays in the MeV energy range during solar flares. Extrasolar gamma rays originate both from sources within the Milky Way and from extragalactic objects. As discussed in Section 1.2, gamma rays can be produced through neutral pion decay, $\pi^0 \to \gamma + \gamma$, where the pions are generated via hadronic processes. Additionally, astrophysical environments rich in plasmas—consisting of free electrons and ions—give rise to various leptonic processes that also contribute to gamma-ray production. These processes include:

- *Bremsstrahlung*: Emission occurs when an electron (e^-) is deflected in the electric field of a nucleus (N). The energy lost during deceleration is emitted as a photon (γ), described by $e^- + N \to e^- + N + \gamma$.
- *Synchrotron Radiation*: Electromagnetic radiation emitted by charged particles gyrating in magnetic fields.
- *Inverse Compton Scattering*: This occurs when a high-energy charged particle (e.g. an electron) collides with a photon, transferring kinetic energy to the photon and increasing its energy, $e^-_i + \gamma_i \to e^-_f + \gamma$, with $E_{e^-_i} > E_{e^-_f}$ and $E_{\gamma_f} > E_{\gamma_i}$.

Figure 1.5 presents a sky map in galactic coordinates showing gamma-ray emission between 10 GeV and 2 TeV observed over 7 years by the *Fermi* Large Area Telescope (LAT) [93]. The map reveals that most gamma rays in this energy range originate from within the Milky Way, with the galactic plane being a dominant feature. In the Milky Way, gamma rays are produced by point sources such as pulsars and by extended sources like supernova remnants and pulsar wind nebulae. Additionally, there is a diffuse contribution from cosmic rays (CRs) interacting with interstellar gas in the Milky Way.

In addition to the galactic component, Figure 1.5 shows an extragalactic gamma-ray component. The cumulative flux of all extragalactic gamma-ray emission is termed the **extragalactic gamma-ray background** (EGB), which consists of two primary components:

- **Resolved gamma-ray sources**: The dominant contributors to the resolved EGB are blazars, which are AGN with relativistic jets directed towards Earth (see Section 1.1.4). Blazars account for approximately $86^{+16}_{-14}\%$ of the resolved EGB, with secondary contributions from objects such as radio galaxies and star-forming galaxies [94]. Among the latter, starburst galaxies—characterized by exceptionally high star formation rates (Section 1.1.4)—are of particular interest for this work.

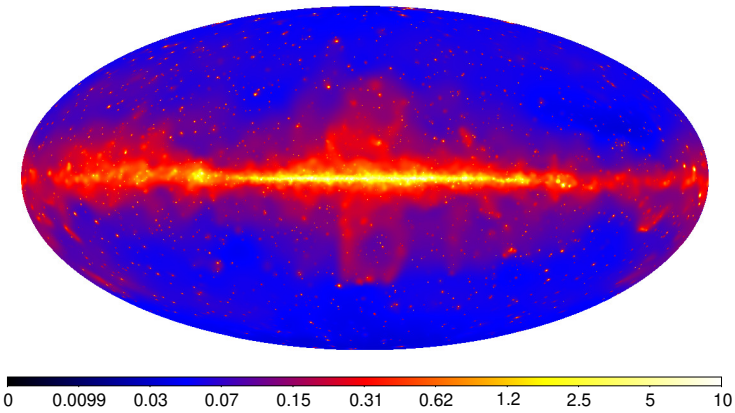

FIGURE 1.5: All-sky gamma-ray map between $10\,\mathrm{GeV}$ and $2\,\mathrm{TeV}$ based on 7 years of *Fermi*-LAT data [93]. The color scale is logarithmic and represents counts per pixel with a resolution of $0.1^\circ \times 0.1^\circ$. The map highlights the prominence of the galactic plane and the existence of extragalactic point sources.

The *Fermi*-LAT collaboration identified 14 star-forming galaxies as gamma-ray point sources over 10 years of observations [95]. A more recent analysis of nearly 15 years of public *Fermi*-LAT data reported evidence for two additional point sources while questioning the significance of one previously identified source [96].

- **Diffuse isotropic gamma-ray background** (IGRB):
  - The IGRB includes contributions from unresolved point sources, such as lower-flux blazars, misaligned AGN, and star-forming galaxies. The population of unresolved sources depends on detector sensitivity, with more sensitive instruments identifying fainter sources.
  - A diffuse component arises from gamma rays cascading down in energy through interactions with radiation fields in the Universe.

    The energy threshold for producing an electron-positron pair is given by $E\epsilon > (m_e c^2)^2$, where E is the energy of the gamma ray, ϵ is the energy of the target radiation field, and m_e is the mass of the electron/positron. Gamma rays above $\sim 100\,\mathrm{GeV}$ (the upper limit of *Fermi*-LAT's energy range) can interact with the extragalactic background light (EBL), which is composed of cumulative radiation from star formation and AGN activity spanning infrared to ultraviolet wavelengths. For example, at around $1\,\mathrm{TeV}$, the gamma-ray horizon due to EBL interactions corresponds to a distance of a few $100\,\mathrm{Mpc}$. Observing gamma rays from sources beyond this distance requires long exposure times. At even higher energies, gamma rays with energies of several $100\,\mathrm{TeV}$ will predominantly interact with the cosmic microwave background (CMB), restricting the gamma-ray horizon to the kpc scale. This interaction makes gamma-ray astronomy infeasible at such extreme energies [97].

Figure 1.6 illustrates the EGB, IGRB, and resolved gamma-ray sources (for galactic latitude $|b| > 20^\circ$) as functions of photon energy [94]. The observed diffuse gamma-ray energy spectrum (Φ_γ, see Appendix A) of both the EGB and IGRB can be modeled

as a single power law with spectral index Γ and an exponential cutoff (E_{cut})

$$\Phi_\gamma \propto \left(\frac{E_\gamma}{100\ \mathrm{MeV}}\right)^{-\Gamma} \exp\left(-\frac{E_\gamma}{E_{\mathrm{cut}}}\right) . \tag{1.11}$$

The best-fit parameters are $\Gamma_{\mathrm{EGB}} = 2.32 \pm 0.02$, $E_{\mathrm{cut,EGB}} = (279 \pm 59)$ GeV for the EGB, and $\Gamma_{\mathrm{IGRB}} = 2.31 \pm 0.02$, $E_{\mathrm{cut,IGRB}} = (362 \pm 64)$ GeV for the IGRB [94].[8] The power-law behavior reflects the non-thermal origin of gamma rays, while the exponential cutoff arises from $\gamma\gamma$-interactions with the CMB and EBL [98]. The consistency of spectral indices between the EGB and IGRB suggests a potentially common origin.

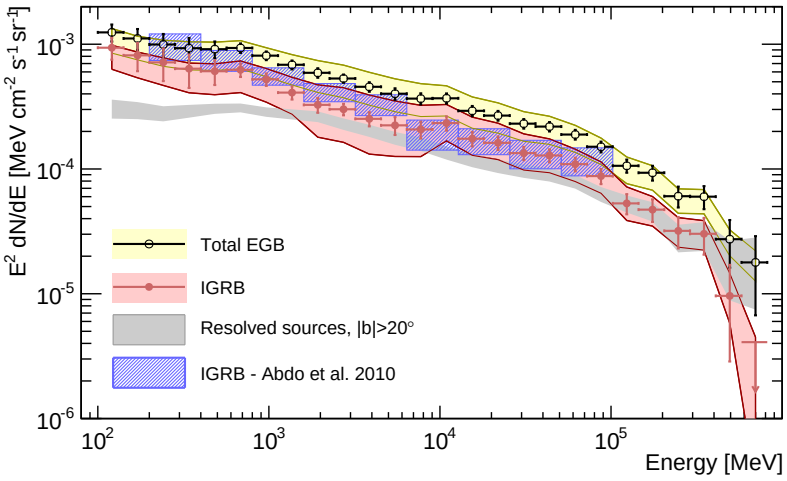

FIGURE 1.6: The energy-squared scaled extragalactic gamma-ray flux as a function of photon energy, derived from 50 months of *Fermi*-LAT data [94]. Yellow open circles represent the total extragalactic gamma-ray background (EGB), while red filled circles indicate the isotropic gamma-ray background (IGRB). Shaded bands reflect uncertainties from the Galactic Foreground model. The grey shaded band corresponds to resolved gamma-ray sources with $|b| > 20°$, and the dashed blue bands show results from an earlier analysis using 10 months of *Fermi*-LAT data for comparison.

Although space-borne gamma-ray observatories, such as *Fermi*-LAT, successfully observe the GeV gamma-ray sky, the direct detection technique becomes increasingly inefficient for *very-high-energy gamma rays* ($>$ 100 GeV to 100 TeV). Similar to CRs, the Earth's atmosphere can be utilized to detect these gamma rays more efficiently. When a primary gamma ray enters the atmosphere, it undergoes pair production, converting into an electron-positron pair. These secondary particles, in turn, emit gamma rays through Bremsstrahlung processes, initiating an electromagnetic cascade. This cascade can be observed using two primary approaches. The first involves directly detecting the surviving particles that reach the ground with surface arrays or water Cherenkov detectors. Observatories such as HAWC on the slopes of the Sierra Negra volcano in Mexico [99] and the Large High Altitude Air Shower Observatory (LHAASO) in China [100] effectively utilize these techniques. The second approach

[8] These values correspond to Galactic Foreground model A, one of three models presented by the *Fermi*-LAT collaboration [94]. Variations between the models are negligible for the purposes of this analysis.

involves studying the Cherenkov light emitted as the cascade develops in the atmosphere, using imaging atmospheric Cherenkov telescopes (IACTs). Notable observatories employing this method include the High Energy Stereoscopic System (H.E.S.S.) in the Khomas Highlands of Namibia [101], the Major Atmospheric Imaging Cherenkov (MAGIC) in the Canary Islands of Spain [102], and the Very Energetic Radiation Imaging Telescope Array System (VERITAS) in Arizona, USA [103].

The existence of *ultra-high-energy gamma rays* ($> 100\ \mathrm{TeV}$) was confirmed in 2019 [104]. In 2021, LHAASO reported the detection of multiple photons exceeding 1 PeV [105]. Most recently, in 2024, LHAASO announced the detection of a 2.5 PeV gamma ray from the Cygnus star-forming region in the plane of the Milky Way [106]. This represents the highest-energy gamma ray ever observed, highlighting the immense range of gamma-ray astronomy, spanning approximately 12 orders of magnitude.

1.4 Diffuse High-Energy Neutrino Astronomy

Neutrinos are electrically neutral fermions produced via the weak force, existing in three flavors: electron (ν_e), muon (ν_μ), and tau (ν_τ). Unlike cosmic rays (CRs) and gamma rays, neutrinos interact only through the weak force and gravity, allowing them to traverse cosmic distances without deflection or significant attenuation. This makes them ideal messengers for astronomy, offering unique insights into CR accelerators, though their weak interactions also make detection challenging.

Extraterrestrial neutrinos were first detected in the late 1960s, attributed to solar nuclear reactions [107], followed by the detection of extragalactic neutrinos from supernova SN1987a [108, 109]. These early detections spanned keV to MeV energies. In 2013, the IceCube Neutrino Observatory (IceCube hereafter) reported the first detection of a **diffuse high-energy neutrino flux** of astrophysical origin, extending the energy range to a few TeV–PeV [4, 5].

While strong evidence has emerged for high-energy neutrino sources from IceCube data—such as TXS 0506+056, a blazar detected in spatial and temporal coincidence with a high-energy neutrino [14, 15], NGC 1068, a Seyfert II galaxy identified as a promising neutrino emitter [16], and the Galactic plane, where evidence for neutrino production in the Milky Way has been observed [13]—the origins of the diffuse flux remain largely unresolved.

Current efforts to expand neutrino astronomy include the development of large-scale observatories, such as KM3NeT in the Mediterranean [110], Baikal-GVD in Russia [111], and P-ONE in the Pacific Ocean [112]. These facilities aim to significantly increase detection rates of astrophysical neutrinos and provide a more complete view of the neutrino sky.

The future next-generation IceCube-Gen2 [113] detector aims to enlarge the detection volume by an order of magnitude compared to the current IceCube array. Moreover, next-generation experiments like the Radio Neutrino Observatory in Greenland (RNO-G) [114], the Radio Echo Telescope for Neutrinos (RET-N) [115], and the Giant Radio Array for Neutrino Detection (GRAND) will incorporate novel detection technologies. These experiments utilize radio detection techniques to observe neutrinos with energies in excess of $\gtrsim 10$ PeV.

The combination of these observatories will provide complementary coverage across a wide energy range, significantly advancing our understanding of neutrino astrophysics and the origins of the diffuse neutrino flux.

At present, however, IceCube remains the only detector to observe a diffuse high-energy neutrino flux at the discovery[9] level, providing the most detailed measurements. Furthermore, data from IceCube will be used in Chapters 5 and 6. Therefore, the following sections focus primarily on the IceCube results. Although technical details of the IceCube detector will be discussed in detail in Chapter 4, some detector concepts need to be introduced here.

IceCube in a nutshell IceCube is a neutrino telescope that instruments a 1-km^3 volume of Antarctic ice at depths of about 1450 to 2450 meters. The detector consists of 86 vertical strings, each equipped with 60 digital optical modules (DOMs) [116]. High-energy neutrinos interacting with nucleons in the ice or bedrock via charged-current (exchange of $W^\pm$ boson) or neutral-current (exchange of Z^0 boson) interactions produce an avalanche of relativistic particles. These particles generate Cherenkov light as they travel faster than the speed of light in the South-Pole ice, which is detected by the DOMs.

Cherenkov signals in IceCube are classified as **tracks** or **cascades**. Tracks, resulting from charged-current interactions of muon neutrinos (ν_μ), offer good angular resolution ($\lesssim 1^\circ$ for $E_\mu \gtrsim 1$ TeV) [117], making them ideal for point-source searches. However, tracks are often poorly contained, leading to limited energy resolution. Cascades, produced by charged-current interactions of electron (ν_e) or tau neutrinos (ν_τ) and neutral-current interactions of all flavors, exhibit more spherical geometries. This ensures good containment and as such good energy resolution [118] but poorer angular resolution ($\gtrsim 8^\circ$) [119]. At the highest energies, tau neutrinos can also create unique double-cascade events. Notably, IceCube cannot distinguish neutrinos from antineutrinos, except in the specific case of the Glashow resonance (Section 1.4.2).

IceCube faces significant background noise from CR-induced atmospheric muons mainly from the Southern Hemisphere ($\sim$3000 per second) [120] and atmospheric neutrinos from both hemispheres (one every few minutes). Advanced techniques are employed to isolate astrophysical neutrinos from these backgrounds.

Finally we note that promising events of astrophysical environments can be communicated in realtime to the multi-messenger community via the Global Coordinates Network (GCN[10]).

1.4.1 Energy spectrum

The use of multiple detection channels is crucial for properly characterizing the diffuse high-energy neutrino flux observed by IceCube, as each channel has its own advantages and limitations. Below, we outline the latest measurements from the detection channels investigated by IceCube.

- **HESE [6]**: The High-Energy Starting Event (HESE) sample isolates high-energy neutrinos from atmospheric muons by using the detector's outer regions as a veto layer, selecting events with vertices contained within the detector volume. This approach reduces the detector's effective volume but ensures a highly pure sample. To focus on astrophysical rather than atmospheric neutrinos, a 60 TeV energy threshold is applied, enhancing the measurement of the diffuse flux. Spanning 7.5 years of data (2010–2017), the sample is predominantly composed of

[9] In (astro)particle physics, *evidence* is claimed with a p-value $\leq 1.35 \times 10^{-3}$ (corresponding to $\geq 3\sigma$ for half of a two-sided Gaussian), while a *discovery* requires a p-value $\leq 2.87 \times 10^{-7}$ (corresponding to $\geq 5\sigma$ for half of a two-sided Gaussian). The p-value reflects the probability that the observed result is consistent with the background hypothesis, as discussed in Chapter 5.

[10] https://gcn.nasa.gov/

cascades, with 17% track events. The initial HESE analysis, based on three years of data, achieved the first discovery of the diffuse astrophysical neutrino flux with 5.7σ significance [5].

- **Upgoing Through-going Tracks [7]**: In contrast to the HESE analysis, this approach utilizes the full detector volume without a veto layer and focuses exclusively on muon-neutrino-induced tracks. The use of the entire detector volume enables IceCube to detect muons produced by muon-neutrino interactions occurring well outside the detector. However, this also leads to an increased background from atmospheric muon neutrinos. To mitigate this, an angular restriction is applied, selecting only events originating from the Northern Hemisphere. This leverages the Earth as a natural shield, effectively filtering out muons from the southern hemisphere. The result is a high-purity dataset comprising 650.000 muon-neutrino-induced tracks.[11] This analysis excludes the background-only scenario (i.e., only contributions from atmospheric processes) with a significance of 5.6σ.

- **Cascades [8]**: This measurement focuses exclusively on cascade-like events, which are predominantly produced by electron and tau neutrinos ($\sim 90\%$). Cascades are particularly valuable due to their excellent neutrino energy resolution and the possibility of being partially contained within the detector, significantly boosting the statistical sample. The study utilizes 6 years of cascade data (2010–2015) from all directions in the sky, extending IceCube's sensitivity to the diffuse flux down to about 16 TeV. This analysis achieves a rejection of the background-only scenario with a significance of 9.9σ.

- **Inelasticity [9]**: This analysis, targeting all neutrino flavors, was constructed to measure the inelasticity, i.e., the energy transferred from the neutrino to the hadrons in inelastic collisions, of multi-TeV neutrinos. The event selection consists of contained neutrino interactions with both tracks and cascades.

- **ESTES [10]**: This diffuse flux measurement is based on 10.3 years of data (2011–2022) comprising track-like events with interaction vertices inside the detector and energies above 1 TeV. This dataset, known as the Enhanced Starting Tracks Event Selection (ESTES), leverages dynamic veto techniques and machine learning to identify starting tracks even in energy regions heavily dominated by atmospheric background, across both hemispheres.

- **Combined (or Global) [11]**: The analysis combines event selections selected from six different studies designed to measure the astrophysical neutrino flux with IceCube. The combined data sample (2008-2013) contains events from all flavors. A global fit is performed to the combined dataset. Recently an updated measurement was presented with more than 10 years of data [121].

To date, all measurements of the diffuse high-energy neutrino flux are well described by an **isotropic, unbroken power law** of the form (see Appendix A for notation):

$$\Phi_{\nu_\ell+\overline{\nu}_\ell}(E_\nu) = \Phi_0 \left(\frac{E_\nu}{100\ \mathrm{TeV}}\right)^{-\gamma} \times 10^{-18}\ \mathrm{GeV}^{-1}\ \mathrm{cm}^{-2}\ \mathrm{s}^{-1}\ \mathrm{sr}^{-1}, \tag{1.12}$$

[11] For comparison, the 7.5-year HESE analysis includes only 102 events, with just 60 exceeding 60 TeV in energy

Analysis	γ	Φ_0	E_ν [TeV]	Coverage	Flavors
HESE (7.5 yrs) [6]	$2.87^{+0.20}_{-0.19}$	$2.12^{+0.49}_{-0.54}$	$60 - 2500$	N+S	e,μ,τ
Tracks (9.5 yrs) [7]	$2.37^{+0.09}_{-0.09}$	$1.44^{+0.25}_{-0.26}$	$40 - 3500$	N	μ
Cascades (6 yrs) [8]	$2.53^{+0.7}_{-0.7}$	$1.66^{+0.25}_{-0.27}$	$16 - 2600$	N+S	e, τ
Inelasticity (5 yrs) [9]	$2.62^{+0.7}_{-0.7}$	$2.04^{+0.23}_{-0.21}$	$3.5 - 2600$	N+S	e, μ, τ
ESTES (10.3 yrs) [10]	$2.58^{+0.10}_{-0.09}$	$1.68^{+0.19}_{-0.22}$	$3 - 550$	N+S	μ
Combined (5 yrs) [11]	$2.50^{+0.09}_{-0.09}$	$2.23^{+0.37}_{-0.40}$	$2.5 - 2800$	N+S	e, μ, τ

TABLE 1.1: IceCube measurements of the astrophysical diffuse neutrino flux across multiple detection channels. For each analysis, assuming a single power-law spectrum, the normalization of the neutrino flux at $E_\nu = 100\,\mathrm{TeV}$ ($\Phi_0[10^{-18}$ GeV^{-1} cm^{-2} s^{-1} sr$^{-1}]$) and the spectral index (γ) are shown. The table also lists the sensitive neutrino energy range (E_ν), sky coverage (with 'S' and 'N' denoting the Southern and Northern Hemispheres, respectively), and the neutrino flavors to wich each analysis is sensitive. See the text for the corresponding references.

where $\ell \in \{e, \mu, \tau\}$ denotes the neutrino flavor. This parameterization provides the best fit to the current observational data. The two free parameters in this expression are the flux normalization at 100 TeV (Φ_0) and the spectral index (γ). Table 1.1 presents the values of the best-fit parameters for various of the latest measurements of the diffuse flux described above, along with the sensitive neutrino energy range, sky coverage (Northern and/or Southern Hemisphere), and the neutrino flavors to which each analysis is sensitive. Taking into account that the analyses are sensitive in different energy ranges, the obtained results for the best-fit parameters present, within uncertainties, a roughly consistent picture of the diffuse high-energy neutrino flux.

More complex models, such as broken power laws with or without exponential cutoffs, have also been tested in these measurements. Although some indications of spectral structure have been observed, they are not yet statistically significant [7, 8].

1.4.2 Flavor composition

The Standard Model of particle physics [29] originally predicted that neutrinos are massless. However, experimental evidence has demonstrated that neutrinos possess a very small, nonzero mass. This conclusion arises primarily from studies of neutrino oscillations, a phenomenon in which neutrino flavor eigenstates are superpositions of mass eigenstates. This mixing enables flavor transitions during propagation over sufficiently large distances. Large-scale neutrino observatories such as IceCube provide a unique opportunity to study neutrino oscillations across a wide range of energies. Particularly due to IceCube's component DeepCore—a region in the detector with an enhanced string density (see also Chapter 4)—it is possible to study oscillations in the GeV-PeV energy range.

First, a brief overview of the theoretical framework underpinning neutrino oscillations is provided. Then, this framework will be used to interpret the flavor composition of the IceCube data. This introduction is needed as the results will be directly used in calculations in Chapters 3, 5, and 6.

Neutrino mixing

Neutrinos are produced in particle decays mediated by the weak force. During such decays, the neutrino emerges with a flavor matching the associated lepton produced in the process, denoted as ν_ℓ, where $\ell \in \{e, \mu, \tau\}$. These flavor states are referred to as the weak eigenstates of the neutrino. However, there is no fundamental reason to assume that these flavor eigenstates correspond directly to the mass eigenstates ν_i, which are the physical states with well-defined masses, where $i \in \{1, 2, 3\}$. In fact, the flavor and mass eigenstates are related through a unitary transformation,

$$\begin{pmatrix} \nu_e \\ \nu_\mu \\ \nu_\tau \end{pmatrix} = \mathcal{U}_{\mathrm{PMNS}} \begin{pmatrix} \nu_1 \\ \nu_2 \\ \nu_3 \end{pmatrix}, \tag{1.13}$$

with $\mathcal{U}_{\mathrm{PMNS}}$ the *Pontecorvo–Maki–Nakagawa–Sakata* (PMNS) matrix. This is a non-diagonal 3×3 unitary matrix that can be described by four free parameters. Most commonly, the PMNS matrix is parameterized by three mixing angles $(\theta_{12}, \theta_{23}, \theta_{13})$ and a complex phase angle related to charge-parity (CP) violations (δ_{CP}) [122].

The probability that a neutrino originally produced with flavor ℓ and energy E_ν will interact as flavor ℓ' after traveling a distance L is given by

$$\begin{aligned} \mathcal{P}(\nu_\ell \to \nu_{\ell'}, L) = \delta_{\ell\ell'} &- 4 \sum_{j>k} \mathrm{Re}\left[\mathcal{U}^*_{\ell j} \mathcal{U}_{\ell' j} \mathcal{U}_{\ell k} \mathcal{U}^*_{\ell' k}\right] \sin^2\left(\frac{\Delta m^2_{jk} L}{E_\nu} \frac{c^3}{4\hbar}\right) \\ &+ 2 \sum_{j>k} \mathrm{Im}\left[\mathcal{U}^*_{\ell j} \mathcal{U}_{\ell' j} \mathcal{U}_{\ell k} \mathcal{U}^*_{\ell' k}\right] \sin\left(\frac{\Delta m^2_{jk} L}{E_\nu} \frac{c^3}{2\hbar}\right). \end{aligned} \tag{1.14}$$

Here $\delta_{\ell\ell'}$ is the Kronecker delta, $\Delta m^2_{jk} \equiv m^2_j - m^2_k$ represents the mass-squared difference of two neutrino mass eigenstates, and the operators Re and Im denote the real and imaginary parts of the expression, respectively.

If $\delta_{\mathrm{CP}} = 0$, the second term vanishes. To date, oscillation experiments have not found conclusive evidence of CP violation in neutrino oscillations [123, 124]. These experiments, however, have established that neutrinos possess non-zero masses. As evident from Eq. (1.14), these experiments measure only the mass-squared differences between the mass eigenstates. The derived values are [125]

$$\Delta m^2_{21} \sim 7.4 \times 10^{-5}\ \mathrm{eV}^2/c^4, \quad |\Delta m^2_{32}| \sim 2.5 \times 10^{-3}\ \mathrm{eV}^2/c^4.$$

The precise mass hierarchy and ordering remain unresolved. Two possibilities exist: the normal ordering, with $m_1 < m_2 < m_3$ and m_3 significantly larger than m_1, and the inverted ordering, with $m_3 < m_1 < m_2$, where m_3 is the smallest.

Laboratory-based experiments aim to determine the absolute neutrino mass scale, primarily by measuring the electron neutrino mass in beta decay. The KATRIN experiment currently sets an upper limit of $m_{\nu_e} < 0.8\ \mathrm{eV}/c^2$ [126]. Nevertheless, the most stringent constraints come from cosmological observations. In 2018, the *Planck* Collaboration placed a bound on the sum of the three neutrino masses $\sum_{i=1}^{3} m_{\nu_i} \lesssim 0.120\ \mathrm{eV}/c^2$ [127].

Oscillation effects are, however, only significant if the oscillation length is sufficiently smaller than the propagation length. To estimate the oscillation length for observed astrophysical neutrinos, consider that in Eq. (1.14) the mixing-angle values

determine the amplitude of the oscillation, while the neutrino energy (E_ν), propagation length (L), and mass-squared difference (Δm^2) define its frequency. Rewriting the argument of the $\sin^2$ term in Eq. (1.14) in units commonly used in astroparticle physics gives,

$$\frac{\Delta(mc^2)^2 L}{E_\nu}\frac{1}{4\hbar c} \approx 3.9\times 10^7 \,\frac{\Delta(mc^2)^2}{\mathrm{eV}^2}\,\frac{L}{\mathrm{pc}}\,\frac{\mathrm{PeV}}{E_\nu}. \tag{1.15}$$

For a neutrino energy of $E_\nu = 1$ PeV and a mass-squared difference of $\Delta m^2 = 10^{-4}\ \mathrm{eV}^2/c^4$, the oscillation length, ΔL_{osc}, is

$$\Delta L_{\mathrm{osc}} \approx \frac{2\pi}{3.09\times 10^{-7}\cdot 10^{-4}} \approx 2\ \mathrm{mpc}\ . \tag{1.16}$$

Given that this oscillation length is significantly smaller than the distances to practically all astrophysical sources of interest in the high-energy sky, oscillation effects will significantly affect the flavor ratio of the high-energy neutrino beam. This can be tested by studying the flavor composition of the observed high-energy neutrinos, as discussed in the following.

Flavor measurements

In the idealized scenario where neutrinos are produced solely via pion and muon decays, the initial flavor ratio at the source is $(\nu_e : \nu_\mu : \nu_\tau) = (1 : 2 : 0)$. As these neutrinos propagate and undergo flavor mixing, this ratio evolves to an approximately equal distribution of $(\nu_e : \nu_\mu : \nu_\tau) \approx (1 : 1 : 1)$ by the time they reach Earth [128]. However, alternative production mechanisms predict different initial flavor ratios, which may lead to variations in the observed spectrum.

For example, in environments with sufficiently strong magnetic fields, muons lose energy through synchrotron radiation and bremsstrahlung on timescales much shorter than their decay timescale. Consequently, high-energy neutrinos are not produced via muon decay. The high-energy neutrinos would, however, still arise through the pion-to-muon decay channel. In such *muon-damped* scenarios, the resulting neutrino flavor ratio at the source is given by $(\nu_e : \nu_\mu : \nu_\tau) = (0 : 1 : 0)$ [129]. Conversely, in *neutron-beam* sources, where neutrinos originate solely from the beta decay of neutrons, the source flavor ratio becomes $(\nu_e : \nu_\mu : \nu_\tau) = (1 : 0 : 0)$ [130].

Direct production of tau neutrinos at the source could occur via charmed-meson production. However, such processes have a low cross section and a high energy threshold, resulting in a charmed meson-to-pion production of 10^{-4} [131]. Note that this does not exclude the observations of astrophysical tau neutrinos at the Earth as they could still be observed due to mixing effects during propagation.

By measuring the flavor ratio of the observed high-energy neutrino flux at the Earth, theoretical models—including exotic scenarios—can be tested, offering valuable insights into the neutrino production mechanisms and the astrophysical environments in which they occur. Deviations from the expected flavor ratios may further signal the presence of physics beyond the Standard Model, but this is outside the scope of this work. Below we discuss some important flavor measurements in more detail.

Astrophysical tau neutrinos When a tau neutrino of sufficiently high energy interacts in the IceCube detector via a charged-current interaction, there are two distinct energy depositions: the neutrino interaction vertex and the tau decay vertex. This can be observed as a double-cascade structure or double-pulse waveform. By analyzing

this signature in the HESE sample, the IceCube Collaboration initially identified two astrophysical tau neutrino candidates, rejecting the null hypothesis of no astrophysical tau neutrinos with a 2.8σ significance [132]. More recently, using convolutional neural networks, seven candidate events were identified with deposited energies ranging from 20 TeV to 1 PeV. The background-only hypothesis was rejected at a 5σ significance, considering contributions from astrophysical and atmospheric neutrinos, as well as muons originating from $\pi^{\pm}$ and $K^{\pm}$ decays [133].

Flavor triangle Figure 4.2 illustrates the neutrino flavor ratios for physically motivated compositions at the source, alongside the 3σ contour of allowed ratios based on observed neutrino mixing angles. Additionally, it displays the measured flavor ratios from three diffuse IceCube analyses. Among these, the HESE measurement included the first candidate astrophysical tau neutrino event, breaking the degeneracy between ν_e and ν_τ observed in the inelasticity and global-fit analyses. The best-fit HESE flavor ratio falls within the 3σ region allowed by neutrino mixing angles. However, due to limited statistics, the uncertainties remain significant, and the measurements are consistent at the 95% confidence level with all theoretical flavor ratio models. Consequently, following the general IceCube approach, we assume a **flavor composition at Earth** of $(\nu_e : \nu_\mu : \nu_\tau) = (1 : 1 : 1)$ in the remainder of this work. This assumption implies that to obtain the single-flavor neutrino flux at Earth, the all-flavor neutrino flux at the source must be divided by a factor of three. This results will be explicitly used in Chapter 3.

Glashow resonance When an electron antineutrino ($\overline{\nu}_e$) interacts with an electron (e^-), the Standard Model predicts the s-channel production of a W-boson via $\overline{\nu}_e + e^- \to W^- \to X$, where X denotes the final state. At a center-of-mass energy equal to the W-boson mass, $\sqrt{s} = M_W = 80.38$ GeV [29], this interaction is resonantly enhanced, known as the Glashow resonance.

The threshold energy for this process—derived using four-vector kinematics in the electron rest frame—is $E_{\overline{\nu}_e} \approx M_W^2 c^2 / 2m_e \approx 6.3$ PeV. Such extreme energies, well beyond the reach of terrestrial accelerators, can arise in astrophysical environments and are detectable by large-volume neutrino observatories. In 2020, the IceCube Collaboration reported a cascade event consistent with W-boson production at the Glashow resonance [134]. The event deposited 6.05 ± 0.72 PeV—the highest-energy cascade event recorded by IceCube—and showed a significance of approximately 5σ for an astrophysical origin.

1.5 Multi-Messenger Constraints & Insights

In previous sections we discussed observations of ultra-high-energy cosmic rays (UHECRs), gamma rays, and high-energy neutrinos. Figure 1.8 shows the diffuse flux (Φ) of these messengers, scaled by the energy squared, which provides a measure of the energy density of the sources producing these particles (see Appendix A). The gamma rays span the GeV–TeV range observed by Fermi-LAT, high-energy neutrinos are observed in the TeV–PeV range through various measurements by IceCube, and UHECRs shown here are detected in the EeV–ZeV range by the Pierre Auger Observatory and Telescope Array (TA).

Interestingly, the energy density of the three messengers is comparable, which may suggest a common origin and allows for deeper investigation. Note, however,

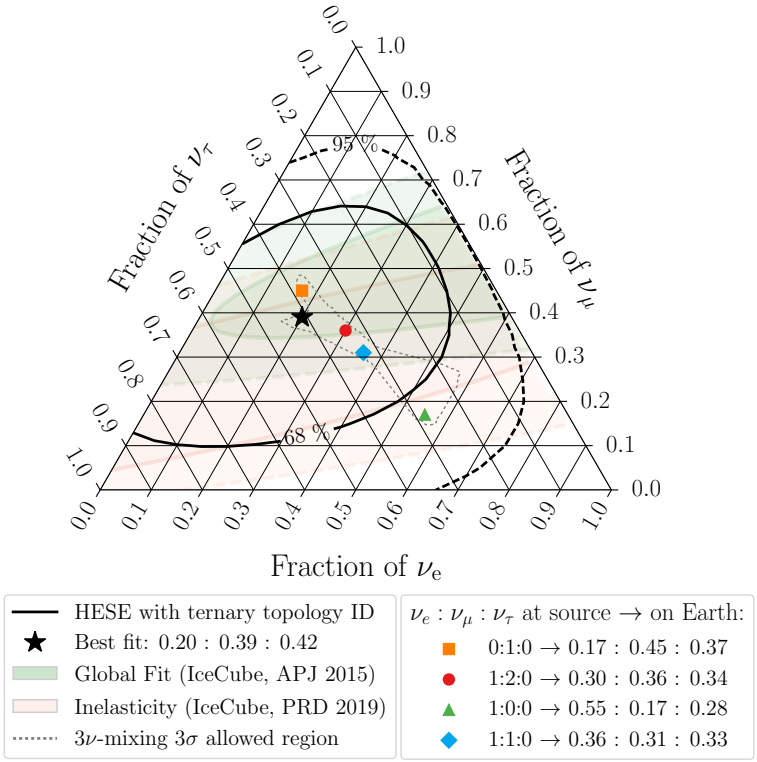

FIGURE 1.7: Flavor constraints on the diffuse astrophysical neutrino flux observed with IceCube. The solid black lines represent the 68% and 95% confidence level intervals for the best-fit measurement from the High-Energy Starting Track (HESE) sample [6]. The shaded regions, outlined by solid and dashed lines, indicate the 68% and 95% confidence level intervals derived from the combined fit [11] and inelasticity analysis [9]. Markers (excluding the black star) denote expected flavor ratios based on flavor ratios at the source and oscillation effects. The grey dotted line shows the range of possible flavor compositions under Standard Model flavor mixing. Figure from [132].

that based on the relationship between the average energies of the different messengers alone, $E_\nu \sim E_\gamma/2 \sim E_{\rm CR}/20$ (see Section 1.2.2), it is not immediately evident that the observed UHECRs are the origin of the observed high-energy neutrinos. Future observatories targeting high-energy neutrinos with $E_\nu > 100$ PeV will be crucial for determining the origin of the UHECR sources. Notably, KM3NeT detected a muon with a reconstructed energy of 120^{+110}_{-60} PeV [135]. Given its extreme energy and near-horizontal trajectory, this muon was very likely produced by a neutrino of even higher energy interacting in the vicinity of the detector. Simulations indicate that the median energy of neutrinos producing such muons is approximately 220 PeV. If this event is indeed the result of a cosmic neutrino interaction, it would represent the highest-energy neutrino-induced muon ever detected; however, its astrophysical origin remains unconfirmed [136–138].

In the following, we present two key insights obtained by comparing different types of observed cosmic messengers. In Section 1.5.1, we derive a somewhat loose upper bound on the diffuse high-energy neutrino flux based on the observed flux of UHECRs. This bound will later serve as a consistency check in Chapter 3. In Section 1.5.2, we contrast diffuse gamma-ray and high-energy neutrino observations to argue that at least a subset of bright neutrino sources must be faint in gamma rays.

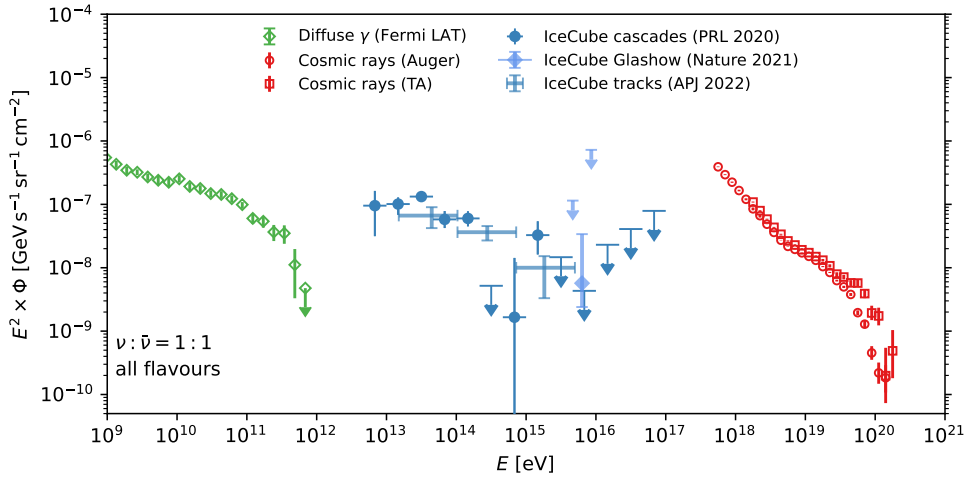

FIGURE 1.8: Diffuse flux of high-energy gamma rays observed with Fermi-LAT, high-energy neutrinos observed by IceCube using three independent detection channels (see Section 1.4), and high-energy CRs observed by the Pierre Auger Observatory and TA. Each of the fluxes is scaled with the energy squared. Figure taken from [139].

1.5.1 Waxman-Bahcall bound

If the observed high-energy neutrino flux originates from UHECR sources that are optically thin to pp and pγ interactions, a theoretical upper bound on the high-energy neutrino flux can be derived. This bound was first derived by Waxman and Bahcall [88, 140].

We derive this upper limit by first obtaining the differential energy generation rate of CRs at the source, assuming they are protons, from the observed UHECR flux. This result is then translated into a diffuse high-energy neutrino flux. Throughout

this derivation, we adopt the notations, dimensions, and relations introduced in Appendix A.

The total energy generation rate of CR protons in the energy range 10^{19} eV to 10^{21} eV at the source, denoted by $\mathcal{Q}_{\rm CR}^{[10^{19},10^{21}]}$, can be estimated by integrating the observed diffuse UHECR flux over this interval. Converting the integrated flux to an energy density by dividing by $c/4\pi$, and then dividing by the Hubble time ($t_H = H_0^{-1}$, with H_0 the Hubble parameter), yields

$$\mathcal{Q}_{\rm CR}^{[10^{19},10^{21}]} \sim 5 \times 10^{44}\ {\rm erg\ Mpc^{-3}\ yr^{-1}}\ . \tag{1.17}$$

From this integrated rate, the differential energy generation rate, $E_{\rm CR}\mathcal{Q}_{E_{\rm CR}}$, which carries the same units as $\mathcal{Q}_{\rm CR}^{[10^{19},10^{21}]}$, can be derived (See Appendix A for the derivation). Assuming a source spectrum proportional to E^{-2}, motivated both by observational fits and by theoretical expectations from first-order Fermi acceleration, it follows that

$$E_{\rm CR}\mathcal{Q}_{E_{\rm CR}} = \frac{\mathcal{Q}_{\rm CR}^{[10^{19},10^{21}]}}{\ln(10^{21}/10^{19})} \approx 10^{44}\ {\rm erg\ Mpc^{-3}\ yr^{-1}}. \tag{1.18}$$

Due to the assumed E^{-2} spectrum, the differential energy generation rate is approximately energy-independent, as discussed in Appendix A.

To estimate the corresponding diffuse high-energy neutrino flux, we assume that UHECR sources are optically thin to both pp and pγ interactions. In this regime, only a fraction of the proton energy is converted into pions. The resulting diffuse neutrino flux is given by [140]

$$E_\nu^2\,\Phi_{\nu+\overline{\nu}} \simeq \xi_z\,\mathcal{E}\,f_\pi\,\frac{c}{4\pi H_0}\,E_{\rm CR}\,\mathcal{Q}_{E_{\rm CR}}, \tag{1.19}$$

where the energy-squared scaled flux has dimensions of energy per unit area, per unit time, per unit solid angle. The parameter $\mathcal{E}$ represents the average fraction of pion energy transferred to neutrinos, which depends on the charged-to-neutral pion ratio K_π—defined in Eq. (1.5)—in the dominant interaction channel. The meson production efficiency f_π reflects the probability of pion production and is governed by the interaction mean free path of CRs within the source environment. The factor ξ_z (typically of order unity) accounts for the cosmological evolution of the source population.[12] Note that $f_\pi < 1$ due to the assumption that UHECR sources are optically thin to pp and pγ interactions.

An upper bound on the diffuse high-energy neutrino flux is obtained by assuming maximal meson production efficiency ($f_\pi = 1$). For $\xi_z = 3$, consistent with the star-formation rate history, and a flavor ratio $(\nu_e : \nu_\mu : \nu_\tau) \approx (1:1:1)$ at Earth due to neutrino mixing, the Waxman-Bahcall bound on the single-flavor diffuse neutrino flux is

$$E_{\nu_\ell}^2\,\Phi_{\nu_\ell+\overline{\nu}_\ell} \lesssim (2\text{–}3)\times 10^{-8}\ {\rm GeV\ cm^{-2}\ s^{-1}\ sr^{-1}}, \quad \ell \in \{e,\mu,\tau\}. \tag{1.20}$$

The limit applies to both pp and pγ interaction scenarios and should be interpreted as an optimistic benchmark rather than a strict upper bound.

Remarkably, this upper limit is close to the diffuse high-energy neutrino flux observed by IceCube (see e.g. Figure 1.8).

[12] In Section 3.4.2 a concrete example is discussed.

Before the formulation of the Waxman-Bahcall bound, theoretical predictions of high-energy neutrino fluxes from sources such as gamma-ray bursts (GRBs) and active galactic nuclei (AGN) often exceeded what would later be recognized as a realistic upper limit by several orders of magnitude. As a result, it was initially believed that detectors with volumes smaller than a gigaton might be sufficient for the detection of such neutrinos. The Waxman-Bahcall bound, however, established that observatories on the gigaton scale would be necessary for successful detection [140].

The first observatory to achieve this scale and to detect the diffuse astrophysical high-energy neutrinos was IceCube, as discussed in Section 1.4 (see also Chapter 4 for a detailed technical overview of the detector).

1.5.2 Hidden sources

Hadronic gamma rays and neutrinos produced via pion decay are expected to be closely correlated, as discussed in Section 1.2.1. This connection can be probed by comparing the extragalactic gamma-ray background (EGB) measured by *Fermi*-LAT (Section 1.3) with the diffuse high-energy neutrino flux detected by IceCube (Section 1.4). Deviations from theoretical expectations may provide insights into the physical conditions within the source environments.

A key aspect of this comparison is the role of blazars, which contribute $\sim 86\%$ of the extragalactic gamma-ray background (EGB) above 50 GeV (Section 1.3) but only marginally to the high-energy neutrino flux. An IceCube search for cumulative neutrino emission from blazars in the Fermi-2LAC catalog found no significant excess, allowing upper limits on their contribution to the diffuse neutrino flux in the 10 TeV–2 PeV range. Assuming an unbroken power-law spectrum $E^{-\gamma}$, this contribution is constrained to $\lesssim 27\%$ for $\gamma = 2.5$ and $\lesssim 50\%$ for $\gamma \leq 2.2$ [141].

Here, we summarize a key conclusion from the analysis in [142], which compares the EGB and the high-energy neutrino flux observed by IceCube under the assumption that both originate from pp-interactions.

The black data points in Figure 1.9 show the diffuse neutrino flux observed by IceCube, based on a combined-fit analysis of five years of data [11]. The red points represent the EGB measured by *Fermi*-LAT. The solid red curve denotes the non-blazar EGB, comprising two components: gamma rays arriving directly at Earth (dashed line) and secondary gamma rays produced via interactions with the cosmic microwave background (CMB) and extragalactic background light (EBL) (dotted line). The solid black curve represents the predicted neutrino flux, inferred from the observed non-blazar EGB. This prediction falls below the high-energy neutrino flux measured by IceCube. In other words, if one were to estimate the non-blazar contribution to the EGB based on the observed IceCube flux, it would exceed the actual observed non-blazar EGB.

In particular, under a generic CR calorimeter scenario, the IceCube neutrino flux exhibits tension with the $\sim 14\%$ non-blazar EGB in the 0.05–1 TeV range [142]. This discrepancy suggests that a significant fraction of gamma rays co-produced with astrophysical neutrinos are attenuated before reaching Earth.

More broadly, as discussed in [18], the non-blazar EGB imposes stringent constraints on gamma-ray transparent sources. This tension can be alleviated if the high-energy neutrino sources are (partially) gamma-ray opaque. In pγ-dominated environments, gamma rays can be attenuated via two-photon annihilation, while in pp-dominated sources, they may be absorbed through interactions with dense baryonic

matter, such as gas and dust. In contrast, high-energy neutrinos, being electrically neutral and weakly interacting, can escape the source environment largely unimpeded.

It is also possible that the environment is more complex: some regions within a given system may be gamma-ray bright due to either leptonic or hadronic processes, while the regions responsible for detectable high-energy neutrino emission remain gamma-ray dark.

These multi-messenger constraints motivate the investigation of (ultra)luminous infrared galaxies as candidate neutrino sources that may appear gamma-ray dark. These galaxies host compact, heavily obscured starburst and AGN regions, where energetic conditions favor both efficient particle acceleration and the production of high-energy neutrinos, while simultaneously enabling gamma-ray attenuation. This will be the focus of the next chapter.

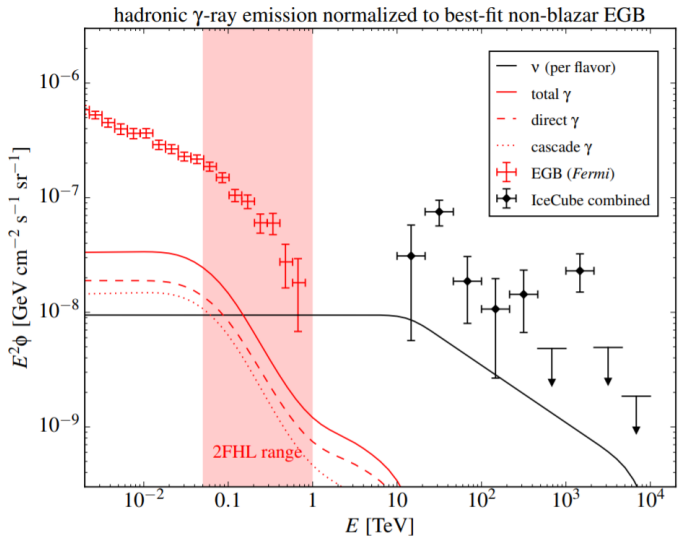

FIGURE 1.9: The diffuse gamma-ray flux (red data points) and neutrino flux (black data points), as observed by *Fermi*-LAT and IceCube respectively, are shown. The predicted neutrino flux (solid black line), derived from the non-blazar gamma-ray component (solid red line), lies below the observed IceCube neutrino flux. One interpretation of this discrepancy is the presence of gamma-ray dim neutrino sources, as discussed in the text. Figure taken from [142].

1.6 Sources of Astrophysical Neutrinos

In addition to measuring the diffuse astrophysical neutrino flux (Section 1.4), IceCube performs a variety of analyses aimed at identifying sources of high-energy neutrinos by searching for clustering patterns in the sky. Such clustering may signal the presence of astrophysical sources, in contrast to the atmospheric background, which is expected to be isotropic within a given declination band. These searches primarily focus on muon neutrinos, owing to their excellent angular resolution ($\lesssim 1^\circ$ for $E_\mu \gtrsim 1$ TeV) [117], making them particularly well-suited for point-source detection.

Below, we provide a non-exhaustive overview of the different types of source searches conducted by the IceCube Collaboration and discuss the emerging neutrino sources in greater detail.

1.6.1 Point-source searches with IceCube

A distinction is made between **time-integrated** and **time-dependent** neutrino-source searches:

- **Time-integrated** searches maximize statistics by accumulating neutrino data over long periods, enhancing sensitivity to steady sources. However, this also lowers the signal-to-background ratio due to the coherent accumulation of signal events as opposed to the incoherent background event accumulation
- **Time-dependent** searches exploit the temporal characteristics of transient phenomena to identify potential neutrino emission, significantly reducing background contamination. The disadvantage of time-dependent searches lies in the need for precise modeling of the expected temporal profile and the necessity of external triggers from additional observatories to define the relevant time window.

For both time-dependent and time-integrated searches, different types of searches can be performed. The technical details are omitted here but are covered in Chapters 5 and 6:

- **All-Sky Scan**: As an unbiased search method independent of prior source information, this approach partitions the sky into pixels of approximately $0.1^\circ \times 0.1^\circ$, which is finer than the typical angular resolution of neutrino events (i.e., the detector resolution). In each pixel, a likelihood analysis is performed to evaluate the significance of clustering.

  The resulting significance for each pixel is quantified using a *p-value*. This p-value represents the probability that the observed clustering at a given sky location is consistent with the background-only (null) hypothesis, i.e., the assumption that all detected neutrinos from that direction originate from atmospheric backgrounds and/or a diffuse astrophysical component. A smaller p-value indicates a lower likelihood of the background-only hypothesis and, correspondingly, a higher likelihood of a contribution from a point-like astrophysical neutrino source.

  The pixel with the smallest p-value (highest significance) is identified as the most likely source candidate. However, because many independent sky locations are tested, background fluctuations can lead to spurious local excesses. To account for this so-called *look-elsewhere effect*, a statistical correction is applied, resulting in the *post-trial* p-value, which reflects the global significance of the observation.

  We remind the reader that in (astro)particle physics, *evidence* is typically claimed for a p-value $\leq 1.35 \times 10^{-3}$ (corresponding to a $\geq 3\sigma$ one-sided significance under a normal distribution), while a *discovery* requires a more stringent threshold of $p \leq 2.87 \times 10^{-7}$ (equivalent to $\geq 5\sigma$ one-sided significance).

- **Catalog Search**: Rather than investigating the whole sky, this type of search uses a predefined catalog of candidate sources, typically selected based on electromagnetic properties or other messengers that can be linked to high-energy neutrino production. By limiting the search to specific locations, this method avoids the large statistical penalty of an all-sky scan, enhancing sensitivity to neutrino sources.
- **Population Study**: This method investigates whether a subset of a predefined catalog of sources, potentially diverse and individually too faint to be detected,

collectively shows a deviation from the null hypothesis. The analysis is performed by applying a binomial test to the pre-trial p-values of the catalog.

It is important to note that, even if a significant deviation is observed, the nature of the test does not allow for a quantitative interpretation of the signal strength. A dedicated stacking analysis would be required to assess the collective signal significance or flux.

- **Stacking Search**: For source classes where individual sources are too faint to be detected individually, a stacked search aggregates the predicted neutrino flux from multiple sources to enhance sensitivity to the entire class [143]. Stacking weights optimize the combined signal, emphasizing the cumulative flux over individual contributions that remains unresolved. Effective stacking requires that the sources share common characteristics (different from the population study), such as similar electromagnetic signatures or other relevant observables, to ensure meaningful results.

Since the (partial) completion of IceCube, many time-(in)dependent source searches of all types have been performed. An overview of recent ongoing analyses can be found here [12]. Below we highlight some important results and those relevant to this work.

Time-integrated searches and promising source classes

In 2019, the IceCube Collaboration performed a time-integrated search for high-energy neutrino sources using 10 years of data (2008–2018) [117], employing multiple search strategies across both hemispheres. Notably, an analysis based on a gamma-ray-selected catalog targeting the Northern Sky identified **NGC 1068** as the most prominent candidate. This galaxy is classified as a Seyfert II type with strong starburst activity. An observed excess at the position of NGC 1068 deviated from the background-only hypothesis with a significance of 2.9σ, just below the conventional 3σ threshold for statistical evidence. Similarly, an all-sky scan conducted within the same analysis found NGC 1068 to be the most significant hotspot in the Northern Sky, with a significance of 1.6σ. In both cases, the results did not reach the level required for conclusive evidence of high-energy neutrino emission from this source. The study also presented declination-dependent all-sky sensitivity and discovery potential for individual sources.

Since the statistical significance of NGC 1068 was near the threshold required to claim evidence, follow-up observations were conducted:

- The first follow-up analysis in 2022, incorporating improved up-going muon-track data and refined methods, increased the significance for NGC 1068 to 4.2σ. This provided statistical evidence for the emission of high-energy neutrinos from this galaxy, though it is still below the threshold for a formal discovery claim. An excess of 79^{+22}_{-20} neutrinos above background expectations from the direction of NGC 1068 was detected, with a soft spectrum characterized by a spectral index of 3.2 ± 0.2.

  In the same analysis, a population study of gamma-ray sources in the Northern Hemisphere, using the same source selection as the 10-year analysis [117], highlighted the top three sources[13]: NGC 1068, and the blazars PKS 1424+240 and TXS 0506+056. Notably, the latter had already been associated with a 290 TeV neutrino in a prior multi-messenger campaign (discussed further in

[13] The binomial test in the 10-year analysis identified the top four sources.

Section 1.6.2). This first follow-up analysis also improved the point-source sensitivity in the Northern Hemisphere.

- The second and most recent follow-up analysis of NGC 1068, conducted in 2025 using the up-going muon-track sample, builds upon the refined methods of the previous study and incorporates an additional four years of data [144]. Although the global significance decreases slightly to approximately 4.0σ, the most significant excess in IceCube's data is now more tightly localized around the optical coordinates of NGC 1068.[14] Within statistical uncertainties, the latest flux measurement from the source is consistent with the previous estimate, but the spectral index becomes slightly softer, now about 3.4 ± 0.2.

  The analysis also revealed a binomial excess when excluding NGC 1068, reaching evidence-level significance for the 11 most significant Seyfert galaxies in the analysis. Including NGC 1068 in the sample further enhances the overall significance.

Finally, we highlight a distinct IceCube analysis, separate from the NGC 1068 studies outlined above, which targets the Swift-BAT AGN Spectroscopic Survey (BASS) to investigate hard X-ray AGN as potential sources of high-energy neutrinos [145]. Although stacked searches across various AGN subtypes did not yield statistically significant results, the Seyfert I galaxy NGC 4151 exhibited a localized excess with a post-trial significance of 2.9σ [145]. Consistent with the previously discussed analyses [16, 117, 144], NGC 1068 again emerged as a leading candidate neutrino emitter.

In Section 1.1.4, AGN were already identified as promising sources of ultra-high-energy cosmic rays (UHECRs). The findings presented in this section underscore that AGN, particularly Seyfert galaxies and blazars, are promising candidates for steady high-energy neutrino emission.

- **Blazars**: recent searches have not revealed new significant sources (e.g. [146, 147]. Notably, [141] concluded that blazars contribute only a limited fraction of the observed diffuse high-energy neutrino flux, as discussed in Section 1.5.2.

- **AGN cores**: In addition to the promising sources NGC 1068 [16, 117, 144], NGC 4151 [145], and the binomial excess from Seyfert galaxies [144], a 2.6σ excess was found in an IceCube analysis focused on AGN-core emission [148]. These results motivate the current increased interest in this source class as sources of high-energy neutrinos.

Beyond AGN, **starburst galaxies** are also considered a promising source class for steady high-energy neutrino emission. Their dense concentrations of gas and dust, combined with strong magnetic fields, should efficiently trap CRs and enhance the probability of interactions leading to high-energy neutrino production ([149]; see Chapter 3). The 10-year IceCube point-source search and subsequent follow-up analyses included a few individual starburst galaxies, but none exhibited statistically significant neutrino emission. To date, only two dedicated stacking searches targeting starbursts have been conducted, roughly a decade apart. The first, using data from a partially completed detector, found no significant excess [143]. A more recent stacking analysis focused on **ultraluminous infrared galaxies** (ULIRGs)—a subclass of starbursts with star-formation rates exceeding $100\ M_\odot\ \mathrm{yr}^{-1}$—also yielded null results [150]. The scarcity of analyses targeting starbursts stems from their heterogeneous

[14] A formal publication presenting these updated results is in preparation by the IceCube Collaboration.

nature, which complicates the construction of a representative sample. Addressing this challenge will be crucial for the IceCube analyses presented in Chapters 5 and 6, where we will also target the less luminous but more numerous **luminous infrared galaxies** (LIRGs).

Time-dependent searches and promising source classes

As discussed in the time-integrated section, the IceCube Collaboration conducted a time-integrated search for high-energy neutrinos using 10 years of data [117]. A complementary time-dependent analysis was performed on the same dataset, utilizing similar source-search strategies [151].

In the all-sky scan, this analysis searched for multiple Gaussian-like flares with characteristic durations across each pixel of the sky. The identified hotspots in both hemispheres were consistent with background expectations, though the analysis provides declination-dependent per-source sensitivity.

Furthermore, within the same analysis, a population study targeted neutrino flares from the same source classes examined in the 10-year time-integrated search, spanning both hemispheres. While no significant excess was observed in the Southern Hemisphere, a post-trial significance for the binomial test of 3.0σ was reported for neutrino flare activity from four Northern Hemisphere sources over the 10-year period [151]. The identified galaxies are: M87, TXS 0506+056, GB6 J1542+6129 and NGC 1068.

Some promising transient high-energy neutrino sources include gamma-ray bursts (GRBs), blazars, and tidal disruption events (TDEs), all of which are also strong candidates for UHECR production (see Section 1.1.4):

- **GRBs**: High-energy neutrino emission from GRBs has been strongly constrained over the years. Recent dedicated GRB searches are detailed in [152, 153]. Notably, the recent multi-wavelength detection of the brightest GRB ever-detected enabled IceCube to place stringent upper limits on its neutrino emission in the MeV–PeV range [154].

- **TDEs**: In 2019, IceCube communicated the real-time alert IC191001A via the General Coordinates Network (GCN). The TDE AT2019dsg, identified by the Zwicky Transient Facility (ZTF), was proposed as a potential counterpart [155]. Similarly, in 2020, the TDE AT2019fdr was associated with the realtime alert IC200530A [156]. A systematic analysis of TDE-like flares, including AT2019dsg and AT2019fdr, found a third possible association: AT2019aalc with IC191119A [157]. However, a follow-up stacking search by IceCube yielded results consistent with background expectations [158].

- **Flaring blazars**: AGN typically exhibit electromagnetic variability. The most notable variability associated with high-energy neutrino emission to date is observed in the gamma-ray flaring blazar TXS 0506+056, which was identified following the IceCube-170922A alert in 2017 [14] (see also Section 1.6.2).

1.6.2 Evidence for the first sources

As discussed in the previous section, most of the point-source searches conducted by IceCube have yielded null detections, enabling the placement of constraints on various high-energy phenomena. Here, we highlight candidate sources that have reached the level of statistical evidence or higher.

Galactic plane

The Galactic plane, a prominent feature of the Milky Way shown optically in Figure 1.10A, has been extensively studied across the electromagnetic spectrum, from radio to gamma-ray wavelengths. Recently, IceCube was able to extend this view by providing a high-energy neutrino perspective.

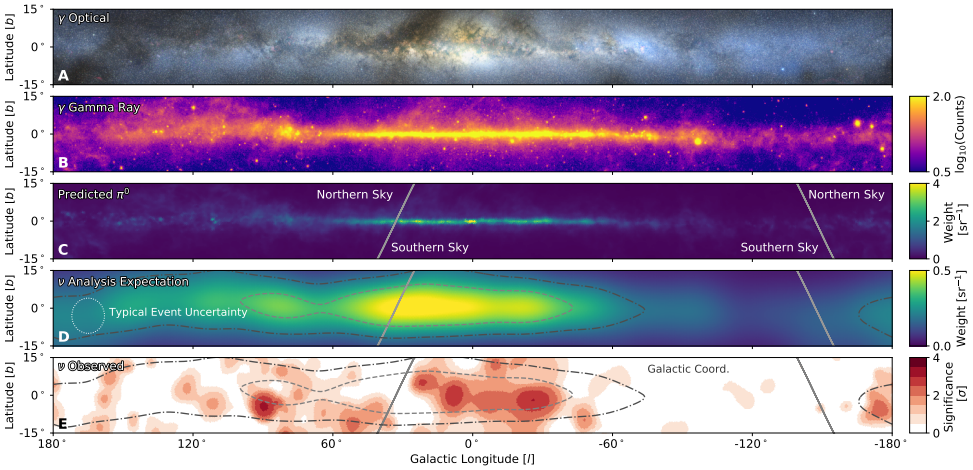

FIGURE 1.10: Panels A through D depict the Galactic plane (GP) in galactic coordinates (l, b), centered on the Galactic center, with latitude spanning $-15°$ to $+15°$ and longitude from $-180°$ to $+180°$. Panel A shows the GP in optical light, obscured by gas and dust. Panel B displays gamma-ray emission above 1 GeV from the *Fermi*-LAT 12-year survey. Panel C presents the neutrino-emission template expected from a π^0 template. Panel D modifies Panel C to include IceCube's cascade neutrino event sensitivity and a typical angular resolution of $7°$, illustrated by the dotted circle. Contours in Panel D enclose regions containing 20% and 50% of the predicted diffuse neutrino flux. Panel E shows the pretrial significance map from the all-sky IceCube point-source search using cascade events, with contours matching those in Panel D. Figure taken from [13].

Gamma rays from the Galactic plane (Figure 1.10B) originate from both leptonic (Section 1.3) and hadronic processes. Above 1 GeV, the dominant mechanism for gamma-ray production is the decay of neutral pions. These pions are generated when cosmic rays (CRs) of (extra)galactic origin interact with interstellar matter, producing both neutral and charged pions. The latter decay into high-energy neutrinos, establishing a connection between gamma-ray and neutrino emission. This relationship implies the presence of a diffuse high-energy neutrino flux accompanying the observed gamma rays.

The IceCube Collaboration recently explored this link [13], constructing high-energy neutrino emission models based on gamma-ray data. These models incorporate assumptions about CR source distributions, propagation and diffusion properties, target gas densities, and IceCube's angular resolution. From these, spatial templates were developed (Figure 1.10C, D) and compared to IceCube data (Figure 1.10E).

The Galactic center, along with most of the expected high-energy neutrino emission from this region, lies in the Southern Hemisphere. Due to its location at the South Pole, IceCube is particularly affected by atmospheric muon backgrounds in this region. These backgrounds can be suppressed by selecting only events that originate within the detector volume. However, this strategy does not mitigate the background from

atmospheric neutrinos. At higher energies, atmospheric neutrino backgrounds can be partially reduced by tagging accompanying muons expected from the same cosmic-ray air shower. Yet, at TeV energies—relevant for neutrino emission from the Galactic center—this background remains substantial and is dominated by atmospheric muon neutrinos.

To address this, the Galactic plane analysis employed a cascade event selection instead of track-like events used in source searches. While tracks offer superior angular resolution, cascades significantly reduce atmospheric neutrino backgrounds at TeV energies, improve energy resolution, and lower the energy threshold.

Deep-learning techniques were instrumental in distinguishing astrophysical neutrinos from background, resulting in a rejection of the background-only hypothesis with a significance of 4.5σ [13]. While the signal is consistent with diffuse neutrino emission from the Galactic plane, it remains unclear whether this emission arises from an unresolved population of Galactic sources.

In contrast to other wavelengths where the Galactic plane is dominant, it contributes only 6-13% of the diffuse high-energy neutrino flux observed by IceCube [13]. This suggests a predominantly extragalactic origin for the observed flux. Nonetheless, only two extragalactic sources have shown tentative evidence for high-energy neutrino emission, a topic addressed in the following section.

Active galaxies: NGC 1068 and TXS 0506+56

On September 22, 2017, IceCube detected a high-energy neutrino event, IC170922A [14]. Within minutes, an automated alert was issued via the Global Coordinates Network (GCN [159, 160]; also discussed in Section 4.5), prompting worldwide follow-up observations. Enhanced gamma-ray emission was subsequently observed from the region indicated by IceCube, identifying the gamma-ray flaring blazar TXS 0506+056 at the corresponding location on the sky. The post-trial significance of the association between the neutrino alert and the gamma-ray flare is disfavored at the $\sim 3\sigma$ level under any scenario where the neutrino and gamma-ray production are linearly correlated [14]. This blazar is located at a distance of approximately $1500\,\mathrm{Mpc}$.

In addition to the coincident detection, an archival search by the IceCube Collaboration revealed an excess of neutrinos from TXS 0506+056 between September 2014 and March 2015 at a significance of 3.5σ [15]. It is noted that this significance lowered when using improved IceCube data [161].

The statistical significance of both the real-time and archival analyses remains below the threshold for a definitive discovery. Moreover, earlier IceCube (strongly) constrained the overall contribution of Fermi blazars, indicating they cannot account for the majority of the diffuse astrophysical neutrino flux [141]. Nevertheless, this multi-messenger campaign has highlighted blazars as intriguing candidates for high-energy neutrino emission.

As detailed in Section 1.6.1, NGC 1068 is the most significant point-source candidate identified by IceCube, with a post-trial significance of $\sim 4.0\sigma$ [16, 144]. Located only about 10 Mpc away—over two orders of magnitude closer than the blazar TXS 0506+056—this archetypal Seyfert galaxy, a subclass of AGN lacking a prominent large-scale jet (Section 1.1.4), exhibits intense star formation, as evidenced by its bright infrared emission (e.g., [162–164]). Moreover, we also note that NGC 1068 is classified as a luminous infrared galaxy, which will be the primary focus of this work.

NGC 1068 is a known gamma-ray emitter. *Fermi*-LAT reports a gamma-ray flux, scaled with energy squared, of $E_\gamma^2 \Phi_\gamma \simeq 10^{-9}\ \mathrm{GeV\ cm^{-2}\ s^{-1}}$ in the 0.1–100 GeV range

[165], while MAGIC places upper limits of 10^{-10}–10^{-9} GeV cm^{-2} s^{-1} at sub-TeV energies [165]. According to Eq. (1.10), hadronic gamma rays and neutrinos are expected to have comparable fluxes when scaled with energy squared. However, IceCube detects a significantly larger neutrino flux from the direction of NGC 1068 than expected, with $E_\nu^2 \Phi_{\nu+\bar{\nu}} \simeq 10^{-7}$ GeV cm^{-2} s^{-1} around 1 TeV [16, 144]. The absence of a corresponding gamma-ray flux suggests substantial internal gamma-ray absorption. This gamma-ray dim, neutrino-bright behavior aligns with the hidden-source hypothesis inferred from diffuse gamma-ray and neutrino observations (Section 1.5.2).

NGC 1068 contains various energetic components such as an obscured AGN [166], starburst regions [167], a relative small-scale jet of $\lesssim 1$ kpc [162], and a molecular outflow [164]. While all these regions could, in principle, contribute to high-energy neutrino production, studies indicate that the vicinity of the AGN is the most likely site that satisfies both the required energy budget for high-energy neutirno production and the necessary conditions for gamma-ray attenuation [168, 169]. In particular, if neutrino production occurs near the central black hole, at distances of approximately 10–100 gravitational radii, the conditions could enable the required level of gamma-ray suppression [168].

In conclusion, although TXS 0506+056 and NGC 1068 are compelling candidates for high-energy neutrino emission, neither meets the threshold for a discovery-level claim. Even if confirmed, their combined contribution to the total diffuse neutrino flux observed by IceCube would be modest, contributing no more than $\sim 1\%$ within their respective energy ranges. Figure 1.11 illustrates the point-source fluxes of TXS 0506+056 and NGC 1068 in comparison to the diffuse high-energy neutrino spectrum measured by IceCube through two detection channels. Together with evidence for high-energy neutrino emission from the Galactic plane, these findings highlight that the majority of the diffuse high-energy neutrino flux remains unaccounted for.

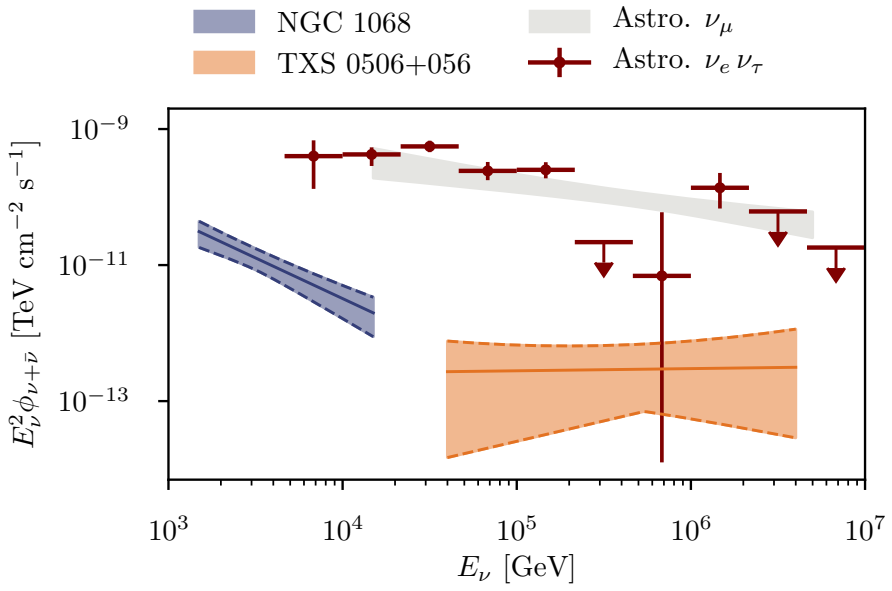

FIGURE 1.11: Comparison of the point-source fluxes of NGC 1068 (blue, left) and TXS 0506+056 (orange, right) with the diffuse astrophysical neutrino flux observed by IceCube through two detection channels (data points and grey band) [8, 170]. All fluxes are scaled by a factor E^2. Figure taken from [16].

In this work, we investigate luminous infrared galaxies (LIRGs) and ultraluminous infrared galaxies (ULIRGs) as potential sources of high-energy neutrinos. These highly energetic systems are predominantly powered by intense, dust-obscured starburst activity, with a fraction also harboring active galactic nuclei (AGN). Such environments offer both efficient mechanisms for particle acceleration and dense target material, likely fulfilling the conditions necessary for high-energy neutrino production. In Chapter 2, we provide a detailed introduction to LIRGs and ULIRGs and underscore their significance as promising candidates for high-energy neutrino sources.

CHAPTER 2

Luminous Infrared Galaxies & Beyond

In 1983, the Infrared Astronomical Satellite (IRAS) was the first space-based telescope to perform an all-sky survey at infrared (IR) wavelengths [171]. IRAS mapped about 96% of the sky, observing over 250.000 sources at 12 μm, 25 μm, 60 μm, and 100 μm. Among the tens of thousands of newly discovered systems, a population of galaxies was identified whose IR output dominates their total energy output. The brightest of these systems have an IR luminosity that is tens to hundreds of times greater than the total output of the Milky Way at all wavelengths. The isotropic bolometric luminosity[1] of the Milky Way is of the order of $10^{10} L_\odot$, with $L_\odot = 3.828 \times 10^{26}$ W being the isotropic bolometric luminosity of the Sun. These IR-bright galaxies discovered by IRAS were classified as:

- **Luminous infrared galaxies** (LIRGs; $10^{11} L_\odot \leq L_{\rm IR} \equiv L_{\rm IR[8-1000\mu m]} < 10^{12} L_\odot$), observed by other surveys as a mixture of interacting galaxies and secularly evolving galaxies.
- **Ultraluminous infrared galaxies** (ULIRGs; $L_{\rm IR} \geq 10^{12} L_\odot$), typically observed as a system of (almost) completely merged galaxies.

Figure 2.1 presents a set of local LIRGs and ULIRGs (U/LIRGs) imaged in optical wavelengths by the Hubble Space Telescope, showing both their dynamic structure and dusty nature. In 1988, follow-up observations after the IRAS mission led to the identification of the first hyper luminous infrared galaxy (HyLIRG; $L_{\rm IR} > 10^{13} L_\odot$) [172–174].

Building on the success of the IRAS mission, several IR observatories followed. The first successor to IRAS was the Infrared Space Observatory (ISO), launched in 1996. Subsequent missions included the Spitzer Space Telescope (2003) [175], the Akari mission (2006) [176], the Herschel Space Observatory (2009) [177], and the Wide-field Infrared Survey Explorer (WISE, 2015) [178]. These observatories facilitated detailed spectroscopic studies and extensive redshift surveys, which revealed that while U/LIRGs are relatively rare in the local Universe, they were significantly more common in the distant past (e.g. [179]).

Advancements in observational techniques also led to the discovery of five extremely luminous infrared galaxies (ELIRGs; $L_{\rm IR} > 10^{14} L_\odot$) at high redshift ($z > 2$) [180], which are the most luminous IR systems known to date. In this work, however, we focus primarily on local systems at much lower redshifts ($z \lesssim 0.09$) in view of the fact that a possible observable neutrino flux decreases with distance. Given the rarity of HyLIRGs and ELIRGs, we define ULIRGs as galaxies with $L_{\rm IR} \geq 10^{12} L_\odot$.

Most recently, the James Webb Space Telescope (JWST) was successfully launched in 2021 [181]. With its unprecedented resolution, JWST allows astronomers to peer deeper into the distant past than any previous IR telescope, offering new insights into

[1] The bolometric luminosity is defined as the total luminosity of a source, obtained by integrating its emission over the entire spectrum (see Appendix A).

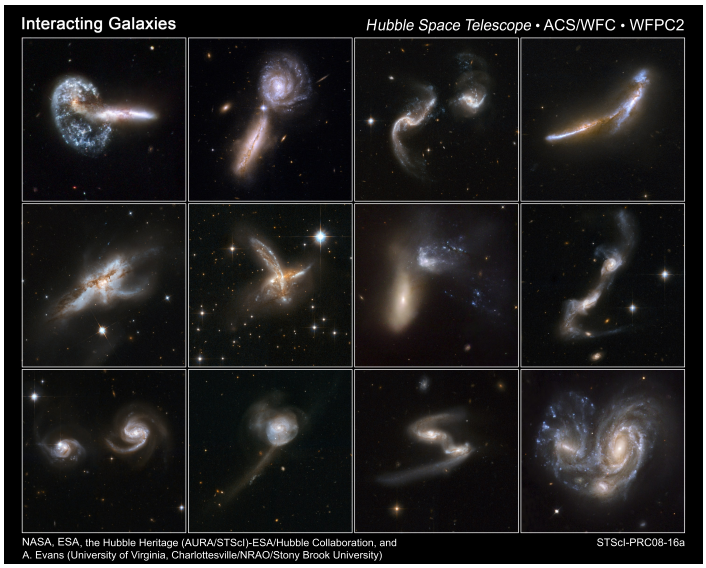

FIGURE 2.1: A selection of local U/LIRGs in the Great Observatories All-Sky LIRG Survey (GOALS) [19]. These optical images reflect the dusty and dynamic nature of U/LIRGs. Credits indicated in the figure.

the (early) Universe.

Since their discovery, significant progress has been made in understanding the physics underlying the formation of U/LIRGs. The intense IR emission from these systems is primarily driven by starburst activity and active galactic nuclei (AGN), both of which are triggered by gravitational interactions in a substantial fraction of U/LIRGs at low redshifts. Radiation from these starburst and AGN regions is absorbed by dust grains, which subsequently re-emit the energy in the IR spectrum. The extraordinary luminosity of U/LIRGs thus reflects intense star formation and AGN activity occurring in highly obscured regions.

As discussed in Section 1.1.4, both starburst regions and AGN are promising sites for CR acceleration. The combination of a large energy budget and the merger-driven enhancement in the density of potential targets makes U/LIRGs excellent candidates for efficient high-energy neutrino production.

This work focuses on local U/LIRGs with redshifts $z < 0.09$—observed as part of the Great Observatories All-Sky LIRG Survey (GOALS) [19]—as potential sources of high-energy neutrinos.

Overview & Context First, we describe the general properties of U/LIRGs in Section 2.1, including their morphology, nuclear activity, and the evolution of their number density with redshift. Then, in Section 2.2, we discuss local U/LIRGs as candidate high-energy neutrino sources. Finally, in Section 2.3, we present the U/LIRG selections that will be targeted in the remainder of this work.

The concepts presented in this chapter are applied in Chapter 3, where we develop a phenomenological framework using GOALS observations to estimate the high-energy neutrino flux from these galaxies. Additionally, Chapters 5 and 6 investigate GOALS sources in the Northern Hemisphere as candidate neutrino sources using data from the IceCube Neutrino Observatory at the South Pole.

2.1 Characteristics

2.1.1 Morphology

When galaxies collide, gravitational interactions disrupt the gas, dust, and stellar orbits within the system. The most extreme form of such interactions is known as a merger, where the original galaxies become indistinguishable in the final morphology. A merger can span hundreds of millions of years, from the initial approach to full coalescence, making it impossible to observe the entire process within a human lifetime. Figure 2.2 illustrates this progression with examples of systems at various stages.

Locally, over 90% of ULIRGs result from major mergers between two similarly sized, gas-rich galaxies. In contrast, the fraction of (strongly) interacting systems among local LIRGs is smaller. For instance, [182] finds that approximately 50% of local LIRGs are interacting or merging systems, while the remaining 50% are classified as spiral galaxies. In this trend, it has been suggested that between 20% and 40% of LIRGs show no signs of major tidal interactions [183, 184]. Additionally, while LIRGs are observed throughout all stages of the merging process, ULIRGs are predominantly found in the later stages, approaching complete coalescence [184].

A correlation between morphology and IR luminosity is also observed in LIRGs, independent of redshift. Below $L_{\mathrm{IR}} \approx 10^{11.5} L_{\odot}$, most LIRGs are classified as non-interacting spiral galaxies, whereas above this threshold, interacting and merging systems dominate [185].

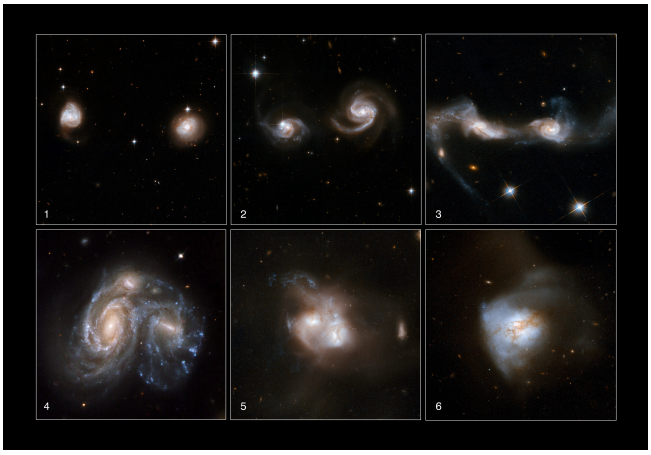

FIGURE 2.2: Six stages of a galaxy merger observed with the Hubble Space Telescope. Each stage is represented by a different galaxy system. *Credits: NASA, ESA, the Hubble Heritage Team (STScI/AURA)-ESA/Hubble Collaboration, A. Evans (University of Virginia/NRAO/Stony Brook University), K. Noll (STScI), and J. Westphal (Caltech).*

The morphological patterns observed in U/LIRGs suggest an evolutionary connection between disk galaxies, U/LIRGs, quasars, and elliptical galaxies. This evolutionary scenario, first proposed in 1988 [186] and building on earlier work [187, 188], posits that interactions between gas-rich disk galaxies trigger nuclear activity, primarily starbursts, and possibly AGN activity. The radiation produced is reprocessed by surrounding dust into thermal IR emission, accounting for the typical IR luminosities of LIRGs. As the merger progresses, nuclear activity—particularly AGN-driven—intensifies, further increasing IR luminosity and leading to a ULIRG phase. Feedback mechanisms from starbursts and AGN could drive gas outflows, depleting the nuclear gas reservoir and eventually exposing the central supermassive black hole, giving rise to a quasar

phase. After the merger completes and nuclear activity subsides, the remnant system can evolve into an elliptical galaxy. This framework provides an explanation for many properties observed in local U/LIRGs.

High-redshift surveys indicate a decreasing fraction of mergers with increasing redshift [185, 189], challenging the notion that mergers dominate the intense IR luminosity of U/LIRGs in distant galaxies. One proposed explanation is that elevated gas fractions in high-redshift galaxies significantly raise the luminosity threshold distinguishing normal star formation from merger-driven starbursts[2], increasing it by an order of magnitude between $z \sim 0$ and $z \sim 2$ [190]. This potential divergence between local U/LIRGs and their high-redshift counterparts is used as a cautionary argument in section 3.4.2, where the locally predicted high-energy neutrino flux of U/LIRGs is extrapolated to high-redshift systems.

2.1.2 Nuclear activity

Extensive simulations have shown that galaxy interactions can drive gas from the kpc scale into the innermost regions (< 100 pc) of the interacting galaxies via gravitational torques. This triggers both star formation at $\sim 10-100$ pc and accretion onto the supermassive black hole(s) (SMBH) at sub-pc scales [192, 193]. The bright radiation produced by these regions heats up the large amounts of dust accumulated during the merger, fueling the intense IR emission observed in U/LIRGs. Below we discuss in more detail the physical properties of star-forming regions, AGN and their connection in U/LIRGs.

(Circum)nuclear starburst region

Pressure waves are generated when large amounts of gas collide in the inner $\sim$100 pc regions of galaxies. This can lead to an enhanced rate of star formation in a region known as the (circum)nuclear starburst region. These regions typically host a higher concentration of short-lived, hot, massive stars compared to more moderate star formation environments like that of the Milky Way. The ultraviolet (UV) radiation from these stars has enough energy to partially ionize the surrounding gas and dust in the giant molecular clouds where they formed, creating H II regions.

Thermal radio emission in these H II regions is produced by Bremsstrahlung, which is directly proportional to the rate of ionizing photon production by the young, hot stars (e.g. [194]). This establishes a clear link between radio emission and recent star formation. Using radio emission as a tracer of star formation is particularly valuable in dust-obscured regions, where radio wavelengths remain relatively unobscured.

Additionally, the strong UV radiation from the newly formed stars significantly heats the surrounding dust, causing it to re-emit the absorbed energy as thermal radiation. This establishes a connection between IR emission and obscured star formation. It is also worth noting that UV emission serves as a good tracer of recent star formation in non-obscured regions (e.g. [195]).

Both simulations and empirical observations have shown that for various electromagnetic tracers, where L_{tracer} is the luminosity of the tracer, the star formation rate

[2] See references [190, 191] for a discussion on why higher gas fractions do not necessarily result in a higher frequency of merger-driven starbursts.

(SFR) can be estimated as (see e.g. [194, 196])

$$\left(\frac{\mathrm{SFR}}{M_{\odot}\mathrm{yr}^{-1}}\right) = A_{\mathrm{tracer}}\left(\frac{L_{\mathrm{tracer}}}{\mathrm{erg\ s}^{-1}}\right) . \tag{2.1}$$

The proportionality constant A_{tracer} is determined through simulations, which depend on two key quantities: the initial mass function (IMF) and the star formation history (SFH). The IMF describes the mass distribution of stars at the time of their formation within a given volume of space. It is typically modeled by one or more power laws of the form $\zeta(M) \propto M^{-\beta}$, where M is the stellar mass and β is the power law index (see, for example, [197] for a review). The index β may vary across different ranges of stellar masses. The SFH, on the other hand, describes the evolution of the star formation rate over time. Star formation can occur in short bursts or at a relatively constant rate over longer periods. While simulations often assume a single burst or a constant rate over 100 Myr, the actual star formation history is likely a complex combination of both scenarios, which is not trivial to model.

To estimate the order of magnitude of the SFR in U/LIRGs, we use the observed IR emission as a tracer. Assuming that dust re-radiates the total bolometric luminosity of stars in the IR and considering a continuous burst lasting $10-100$ Myr, with solar abundances and a Salpeter IMF [59], the resulting constant SFR ranges from $\sim 20-200\ M_{\odot}\ \mathrm{yr}^{-1}$ for IR luminosities between $10^{11}\ L_{\odot}$ and $10^{12}\ L_{\odot}$. This estimate may vary depending on the choice of IMF, SFH, and potential AGN contamination. A more detailed discussion of these factors is presented in Chapter 3.

An enhanced SFR directly leads to an elevated **core-collapse supernova** rate, marking the endpoints of massive stars with progenitor masses $\gtrsim 8\ M_{\odot}$.[3] Core-collapse supernovae eject the progenitor's outer layers, generating optical bursts that outshine entire galaxies and releasing $\sim 10^{51}$ erg [198, 199]. Typical supernova rates are $\sim 0.01\ \mathrm{yr}^{-1}$ in galaxies like the Milky Way [60], compared to $\sim 0.1-1\ \mathrm{yr}^{-1}$ in U/LIRGs [200, 201]. Hypernovae, an energetic supernova subtype, result from the direct collapse of stars with masses exceeding $30\ M_{\odot}$ into black holes, releasing $\sim 10^{52}$ erg [202].

The expelled outer layers travel at $\sim 10^4$ km s^{-1}, generating shock waves upon impact with the surrounding medium and accelerating particles via diffusive shock acceleration (Section 1.1.3). This produces non-thermal radio synchrotron emission and likely high-energy hadrons [41, 44].

At the explosion's core, a so-called neutron star remains, possessing extreme density, rapid rotation, and strong magnetic fields. Magnetars exhibit magnetic fields thousands of times stronger than typical neutron stars, while pulsars emit lighthouse-like beams of radiation. Some neutron stars exhibit both properties. Notably, magnetars and pulsars are also candidates for cosmic-ray acceleration to high energies (Section 1.1.4).

In dust-obscured U/LIRGs, estimating supernova and hypernova rates through optical or radio methods for large samples is challenging. An alternative, albeit more uncertain approach involves using tracers linked to supernova rates via models and simulations, enabling the study of larger populations of galaxies. In Chapter 3, the supernova rate in a set of local U/LIRGs is calibrated using their IR luminosity as a

[3] Thermonuclear supernovae, with $\lesssim 8\ M_{\odot}$, originating from white dwarfs accreting mass in binary systems, exhibit significant time delays relative to progenitor mass and are not expected to show enhanced rates in LIRGs.

tracer. These supernova rates will be crucial in estimating the high-energy neutrino emissio from GOALS galaxies.

Tidal disruption events

In the LIRG Arp 299, a nearby pair of merging galaxies at about 50 Mpc [19], a bright transient at near-IR wavelengths has been detected near the AGN of one of the galaxies [203]. This event was identified as a tidal disruption event (TDE), wherein a star is torn apart by the gravitational forces of a black hole (see Section 1.1.4). The expected optical emission was obscured by dust, which redirected the energy into intense IR radiation. Furthermore, radio observations revealed the formation of a jet, which is likely the result of the stellar material being accreted onto the central black hole. These findings suggest that massive stars are being accreted onto the SMBH in U/LIRGs. Supporting this scenario, an optical flare observed in the central region of the ULIRG F01004-2237 was also most likely a TDE [204].

An elevated TDE rate in U/LIRGs compared to field galaxies could be attributed to concentrated nuclear star formation, which increases stellar densities near the central SMBHs. Additional contributing factors may include the formation of close SMBH binaries [205] and SMBH recoils resulting from coalescence of these binary systems [206].

Active Galactic Nuclei

If a merger persists long enough, kpc-scale gas and plasma in the interacting galaxies can be funneled toward the vicinity of the central spinning SMBH. This gas may then accrete onto the SMBH, triggering an enhanced state of activity known as an AGN, introduced in Section 1.1.4. Figure 2.3 shows a visual representation of the central region of a galaxy hosting a circumnuclear starburst at $\sim 10-100$ pc and a SMBH surrounded by an accretion disk and torus, launching two relativistic large-scale particle jets. Note that although small-scale jets (order of kpc) are observed in U/LIRGs, the large-scale relativistic Mpc-scale jets are not. Below we discuss some observables of AGN in U/LIRGs:

- **Presence:** AGN are observed in both LIRGs and ULIRGs. In [207], multiple selection techniques based on multi-wavelength data were applied to identify AGN in a sample of local U/LIRGs. The study found that approximately 25% of LIRGs and 60% of ULIRGs were classified as AGN based on at least one selection criterion. While the absolute AGN identification rates in U/LIRGs may differ across studies, there is broad consensus that AGN are more prevalent in ULIRGs than in LIRGs [208, 209].

- **Luminosity:** The contribution of the bolometric[4] AGN luminosity ($L_{\mathrm{AGN,bol}}$) to the total IR luminosity (L_{IR}) is generally very low in LIRGs, at the percent level [210], compared to ULIRGs, where it is at the ten percent level [211]. This could be explained by the evolutionary link discussed in Section 2.1.1.

  In [212], it was concluded from a local volume-limited sample of LIRGs that the contribution of the AGN to the IR luminosities of the galaxies is generally small, with 70% of them having $L_{\mathrm{AGN,bol}}/L_{\mathrm{IR}} \leq 0.05$, and only approximately 8% of the sources having a significant contribution ($L_{\mathrm{AGN,bol}}/L_{\mathrm{IR}} > 0.25$). The study concludes that, at least in the local Universe, the IR emission from U/LIRGs

[4] See Appendix A for the definition of a bolometric luminosity.

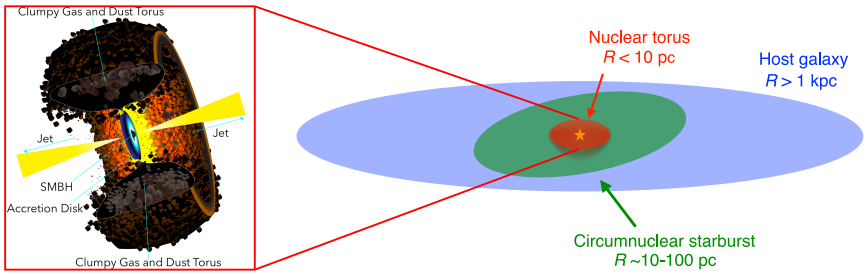

FIGURE 2.3: Artist's impression of an active galactic nucleus (AGN) containing a supermassive black hole (SMBH) surrounded by an accretion disk and a torus-like structure. Two jets, observed in a subdominant fraction of the AGN and typically not observed in U/LIRGs, are also shown. The typical scales of the circumnuclear starburst and AGN environments observed in U/LIRGs are indicated. Figure taken from [150], which was adapted from [71, 214]

appears to be dominated by starburst activity. However, it should be noted that for individual U/LIRGs, the AGN can still be the dominant source of high-energy radiation.

- **Obscuration:** Due to accretion onto the SMBH during mergers, AGN in U/LIRGs are often heavily obscured. This is supported not only by simulations [213] but also by observations. A study of 60 local U/LIRGs hosting AGN found that, regardless of the merger stage, the median column density (measure for the matter along the line of sight) of accreting SMBHs is systematically higher than that of local hard X-ray-selected AGN [166]. This analysis also revealed that the fraction of AGN in U/LIRGs classified as Compton-thick (hydrogen column density $N_{\rm H} \geq 1.5 \times 10^{24}\,{\rm cm}^{-2}$; see Section 1.1.4) peaks at $74^{+14}_{-19}\%$ during the late merger stage, just before coalescence, when the projected nuclear separation is approximately 0.4–6 kpc. Furthermore, in the final stages of merging in U/LIRGs ($\lesssim 10$ kpc separation), the vast majority ($85^{+7}_{-9}\%$) of AGN are obscured, characterized by $N_{\rm H} \geq 10^{23}\,{\rm cm}^{-2}$. A correlation between obscuration and merger stage has also been observed in other U/LIRG studies (e.g., [184]).

Nuclear hydrogen-cyanide emission

A subset of local U/LIRGs hosts highly obscured ($N_{\rm H} \gtrsim 10^{25}\,{\rm cm}^{-2}$) and hot ($> 100\,{\rm K}$) nuclei within the central 100 pc, known as **compact obscured nuclei** (CONs, e.g., [215]). These dense and energetic central regions can contribute significantly to the total IR luminosity of their host galaxies (see, for example, the case of IC 860 [216]).

The extreme column densities in CONs yield dust optical depths greater than unity, even at far-IR wavelengths, rendering their most obscured nuclear regions transparent only at millimeter-like radio wavelengths. This behavior is exemplified in the closest ULIRG Arp 220 [217] and the LIRGs IC 860 [216] and NGC 4418 [218]. The driving mechanism for such compact obscured regions remains unclear, potentially involving a hidden AGN, a nascent nuclear starburst, or both [216].

Traditional diagnostics, including mid-IR, optical, and X-ray emission, fail for CONs due to severe attenuation. Instead, rotational lines of vibrationally excited hydrogen cyanide (referred to as HCN-vib) provide a robust tracer [215, 219]. The excitation of HCN-vib is radiatively driven by intense mid-IR radiation from hot dust heated by AGN and/or starburst activity. Sufficiently high temperatures and bright mid-IR fields

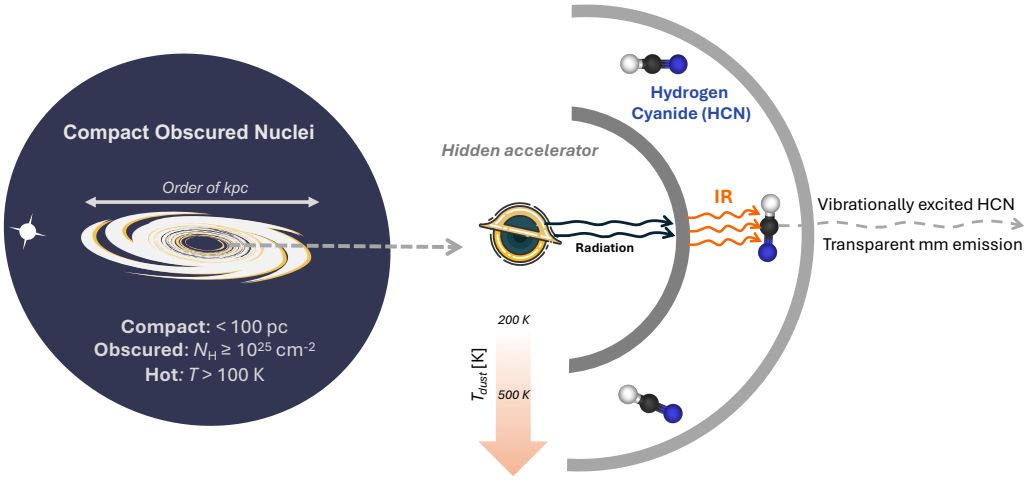

FIGURE 2.4: A fraction of U/LIRGs contains extremely compact ($< 100\,\mathrm{pc}$), heavily obscured ($N_\mathrm{H} \gtrsim 10^{25}\,\mathrm{cm}^{-2}$), and warm ($> 100\,\mathrm{K}$) cores heated by AGN and/or starburst activity. Trapped heat raises core temperatures, producing bright mid-IR radiation that excites HCN molecules. Their de-excitation generates millimeter (mm) emissions detectable from Earth with observatories such as the Atacama Large Millimeter Array (ALMA). Figure adapted from [215].

excite HCN molecules, producing millimeter and sub-millimeter emissions capable of penetrating thick obscuring material, as illustrated in Figure 2.4. HCN-vib detection with ALMA allowed for the first systematic survey of CONs in local U/LIRGs [219]. A volume-limited sample of 46 far-IR-selected sources was targeted and it was concluded that CONs are exclusive to U/LIRGs, appearing frequently in about 20% of LIRGs and 40% of ULIRGs.

Currently, the definition of these remarkable CONs remains ambiguous. One criterion uses the ratio $L_{\mathrm{HCN-vib}}/L_{\mathrm{IR}} > 10^{-8}$ [215], though it may miss galaxies with spatially extended IR emission. Alternatively, one can identify [219] CONs as systems where HCN-vib surface brightness exceeds 1 solar luminosity per pc squared ($\Sigma_{\mathrm{HCN-vib}} > 1\ L_\odot\,\mathrm{pc}^{-2}$) over a region with a radius of at least 5 pc.

In Figure 2.5, the left panel displays NGC 4418, classified as a CON by all diagnostic criteria [219], while the right panel shows NGC 1068, which lacks significant HCN-vib emission at the spatial scales characteristic of other archetypal CONs [219, 220]. Notably, NGC 4418 appears relatively inconspicuous at optical wavelengths, in stark contrast to its compact, highly energetic core—less than 20 pc in size—that dominates the galaxy's infrared luminosity [218]. By comparison, NGC 1068 also exhibits substantial attenuation, but its emission originates from a more extended structure with less compact nuclear activity [163].

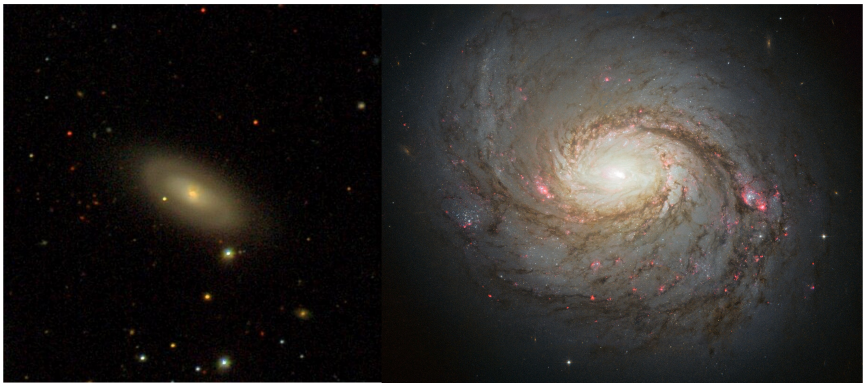

FIGURE 2.5: NGC 4418 (left) and NGC 1068 (right). NGC 4418 exhibits a highly compact morphology that completely obscures its intensely active nuclear region (within < 20 pc), whereas NGC 1068 shows a less compact and more extended structure. *Image credits–left: Sloan Digital Sky Survey; right: NASA, ESA, and A. van der Hoeven.*

2.1.3 Redshift evolution

In the local universe ($z < 0.3$), spiral galaxies (with $L_{\rm IR} < 10^{11} L_{\odot}$, hereafter referred to as *normal* galaxies) dominate the population, while U/LIRGs are relatively rare.[5] Deep-sky IR observations reveal that the comoving number densities of U/LIRGs increase significantly with redshift [179, 222, 223].

At $z \sim 1$, the comoving number densities of LIRGs and ULIRGs are approximately 40 and 100 times greater, respectively, than at $z \sim 0$ [223] (see the left panel of Figure 2.6). For both LIRGs and ULIRGs, this number density remains relatively constant between $1.3 \lesssim z \lesssim 2.3$ [179], illustrating the rapid evolution of these galaxies over the past eight billion years.

As a consequence of this evolution, LIRGs contribute approximately 50% of the total IR luminosity density[6] of the universe for $0.5 \lesssim z \lesssim 1$ [223] and become the dominant contributors above $z \simeq 1.5$, as depicted in the right panel of Figure 2.6. The right panel of Figure 2.6 also presents the star-formation rate (SFR) density as a function of redshift. The SFR density is derived using Eq. (2.1), with IR as the tracer, and adopting the scaling factor provided in Eq. (3) of [59]. This approach is justified because star formation across cosmic history has been significantly obscured by dust [224].

The redshift-dependent IR luminosity density, $\mathcal{Q}_{\rm IR}(z)$ (quantity on left axis of right plot in Figure 2.6), is typically expressed as (see, e.g., [150]):

$$\mathcal{Q}_{\rm IR}(z) = \mathcal{Q}_{\rm IR}(z=0)\mathcal{H}(z),$$

where $\mathcal{Q}_{\rm IR}(z=0)$ represents the IR luminosity density at $z = 0$, and $\mathcal{H}(z)$ describes the redshift evolution of the source class under consideration. These parameterizations are important for the study presented in this work, as they will be used to estimate the diffuse high-energy neutrino flux from LIRGs and ULIRGs in Section 3.4.2. Below, we outline the relevant redshift evolution parameterizations for this work.

[5] However, the number density of LIRGs exceeds that of optically selected starburst and Seyfert galaxies at comparable redshifts and bolometric luminosities (e.g., [221]).

[6] For future convenience it is noted here that the IR luminosity density in the right panel of Figure 2.6 has the dimensions of a generation rate (See Appendix A). As such the IR luminosity density will be expressed as $\mathcal{Q}_{\rm IR}$ and the star-formation rate density as $\mathcal{Q}_{\rm SFR}$.

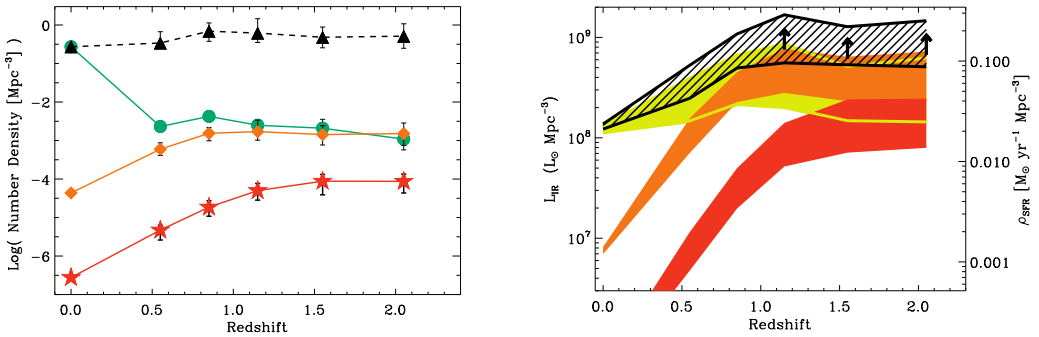

FIGURE 2.6: Left: Redshift evolution of the comoving number density for *normal* galaxies (black triangles, $10^7 L_\odot < L_{\rm IR} < 10^{11} L_\odot$), LIRGs (orange diamonds), and ULIRGs (red stars). Green circles show the total number density above the survey's flux detection threshold. Right: Redshift evolution of the comoving IR luminosity density for normal galaxies (solid yellow band), LIRGs (solid orange band), and ULIRGs (solid red band). The total IR luminosity density, combining all populations, is shown as a dashed black band. Bands represent $\pm 1\sigma$ uncertainties. Furthermore, the star formation rate density, $\rho_{\rm SFR}$, as a function of redshift is derived using Eq. (2.1) defined in this work with the scaling factor from Eq. (3) of [59]. Taken from [179]. .

Using the parametrization from [225, 226], the evolution of the total SFR density with redshift, $\mathcal{Q}_{\rm SFR}(z)$, is

$$\mathcal{H}_{\rm SFR}(z) \propto \begin{cases} (1+z)^{3.4}, & \text{for } 0 \leq z < 1, \\ (1+z)^{-0.3}, & \text{for } 1 \leq z < 4, \\ (1+z)^{-3.5}, & \text{for } z \geq 4. \end{cases} \tag{2.2}$$

The normalization is chosen such that $\mathcal{H}_{\rm SFR}(z=0) = 1$, ensuring continuity across redshift intervals.

For the ULIRG population, we adopt the parametrization $\mathcal{H}_{\rm ULIRG}(z)$ from [150, 227],[7]

$$\mathcal{H}_{\rm ULIRG}(z) \propto \begin{cases} (1+z)^{4}, & \text{for } 0 \leq z < 1, \\ \text{flat}, & \text{for } 1 \leq z < 4. \end{cases} \tag{2.3}$$

Motivated by Figure 2.6, we propose that the redshift evolution of LIRGs ($\mathcal{H}_{\rm LIRG}$) follows a similar trend. Therefore, the same parameterization will be applied to both LIRGs and ULIRGs in this study.

Future observations from the James Webb Space Telescope will enable more detailed modeling of the redshift evolution of U/LIRGs, although such an analysis is beyond the scope of this work.

[7] Other studies suggest a more rapid evolution, e.g. $\mathcal{H}_{\rm ULIRG}(z) \propto (1+z)^7$ for $0 \leq z < 1.5$ [228].

2.2 U/LIRGs as Candidate Neutrino Sources

As discussed in Section 2.1.2, the nuclear regions of U/LIRGs host (circum)nuclear starburst regions and/or active galactic nuclei (AGN), both of which provide environments with ample cosmic-ray (CR) acceleration possibilities. Due to the interacting and merging nature of many local U/LIRGs, their central regions are frequently obscured by dense baryonic matter and intense radiation fields that could serve as target for the accelerated particles. Coupled with their substantial energy budgets ($L_{\rm IR} \geq 10^{11}\ L_{\odot}$), U/LIRGs create favorable conditions for efficient high-energy neutrino production. Furthermore, the positive evolution of their number density with redshift could lead to a non-negligible contribution to the diffuse high-energy neutrino flux if high-energy neutrino production occurs consistently.

2.2.1 Neutrino production models

This section first provides an overview of the primary neutrino source models applicable to U/LIRGs. These models are categorized as either starburst- or AGN-related, which are the main drivers of the enormous energy budget in U/LIRGs. Next, we discuss the IceCube Collaboration's investigations of U/LIRGs as high-energy neutrino sources in more detail.

Starburst-driven: reservoir models

In the (circum)nuclear regions of local U/LIRGs, elevated star-formation rates ($\gtrsim$ 10–100 $M_{\odot}$ yr^{-1}; Section 2.1.2) drive enhanced supernova rates ($\sim$0.1–1 yr^{-1}, e.g., [200, 201]). These rates are 10 to 100 times larger than expected in more quiescent galaxies such as the Milky Way [60].

The supernova ejecta generate shock waves in the surrounding medium, creating environments suitable for particle acceleration. The strong magnetic fields ($\sim$ 10^2–10^4 μG; [229]) and high target densities ($\gtrsim$ 100–1000 cm^{-3}; e.g., [230]) characteristic of starburst regions in U/LIRGs enable high-energy particles to be confined and interact with substantial matter over time. As a result, the timescale over which hadronuclear interactions occur can become significantly shorter than the timescale at which CRs escape, resulting in a high probability of secondary particle production.[8] These collisions produce charged pions that decay into high-energy neutrinos, gamma rays, and electrons or positrons. Environments where CRs lose most of their energy before escaping are referred to as CR **reservoirs** or **calorimeters**. Similar reservoir models may also apply to hypernovae, the high-energy variant of supernovae.

In Chapter 3, we develop a novel reservoir model to estimate the high-energy neutrino emission from the nuclear regions of local U/LIRGs, utilizing a range of electromagnetic tracers specific to each source.

AGN-driven: disk-corona and beam-dump

Although starburst activity dominates most local LIRGs, obscured AGN activity is also observed in U/LIRGs (Section 2.1.2). High-energy neutrino production from obscured AGN has gained attention, particularly following evidence of high-energy neutrino emission from the direction of NGC 1068 (see Section 1.6.1). As a LIRG and Seyfert

[8] Although photohadronic interactions can theoretically occur in starburst regions, they are unlikely to be the dominant process. This is mainly due to the higher energy threshold of the process and the limited acceleration power of U/LIRGs.

II AGN, NGC 1068 hosts multiple potential high-energy neutrino production sites, including the AGN, starburst regions, and outflows. However, studies suggest the vicinity of the SMBH as the most promising site [168, 169], supported by both energy requirements and the requirement for strong gamma-ray attenuation (Section 1.6.2).

Below, we summarize potential mechanisms for high-energy neutrino production near SMBHs in U/LIRGs, primarily following [231].

- **RIAF/MAD:** In radiatively inefficient accretion flows (RIAFs)[9] and magnetically arrested disks (MADs), particle acceleration via magnetic reconnection or turbulence leads to inelastic collisions with baryonic matter and radiation.
- **Accretion shocks:** Diffusive shock acceleration at the inner disk edge enables meson production via pγ-interactions with ultraviolet and X-ray photons. Deeply produced gamma rays and cosmic rays are attenuated, making neutrinos the dominant observable signature.
- **Magnetized coronae:** The corona, energized by magnetic fields from the disk, likely undergoes magnetic reconnection, heating electrons that Comptonize disk photons into X-rays. Its turbulent, collisionless nature favors stochastic particle acceleration, leading to both pp and pγ interactions with disk and coronal photons. While Bethe-Heitler pair production can be significant, coronae are expected to be calorimetric, efficiently converting accelerated proton energy into neutrinos. Additionally, photon-photon interactions likely induce gamma-ray attenuation.

In addition to high-energy neutrino production near the SMBH, in the disk and/or corona, a fraction of local U/LIRGs contains sufficient target material on larger scales to efficiently convert a proton beam into high-energy neutrinos.

The work in [85, 227] investigates an **AGN beam-dump** model, where relativistic particles from the AGN are injected into dense Compton-thick columns of surrounding matter. In this scenario, hadrons undergo pp-interactions, with gas and dust nucleons, thereby generating high-energy neutrinos via pion production. The associated gamma rays are attenuated depending on the column density.

The beam-dump analysis in [85, 227] tests the potential contribution of ULIRGs to the diffuse high-energy neutrino flux detected by IceCube, using two approaches. First, assuming a conservative electron-to-proton luminosity ratio, it is concluded that ULIRGs alone are unlikely to dominate the diffuse IceCube flux. Second, normalizing the proton luminosity to match IceCube observations requires a column density of $N_{\rm H} \gtrsim 5 \times 10^{25}$ cm^{-2}, implying highly Compton-thick regions to remain consistent with the non-blazar extragalactic gamma-ray background constraint above 50 GeV. Interestingly, a fraction of the local U/LIRGs posses such column densities (Section 2.1.2). However, due to the extreme obscuration of these regions, it is currently unclear whether a beam of highly energetic particles can form in these compact regions. This is explored further in Chapter 6.

2.2.2 Searches using IceCube

The IceCube Collaboration conducted a search for a cumulative signal of high-energy neutrinos from a representative sample of 75 ULIRGs with redshifts $z \leq 0.13$, utilizing 7.5 years of data [150]. Although no significant signal was found, 90% confidence level

[9] Flows where Coulomb collisions occur on timescales longer than gas infall timescales, enabling particle acceleration.

upper limits on the diffuse high-energy neutrino flux from ULIRGs were derived. This is done by extrapolating the results of the representative sample of 75 ULIRGs across cosmic history. Figure 2.7 presents the integral upper limits on the ULIRG population's contribution to the diffuse neutrino flux up to redshift $z = 4$ for different unbroken power-law spectra, $E^{-\gamma}$ with $\gamma \in \{2.0, 2.5, 3.0\}$. The integral upper limits for E^{-2} and $E^{-2.5}$ rule out ULIRGs as the sole contributors to the diffuse neutrino flux up to approximately 3 PeV and 600 TeV, respectively.

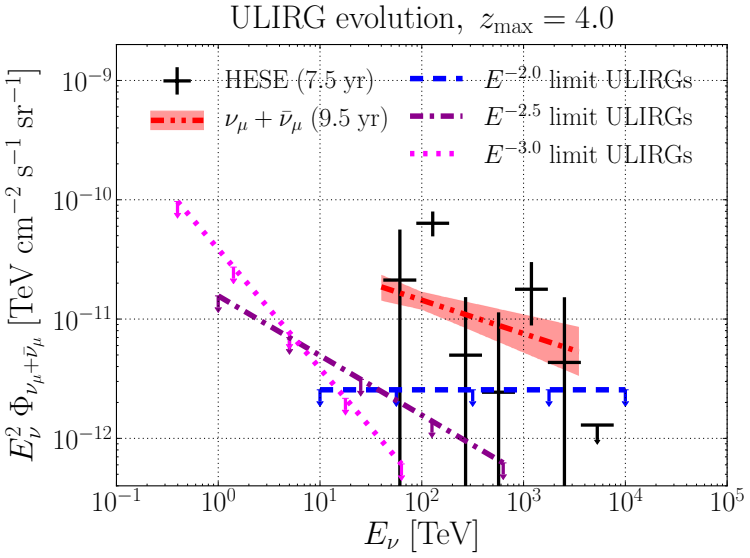

FIGURE 2.7: 90% confidence level upper limits on the diffuse muon-neutrino flux from the ULIRG population up to redshift $z = 4$. The integral upper limits are shown for unbroken power-law spectra of E^{-2} (dashed blue line), $E^{-2.5}$ (dash-dotted magenta line), and E^{-3} (dotted pink line). These limits are compared to the diffuse high-energy neutrino flux measured by IceCube via differential per-flavor measurements using the high-energy starting event (HESE [6]) sample (black crosses) and the 9.5-year best-fit unbroken power-law spectrum for astrophysical muon neutrinos from the Northern Hemisphere (red band) [7]. Figure taken from [150].

The authors of the ULIRG analysis compare the upper limits at the 90% confidence level with three phenomenological models predicting the diffuse high-energy neutrino flux from ULIRGs:

- A comarison is made with the model presented by [232], which assumes a CR reservoir scenario with hypernovae as hadronic accelerators (Section 2.2.1). This model shows tension with the E^{-2} IceCube upper limits for ULIRGs. Additional observational data are necessary to further test the validity of this model.

- A comparison is made with a general CR reservoir model targeting hadronically powered gamma-ray galaxies (HAGS) [233]. The model includes both ULIRGs and starburst galaxies with $L_{\rm IR} < 10^{12} L_\odot$. For a power-law spectrum with a spectral index $\gamma \leq 2.12$, this model can partially explain the diffuse high-energy neutrino flux observed by IceCube while remaining consistent with the non-blazar extragalactic gamma-ray background (EGB) constraint above 50 GeV. However, the IceCube upper limit for $E^{-2.12}$ excludes ULIRGs as the sole HAGS responsible for the diffuse neutrino observations. Importantly, this result does not exclude other HAGS candidates, such as starburst galaxies with $L_{\rm IR} < 10^{12}\,L_\odot$.

- A comparison is made with the AGN beam-dump model discussed in Section 2.2.1. Using the IceCube upper limits for ULIRGs, the authors derive a lower limit on the electron-to-proton luminosity ratio of $\gtrsim 10^{-3}$ [85, 227]. This value, however, should be regarded as an order-of-magnitude estimate due to substantial uncertainties in the derivation.

While the IceCube Collaboration and various modeling efforts have specifically targeted the ULIRG population [150, 227, 232, 233], only a few individual local LIRGs—most notably NGC 1068—have occasionally been included in broader source catalogs for IceCube searches (see Section 1.6.1), but never as a distinct population. This omission is partly due to the diversity within the LIRG class. As discussed in Section 2.1.1, local LIRGs span the entire merger sequence and exhibit a wide range of nuclear activity and environmental properties. Moreover, substantial differences may exist between local and high-redshift U/LIRGs (Section 2.1.1), further complicating modeling efforts, diffuse flux predictions, and the interpretation of results.

Additionally, the investigation of individual ULIRGs remains significantly underrepresented in current IceCube searches. This work specifically aims to address these gaps in the current state of the art, as outlined in the next section.

2.3 Source Selections for Multi-Messenger U/LIRG Studies

In this work we present the first comprehensive investigation of high-energy neutrino emission from a large sample of local LIRGs, employing both per-source modeling (Chapter 3) and an IceCube search (Chapters 5 and 6). Specifically, we focus on U/LIRGs from the Great Observatories All-Sky LIRG Survey (GOALS).

The model in Chapter 3 enables predictions of high-energy neutrino emission from individual galaxies within U/LIRGs. By leveraging the extensive archival data from GOALS [234], we can make predictions for all GOALS U/LIRGs across the entire sky. However, in our correlation study between IceCube neutrino data and GOALS U/LIRGs, we restrict the analysis to the Northern Hemisphere, where the sensitivity is approximately an order of magnitude higher than in the Southern Hemisphere. Furthermore, due to IceCube's limited pointing resolution, we do not analyze individual galaxies within U/LIRGs but instead consider them collectively. As such, the source selections for the studies we perform in Chapter 3 and Chapters 5 and 6 are different.

In Section 2.3.1, we formally introduce GOALS and in Section 2.3.2 we outline the sources selected for the per-source modeling in Chapter 3. Finally, in Section 2.3.3, we describe the different source selections for the IceCube source searches presented in Chapters 5 and 6.

2.3.1 Great Observatories All-Sky LIRG Survey (GOALS)

GOALS[10] aims to characterize the diversity of properties observed in a large, statistically significant sample of the nearest ($z < 0.088$) and brightest U/LIRGs. The GOALS sample consists of 180 LIRGs and 22 ULIRGs with a median redshift of $\langle z \rangle = 0.0212$ [19]. The closest source in the sample is located at $z_{\rm min} = 0.0030$, and the most distant one at $z_{\rm max} = 0.0876$.

GOALS objects were originally selected from the IRAS Revised Bright Galaxy Sample (RBGS [235]) as sources with a luminosity of $L_{\rm IR,IRAS} \geq 10^{11} L_\odot$. The RBGS is a complete flux-limited sample of 629 galaxies that have an IRAS 60-μm flux density $f_{60\mu{\rm m,IRAS}} > 5.24\,{\rm Jy}$ and Galactic latitude $|b| > 5^\circ$ [235].

[10] Available at: goals.ipac.caltech.edu/.

The GOALS sample encompasses all types of nuclear activity, including Seyfert type-1 and type-2 AGN (see Section 1.1.4), low-ionization nuclear emission-line regions (LINERs), and nuclear starburst regions. Additionally, the sources span the entire evolutionary merger sequence, ranging from early interacting systems to advanced mergers. In addition, GOALS includes secularly evolving LIRGS, of which NGC 1068 is an example.

To characterize the wide variety of local U/LIRGs, GOALS combines data from space-based observatories such as the Spitzer Space Telescope [175, 184, 208, 210, 236, 237] and the Herschel Space Observatory [177, 238–244] at mid-IR and far-IR wavelengths, the Hubble Space Telescope for near-IR and optical observations [245, 246], the Galaxy Evolution Explorer (GALEX) UV telescope [195, 247], and the Chandra X-ray Observatory for X-ray studies [248, 249]. Recently, the James Webb Space Telescope (JWST) observed GOALS LIRGs with unprecedented resolution [250–259]. Four nearby LIRGs were selected for the *Director's Discretionary Early Release Science Programs*.[11]

In addition to space-based facilities, GOALS galaxies are observed with ground-based observatories, including radio and submillimeter telescopes like the Very Large Array (VLA) [260] and the Atacama Large Millimeter/submillimeter Array (ALMA) [261], as well as large optical-IR observatories such as the Keck Telescopes [262–264].

The multi-wavelength data from both ground-based and spaceborne facilities are integrated into comprehensive imaging and spectroscopic surveys. A primary motivation for targeting the GOALS galaxies in this work is the extensive electromagnetic data available, combined with a deep understanding of the associated sources. In the following sections we define the source selections used in this work.

2.3.2 All-sky GOALS selection for source modeling

GOALS is fundamentally based on observations by IRAS, which had a relatively low angular resolution of $\sim 0.5'$ at $12\ \mu\mathrm{m}$ and $\sim 2'$ at $100\ \mu\mathrm{m}$ [265]. Consequently, the IRAS emission of a single GOALS object may represent the cumulative emission from individual galaxies within an interacting system. However, the framework presented in Chapter 3 models neutrino production in the cores of U/LIRGs based on the electromagnetic emission from these regions. Consequently, the IR luminosity of each galaxy in an interacting system is of primary interest, rather than the total IRAS IR luminosity of the system.

We begin by describing how the IR luminosities of individual galaxies in interacting systems were determined by GOALS (see [234] for further details). Next, we identify the corresponding galaxies and introduce source-specific observables that will be used in Chapter 3 to estimate high-energy neutrino fluxes from the targeted GOALS galaxies.

Disentangling interacting systems

The Spitzer Space Telescope, one of IRAS' successors with a higher angular resolution, allowed to spatially disentangle galaxies within the same U/LIRG system. This yields more than 290 *individual* galaxies for the GOALS sample. A fraction of these galaxies

[11] This program was introduced to familiarize the scientific community with the telescope's capabilities and instruments at an early stage.

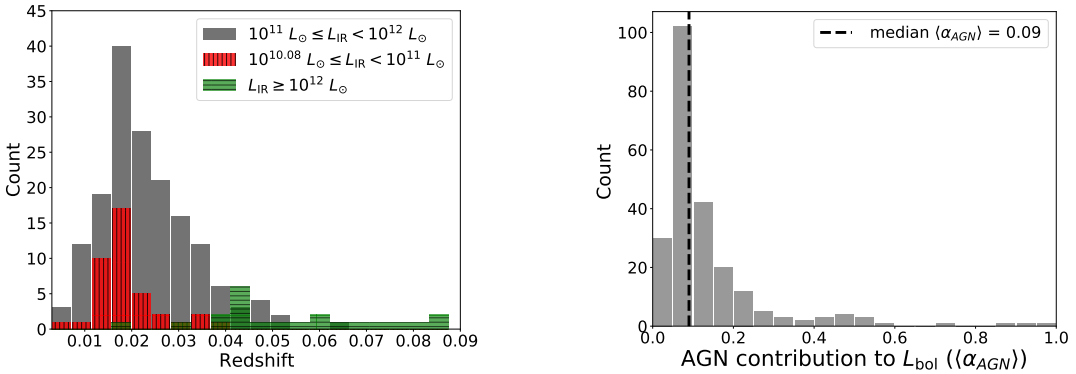

FIGURE 2.8: Left panel: Redshift distributions of 229 disentangled GOALS galaxies, consisting of 40 galaxies with $10^{10.08} L_\odot \leq L_{\rm IR} < 10^{11} L_\odot$, 167 galaxies with $10^{11} L_\odot \leq L_{\rm IR} < 10^{12} L_\odot$, and 22 galaxies with $L_{\rm IR} \geq 10^{12} L_\odot$. Right panel: Distribution of the average AGN contribution to the bolometric luminosity, $\langle\alpha_{\rm AGN}\rangle$, for the 229 disentangled GOALS galaxies. Data from [234].

were targeted by the *Photodetecting Array Camera and Spectrometer* (PACS) onboard the Herschel Space Observatory.

For U/LIRGs composed of two or more galaxies, the Herschel Space Observatory targeted the fainter companion galaxies only if their contribution to the total 24-μm flux density in the *Multiband Imaging Photometer for Spitzer* (MIPS) exceeded a ratio of 1:5 relative to the brightest galaxy in the system. For those constituent galaxies observed with Herschel, the individual infrared luminosity ($L_{\rm IR,\,individual}$) was estimated by scaling the total IRAS infrared luminosity of the system ($L_{\rm IR,\,IRAS}$).

The scaling factor is defined as the ratio of the individual galaxy's continuum flux density measured at 63 μm in the PACS spectrum ($f_{63\,\mu{\rm m},\,\rm PACS}$) to the system's total 60-μm flux density from IRAS ($f_{60\,\mu{\rm m},\,\rm IRAS}$). The individual infrared luminosity for a given component is then computed as

$$L_{\rm IR,individual} = \frac{f_{63\mu{\rm m,PACS}}}{f_{60\mu{\rm m,IRAS}}} \cdot L_{\rm IR,IRAS}\ . \tag{2.4}$$

This yields individual IR luminosities for the 229 GOALS galaxies, comprising 40 galaxies with $10^{10.08} L_\odot \leq L_{\rm IR} < 10^{11} L_\odot$, 167 galaxies with $10^{11} L_\odot \leq L_{\rm IR} < 10^{12} L_\odot$, and 22 galaxies with $L_{\rm IR} \geq 10^{12} L_\odot$ [234]. These luminosities are utilized in Sections 3.2 and 3.3 to investigate starburst-driven neutrino production in the respective sources. The redshift distributions for these galaxy groups are shown in Figure 2.8. Notably, LIRGs span the entire redshift range, while the nearest ULIRG, Arp 220, is much more distant at $z \sim 0.018$. This makes LIRGs especially interesting as point sources of high-energy neutrinos.

A comprehensive table, compiled as part of this study, presents the redshift and IR luminosity for all 229 galaxies, along with additional source data to be introduced in Chapter 3. This table is available in Appendix D.

AGN-contaminated IR luminosity

As previously discussed in Section 2.1.2, a fraction of the IR luminosity observed in U/LIRGs may originate from AGN activity. An analysis of the GOALS sample has estimated the average AGN contribution to the total bolometric luminosity, $\langle\alpha_{\rm AGN}\rangle \in [0, 1]$, for each galaxy introduced in Section 2.3.2 [234].

Using low-resolution spectral measurements from the *InfraRed Spectrograph* (IRS) onboard the Spitzer Space Telescope, the $\langle\alpha_{\rm AGN}\rangle$ values were derived from multiple independent diagnostics, including the [Ne V]/[Ne II] and [O IV]/[Ne II] line ratios, the mid-IR continuum slope, and the equivalent width of polycyclic aromatic hydrocarbon (PAH) emission bands [234].

Since the total IR luminosity of U/LIRGs is a good approximation of the total bolometric luminosity ($L_{\rm bol}$) [266], the IR luminosity can be corrected for AGN contributions by multiplying it by the factor $1-\langle\alpha_{\rm AGN}\rangle$. This correction is applied in Sections 3.2 and 3.3 to remove the AGN contribution, ensuring an accurate estimate of the starburst-driven neutrino flux expected from GOALS galaxies. The $\langle\alpha_{\rm AGN}\rangle$-values are provided for each of the targeted sources in the table in Appendix D

A word of caution The physical area of a galaxy probed by IRS observations depends on the angular scale covered by the short-low slit, $\sim 4" \times 4"$ [184]. Because of this limitation, the estimated $\langle\alpha_{\rm AGN}\rangle$-values are representative of an entire galaxy only for sources at luminosity distances $D_L \gtrsim 50-100$ Mpc. Therefore, as noted by GOALS in [234], the galaxy-wide $\langle\alpha_{\rm AGN}\rangle$-values are to be interpreted as upper limits for more nearby sources. The most prominent example of this is NGC 1068 with a reported value $\langle\alpha_{\rm AGN}\rangle = 1$. This galaxy is the closest Seyfert II galaxy to Earth, located at $D_L \sim 16$ Mpc. Only two other sources within 50 Mpc have $\langle\alpha_{\rm AGN}\rangle > 0.3$, i.e. the LIRGs NGC 1365 and NGC 4418. As the $\langle\alpha_{\rm AGN}\rangle$-value of these sources are only tracing the inner central part of the galaxy, it follows that, when considering the full system, these sources potentially have a smaller $\langle\alpha_{\rm AGN}\rangle$.

The distribution of $\langle\alpha_{\rm AGN}\rangle$-values in the GOALS sample is shown in the right panel of Figure 2.8. This distribution shows that in the majority of GOALS galaxies the AGN has a secondary contribution to the total bolometric luminosity. However, some of the sources show large $\langle\alpha_{\rm AGN}\rangle$-values, i.e. 14% have $\langle\alpha_{\rm AGN}\rangle > 0.2$ and 3% have $\langle\alpha_{\rm AGN}\rangle > 0.5$ (AGN dominates over star formation). This implies, with a good consistency among different estimators, that only for 3% of the GOALS U/LIRGs an AGN is the dominant power source. This observation serves as one of the motivations to focus, in the initial approach, solely on the starburst-driven high-energy neutrino flux in U/LIGRs, as discussed in Chapter 3.

2.3.3 Northern-Sky GOALS selection for an IceCube search

Any search for astrophysical neutrinos with IceCube is complicated by the large atmospheric background produced by cosmic-ray interactions in the atmosphere. Among these, atmospheric muons and muon neutrinos are the most abundant particles reaching the detector, with muons dominating the trigger (a more detailed discussion will be given in Section 4.2). Due to IceCube's location at the Geographic South Pole, most of this atmospheric background originates from the Southern Hemisphere, directly overhead. These events are commonly referred to as down-going muons, illustrated in Figure 2.9.

Focusing on the Northern Hemisphere, and thus on up-going events, significantly reduces the atmospheric background, as the ice overburden and the Earth's core act as natural shields for atmospheric muons [170]. This, in turn, improves the sensitivity of analyses searching for astrophysical neutrino sources. For this reason, in Chapters 5 and 6, we restrict our search for high-energy neutrinos from GOALS U/LIRGs to the Northern Hemisphere.

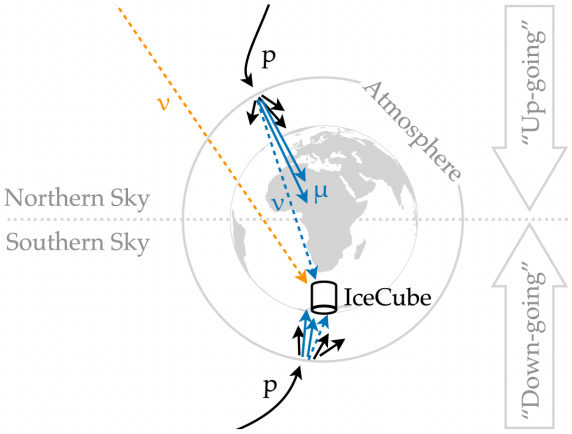

FIGURE 2.9: Illustration of the atmospheric background reaching IceCube from both the Northern and Southern Sky, adapted from [267]. This background originates from cosmic rays (depicted here as protons) interacting with atmospheric nuclei. The resulting particles include muon neutrinos (dashed blue arrow) and muons (solid blue arrows), which produce track-like events in the IceCube detector. However, atmospheric muons, which dominate IceCube's trigger, can only reach the detector from the Southern Sky. Events from the Northern Sky are termed up-going, while those from the Southern Sky are down-going. Restricting the view to the Northern Sky enhances sensitivity to astrophysical neutrinos (dotted orange arrow).

Furthermore, since the spatial extent of GOALS U/LIRGs in electromagnetic wavelengths is well below the angular resolution of high-energy track events in IceCube ($\lesssim 1^\circ$ [117]), we do not consider individual galaxies within the northern U/LIRG systems, as was done for the all-sky GOALS selection in Section 2.3.1. Instead, each U/LIRG system comprising interacting or merging galaxies is treated as a single entity in the IceCube search.

In Chapters 5 and 6, we perform several types of time-integrated point source searches targeting northern GOALS U/LIRGs. The general methodology underlying these searches was introduced in Section 1.6.1. Below, we outline the specific subsets of GOALS U/LIRGs selected for each search type.

Catalog search & binomial test

In Chapters 5 and 6 we perform a cross correlation between up-going muon tracks and a *catalog* of GOALS sources in the Northern Hemisphere using a maximum likelihood analysis. This will allow to naturally extend the multi-wavelength information available for GOALS galaxies, thereby establishing a clear link between classical astronomy (GOALS) and neutrino astronomy (IceCube).

For reasons related to analysis performance, discussed in more detail in Chapter 5, we restrict the sky to a declination of $\delta > -3^\circ$. Doing so, we identify 115 GOALS U/LIRGs in this part of the sky. However, two objects are excluded:

- ***NGC 1068***: As discussed in Section 1.6.1, previous analyses have claimed evidence for high-energy neutrino emission from the direction of NGC 1068. To avoid biasing the analysis and improve our chances of finding new sources, NGC

1068 is initially excluded. However, a-posteriori checks will be performed including this galaxy.

- *IRAS 05223+1908*: This system is possibly a young stellar object [244] and thus excluded.

Excluding these galaxies results in a final sample of 113 GOALS U/LIRGs, comprising 101 LIRGs and 12 ULIRGs. The catalog search investigates the high-energy neutrino emission from each of these 113 sources. For this search, only the sky positions of the sources, as reported in [244], are utilized. This source selection, and the result of the anlysis presented in Chapters 5 and 6 can be found in Table F.1.

As outlined in Section 2.1, U/LIRGs exhibit a wide range of physical conditions that may influence high-energy neutrino production. Given this diversity, a population-level analysis of the 113-source sample is performed using a binomial test. If statistically significant, this analysis could help identify promising subsets of infrared-bright galaxies as potential high-energy neutrino sources.

Stacking search

Instead of searching for high-energy neutrino emission from individual sources, one can probe the cumulative signal from multiple sources—a method known as a stacking search—which enhances sensitivity to sources that are individually too faint to be detected. Stacking all northern GOALS LIRGs is technically feasible and, given the number of sources, potentially advantageous. However, the wide range of nuclear activity and morphological diversity among LIRGs—and the resulting variety of potential neutrino production mechanisms—complicates the interpretation of, and extrapolation from, a likely null result to the broader LIRG population.

Moreover, combining such a stacking search with the already intensive catalog analysis of 113 sources (as discussed in Chapter 5) would significantly increase the computational load. For these reasons, we instead focus on a specific, relatively small subset of GOALS U/LIRGs characterized by vibrationally excited hydrogen cyanide (HCN-vib) emission.

As discussed in Section 2.1.2, strong HCN-vib emission traces warm ($\gtrsim 100\,\mathrm{K}$), heavily obscured environments with hydrogen column densities of $\log_{10}(N_\mathrm{H}/\mathrm{cm}^{-2}) = 24{-}25$, typically associated with deeply embedded AGN and/or compact starburst activity. In the literature, these intriguing systems are often referred to as compact obscured nuclei (CONs) when the HCN-vib luminosity exceeds a specific threshold. However, given the recent identification of these objects, their precise classification remains somewhat fluid. In this work, we adopt a broader criterion and include all U/LIRGs with confirmed HCN-vib detections in our stacking analysis. The presence of HCN-vib emission indicates both substantial obscuration and a powerful central energy source—conditions favorable for high-energy neutrino emission, yet likely to suppress gamma-ray signals. As argued in Section 1.5.2, such hidden sources are well motivated by both individual detections and diffuse flux observations.

Applying the same declination cut of $\delta > -3^\circ$ as for the catalog search, we identify 10 GOALS galaxies exhibiting HCN-vib emission, comprising 4 LIRGs and 6 ULIRGs. These 10 U/LIRGs form the target set for the stacking search presented in Chapters 5 and 6.

Notably, while NGC 1068 shows confirmed HCN-vib emission on small (~ 2 pc [268]) scales, its integrated flux is significantly lower than that of the selected sample [219]. Furthermore, since there is already evidence linking NGC 1068 to high-energy neutrino emission, its inclusion would bias the stacking analysis. For these reasons,

NGC 1068 is excluded from our target list.

The underlying mathematical framework of the stacking analysis allows us to assign weights to individual galaxies, representing their relative contributions to the total expected neutrino signal. As elaborated on in Chapter 5, the weights in this analysis depend only on the luminosity distance to each source. Accordingly, the key parameters for the stacking search are the sources' luminosity distances and sky coordinates in right ascension and declination. Table F.2 in the appendix provides the right ascension, declination, and luminosity distances for the 10 selected HCN-vib bright sources, which are used to compute the stacking weights.

Basic source properties

Figure 2.10 shows the IR luminosity ($L_{\rm IR}$) and corresponding IR flux ($F_{\rm IR} = L_{\rm IR}/4\pi D_L^2$) as functions of luminosity distance (D_L) for all sources included in the catalog and stacking analyses. U/LIRGs with HCN-vib emission—used in the stacking analysis—are indicated with hollow symbols, and the four brightest U/LIRGs are labeled. NGC 1068, though excluded from the main analysis, is shown for comparison.

Although the IR information is not directly used in the technical analysis—aside from defining the source catalog—it provides valuable context for identifying particularly bright or faint IR sources, as well as assessing their proximity. This, in turn, offers additional insight into the results of the IceCube analysis presented in Chapter 6. For example, Arp 220 is of particular interest due to its relative proximity and high IR luminosity compared to other ULIRGs. Additionally, NGC 2146 and NGC 1068 are especially nearby LIRGs, resulting in strong IR fluxes. While the former exhibits strong starburst activity at a relatively unfavorable declination of $\delta = 78.36°$ for IceCube, the latter hosts a prominent active galactic nucleus at a favorable declination of $\delta = -0.01°$, where IceCube's sensitivity is highest.

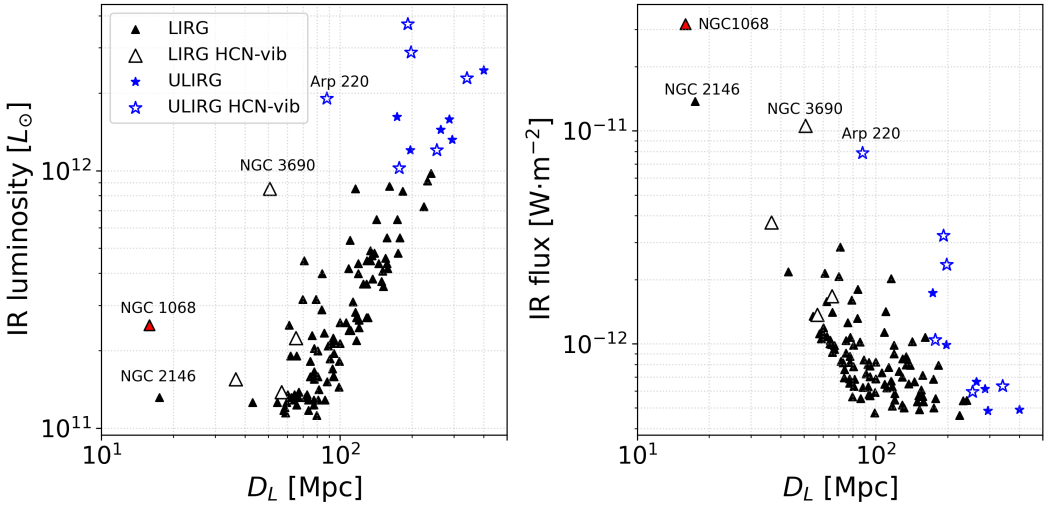

FIGURE 2.10: Infrared (IR) luminosity (left) and IR flux (right) for each source in the stacking and catalog search as a function of their luminosity distance (D_L). The four brightest sources in terms of flux are highlighted and the U/LIRGs with HCN-vib emission are indicated by a hollow marker. Although not initially included in the analysis, NGC 1068 is shown for comparison.

CHAPTER 3

Framework for High-Energy Neutrino Emission from GOALS Galaxies

Obscured star formation and active galactic nuclei (AGN) in U/LIRGs provide favorable conditions for high-energy neutrino production (Section 2.2). Motivated by the fact that the vast majority of U/LIRGs are powered by starburst activity rather than AGN activity, as discussed in Sections 2.1.2 and 2.3.2, we opt to develop a framework that focuses solely on starburst-driven high-energy neutrino production in the dense central regions of starburst galaxies. Regarding our model we note:

- Specifically the model focuses on steady high-energy neutrino production via supernova activity. This does not exclude other starburst activity, e.g. pulsars [65], and AGN-related processes as promising regions for high-energy neutrino production. In fact, the recent detection of high-energy neutrinos from the direction of the LIRG NGC 1068 points toward the AGN being the dominant source of neutrinos in that galaxy [16, 144]. Additionally, we note that tidal disruption events (TDEs) have gained interest as candidate sources of high-energy neutrinos in the recent year [269]. U/LIRGs could have an increased rate of TDEs due to the amplified star-formation rate in their nuclear regions (see Section 2.1.2).

- In terms of neutrino-production channels, the starburst-driven model developed in this chapter only considers hadronuclear interactions and does not take into account photohadronic interactions. For U/LIRGs, the target radiation field in the starburst region is likely dominated by IR emission. Assuming the production of Δ^+-resonance (see Section 1.2.1), the threshold energy for a cosmic ray (CR) to interact with a near-IR background photon (~ 1 eV) is of the order of $100\ \mathrm{PeV}$. The threshold energy for the CR is even larger for a target field dominated by far-IR radiation. Such extreme CR energies are unlikely to be produced efficiently by the starburst activity considered in this work.

- Our framework builds on the model of CR transport in the central regions of starburst galaxies presented in [270] and previous investigations of starburst regions as high-energy neutrino sources (e.g. [271–275]). We contribute to these models by contextualizing them within the local GOALS U/LIRGs, presenting the first per-source and diffuse neutrino flux predictions for the GOALS sample, based on source-specific electromagnetic data provided by the GOALS survey.

Overview & Context In Section 3.1, we first outline the underlying mathematical framework of the model before applying it to a detailed case study of the LIRG NGC 3690 (Arp 299, Mrk 171) in Section 3.2. Subsequently, in Section 3.3, we present per-source flux predictions for all U/LIRGs in the GOALS sample and use these predictions to estimate the diffuse starburst-driven neutrino flux from the sample. In Section 3.4, we extend these results to estimate the diffuse flux from the broader U/LIRG population, and we conclude our analysis in Section 3.5. Finally, in Section 3.6, we discuss

the future application of this framework in cosmological hydrodynamical simulations to refine predictions of the diffuse high-energy neutrino flux from starburst activity throughout cosmic history in the TeV-PeV energy range.

3.1 Theoretical Framework

A (circum)nuclear starburst region has an associated core-collapse supernova rate ($\mathcal{R}_{\mathrm{SN}}$, typically in units [$\mathrm{yr}^{-1}$]). This rate drives the high-energy proton injection rate (Q_{p} [$(\mathrm{GeV/c})^{-3}$ cm^{-3} s^{-1}]) into the starburst volume (V_{SBR} [pc^3]). After injection, these CRs remain in the central volume for an average time of (τ [s]). The interaction between the proton injection rate and the dwell time determines the distribution of high-energy proton momenta ($\mathcal{F}_{\mathrm{p}}$ [$(\mathrm{GeV/c})^{-3}$ cm^{-3}]). The latter provides information on the available energy budget for charged pion production, which is needed to calculate the neutrino production rate ($q_{\nu+\bar{\nu}}$ [GeV^{-1} cm^{-3} s^{-1}]). Finally, the expected neutrino flux ($\Phi_{\nu+\bar{\nu}}$ [GeV^{-1} cm^{-2} s^{-1}]) is obtained by integrating the neutrino production rate over the starburst volume and taking into account the luminosity distance to the source (D_L [Mpc]). In the following sections, we construct a phenomenological framework based on all these parameters. The parameters are subsequently estimated where possible, from GOALS data.

3.1.1 Supernova rate

The optical emission from a supernova explosion can outshine an entire galaxy. However, due to the large amount of obscuring matter in the central region of GOALS galaxies, most of the optical emission is obscured. Therefore, optical counts over time cannot be used to calculate reliable supernova rates in (all) GOALS galaxies. The obscuring matter will, however, convert a fraction of the ultraviolet (UV) photons into thermal emission (IR), and the same supernova activity can also accelerate the surrounding electrons, resulting in radio emission. Both radio and IR wavelengths are (almost) unobscured and are therefore viable tracers of supernova activity in obscured regions. There have been supernova counting experiments in U/LIRGs using near-IR emission (e.g. [276]) and radio emission (e.g. [200]). Unfortunately, it is not feasible to do this for the entire GOALS sample of more than 200 individual galaxies. We therefore opt for two scaling relations to estimate the supernova rate in each galaxy:

1. A scaling relation between the **total IR luminosity of the galaxy and the star-formation rate**: The bolometric luminosity of young stellar populations is dominated by massive, short-lived, UV-bright stars. These UV photons will be reprocessed in dust-enshrouded regions, resulting in IR emission. As such, IR and UV emission are viable tracers for obscured and unobscured star formation, respectively. A study of 135 GOALS U/LIRGs shows, however, that the far-UV measured by GALEX contributes on average $\sim 4\ \%$ to the total star-formation rate of these galaxies [195].[1] We therefore choose to only use the IR luminosity to estimate the supernova rate.

2. A scaling relation between the **star-formation rate and the supernova rate**.

By combining the calibration factors from these two scaling relations, we can estimate the total supernova rate from the total IR luminosity of the galaxy. We rely

[1] Radio emission is also an interesting tracer for star formation (e.g. [194]). However, such data are not available for all GOALS U/LIRGs.

on simulations to compute the calibration factors that define the scaling relations and compare them to observations. Additionally, we account for the possibility that some of the total IR luminosity may be produced by AGN activity or originate from regions outside the central ~ 100 pc of interest. This approach allows us to estimate the AGN-corrected nuclear supernova rate based on the total IR luminosity of the galaxy, which is the main result of this section.

Calibration to IR luminosity

As discussed in Section 2.1.2, given an initial mass function (IMF), star-formation history (SFH), and a stellar-evolution model, it is possible to compute from simulations the calibration factor that relates the electromagnetic tracer of interest to the star-formation rate and the supernova rate. In this work, we make use of the web-based software `Starburst99` (SB99)[2] to compute the calibration factors [277–280].

1. **IR luminosity to star-formation rate**: Following the procedure outlined in [194] (hereafter Murphy2011), we assume that the entire Balmer continuum, i.e., stellar UV emission between 912 Å $< \lambda < 3646$ Å, is absorbed by dust and re-radiated as optically-thin IR emission.

   This implies that the IR luminosity due to reprocessed stellar emission, $L_{\mathrm{IR,SED}}$, is obtained by integrating the Balmer range of the SB99-simulated SED of the stellar population. As such, the calibration factor A_{IR} is defined as

   $$\left(\frac{\mathrm{SFR}_{\mathrm{SB99}}}{M_\odot\ \mathrm{yr}^{-1}}\right) = A_{\mathrm{IR}} \cdot \left(\frac{L_{\mathrm{IR,SED}}}{\mathrm{erg\ s}^{-1}}\right), \tag{3.1}$$

   with $\mathrm{SFR}_{\mathrm{SB99}}$ the star-formation rate used as input to run the SB99 simulation.

   The left panel of Figure 3.1 shows an example of the spectral energy distribution of a stellar population after 100 Myr assuming a continuous star-formation rate of $1\ M_\odot \mathrm{yr}^{-1}$ and otherwise default SB99 parameters. The Balmer range is also shown in Figure 3.1.

   In Murphy2011, the value of the calibration factor was found to be $A_{\mathrm{IR}} = 3.88 \times 10^{-44}$, assuming a Kroupa IMF, solar metallicity, and a constant SFH. In a follow-up study [196] (hereafter Murphy2012), an empirical approach resulted in a linear relation between the star-formation rate and L_{IR}, with $A_{\mathrm{IR}} = 3.15 \times 10^{-44}$. This empirical relation is quoted to be reliable within a factor of two.

   The calibration factor obtained in Murphy2011 using SB99 is therefore consistent with the empirical calibration factor from Murphy2012. In this work, we compute A_{IR} for various types of IMFs that are relevent for U/LIRGs using SB99, including the IMF used in Murphy2011 for comparison.

2. **Star-formation rate to supernova rate:** Using SB99, we also compute the total supernova rate ($\mathcal{R}_{\mathrm{SN,SB99}}$) as a function of time for the same stellar population used to calibrate the IR luminosity to the star-formation rate. This enables the calculation of a calibration factor between the supernova rate and the star-formation rate as

[2] Available at: `stsci.edu/science/starburst99/docs/default.htm`. This software allows the modeling of spectrophotometric properties of star-forming galaxies, such as the time-dependent spectral energy distribution (SED) of a stellar population.

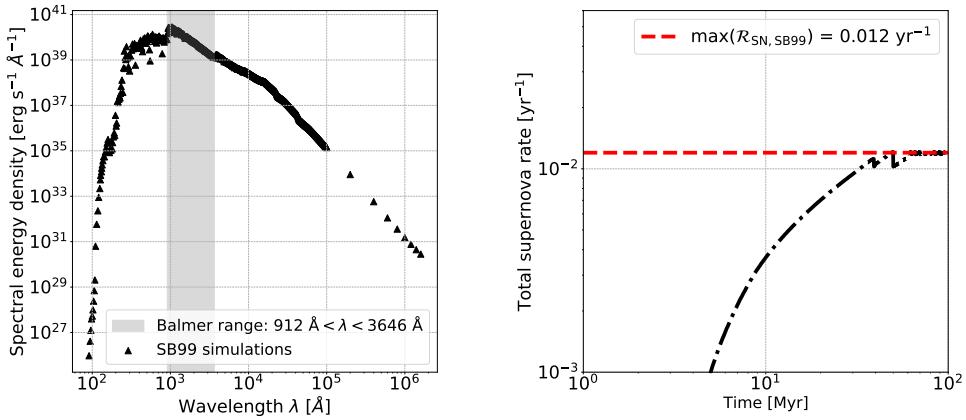

FIGURE 3.1: Left: Spectral energy density as a function of wavelength λ for a stellar population at 100 Myr after the onset of star formation. The distribution is obtained using default SB99 parameters and a continuous star-formation rate of 1 $M_\odot \mathrm{yr}^{-1}$. The gray shaded band indicates the Balmer continuum, i.e. stellar UV emission between 912 Å $< \lambda <$ 3646 Å. Right: The total supernova rate as a function of time for the same stellar population as used in the left plot. The red-dashed line indicates the maximum supernova rate reached.

$$\left(\frac{\mathcal{R}_{\mathrm{SN,SB99}}}{\mathrm{yr}^{-1}}\right) = A_{\mathrm{SFR}} \cdot \left(\frac{\mathrm{SFR}_{\mathrm{SB99}}}{M_\odot\ \mathrm{yr}^{-1}}\right), \tag{3.2}$$

where $\mathcal{R}_{\mathrm{SN,SB99}}$ is provided by SB99. In Figure 3.1 (right panel), we show the supernova rate as a function of time using SB99, assuming the same parameters as those in the left panel of Figure 3.1.

Both A_{IR} and A_{SFR} are computed in a regime where the spectral energy distribution (SED) and supernova rate reach equilibrium. Combining these calibration factors, we define $\Lambda_{\mathrm{IR}} = A_{\mathrm{SFR}} \cdot A_{\mathrm{IR}}$, allowing the total supernova rate in a galaxy to be estimated as

$$\left(\frac{\mathcal{R}_{\mathrm{SN}}}{\mathrm{yr}^{-1}}\right) = \Lambda_{\mathrm{IR}} \cdot \left(\frac{L_{\mathrm{IR}}}{\mathrm{erg\ s}^{-1}}\right), \tag{3.3}$$

where L_{IR} is the total IR luminosity of the galaxy.

Calculating calibration factors

To get a numerical value for the calibration factors, A_{IR} and A_{SFR}, the SB99 input parameters must be fixed. We consider a constant SFH and solar metallicity. As the parametrization of the IMF and its universality remains uncertain, it is not straightforward to select an appropriate IMF. We therefore investigate the effect of two different classes of IMFs:

1. The first class consists of the **Salpeter IMF** (1953) [281], which has a single power-law exponent $\beta = 2.35$, and a **Kroupa IMF** (2001) [282], with $\beta_{\mathrm{low}} = 1.3$ for $0.1 < m/M_\odot < 0.5$ and $\beta_{\mathrm{high}} = 2.3$ for $0.5 < m/M_\odot < 100$. These so-called canonical IMFs are based on resolved stellar populations in the Milky Way and nearby galaxies.

2. The second class consists of two **top-heavy IMFs**, which predict a relatively larger fraction of high-mass stars compared to canonical IMFs. The interest in a

top-heavy IMF for starburst regions is supported by both theoretical considerations and observational evidence.

Theoretically, the increased temperature in star-forming clouds within starburst regions, driven by the enhanced CR density, leads to a larger Jeans mass in these clouds. This suppresses the formation of low-mass stars and results in a shift of the IMF shape toward a top-heavy distribution [283].

Observationally, high-resolution ALMA observations of nearby U/LIRGs reveal unusually low $^{13}\mathrm{C}/^{18}\mathrm{O}$ isotope abundance ratios [284–286]. Massive stars ($\gtrsim 8\ M_\odot$) are the primary producers of $^{18}\mathrm{O}$ in the interstellar medium, whereas $^{13}\mathrm{C}$ is synthesized in the envelopes of long-lived, low-mass stars ($\lesssim 8\ M_\odot$). Consequently, the observed low abundance ratios suggest a relative increase in the number of short-lived, high-mass stars, supporting the notion of a top-heavy IMF.

Since SB99 simulations show that the supernova rate stabilizes (see Figure 3.1) after approximately 60 Myr after the onset of star formation, assuming a constant SFH, we decided to compute all calibrations beyond this timestamp. Table 3.1 shows an overview of the computed calibration factors at 100 Myr assuming a Salpeter, Kroupa, and two top-heavy IMFs. The top-heavy IMFs have the same low-mass exponent $\beta_{\mathrm{low}} = 1.3$ as the canonical Kroupa IMF discussed earlier, but the high-mass exponent is taken to be $\beta_{\mathrm{high}} = 1.0$ and $\beta_{\mathrm{high}} = 1.5$. An exponent such as the latter has been suggested to explain the reionization of the intergalactic medium at $z \lesssim 11$ [287]. The value $\beta_{\mathrm{high}} = 1.0$ is chosen as an arbitrary extreme case. From the results in Table 3.1 we conclude that:

- The calibration factor A_{IR} obtained from the Kroupa IMF is 1.27 times larger than the value obtained in Murphy2011 using the same IMF. This increase remains consistent with the empirical calibration between star-formation rate and total IR luminosity presented in Murphy2012.

- Comparing the A_{IR} values obtained across all studied IMFs, we find that A_{IR} is significantly lower for top-heavy IMFs compared to canonical IMFs. For a given IR luminosity, this results in a lower star-formation rate for top-heavy IMFs relative to canonical IMFs. However, the difference is less pronounced for the Λ_{IR} calibration factor. Specifically, for $L_{\mathrm{IR}} = 10^{11} L_\odot$, the supernova rate derived using a top-heavy IMF with $\beta_{\mathrm{high}} = 1.5$ is 1.31 times lower than that derived from the canonical Kroupa IMF, and for $\beta_{\mathrm{high}} = 1.0$, it is 1.75 times lower.

Although the overall predicted supernova rate is lower for top-heavy IMFs compared to canonical IMFs, the average progenitor mass per supernova event must be larger. Consequently, this implies a higher average explosion energy per supernova event, E_{SN} (see e.g., [198]). This increase impacts the supernova luminosity, $\mathcal{L}_{\mathrm{SN}} = E_{\mathrm{SN}} \cdot \mathcal{R}_{\mathrm{SN}}$, which is crucial for estimating the high-energy particle budget available for neutrino production. The following section discusses how this effect is incorporated into the calculations in this work.

Progenitor mass and supernova luminosity

To account for the increase in average progenitor mass when considering top-heavy IMFs, we use the canonical Kroupa IMF as a benchmark (bm) and fix the average energy per supernova event to $E_{\mathrm{SN,bm}} = 10^{51}\ \mathrm{erg}$. In this work, we assume that the explosion energy scales linearly with the average progenitor mass. Under this

TABLE 3.1: Calibration factors for different IMFs at an age of 100 Myr, assuming solar metallicity and a constant star formation history (SFH). The supernova rate, $\mathcal{R}_{\rm SN}$, is calculated for a fixed infrared luminosity of $L_{\rm IR} = 10^{11}\,L_\odot$ using Eq. (3.3). For each IMF, the scaling factor $\mathcal{M}$ is also provided, accounting for the average progenitor mass per supernova event relative to that of the Kroupa IMF.

	$A_{\rm IR} \times 10^{44}$	$A_{\rm SFR}$	$\Lambda_{\rm IR} \times 10^{46}$	$\mathcal{R}_{\rm SN}$ [yr^{-1}]	$\mathcal{M}$
Salpeter	7.48	0.008	6.03	0.23	0.93
Kroupa	4.93	0.012	5.97	0.23	1.00
TH $\beta_{\rm high} = 1.5$	1.54	0.027	4.22	0.16	1.50
TH $\beta_{\rm high} = 1.0$	1.24	0.026	3.22	0.12	2.01

assumption, the average energy per supernova event for a different IMF is determined using the scaling relation

$$E_{\rm SN} = \frac{\langle M_{\rm SN,IMF}\rangle}{\langle M_{\rm SN,bm}\rangle} \cdot E_{\rm SN,bm} = \mathcal{M} \cdot E_{\rm SN,bm}\ , \tag{3.4}$$

where $\mathcal{M}$ is the ratio of the typical progenitor mass per supernova event for the chosen IMF, $\langle M_{\rm SN,IMF}\rangle$, to the typical progenitor mass per supernova event for the benchmark case, $\langle M_{\rm SN,bm}\rangle$.

Based on our SB99 simulations, we find $\mathcal{M} = 1.37$ for a top-heavy IMF with $\beta_{\rm high} = 1.5$ and $\mathcal{M} = 2.01$ for a top-heavy IMF with $\beta_{\rm high} = 1.0$. Taking this factor into account, we calculate the supernova luminosity, $\mathcal{L}_{\rm SN}$, and find that for the top-heavy IMF with $\beta_{\rm high} = 1.5$, the supernova luminosity differs by approximately 5% compared to the benchmark case. For the top-heavy IMF with $\beta_{\rm high} = 1.0$, the correction results in a supernova luminosity that is approximately 15% larger than that obtained for the canonical Kroupa IMF.

AGN contamination and extended IR emission

The SB99 simulations do not include AGN activity. However, strong AGN activity in U/LIRGs can heat the matter in the (circum)nuclear region surrounding the supermassive black hole. This heating can contribute significantly to the observed IR luminosity of the host galaxy. Consequently, using the total IR luminosity as a tracer of the star-formation rate in the presence of a strong AGN can overestimate the true supernova rate.

To correct the IR luminosity for this additional contribution, we use the relative AGN contribution to the bolometric luminosity, $\langle\alpha_{\rm AGN}\rangle$ (see Section 2.3.2). This correction is justified by the relationship between the bolometric and IR luminosities for U/LIRGs, where $L_{\rm bol} \sim L_{\rm IR}$ (e.g., [266]). Furthermore, in this work, we are particularly interested in the nuclear supernova rate within the central ~ 100 pc. Therefore, the AGN-corrected IR luminosity of the nuclear region, $L_{\rm IR,nuclear}$, is required instead of the total IR luminosity of the galaxy. To account for this, we introduce a factor $\mathcal{G} \in [0, 1]$, which represents the fraction of IR luminosity produced by nuclear starburst activity. The AGN-corrected IR luminosity of the nuclear region is then expressed as

$$L_{\rm IR,nuclear} = \mathcal{G} \cdot ([1 - \langle\alpha_{\rm AGN}\rangle] \cdot L_{\rm IR})\ .$$

IR observations of U/LIRGs show that systems with higher $L_{\rm IR}$ tend to have more centrally concentrated emission (e.g., [208, 210]). Thus, $\mathcal{G}$ is likely closer to unity for

systems with higher $L_{\rm IR}$. Targeted observations of four GOALS LIRGs further support this, showing that $\mathcal{G} \gtrsim 0.5$ for these galaxies [288].

We conclude that the nuclear AGN-corrected supernova rate per resolved galaxy in the GOALS sample can be calculated as

$$\left(\frac{\mathcal{R}_{\rm SN}}{\rm yr^{-1}}\right) = \Lambda_{\rm IR} \cdot \left(\frac{\mathcal{G} \cdot [1 - \langle\alpha_{\rm AGN}\rangle] \cdot L_{\rm IR}}{\rm erg\ s^{-1}}\right) . \tag{3.5}$$

Using Eq. (3.5), we can estimate the supernova rates in each of the 229 individual GOALS galaxies for which GOALS obtained a value for the IR luminosity ($L_{\rm IR}$) and an average AGN contribution to the bolometric luminosity, $\langle\alpha_{\rm AGN}\rangle$, as discussed in Section 2.3.1. Then, for a calibration factor $\Lambda_{\rm IR} = 5.97 \times 10^{-46}$ (Table 3.1) and $\mathcal{G} = 1$ in all galaxies, we find a median supernova rate of $\mathcal{R}_{\rm SN} = 0.43$ yr^{-1}, a minimum supernova rate of $\mathcal{R}_{\rm SN} = 0.02$ yr^{-1}, and a maximum supernova rate of $\mathcal{R}_{\rm SN} = 7.53$ yr^{-1}.

3.1.2 Proton injection rate

CR acceleration via diffusive shock acceleration is expected along the forward shock in core-collapse supernova remnants (Section 1.1.3). This mechanism gives rise to a power-law differential momentum distribution of accelerated particles. Therefore, a $p^{-\gamma_{\rm SN}}$ power-law relation between the proton injection rate ($Q_{\rm p}$) and the injected momentum p is adopted. In addition, an exponential cutoff is considered at the maximum momentum $p_{\rm max}$ achieved in the acceleration process.

The total injection rate of high-energy protons per unit volume due to all core-collapse supernova remnants in a (circum)nuclear starburst region is then expressed as

$$Q_{\rm p} = \frac{N_C}{V_{\rm SBR}} \left[\frac{p}{m_{\rm p}c}\right]^{-\gamma_{\rm SN}} e^{\frac{-p}{p_{\rm max}}} . \tag{3.6}$$

N_C is the normalization constant to be fixed by the supernova rate in the starburst region, $V_{\rm SBR}$ is the volume of the region under consideration, and $m_{\rm p}$ is the proton mass. In the following each of the parameters of Eq. (3.6) are discussed in more detail.

Supernova luminosity as normalization

The normalization constant N_C in Eq. (3.6) for the proton injection rate is determined by requiring that the total CR luminosity from core-collapse supernovae in the nuclear starburst region, $\mathcal{L}_{\rm CR}$, satisfies

$$\mathcal{L}_{\rm CR} = \int_{p_{\rm min}}^{p_{\rm max}} 4\pi p^2 \cdot N_C \cdot \left(\frac{p}{m_{\rm p}c}\right)^{-\gamma_{\rm SN}} \cdot e^{-p/p_{\rm max}} \cdot \mathcal{T}(p)\ {\rm d}p\ , \tag{3.7}$$

where $\mathcal{T}(p) = \sqrt{p^2c^2 + m_{\rm p}^2c^4} - m_{\rm p}c^2$ is the kinetic energy of a single CR proton. The minimum proton momentum is fixed at $p_{\rm min} = 0.1$ GeV$/c$.[3]

The total CR luminosity, $\mathcal{L}_{\rm CR}$, is given by

[3]The value of N_C is only weakly sensitive to the choice of $p_{\rm min}$ for $p_{\rm min} \lesssim 0.1$ GeV$/c$.

$$\mathcal{L}_{\rm CR} = \eta_{\rm SN} \cdot \mathcal{R}_{\rm SN} \cdot E_{\rm SN} = \eta_{\rm tot} \cdot L_{\rm IR} \ , \tag{3.8}$$

where the parameters are defined as follows:

- The total core-collapse supernova rate, $\mathcal{R}_{\rm SN}$, and the kinetic energy released per supernova, $E_{\rm SN}$, are estimated as described in Section 3.1.1.
- The conversion efficiency $\eta_{\rm SN}$ quantifies the fraction of supernova kinetic energy transferred to CRs. The observed CR spectrum up to ~ 3 PeV can be explained with $\eta_{\rm SN} \simeq 0.10{-}0.30$ for typical Galactic supernovae (see, e.g., [41, 42] for reviews). Kinetic simulations support this range, indicating that $\eta_{\rm SN} \simeq 0.10{-}0.20$ is plausible [43]. This suggests that values of $\eta_{\rm SN}$ within $0.10{-}0.30$ are physically motivated, provided the resulting predictions remain consistent with observational constraints.
- The factor $\eta_{\rm tot}$, introduced here for convenience, represents the fraction of the infrared luminosity, $L_{\rm IR}$, that is associated with CR production due to starburst activity.

Geometry of the starburst volume

Hydrodynamic simulations of mergers between gas-rich galaxies predict the formation of nuclear gas disks on scales of $\sim 10{-}100$ pc (e.g. [289]). Observational evidence for such gas disks in the nuclear regions of GOALS U/LIRGs is provided by a survey targeting 17 nearby U/LIRGs [262]. Within this gas-disk configuration, stars are formed, which eventually explode as supernovae and thereby inject CRs into the central interstellar medium. Based on these simulations and observations, we opt for a disk geometry to model the volume in which CRs propagate. This disk is parametrized by a radius $R_{\rm SBR}$ and a scale height $H_{\rm SBR}$. As a result, the volume of the starburst region is computed as $V_{\rm SBR} = 2H_{\rm SBR}\pi R_{\rm SBR}^2$, with $2H_{\rm SBR}$ the total thickness of the nuclear disk.

Spectral index

Diffusive shock acceleration in the presence of strong shock waves, such as those driven by supernova ejecta, predicts $Q_{\rm p} \propto p^{-(\gamma_{\rm SN}=4)}$. However, observations of Galactic supernova events typically require softer spectra to model their gamma-ray emission (e.g., [62, 290]).

In principle, the value of $\gamma_{\rm SN}$ for a GOALS galaxy can be inferred from the spectral index that describes the starburst-driven hadronic gamma-ray spectrum of that galaxy, Γ (see, e.g., [270, 275]). The parameter Γ can be obtained by fitting the observed gamma-ray flux Φ_γ of a galaxy with a functional form $\Phi_\gamma \propto E^{-\Gamma}$. The spectral indices are related by $\Gamma = \gamma_{\rm SN} - 2$, where $\gamma_{\rm SN}$ pertains to momentum space and Γ to energy space.

The hadronic gamma and neutrino flux originating from pp collisions in the same source are expected to share the same spectral shape. Therefore, the spectral index γ of the neutrino flux Φ_ν can be estimated using $\gamma = \gamma_{\rm SN} - 2$. Note that $\Phi_\nu \propto E^{-\gamma}$. However, with approximately 10 years of gamma-ray data from *Fermi*-LAT, only eleven star-forming galaxies have been identified as gamma-ray sources [95]. Among these, three are LIRGs and one is a ULIRG, all of which are part of the GOALS sample. A subsequent analysis using approximately 15 years of *Fermi*-LAT data finds evidence for two additional sources and challenges the identification of one source from the

10-year analysis [96]. Given the limited number of detected gamma-ray sources, it is currently not feasible to systematically constrain $\gamma_{\rm SN}$ for individual galaxies in the GOALS sample.

Maximum momentum

The maximum proton energy reached in the acceleration process ($E_{\rm max}$=$p_{\rm max}c$) determines up to which energy neutrinos are significantly produced. About 5% of the primary proton energy is transferred to the high-energy neutrino in an inelastic collision (see Section 1.2.1). As such, to produce neutrinos of about ~ 10 PeV, a cosmic accelerator should be able to accelerate particles up to about $E_{\rm max} \sim 100$ PeV. This reduces to $E_{\rm max} \sim 1{-}10$ PeV to produce neutrinos of about 100 TeV.

Observed CRs with energies up to ~ 3 PeV are generally attributed to galactic supernovae. This is based on energy considerations and GeV-TeV gamma-ray observations of supernova remnants [62, 291]. Modeling efforts are also in favor of particles reaching energies of $\sim 10{-}100$ PeV in supernova acceleration. This relies on the presence of sufficiently strong magnetic fields and/or the presence of a magnetic-plasma wind of the progenitor star [17, 61, 63, 64]. In (circum)nuclear starburst regions of U/LIRGs, the magnetic field strength is indeed significantly amplified (e.g. [229]), and the newly formed stars could be on average more massive as opposed to normal star-forming regions. The latter implies an increase in the average explosion energy per supernova and an enhancement of stellar-mass loss via stellar winds. This, in combination with the amplified magnetic field, indicates on average larger $p_{\rm max}$ values as opposed to star-forming galaxies such as the Milky Way.

3.1.3 Timescales & calorimetric conditions

A leaky-box model is assumed to model the confinement of the supernova-injected particles in the nuclear disk. This framework dictates that the injected CRs are allowed to move freely in the starburst volume and have a nonzero chance to escape the boundaries. The rate at which particles escape these boundaries is defined as the inverse of the average escape time $\tau_{\rm esc}$. We consider advection via a galactic-scale outflow and spatial diffusion as CR-removing processes. The average escape time $\tau_{\rm esc}$ in a particular starburst region in this framework is thus computed as

$$\tau_{\rm esc} = \left[\tau_{\rm diff}^{-1} + \tau_{\rm adv}^{-1}\right]^{-1} \ , \tag{3.9}$$

with $\tau_{\rm diff}$ and $\tau_{\rm adv}$ the average timescales over which diffusion and advection occur, respectively. In addition, CRs can also participate in inelastic pp-interactions before being removed from the starburst volume. These catastrophic collisions result in energy loss over an average timescale $\tau_{\rm pp}$. Continuous energy losses such as Coulomb interactions and ionization also affect the propagation of CRs. However, for particle energies larger than 1 GeV, such energy losses are negligible as opposed to the catastrophic interactions (e.g. [86]). Therefore, as a primary CR energy of $E \gtrsim 1$ PeV is required to produce neutrinos at the level of IceCube observations, the continuous energy-loss processes can be safely neglected for the purposes of this work. Moreover, proton-synchrotron losses are negligible for typical magnetic field strengths at the scale of the starburst region.

The average residence time of a CR in the central starburst regions relevant to this study is computed as

$$\tau = \left[\tau_{\rm diff}^{-1} + \tau_{\rm adv}^{-1} + \tau_{\rm pp}^{-1}\right]^{-1} \ . \tag{3.10}$$

The diffusion timescale ($\tau_{\rm diff}$), advection timescale ($\tau_{\rm adv}$), and the energy-loss timescale due to inelastic pp-collisions ($\tau_{\rm pp}$) are discussed in more detail in the following sections.

Diffusion

CRs injected by supernova activity will interact with the turbulent magnetic field in the starburst region. This leads to a random walk driven by the gyroradius $r_{\rm g}$ of the particle. Eventually, the random walk leads to diffusion away from the central starburst region, assuming no other processes are affecting the propagation. The timescale over which diffusion happens is therefore conservatively approximated as

$$\tau_{\rm diff} = \frac{H_{\rm SBR}^2}{D} \ , \tag{3.11}$$

with D the diffusion coefficient, which depends on the magnetic field strength (B) in the central starburst region, and the scale height of the nuclear disk ($H_{\rm SBR}$) introduced in Section 3.1.2.

Following [270], we parameterize the diffusion coefficient in Eq. (3.11) as

$$D = \frac{r_{\rm g} \cdot v_\perp}{3\mathcal{F}(k)} \ . \tag{3.12}$$

In this case, the value of the diffusion coefficient D scales with:

- The relativistic gyroradius $r_{\rm g} = p_\perp/|q|B$ of the CR, with q its charge, $p_\perp$ the component of the momentum perpendicular to the magnetic field direction, and B the magnetic field strength in the central starburst region. The strength of the magnetic field in the central region of a starburst galaxy is typically $\gtrsim 100$ μG and can even reach a few mG [229]. In the relativistic case the gyroradius can be rearranged to the convenient form

$$r_{\rm g} = 3.3 \times \frac{(E_{\rm CR}/{\rm GeV})(v_\perp/c)}{(|q|/e)(B/{\rm T})} \ {\rm meter}, \tag{3.13}$$

  where $E_{\rm CR}$ is the energy of the CR particle and e is the elementary charge.

- The speed component of the CR perpendicular to the magnetic field ($v_\perp$), which can be set to the speed of light c for the purposes of this work.

- The parameter $\mathcal{F}(k)$, wich is the normalized energy density per unit logarithmic wave number k in the turbulent magnetic field. This parameter is expressed as

$$\mathcal{F}(k) = k \cdot W(k) = k \cdot W_0 \cdot (k/k_0)^{-d} \ , \tag{3.14}$$

  and normalized as

$$\int_{k_0}^{\infty} \mathcal{F}(k) {\rm d}(\ln k) = \int_{k_0}^{\infty} W_0 \cdot \left(\frac{k}{k_0}\right)^{-d} {\rm d}k = \eta_B \ . \tag{3.15}$$

The parameter $\eta_B \equiv (\delta B/B)^2$ is the turbulence ratio, δB the turbulent component of the magnetic field, and $k_0^{-1} = L_0$ is the characteristic length-scale at which the turbulence is injected. In this framework we consider that CRs interact with large-scale Kolmogorov turbulence such that $d = 5/3$, and assume that the turbulence ratio and typical perturbation length are $\eta_B = 1$ and $L_0 = 1$ pc, respectively.

To evaluate the diffusion timescale $\tau_{\rm diff}$, it is assumed that CRs predominantly interact with the resonant mode $k_{\rm res} = 1/r_L$, such that

$$\mathcal{F}(k_{\rm res}) \propto k_{\rm res}^{-\frac{2}{3}} = r_{\rm g}^{\frac{2}{3}} \propto p^{\frac{2}{3}} \xrightarrow{\text{Eq. (3.12)}} D \propto p^{\frac{1}{3}} \ . \tag{3.16}$$

As a result, the diffusion timescale scales with momentum of the particle as $\tau_{\rm diff} \propto p^{-\frac{1}{3}}$.

Advection

Galactic-scale outflows in starburst galaxies are commonly observed (see e.g. [67] for a review). A possible driving mechanism for such an outflow is the mechanical energy transfer to the interstellar medium via stellar winds and supernova explosions. These interactions induce strong shocks that heat and pressurize the interstellar medium. In addition, AGN activity and CRs are also proposed as driving mechanisms (e.g. [67]). A cavity of very hot gas is formed as a result of the energy transfer to the interstellar medium. Due to the pressure imbalance between the central region and the interstellar medium of the host galaxy, this gas starts expanding above and below the galactic disk. Once the scale height of the galactic disk is reached, the wind breaks out into the galactic halo [292] and thereby advects part of the CR population out of the nuclear region. As such, these CRs will not contribute to the high-energy neutrino production in the nuclear region. It should be noted that advected CRs could be accelerated and converted to high-energy neutrinos within the galactic-scale wind [293]. This contribution is not considered within our framework.

The velocity profile of the expanding bubble described above is such that the wind speed increases as it reaches the edge of the core region. Then, as the expanding wind breaks out into the galactic halo, the terminal velocity (v_∞) is quickly reached [292]. The wind speed at the point of CR advection ($v_{\rm adv}$) is therefore bound by the terminal velocity, i.e. $v_{\rm adv} < v_\infty$.

The velocity of galactic-scale outflows is inferred from spectral line emission of the wind. Strong winds with speeds of $500-1500$ km s^{-1} have been detected by the Herschel Space Observatory in ULIRGs [294]. These winds are also observed in LIRGs. ALMA observations of the LIRG NGC 3256, for example, reveal a molecular outflow from the northern nuclear disk. This outflow is part of a starburst-driven superwind with a maximum velocity > 750 km s^{-1} [295]. As indicated above, the advection speed is likely smaller than these terminal velocities.

The advection timescale $\tau_{\rm adv}$ is approximated as the ratio of the scale height of the nuclear disk $H_{\rm SBR}$ and the advection speed $v_{\rm adv}$,

$$\tau_{\rm adv} = \frac{H_{\rm SBR}}{v_{\rm adv}} \ . \tag{3.17}$$

Energy loss

To evaluate the rate at which CRs lose their energy by inelastically colliding with the interstellar medium in the nuclear region, we make the critical assumption that

the CRs encounter the average proton density in the nuclear region (n). The rate at which high-energy protons interact in the starburst region via inelastic pp-collisions then scales with the average proton density in the nuclear region n, the cross section of inelastic pp-collisons ($\sigma_{\rm pp}$), and the velocity of the CR. As the CRs of interest are highly relativistic, the speed of the CRs is fixed to the speed of light c. The inelasticity of a collision is fixed to $\zeta = 0.5$ [296]. As such, the timescale for energy loss via inelastic pp-scattering can be expressed as

$$\tau_{\rm pp} = \frac{1}{n \cdot \sigma_{\rm pp}(E) \cdot c \cdot \zeta}. \tag{3.18}$$

For the cross section, we use the parametrization given in [87], constructed from accelerator and simulation data, such that $\sigma_{\rm pp} = 34.3 + 1.88 \ln L + 0.25 L^2$ mb with $L = \ln(E/1 \text{ TeV})$. See also the left panel of Figure 1.4.

Calorimeter conditions

A starburst region efficiently converts high-energy protons into neutrinos if the energy-loss timescale is significantly shorter than the timescale over which diffusion and advection occur. In that case, the starburst region acts as a calorimeter. To quantify the calorimeter conditions, the parameter $\mathcal{C}_{\rm pp} \in [0, 1]$ is introduced as

$$\mathcal{C}_{\rm pp} = \frac{\tau}{\tau_{\rm pp}} = \frac{f_\pi}{1 + f_\pi}\ . \tag{3.19}$$

The parameter f_π is the meson production efficiency for pp-interactions, also known as the effective optical depth, and is defined here as $f_\pi = \tau_{\rm esc}/\tau_{\rm pp}$, with $\tau_{\rm esc}$ defined in Eq. (3.9). It follows that:

- If f_π is large, then $\mathcal{C}_\pi \to 1$. In this case secondary particle production will dominate over particle escape. The starburst resembles a complete calorimeter in this limit.
- If f_π is small, then $\mathcal{C}_{\rm pp} \ll 1$. In this case particle escape dominates over secondary particle production.
- Between the two extremes in the first two bullets, $\mathcal{C}_{\rm pp} > 0.5$ indicates the conditions for which $\tau_{\rm pp}$ is on average the shortest timescale in the system. This is discussed in more detail in Appendix B.

Figure 3.2 shows the parameter space of $\mathcal{C}_{\rm pp}$ for variable proton density in the interstellar medium of the nuclear region (n) and advection speed of a galactic-scale outflow ($v_{\rm adv}$). For this, we assume a 10 PeV proton that propagates in a nuclear disk with scale height $H_{\rm SBR} = 150$ pc, taking a Kolmogorov-type diffusion model. The dash-dotted line shows for which combinations of n and $v_{\rm adv}$ a value of $\mathcal{C}_{\rm pp} = 0.5$ is obtained. The black hatched region indicates $\mathcal{C}_{\rm pp}$ values for typical proton densities in the interstellar medium of the nuclear region of U/LIRGs, $n \gtrsim 1000$ cm^{-3} ([230], see also Section 3.2), and advection speeds between 500 km s^{-1} and 1500 km s^{-1}. Note that, although terminal velocities of ~ 1500 km s^{-1} are observed in U/LIRGs, it is unlikely that the advection speed $v_{\rm adv}$ is equally high (Section 3.1.3).

GOALS U/LIRGs in a late merger stage are on average more obscured in the central region (e.g. [184]). This is the result of gas and dust being funneled toward the central regions as the galaxies merge (see Section 2.1). As such, ULIRGs, which are nearly

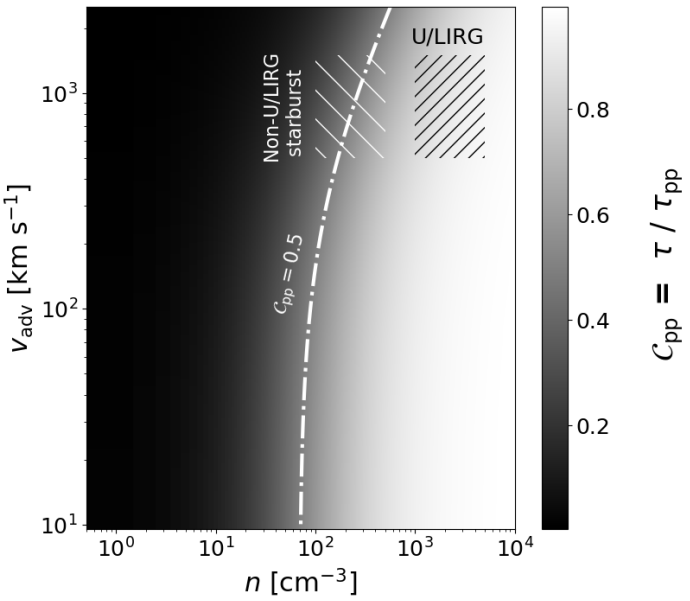

FIGURE 3.2: Parameter space of $\mathcal{C}_{\rm pp}$, defined in Eq. (3.19), for variable interstellar medium proton density in the nuclear region (n) and advection speed ($v_{\rm adv}$). A 10 PeV proton is assumed to propagate in a nuclear disk with scale height $H_{\rm SBR} = 150$ pc and the diffusion is fixed to a Kolmogorov-type diffusion model. The free parameters of the diffusion model are fixed as discussed in Sec. 3.1.3. The white dash-dotted line shows the combinations of $v_{\rm adv}$ and n for which $\mathcal{C}_{\rm pp} = 0.5$. The white and black hatched regions indicate expected $\mathcal{C}_{\rm pp}$ values for nuclear starburst regions in non-U/LIRGs and U/LIRGs, respectively.

always in the final stage of a merger, are expected to be located at the high end of the particle densities indicated in Figure 3.2. For LIRGs, which are observed in every merger stage, this could strongly depend on how advanced the merger is. In any case, high-energy protons are expected to lose a significant fraction of their initial energy in the nuclear region of U/LIRGs.

For comparison, we also investigate typical conditions in non-U/LIRG starburst galaxies. Prototypical examples of such galaxies are the nearby starburst galaxies M82 and NGC 253. This type of starburst galaxy typically has a lower proton density in the nuclear region as opposed to ULIRGs and a fraction of the LIRGs, i.e. $n \sim 100$ cm^{-3} (e.g. [270, 297–299]). The white hatched region in Figure 3.2 shows $\mathcal{C}_{\rm pp}$ values corresponding to proton number densities between 100 and 500 cm^{-3} in the interstellar medium of the nuclear region, and the same advection speeds as investigated for the U/LIRGs. From Figure 3.2 we conclude that, compared to U/LIRGs, non-U/LIRG starburst galaxies are expected to be less efficient calorimeters on average.

The scale height of the nuclear disk ($H_{\rm SBR}$) also affects $\mathcal{C}_{\rm pp}$. Figure 3.3 shows how $\mathcal{C}_{\rm pp}$ is affected when varying $H_{\rm SBR}$ between 50 and 400 pc for a starburst region with an interstellar medium density in the nuclear region of $n = 350$ cm^{-3}, $n = 1000$ cm^{-3}, and $n = 5000$ cm^{-3}. The range of scale heights is consistent with the values derived for nearby U/LIRGs [262]. The particle density values for the interstellar medium are chosen to model a wide range of starburst conditions. For each of these starburst configurations, an advection speed of $v_{\rm adv} = 500$ km s^{-1} and $v_{\rm adv} = 1500$ km s^{-1} is considered. The results show that calorimeter assumptions are robust against changes in $H_{\rm SBR}$ and $v_{\rm adv}$ if the particle density in the nuclear region is high. We note that this

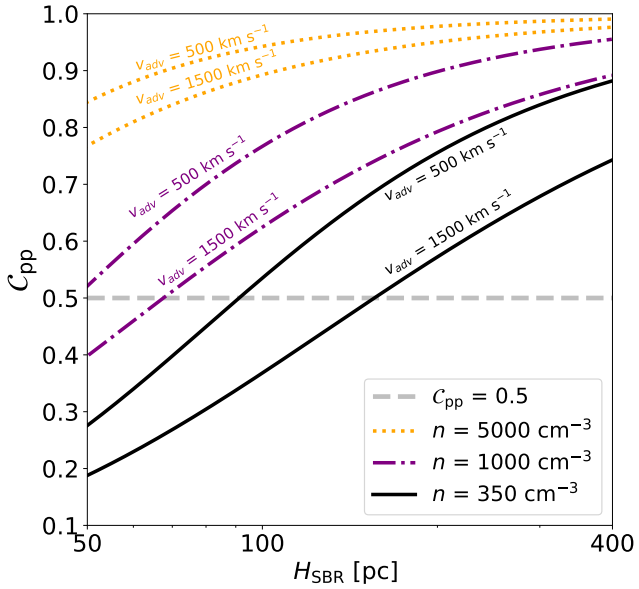

FIGURE 3.3: The $\mathcal{C}_{\rm pp}$-parameter for three different starburst configurations at variable scale height ($H_{\rm SBR}$). The interstellar medium proton density is fixed to $n = 350$ cm^{-3}, $n = 1000$ cm^{-3}, and $n = 5000$ cm^{-3}. For each of these configurations, a galactic superwind with $v_{\rm adv} = 500$ km s^{-1} and $v_{\rm adv} = 1500$ km s^{-1} is considered.

statement also applies to changes in the diffusion model.

3.1.4 Neutrino luminosity to flux

The distribution of high-energy proton momenta in the nuclear region of U/LIRGs ($\mathcal{F}_{\rm p}$) is determined by the interplay between the injection rate of high-energy protons by supernovae and subsequent particle transport, as described in this chapter. Assuming a spatially homogeneous starburst region in a steady state, the momentum distribution of high-energy protons in the nuclear region is expressed as,

$$\mathcal{F}_{\rm p} = Q_{\rm p} \cdot \tau = Q_{\rm p} \cdot \tau_{\rm pp} \cdot \mathcal{C}_{\rm pp} \tag{3.20}$$

These high-energy protons can collide inelastically with a proton in the interstellar medium of the nuclear region. Such collisions produce, among other particles, charged ($\pi^{\pm}$) and neutral pions (π^0) (see Section 1.2). The charged pions decay as

$$\begin{cases} \pi^+ \rightarrow \mu^+ + \nu_\mu^{(1)} \rightarrow e^+ + \nu_e + \bar{\nu}_\mu^{(2)} + \nu_\mu^{(1)} \\ \pi^- \rightarrow \mu^- + \bar{\nu}_\mu^{(1)} \rightarrow e^- + \bar{\nu}_e + \nu_\mu^{(2)} + \bar{\nu}_\mu^{(1)} \end{cases}, \tag{3.21}$$

and the neutral pions decay to gamma rays, $\pi^0 \rightarrow \gamma + \gamma$. The label (1) denotes the muon neutrinos produced in pion decay and the label (2) denotes the muon neutrinos produced in muon decay. To compute the neutrino-production rate ($q_{\nu+\bar{\nu}}$) from the energy distribution of high-energy protons ($n_{\rm p}$). We adopt the approach described in [87], expressing the energy distribution as

$$n_{\rm p}(E) = 4\pi p^2 \mathcal{F}_{\rm p}(p)\, {\rm d}p\ . \tag{3.22}$$

The authors provide analytical fits to neutrino spectra obtained from meson spectra simulated with Monte Carlo generators SIBYLL [300] and QGSJET [301]. Doing so, the neutrino production rate $q_{\nu+\bar{\nu}}$ at the source, including neutrinos and antineutrinos, is expressed as

$$q_{\nu+\bar{\nu}} = cn \int_0^1 F_\nu \left(x, \frac{E_\nu}{x}\right) \sigma_{\mathrm{pp}} \left(\frac{E_\nu}{x}\right) n_{\mathrm{p}} \left(\frac{E_\nu}{x}\right) \frac{\mathrm{d}x}{x} \,, \tag{3.23}$$

where c is the speed of light, x is the neutrino-to-proton energy fraction ($x = E_\nu/E_{\mathrm{p}}$), n is the nuclear proton density of the interstellar medium, σ_{pp} is the cross section for inelastic pp-interactions (Section 3.1.3), and $F_\nu = F^{(1)}_{\nu_\mu} + F^{(2)}_{\nu_\mu} + F_{\nu_e}$ are the neutrino distribution functions corresponding to the decays given in Eq. (3.21).

The spectra of muon neutrinos and antineutrinos from muon decay are denoted by $F^{(2)}_{\nu_\mu}$, while the spectra of electron neutrinos and positron neutrinos from muon decay are denoted by F_{ν_e}. The former follows the same functional form as the spectrum of electrons and positrons produced in muon decay, denoted by F_e, such that $F^{(2)}_{\nu_\mu} = F_e$. Additionally, $F_{\nu_e} \approx F_e$ within a 5% accuracy. Therefore, we adopt the total neutrino spectrum as $F_\nu = F^{(1)}_{\nu_\mu} + 2 \cdot F_e$, with $F^{(1)}_{\nu_\mu}$ describing the spectra of muon neutrinos and antineutrinos from pion decay. The analytical expressions for these distribution functions are provided in Appendix C. Note that these expressions are valid only for secondary particles with energies exceeding 100 GeV.

Integrating the neutrino-production rate $q_{\nu+\bar{\nu}}$ over the volume of the starburst region yields the neutrino luminosity at the source. Therefore, the all-flavor neutrino flux at Earth generated by a single GOALS galaxy ($\Phi_{\nu+\bar{\nu}}$), containing neutrinos and antineutrinos, is computed as

$$\Phi_{\nu+\bar{\nu}}(E_\nu) = \frac{V_{\mathrm{SBR}}}{4\pi D_L^2} \cdot q_\nu(E_\nu) \,, \tag{3.24}$$

with D_L the luminosity distance to the galaxy. We take advantage of the fact that GOALS galaxies are sufficiently close by ($z < 0.09$) to neglect redshift effects.

As shown in Eq. (3.21), inelastic pp-interactions at the source produce neutrinos with an initial flavor ratio of $(\nu_e : \nu_\mu : \nu_\tau) = (1 : 2 : 0)$. However, as neutrinos propagate over extragalactic distances, the phenomenon of neutrino oscillations results in an approximately equal distribution among the three neutrino flavors. Consequently, the flavor ratio at Earth is $(\nu_e : \nu_\mu : \nu_\tau) \approx (1 : 1 : 1)$, as discussed in detail in Section 1.4.2. This implies that the single-flavor neutrino flux at Earth, denoted by $\Phi_{\nu_\ell+\bar{\nu}_\ell}$ with $\ell \in \{e, \mu, \tau\}$, is obtained by dividing the total all-flavor neutrino flux by a factor of three.

In conclusion, the starburst-driven neutrino flux, as expressed in Eq. (3.24), is determined by the following starburst-specific parameters:

$$\Phi_{\nu_\ell+\bar{\nu}_\ell} = \Phi_{\nu_\ell+\bar{\nu}_\ell} \left(\mathcal{R}_{\mathrm{SN}}, \gamma_{\mathrm{SN}}, p_{\mathrm{max}}, H_{\mathrm{SBR}}, v_{\mathrm{adv}}, n, B, D_L\right) , \tag{3.25}$$

where the AGN-corrected nuclear supernova rate $\mathcal{R}_{\mathrm{SN}}$, defined in Eq. (3.5) depends on the following parameters:

$$\mathcal{R}_{\mathrm{SN}} = \mathcal{R}_{\mathrm{SN}} \left(L_{\mathrm{IR}}, \langle \alpha_{\mathrm{AGN}} \rangle, \mathcal{G}\right) . \tag{3.26}$$

3.2 Case Study: LIRG NGC 3690

In this section, the high-energy starburst-driven neutrino-production framework constructed in Section 3.1 is applied to the LIRG NGC 3690 (also known as Arp 299 and Mrk 171).[4] This intermediate-stage merger of two gas-rich galaxies, shown in Figure 3.4, is one of the most powerful mergers in the local Universe at a luminosity distance $D_L \sim 50.7$ Mpc [19]. The system is located in the Northern Hemisphere at equatorial coordinates $\alpha_{\rm J2000} = 11{\rm h}28{\rm m}32.3{\rm s}$ (172.13°) and $\delta_{\rm J2000} = 58{\rm d}33{\rm m}43{\rm s}$ (58.56°). The eastern part of the galaxy system (NGC 3690E) has a luminosity of $\log_{10}(L_{\rm IR}/L_\odot) = 11.37$ and the western part (NGC 3690W) has luminosity of $\log_{10}(L_{\rm IR}/L_\odot) = 11.09$, both obtained from data of the Herschel Space Observatory [234].

Mid-IR and radio continuum maps of this LIRG reveal distinct regions A, B, and C+C' which dominate at these wavelengths [303]. These regions are indicated in the right panel of Figure 3.4. Region A is the nuclear region of the eastern galaxy (NGC 3690E-A) and region B is the nuclear region of the western part (NGC 3690W-B). The C'+C component is located in the overlapping region between the two galaxies. Multiwavelength follow-up studies showed that the nature of the nuclear regions are very different. Hard X-ray observations indicate the presence of a Compton thick AGN in region B [304] and high-resolution radio observations reveal a strong nuclear starburst in region A [201]. Moreover, a TDE has also been observed in region B [203].

Region A is of main interest for this work and is used as a case study for the neutrino production model introduced in Section 3.1. In the following, we first describe the model parameters related to CR injection in region A, followed by those related to CR propagation in that region. Finally, we use these parameters to estimate the starburst-driven muon-neutrino flux from region A in NGC 3690.

3.2.1 Cosmic-ray injection

NGC 3690E-A is a highly dust-enshrouded region, such that even near-IR wavelengths suffer from attenuation effects [201]. Therefore, high-resolution radio observations are required to identify the supernova activity in this region. The best direct observational constraints on the supernova activity in the central $R_{\rm SBR} = 150$ pc of NGC 3690E-A were obtained by a ~ 2.5 year monitoring campaign at 5.0 GHz. This campaign revealed two core-collapse supernovae in the starburst region, leading to an estimated lower limit of $\mathcal{R}_{\rm SN} \gtrsim 0.80^{+1.06}_{-0.52}$ yr^{-1} with uncertainties corresponding to 1σ errors [201]. In addition to these direct observations, the authors also present a supernova rate estimated from diffuse synchrotron observations, which is found to be $\mathcal{R}_{\rm SN} \simeq 0.45 - 0.65$ yr^{-1}. This estimate agrees well with our supernova rate estimates for NGC3690E obtained from Eq. (3.5) for various IMFs, given in Table 3.2. This table also provides the corresponding mass-scaling factor $\mathcal{M}$ (Section 3.1.1) and CR luminosity, i.e. $\mathcal{L}_{\rm CR} = \eta_{\rm SN} \cdot E_{\rm SN} \cdot \mathcal{R}_{\rm SN}$. The latter is the relevant parameter to compute the neutrino flux as it is used to normalize the high-energy proton injection spectrum. To convert the supernova rates to a CR luminosity, the kinetic energy conversion factor is fixed to $\eta_{\rm SN} = 0.10$.

We estimate the spectral index of the proton injection rate generated by the supernova activity, $\gamma_{\rm SN}$, from the photon index, Γ, that best fits the gamma-ray spectrum of

[4] In the literature, the eastern and western members of the galaxy pair in Figure 3.4 are often given the names IC 694 and NGC 3690, respectively. However, IC 694 is actually a small E/S0 galaxy ∼1' to the northwest of the merging galaxy pair, while NGC 3690 correctly refers to the merging pair [302]. The merger is also commonly known as Arp 299. In this work, we choose the name NGC 3690 to refer to the whole system, in line with the name given by GOALS.

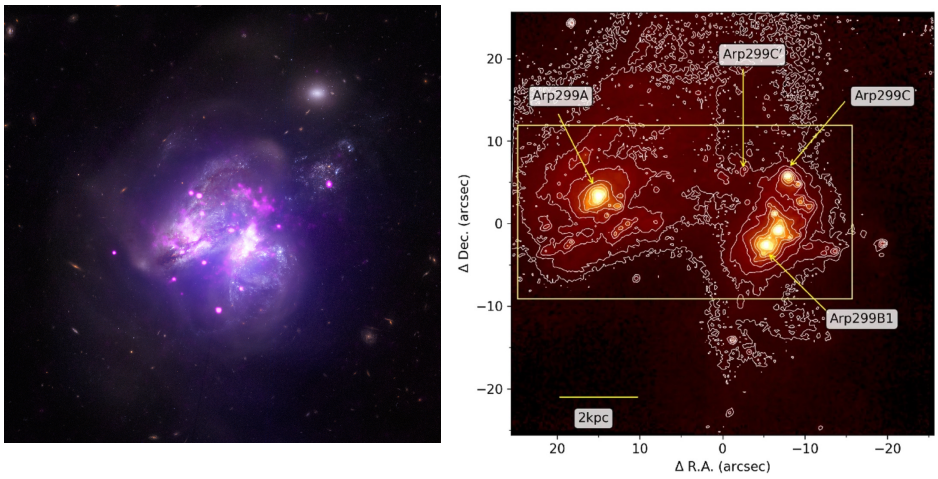

FIGURE 3.4: Left: Composite image of the merger Arp 299, including X-ray data from Chandra (pink), higher-energy X-ray data from NuSTAR (purple), and optical data from the Hubble Space Telescope (white and faint brown) [305]. Right: Near-IR image at $\lambda \approx 1.6$ μm which mostly traces the stellar emission (Hubble Space Telescope/NICMOS) [306].

TABLE 3.2: The supernova rate $\mathcal{R}_{\rm SN}$ of the nuclear region in NGC 3690E for different intitial mass functions, together with the progenitor mass-scaling factor $\mathcal{M}$, and the CR luminosity $\mathcal{L}_{\rm CR}$. The supernova rate is computed using Eq. (3.5), with $\log_{10}(L_{\rm IR}/L_\odot) = 11.37$, $\langle \alpha_{\rm AGN} \rangle = 0.04$, and $\mathcal{G} = 1$. To compute the CR luminosity $\mathcal{L}_{\rm CR}$, we take $\eta_{\rm SN} = 0.10$ in Eq. (3.8).

	$\mathcal{R}_{\rm SN}$ [yr^{-1}]	$\mathcal{M}$	$\mathcal{L}_{\rm CR}$ [10^{49} erg yr^{-1}]
Salpeter	0.52	0.93	4.85
Kroupa	0.51	1.00	5.14
TH $\beta_{\rm high} = 1.5$	0.36	1.37	4.97
TH $\beta_{\rm high} = 1.0$	0.28	2.01	5.58

NGC3690. This means, $\gamma_{\rm SN} = \Gamma_{\rm NGC3690} + 2$, with $\Gamma_{\rm NGC3690} = 2.11 \pm 0.19$ determined from gamma-ray observations [95]. However, the location of the gamma-ray emission in NGC 3690 is unresolved. As such, the gamma rays could also (partially) originate from the AGN in region B or an off-nuclear star-forming region. To demonstrate the effect of changing the spectral index, the neutrino flux is also computed for a harder spectrum of $\gamma_{\rm SN} = 4$, which corresponds to $\Gamma = 2$.

The maximum momentum $p_{\rm max}$ reached via supernova acceleration in NGC3690E is not constrained. Therefore, we opt to calculate the neutrino flux for a maximum momentum $p_{\rm max}$ of 10 PeV/c, 20 PeV/c, 30 PeV/c, and 100 PeV/c. This covers a wide range of likely $p_{\rm max}$ values (see Section 3.1.2).

3.2.2 Timescales & calorimetric conditions

From aperture synthesis CO maps an H_2 mass of about 3.9×10^9 $M_\odot$ is inferred for the central ≤ 250 pc of NGC 3690E [307]. Here, we assume that this mass is distributed in a uniform way within a disk with radius of $R_{\rm SBR} = 250$ pc and scale height $H_{\rm SBR} = 150$ pc. This corresponds to an average H_2 particle density of

$$n_{\mathrm{H}_2} \approx 1340 \cdot \left(\frac{H_{\mathrm{SBR}}}{150\mathrm{pc}}\right)^{-1} \cdot \left(\frac{R_{\mathrm{SBR}}}{250\mathrm{pc}}\right)^{-2} \mathrm{cm}^{-3} \,. \tag{3.27}$$

We are, however, interested in the proton number density (n), which is a factor two larger than n_{H_2}. We also note that the proton density inferred from the H_2 number density is a lower limit on the proton density in the interstellar medium, since there is also a subdominant contribution of neutral atomic hydrogen (e.g. [308]) and heavier elements. For this work, therefore, we make the conservative choice of $n = 2500\ \mathrm{cm}^{-3}$ for the proton number density.

Observations of NGC 3690E with the International Low Frequency Array (LOFAR) Telescope at 150 MHz reveal a two-sided structure emanating from the nucleus [309]. The outflow is detected via radio wavelengths from synchrotron-emitting electrons. Under the assumption that the outflow is driven by a supernova rate of $\mathcal{R}_{\mathrm{SN}} \gtrsim 0.80\ \mathrm{yr}^{-1}$, the outflow is estimated to move at $370{-}890$ km s^{-1} [309]. Here we assume an advection speed of $v_{\mathrm{adv}} = 500$ km s^{-1}, consistent with observations of other U/LIRGs (Section 3.1.3). Moreover, LOFAR observations at 150 MHz indicate a minimum equipartition magnetic field for the nuclear region of $B \gtrsim 250\ \mu\mathrm{G}$ [310]. To compute the neutrino flux, a magnetic field strength of $B = 250\ \mu\mathrm{G}$ and Kolmogorov-type diffusion model are assumed.

Figure 3.5 shows the diffusion timescale, advection timescale, and pp energy-loss timescale as functions of proton energy for the nuclear region of NGC 3690E. Based on the values found for n, H_{SBR}, v_{adv}, and B, it is also concluded that $\mathcal{C}_{\mathrm{pp}} = 0.95$ (Section 3.1.3). This implies that the nuclear starburst region in NGC 3690E is expected to efficiently convert CR energy into high energy neutrinos.

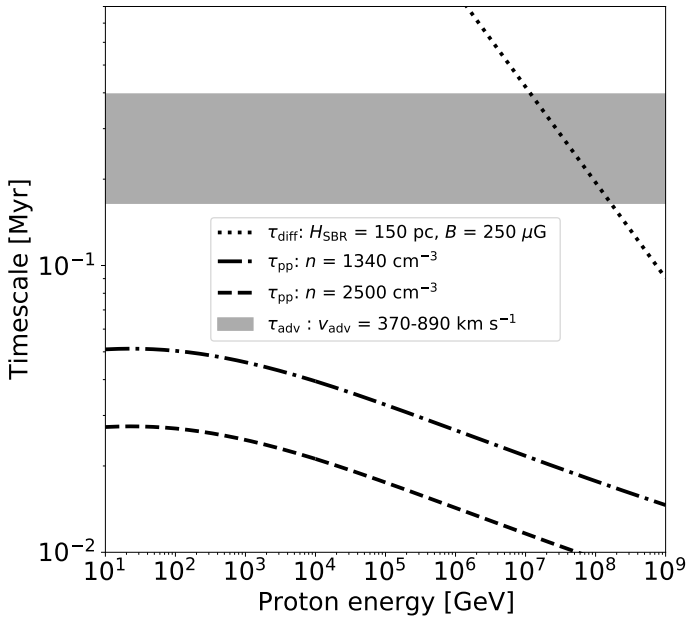

FIGURE 3.5: Diffusion, advection, and pp-energy loss timescales as functions of proton energy for the nuclear starburst region of NGC 3690E.

3.2.3 Neutrino-flux predictions

Figure 3.6 presents the expected muon-neutrino flux for region A in NGC 3690E, considering two supernova rates: $\mathcal{R}_{\rm SN} = 0.28\ {\rm yr}^{-1}$ and $\mathcal{R}_{\rm SN} = 1.86\ {\rm yr}^{-1}$. These values correspond to the 1σ uncertainties derived from direct observations. The figure demonstrates that the predicted flux scales linearly with the supernova rate and that small variations in the spectral index $\gamma_{\rm SN}$ can significantly influence the flux predictions.

It should be noted that the high-energy tail of $E^2_{\nu_\mu}\Phi_{\nu_\mu+\bar{\nu}_\mu}(E_{\nu_\mu})$ requires cautious interpretation. While the exponential cutoff in the proton injection rate is a reasonable assumption, it lacks direct observational constraints. Next-generation neutrino observatories, such as IceCube-Gen2 [113] and KM3NeT [110], are expected to test the validity of this cutoff.

The horizontal solid gray line in the figure represents the point-source sensitivity, based on 10 years of IceCube data, for an E^{-2} neutrino spectrum at the declination (δ) of NGC 3690 [117]. None of the investigated parameter combinations exceed this sensitivity, providing a consistency check for the model. This is consistent with the fact that NGC 3690 has not been identified as a significant neutrino emitter in previous IceCube analyses.

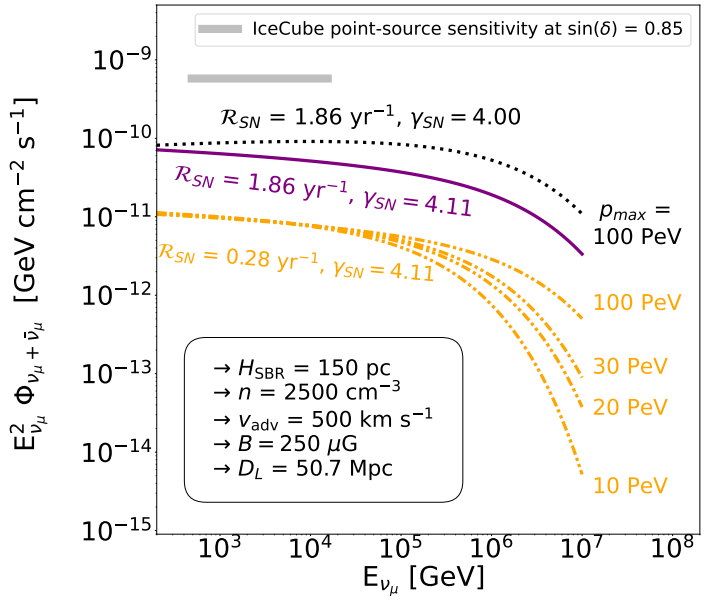

FIGURE 3.6: Predictions for the starburst-driven muon-neutrino flux of NGC 3690E using our model. All model parameters, except for the maximum proton momentum $p_{\rm max}$, are driven by multiwavelength observations as discussed in the text. Note that $\gamma = \gamma_{\rm SN} - 2$, where $\Phi_{\nu_\mu+\bar{\nu}_\mu} \propto E^{-\gamma}$. The 10-year E^{-2} IceCube point-source sensitivity for a source at the declination of NGC 3690 is also indicated by the gray solid line [117].

3.3 Framework Applied to GOALS

In this section, we first compute the per-source muon-neutrino flux generated by starburst activity ($\Phi_{\nu_\mu+\bar{\nu}_\mu}$) for all GOALS galaxies. For this we use the $N = 229$ individual GOALS galaxies for which GOALS obtained an IR luminosity and the average AGN contribution to the bolometric luminosity (see Section 2.3.1). The calculations are

done using our framework constructed in Section 3.1. Then, based on these predictions, the corresponding diffuse muon-neutrino flux from all GOALS galaxies ($\Phi^{\text{diffuse}}_{\nu_\mu+\bar{\nu}_\mu}$) is estimated as

$$\Phi^{\text{diffuse}}_{\nu_\mu+\bar{\nu}_\mu}(E_{\nu_\mu}) = \frac{1}{4\pi}\sum_{i=1}^{N=229}\Phi_{i,\nu_\mu+\bar{\nu}_\mu}(E_{\nu_\mu})\,. \tag{3.28}$$

As derived in Section 3.1, the parameters required per GOALS galaxy to calculate the corresponding neutrino flux ($\Phi_{\nu_\ell+\bar{\nu}_\ell}$) are

$$\Phi_{\nu_\ell+\bar{\nu}_\ell} = \Phi_{\nu_\ell+\bar{\nu}_\ell}\left(\mathcal{R}_{\text{SN}}, \gamma_{\text{SN}}, p_{\text{max}}, H_{\text{SBR}}, v_{\text{adv}}, n, B, D_L\right),$$

for a given diffusion model in the nuclear region and the supernova rate calculated as $\mathcal{R}_{\text{SN}} = \mathcal{R}_{\text{SN}}\left(L_{\text{IR}}, \langle\alpha_{\text{AGN}}\rangle, \mathcal{G}\right)$.

To calculate the per-source and diffuse neutrino flux prediction from all GOALS galaxies we take the following approach:

- The supernova rate in the nuclear region ($\mathcal{R}_{\text{SN}}$) is calculated from source-specific data. Using Eq. (3.5), the supernova rate per galaxy is derived from the IR luminosity obtained by the Herschel Space Observatory and the relative AGN contribution to the bolometric luminosity, $\langle\alpha_{\text{AGN}}\rangle$. As discussed in Section 2.3.1, both parameters are available for all 229 galaxies. Furthermore, a canonical Kroupa IMF with $\Lambda_{\text{IR}} = 5.97\times10^{-46}$ (Table 3.1) is used and is assumed that half of the total IR luminosity of a galaxy originates from the nuclear region (i.e., $\mathcal{G} = 0.5$). The supernova rates are provided in the table in Appendix D.

- To normalize the injection rate of high-energy particles to the nuclear supernova activity, the spectral index of the injection spectrum of cosmic rays (γ_{SN}), the maximum momentum achieved during supernova acceleration (p_{max}), and the conversion efficiency of supernova explosion energy to cosmic ray acceleration (η_{SN}) are required. For each supernova event, we assume $\eta_{\text{SN}} = 0.10$ and $E_{\text{SN}} = 10^{51}$ erg. However, γ_{SN} remains unconstrained for most GOALS galaxies. Therefore, we adopt the same spectral index across all galaxies and compute the diffuse neutrino flux for three cases: $\gamma_{\text{SN}} = 4.00$, $\gamma_{\text{SN}} = 4.25$, and $\gamma_{\text{SN}} = 4.50$. This corresponds to $\gamma = \gamma_{\text{SN}} - 2.00$, where $\Phi_{\nu+\bar{\nu}} \propto E^{-\gamma}$. For all cases, an exponential cutoff is applied to the proton injection spectrum at $p_{\text{max}} = 100\ \text{PeV}/c$.

- The scale height (H_{SBR}), advection speed (v_{adv}), magnetic field strength (B), and proton density in the interstellar medium of the central region (n) are largely unknown for the majority of the GOALS galaxies. To address this, we assume similar conditions to those found in the case study of NGC 3690E (Section 3.2). The corresponding parameter values are summarized in Table 3.3.

Given the above assumptions, the neutrino luminosity at the source can be computed for the 229 targeted galaxies. To find the corresponding neutrino flux at Earth, the luminosity distances (D_L) provided by GOALS [19] are used .

3.3.1 Per-source flux predictions

Figure 3.7 shows the high-energy starburst-driven muon-neutrino fluxes per source at 1 TeV ($\Phi^{1\text{TeV}}_{i,\nu_\mu+\bar{\nu}_\mu}$) obtained with our model as a function of the sine of the declination of these sources. The fluxes are computed for $\gamma = 2$. Each galaxy is categorized as a

TABLE 3.3: Fixed parameters used in each of the GOALS galaxies to compute the per-source and diffuse muon-neutrino flux.

$p_{\max}$ [PeV/c]	H_{SBR} [pc]	v_{adv} [km s^{-1}]	n [cm^{-3}]	B [μG]	$\mathcal{G}$
100	150	500	1000	250	0.5

galaxy with $10^{10.08} L_\odot \leq L_{\mathrm{IR}} < 10^{11} L_\odot$, a LIRG, or an ULIRG. The color scale indicates the $1 - \langle \alpha_{\mathrm{AGN}} \rangle$ value of the corresponding galaxy. The plot also displays the 10-year E^{-2} IceCube point-source sensitivity at 1 TeV, represented by the dashed gray line, along with the ranges defined by dividing this sensitivity by factors of five and ten. A sensitivity improvement by at least a factor of five is anticipated with next-generation neutrino observatories such as IceCube-Gen2 ([113]; see also Section 4.2.1).

The labels in Figure 3.7 (NGC 2146, Arp 220, and NGC 3256) identify the top three galaxies with the highest expected starburst-driven neutrino flux in the GOALS sample. Notably, one of the closest GOALS galaxies, NGC 1068, is not included in this plot. This exclusion is due to the $\langle \alpha_{\mathrm{AGN}} \rangle$ value for NGC 1068 being set to one by GOALS, which implies no starburst-driven flux since Eq. (3.5) dictates that the supernova rate would be zero. However, given NGC 1068's proximity to Earth, its $\langle \alpha_{\mathrm{AGN}} \rangle$ value is likely less than one, as discussed in Section 2.3.2. For $\langle \alpha_{\mathrm{AGN}} \rangle \leq 0.54$, NGC 1068 would have the highest expected neutrino flux of all the GOALS galaxies examined. This is attributable to its close proximity and moderate IR luminosity of $\log_{10}(L_{\mathrm{IR}}/L_\odot) = 11.39$ [234].

In the most optimistic scenario, with $\gamma = 2$ and $\langle \alpha_{\mathrm{AGN}} \rangle = 0$, our model predicts a starburst-driven muon-neutrino flux from NGC 1068 at 1 TeV of $\Phi^{1\mathrm{TeV}}_{\nu_\mu + \bar{\nu}_\mu} = 2.44 \times 10^{-13}$ TeV^{-1} cm^{-2} s^{-1}. This prediction is approximately two orders of magnitude smaller than the neutrino flux observed by IceCube from the direction of NGC 1068. Furthermore, the IceCube flux is compatible with a significantly softer spectral index of $\gamma \approx 3.2$ [16]. If the observed neutrino flux is indeed associated with NGC 1068, our model suggests that the dominant contribution arises from an additional component, such as AGN-related activity.

Looking at the different source classes, Figure 3.7 also shows that the most luminous IR sources in the GOALS sample, the ULIRGs, are not necessarily the nearest and brightest neutrino sources. This is explained by the redshift distribution of Figure 2.8 (left panel), which shows that many of the ULIRGs are found in the tail of the redshift distribution, while LIRGs are found across the whole redshift range. Some ULIRGs therefore have a strong distance squared suppression, which is not compensated by their higher IR luminosity. This allows nearby LIRGs to have comparable or larger expected neutrino fluxes than ULIRGs.

In conclusion, if local U/LIRGs produce only high-energy neutrinos within the framework outlined in this chapter, then it is unlikely that they can be detected as point sources with the current IceCube detector. However, the next generation of neutrino observatories should be able to constrain the optimistic scenarios within this framework. We note that this does not exclude the possibility that local U/LIRGs are observable as point sources of high-energy neutrinos with IceCube. Other transient or steady starburst-driven activity and/or AGN activity in U/LIRGs could still produce high-energy neutrinos detectable by IceCube. This appears to be the case for the LIRG NGC 1068, which hosts a strong starburst component, though its high-energy neutrino

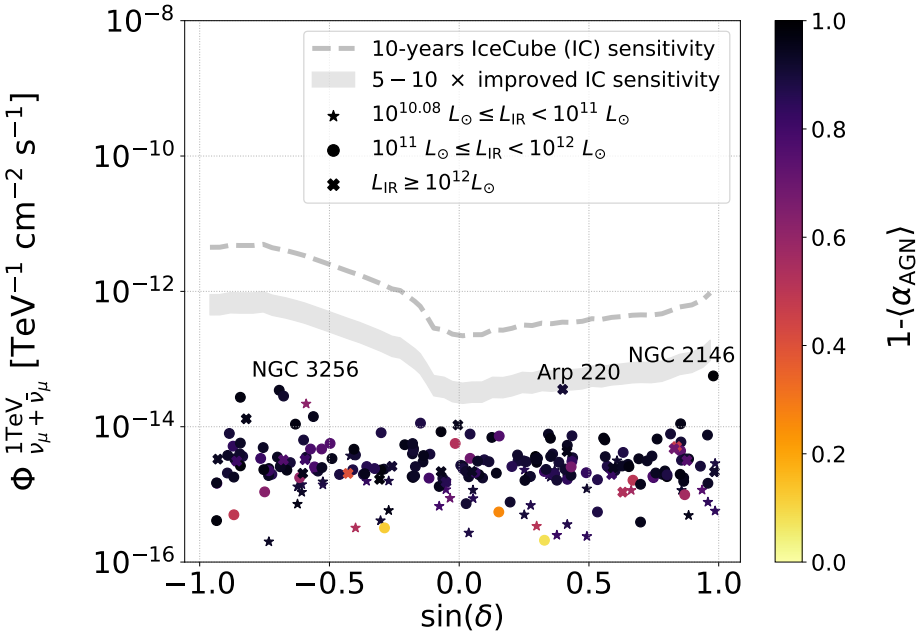

FIGURE 3.7: Per-source muon-neutrino flux predictions at 1 TeV as a function of the sine of the declination of the 229 GOALS galaxies targeted in this chapter. All fluxes are computed for a spectral index γ_{SN} = 4, with $\gamma = \gamma_{SN} - 2$ and the other model parameters as discussed in the text. The color scale indicates the value of the $1 - \langle\alpha_{AGN}\rangle$ per galaxy. For each of the galaxies, it is indicated whether it is a galaxy with $10^{10.08} L_\odot \leq L_{IR} < 10^{11} L_\odot$ (star), $10^{11} L_\odot \leq L_{IR} < 10^{12} L_\odot$ (circle), or $L_\odot \geq 10^{12} L_\odot$ (cross). For comparison, the 10-year E^{-2} IceCube point-source sensitivity as a function of the sine of the declination is shown [117]. The gray band indicates the range obtained by dividing the 10-year E^{-2} IceCube point source by a factor of five and ten, which could be reached by next-generation neutrino observatories.

flux is likely due to neutrino production near the supermassive black hole ([168]; See also Section 1.6.2).

In Chapters 5 and 6 we will use IceCube data to perform a time-integrated search for high-energy neutrino emission from GOALS U/LIRGs with a declination $\delta > -3°$. This search will only assume a high-energy neutrino spectrum with a power-law behavior, but will remain agnostic about the exact neutrino-production mechanism.

3.3.2 Per-source vs generic approach

To estimate the per-source flux predictions in previous section, all model parameters were fixed in the targeted galaxies except for the IR luminosity and the luminosity distance. However, electromagnetic observations reveal that the fixed model parameters are potentially significantly different among GOALS galaxies. In this section, we highlight the importance of doing per-source investigations to estimate the model parameters and as such properly constrain the neutrino flux of a source.

We consider four GOALS U/LIRGs identified as gamma-ray sources in [95]. These galaxies and their respective spectral indices describing the gamma-ray spectrum (Γ) are NGC 1068 ($\Gamma = 2.27 \pm 0.09$), NGC 2146 ($\Gamma = 2.27 \pm 0.07$), NGC 3690 ($\Gamma = 2.11 \pm 0.19$), and Arp 220 ($\Gamma = 2.48 \pm 0.14$). Assuming that these gamma rays are generated by nuclear starburst activity, this hints toward different spectral indices for

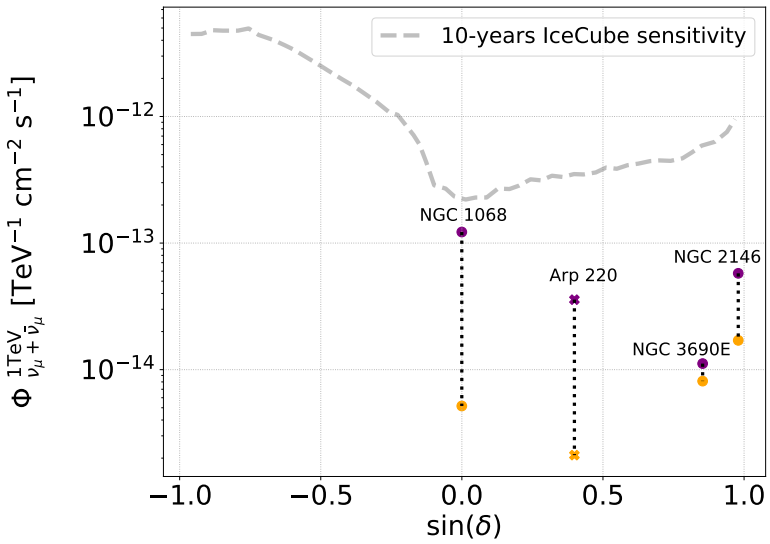

FIGURE 3.8: Muon-neutrino flux predictions at 1 TeV as a function of the sine of the declination of four GOALS galaxies identified as gamma-ray sources. For each of the galaxies, the flux prediction is shown for $\gamma_{\mathrm{SN}} = 4$ (blue) and $\gamma_{\mathrm{SN}} = \Gamma + 2$ (red) with Γ obtained from gamma-ray observations. These galaxies and their respective Γ-values are NGC 1068 ($\Gamma = 2.27 \pm 0.09$), NGC 2146 ($\Gamma = 2.27 \pm 0.07$), NGC 3690 ($\Gamma = 2.11 \pm 0.19$), and Arp 220 ($\Gamma = 2.48 \pm 0.14$). The symbols have the same meaning as in Figure 3.7.

the neutrino spectra, $\gamma = \gamma_{\mathrm{SN}} - 2$. This motivates us to change the spectral index value, while keeping the other model parameters constant, and investigate the effect on the neutrino flux predictions.[5]

Figure 3.8 shows the muon-neutrino flux prediction at 1 TeV as a function of the sine of the declination of the investigated gamma-ray sources. Per galaxy, the muon-neutrino flux is shown for $\gamma_{\mathrm{SN}} = 4$ and for $\gamma_{\mathrm{SN}} = \Gamma + 2$. Note that, for NGC 1068, $\langle \alpha_{\mathrm{AGN}} \rangle$ is put to zero to compute the neutrino flux, which assumes that all IR luminosity in NGC 1068 is due to starburst activity. This starburst-driven neutrino flux prediction for NGC 1068 at a given spectral index should therefore be interpreted as an upper limit.

Figure 3.8 shows that the relative strength of the neutrino flux predictions at $\gamma_{\mathrm{SN}} = 4$ is significantly different from the case where γ_{SN} is variable. Moreover, the flux predictions per source significantly decrease for a spectral index of $\gamma > 2$.

We also note that, due to the wide range of morphologies observed among U/LIRGs (Section 2.1.1), the average target density encountered by CRs can vary significantly. For instance, NGC 1068 hosts an AGN surrounded by a starburst ring at ~ 1.3 kpc [311], whereas Arp 220 is a late-stage merging system characterized by a much more compact and dense central region of ~ 300 pc [200]. Consequently, the average particle density sampled by CRs may be considerably lower in NGC 1068 than in Arp 220. If, for example, the effective target density in NGC 1068 is $n = 100$ cm^{-3}—a factor of 10 lower than assumed in Table 3.3—the resulting neutrino flux would be reduced by approximately a factor of two, and would decline rapidly for even smaller values of n. Furthermore, as n decreases, the predicted neutrino flux becomes increasingly sensitive to variations in other model parameters (see Figure 3.3). Understanding

[5] Even if these gamma rays are not representative for the neutrino production in the nuclear region, it is still informative to study the effect of changes in γ_{SN}.

CR propagation and interactions within the nuclear interstellar medium is therefore essential for accurate flux predictions.

The discussion above shows the importance of also performing per-source analyses to constrain the neutrino flux for specific sources rather than inferring the latter only from population studies.

3.3.3 Diffuse-flux predictions

Figure 3.9 shows the diffuse starburst-driven muon-neutrino flux expected from the GOALS sample for three different spectral indices of the proton injection rate, computed with Eq. (3.28). For each case, the diffuse flux is shown with and without the use of AGN-corrected IR luminosities indicated by the full lines and dashed lines, respectively. The largest neutrino flux in each case corresponds to the calculations done without correcting for the AGN contribution to the IR luminosity. This increase in flux, observed for all three cases, is driven by the galaxy NGC 1068. It is also concluded from the predictions that none of the parameter combinations violate the diffuse neutrino flux observed by IceCube.

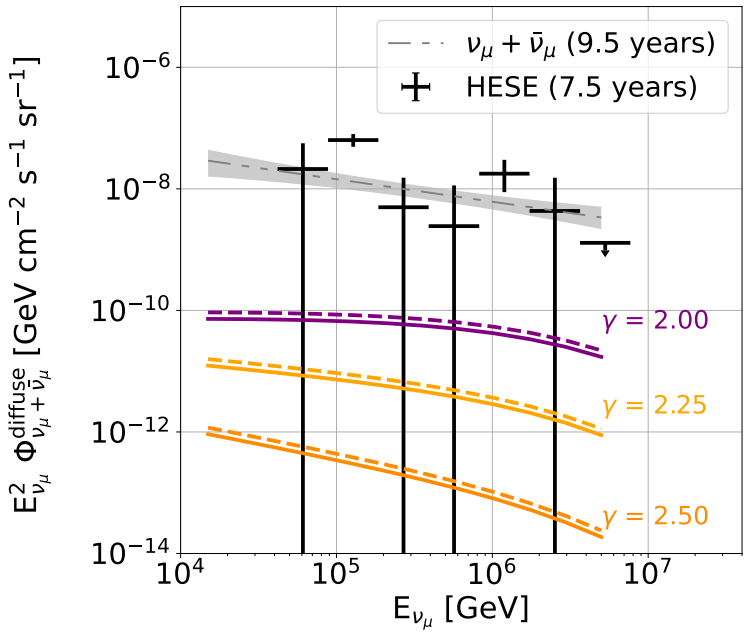

FIGURE 3.9: The diffuse starburst-driven muon-neutrino flux expected from 229 galaxies in GOALS for spectral indices $\gamma_{\text{SN}} = 4.00$, $\gamma_{\text{SN}} = 4.25$, and $\gamma_{\text{SN}} = 4.50$. Note that $\gamma = \gamma_{\text{SN}} - 2$. Per spectral index, the diffuse flux is shown with and without correcting the IR luminosity for AGN activity (solid and dashed lines, respectively). The black data points are the IceCube measurements using the high-energy starting event (HESE) sample [6]. The gray band is the best-fit unbroken power-law spectrum of astrophysical muon neutrinos observed by IceCube in the Northern Hemisphere [312].

However, not only GOALS U/LIRGs in the nearby Universe can contribute to the diffuse neutrino flux, but also the U/LIRGs at higher redshifts. This is expected as the number density of U/LIRGs strongly increases with redshift (see Section 2.1.3). As such, certain combinations of parameter values could still violate the IceCube flux when integrating the U/LIRG contribution over cosmic history. This is discussed in next section.

3.4 Diffuse Flux from the LIRG & ULIRG Populations

In this section, we extend our focus beyond local LIRGs and ULIRGs to estimate the diffuse starburst-driven neutrino flux produced by these two populations separately.

To derive the diffuse high-energy neutrino flux from a cosmologically distributed source population, we follow the methodology described in [17, 18]. We first outline this methodology and then apply it to our specific case. The conventions for flux and luminosity, as well as the relationships between observables used in this calculation, are detailed in Appendix A.

3.4.1 Methodology

Assuming that the total differential energy generation rate of CRs in the population at $z = 0$ is given by $(E_{\rm CR}\mathcal{Q}_{E_{\rm CR}})_{z=0}$, typically expressed in $\mathrm{erg\,Mpc^{-3}\,yr^{-1}}$, the corresponding differential all-flavor energy generation rate of neutrinos, with the same units, can be written as

$$E_\nu \mathcal{Q}_{\nu+\bar{\nu}} \approx \mathcal{E}\,\min[1, f_\pi]\,(E_{\rm CR}\mathcal{Q}_{E_{\rm CR}})_{z=0}\ . \tag{3.29}$$

The parameter f_π represents the energy-dependent meson production efficiency, also known as the effective optical depth. The parameter $\mathcal{E}$ describes the fraction of meson energy transferred to neutrinos in these interactions and is given by,

$$\mathcal{E} = \frac{3K_\pi}{4(1+K_\pi)}\ . \tag{3.30}$$

Here, K_π is the charged-to-neutral pion ratio, which takes values of $K_\pi \approx 2$ for pp interactions and $K_\pi \approx 1$ for pγ interactions (see Section 1.2). The factor $K_\pi/(1+K_\pi)$ represents the fractional energy carried by charged pions, while the factor $3/4$ accounts for the fraction of neutrino energy in the total decay products of the charged pion decay chain.

To convert the differential neutrino energy generation rate at the source into the diffuse neutrino flux observed at Earth, we begin by averaging the differential energy generation rate in Eq. (3.29) over a Hubble time, $t_{\rm H} = H_0^{-1}$. Multiplying this time-averaged rate by $c/(4\pi)$ yields the corresponding diffuse neutrino flux at Earth. Due to neutrino oscillations over cosmological distances, the flux becomes approximately equally distributed among the three neutrino flavors (see Section 1.4.2). Therefore, the flux per neutrino flavor is obtained by applying an additional factor of $1/3$.

Finally, to account for the cumulative neutrino flux from the source population up to redshift z, we include the redshift-dependent factor ξ_z, which integrates the source luminosity function up to z.

Taking all these factors into account, the final expression for the scaled, per-flavor neutrino flux is given by

$$E_{\nu_\ell}^2 \Phi_{\nu_\ell+\bar{\nu}_\ell} \approx \frac{1}{3}\xi_z t_H \frac{c}{4\pi}\mathcal{E}\,\min[1, f_\pi]\,(E_{\rm CR}\mathcal{Q}_{E_{\rm CR}})_{z=0}\,, \tag{3.31}$$

where $\ell \in \{e, \mu, \tau\}$ denotes the neutrino flavor. The energy-squared weighted flux expected at Earth is typically expressed in units of $\mathrm{GeV\,cm^{-2}\,s^{-1}\,sr^{-1}}$.

Note that this approach assumes that all sources are standard candles with similar physical conditions for high-energy neutrino production.

In the following sections, we first estimate the differential energy generation rate for LIRGs and ULIRGs at $z = 0$, denoted as $(E_{\rm CR}\mathcal{Q}_{E_{\rm CR}})_{z=0}$, based on their IR luminosity. Next, we discuss the meson production efficiency, f_π, which governs part of the conversion of the CR into neutrino energy. Subsequently, we discuss how to extrapolate this budget to estimate the diffuse neutrino flux up to a given redshift z by incorporating the redshift evolution parameter ξ_z.

Local cosmic-ray generation rate

We assume that CRs are injected in LIRGs and ULIRGs following a power-law energy distribution, $E_{\rm CR}^{-\gamma}$. The differential energy generation rate of CRs, typically expressed in units of $\mathrm{erg\,Mpc^{-3}\,yr^{-1}}$, then scales as

$$E_{\rm CR}\mathcal{Q}_{E_{\rm CR}} \propto E_{\rm CR}^{2-\gamma}, \tag{3.32}$$

where the proportionality is determined by an energy-independent normalization constant. This expression is assumed to hold within the energy range $E_{\rm min} \leq E_{\rm CR} \leq E_{\rm max}$. Then, the total CR energy generation rate, also expressed in $\mathrm{erg\,Mpc^{-3}\,yr^{-1}}$, is per definition given by

$$\mathcal{Q}_{\rm CR} = \int_{E_{\rm min}}^{E_{\rm max}} \mathcal{Q}_{E_{\rm CR}}\,\mathrm{d}E_{\rm CR}. \tag{3.33}$$

The parameter $\mathcal{Q}_{\rm CR}$ is related to $E_{\rm CR}\mathcal{Q}_{E_{\rm CR}}$ by the factor $R(E_{\rm CR}, \gamma, E_{\rm min}, E_{\rm max})$, given by

$$R \equiv \frac{\mathcal{Q}_{\rm CR}}{E_{\rm CR}\mathcal{Q}_{E_{\rm CR}}} = \begin{cases} \dfrac{E_{\rm min}^{-\gamma+2} - E_{\rm max}^{-\gamma+2}}{\gamma - 2} E_{\rm CR}^{\gamma-2}, & \gamma \neq 2, \\ \ln\left(\dfrac{E_{\rm max}}{E_{\rm min}}\right), & \gamma = 2\,, \end{cases} \tag{3.34}$$

as detailed in Appendix A. The parameters $E_{\rm max}$ and $E_{\rm min}$ correspond to the maximum and minimum energies attainable in astrophysical accelerators, such as supernova shocks. Further details on R can be found in [18].

For $\gamma = 2$, the quantity R is independent of energy. Assuming $E_{\rm min} = 10$ GeV and $E_{\rm max} = 10^{11}$ GeV, which spans the observed energy spectrum of CRs from beyond the Solar System (see Chapter 1), we find $R \approx 23$. If, for instance, $\gamma = 2.2$, we obtain $R \approx 200$ at $E = 100$ PeV.

From Eq. (3.34), it follows that $\mathcal{Q}_{\rm CR}$ is required to determine $E_{\rm CR}\mathcal{Q}_{E_{\rm CR}}$ at redshift $z = 0$. To achieve this, we make the key assumption that a constant fraction $\eta_{\rm tot}$ of the total IR luminosity is converted into CR luminosity,

$$\mathcal{Q}_{\rm CR} = \eta_{\rm tot}\mathcal{Q}_{\rm IR}, \tag{3.35}$$

where $\mathcal{Q}_{\rm IR}$ is the total IR energy generation rate of local LIRGs or ULIRGs. Substituting Eq. (3.35) into Eq. (3.34) then yields

$$E_{\rm CR}\mathcal{Q}_{E_{\rm CR}} = \frac{\eta_{\rm tot}\mathcal{Q}_{\rm IR}}{R}. \tag{3.36}$$

We determine $\mathcal{Q}_{\rm IR}$ by summing the IR luminosities of a representative local sample of IR sources and dividing by the spherical volume, $V_{\rm local}$, defined by the luminosity

distance to the most distant LIRG or ULIRG in the local sample, $D_{L,\mathrm{local}}$. As such,

$$\mathcal{Q}_{\mathrm{IR}} = \frac{\sum_{i=1}^{N} L_{\mathrm{IR},i}}{V_{\mathrm{local}}} = \left(\frac{4\pi D_{L,\mathrm{local}}^3}{3}\right)^{-1} \sum_{i=1}^{N} L_{\mathrm{IR},i}. \tag{3.37}$$

Here N denotes the number of LIRGs or ULIRGs in the sample, each with IR luminosity $L_{\mathrm{IR},i}$.

In conclusion, the differential CR generation rate at $z = 0$, denoted as $(E_{\mathrm{CR}}\mathcal{Q}_{E_{\mathrm{CR}}})_{z=0}$, can be computed for a representative sample of N local LIRGs or ULIRGs as:

$$(E_{\mathrm{CR}}\mathcal{Q}_{E_{\mathrm{CR}}})_{z=0} = \frac{3\eta_{\mathrm{tot}}}{4\pi R} \cdot D_{L,\mathrm{local}}^{-3} \cdot \sum_{i}^{N} L_{\mathrm{IR},i}\ . \tag{3.38}$$

The parameter n_{tot} determines the fraction of IR luminosity converted into CR luminosity, the factor $R(E_{\mathrm{CR}}, \gamma, E_{\mathrm{min}}, E_{\mathrm{max}})$ as defined in Eq. (3.34), and $D_{L,\mathrm{local}}$ the luminosity to the most distant source in the local representative LIRG or ULIRG sample under consideration.

Meson production efficiency

Only a fraction of the CRs injected into the U/LIRGs interact to produce secondary particles, such as high-energy neutrinos. The efficiency of this conversion is quantified by the meson production efficiency, f_π, which is different for pp and pγ-interactions.

In the framework developed in this chapter, and now applied in this diffuse flux prediction, we consider only pp-interactions. Then, the meson production efficiency is generally defined as

$$f_\pi \approx \zeta \sigma_{\mathrm{pp}} n c t_{\mathrm{int}}, \tag{3.39}$$

with c representing the speed of light, $\zeta \approx 0.5$ the inelasticity of the collision, σ_{pp} the cross section for inelastic pp-collisions (see Section 3.1.3), n the average particle density in the nuclear region of the U/LIRG, and t_{int} the interaction timescale. The latter is defined as the minimum between the CR injection timescale, t_{inj}, and the escape timescale of CRs t_{esc}, such that

$$t_{\mathrm{int}} \approx \min[t_{\mathrm{esc}}, t_{\mathrm{inj}}] \quad \text{with} \quad t_{\mathrm{esc}}^{-1} = \sum_i t_i^{-1}\ .$$

The sum extends over the timescales t_i associated with all processes that contribute to CR losses without producing secondary particles.

Using the parameters from Table 3.3, which reflect model inputs informed by the case study of the LIRG Arp 299, we find that the meson production efficiency satisfies $f_\pi > 1$ for CR energies relevant to the production of high-energy neutrinos detectable by IceCube. However, if CRs encounter a significantly lower target density than assumed—e.g., $n = 100\ \mathrm{cm}^{-3}$, typical of non-ULIRG starburst regions (see Section 3.1.3) instead of $n = 1000\ \mathrm{cm}^{-3}$—then the meson production efficiency decreases to $f_\pi \approx 0.3 - 0.4$ over the same energy range. This underscores the importance of better constraining the average target density sampled by CRs in astrophysical environments.

As shown in Appendix B, the meson production efficiency f_π for pp-interactions in the regime $t_{\rm esc} < t_{\rm inj}$ is directly related to the parameter $\mathcal{C}_{\rm pp}$, introduced in Section 3.1.3, which quantifies the calorimetric conditions in the starburst region.

Redshift evolution

The redshift evolution factor, ξ_z, effectively integrates the luminosity function of a source class up to redshift z (e.g., [88, 89, 227]). This allows to extrapolate the contribution of a sample of nearby sources to a contribution of the entire population up to a given redshift.

For a neutrino emission spectrum following an unbroken power-law, $\Phi_{\nu+\bar{\nu}} \propto E^{-\gamma}$, this factor becomes energy-independent and is expressed as (see e.g. [227, 313] for a detailed derivation)

$$\xi_z = \xi(z,\gamma) = \int_0^z \frac{{\rm d}z'}{\sqrt{\Omega_m(1+z')^3+\Omega_\Lambda}} \mathcal{H}(z')(1+z')^{-\gamma}, \tag{3.40}$$

where Ω_m and Ω_Λ denote the matter and dark energy density parameters, respectively, and $\mathcal{H}(z')$ represents the redshift evolution parametrization of the source class under investigation. A more detailed discussion of $\mathcal{H}(z')$ is presented in Section 2.1.3.

Figure 3.10 illustrates $\xi(z,\gamma)$ for spectral indices $\gamma = 2$ and $\gamma = 3$, following different evolutionary scenarios: ULIRG evolution, star-formation rate evolution, and a flat evolution model where $\mathcal{H}_{\rm flat} = 1$. In this work, we assume that LIRGs and ULIRGs exhibit similar redshift evolution, i.e., $\mathcal{H}_{\rm LIRG} \approx \mathcal{H}_{\rm ULIRG}$, as motivated by the density comparison shown in Figure 2.6.

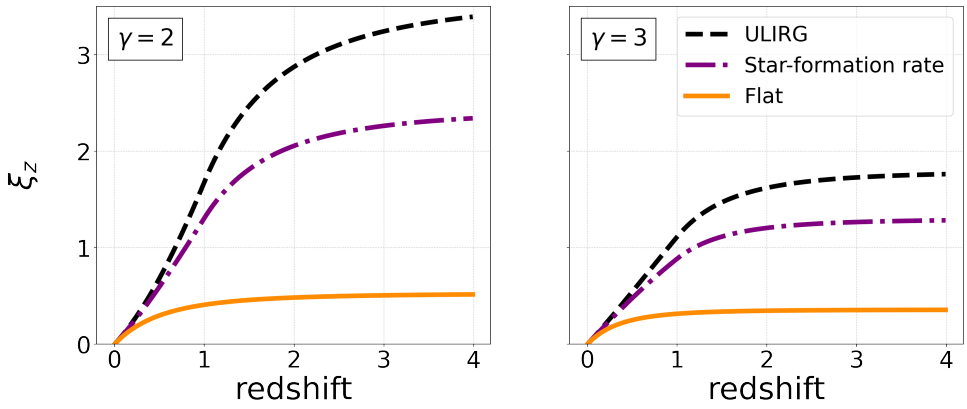

FIGURE 3.10: Redshift evolution parameter $\xi(z,\gamma)$ as a function of redshift for different evolution scenarios: ULIRGs, the star formation rate, and a flat evolution. The left panel assumes a spectral index of $\gamma = 2$, while the right panel assumes a spectral index of $\gamma = 3$.

3.4.2 Diffuse flux predictions

Below we estimate the expected diffuse starburst-driven neutrino flux from the ULIRG and LIRG populations using Eq. (3.31) in tandem with the framework developed in this chapter.

ULIRG population

Since observatories have limited sensitivity, sources below a certain flux threshold may remain undetected. In this context, we consider a complete, volume-limited sample

that includes all sources within a distance beyond which such faint sources are expected to be missed.

To estimate the total IR luminosity generation rate of local ULIRGs, denoted by $\mathcal{Q}_{\rm IR}$, we adopt the volume-limited sample of 75 ULIRGs within $z \leq 0.13$, as defined in the IceCube Collaboration's search for high-energy neutrinos from ULIRGs [150, 313]. This yields an estimate of $\mathcal{Q}_{\rm IR} \approx 1.3 \times 10^{46}\,\mathrm{erg\,Mpc^{-3}\,yr^{-1}}$. To convert this estimate into the corresponding differential CR energy generation rate, $E_{\rm CR}\mathcal{Q}_{\rm CR}$ through Eq. (3.36), we need the following parameters:

- The efficiency parameter $\boldsymbol{\eta_{\rm tot}}$, which quantifies the conversion of IR luminosity into CR luminosity. In our model developed in this chapter, this conversion follows Eq. (3.8), which relates the CR luminosity of supernovae to the galaxy's IR luminosity via the supernova rate. We assume typical values: $\eta_{\rm SN} = 0.10$ (supernova explosion efficiency for particle acceleration), $E_{\rm SN} = 10^{51}$ erg (energy output per supernova), and $\Lambda_{\rm IR} = 5.97 \times 10^{-46}$ (scaling factor between IR luminosity and supernova rate). Using these, we find that approximately $\eta_{\rm tot} \approx 0.18\%$ of a ULIRG's total IR luminosity is converted into supernova-driven CR luminosity, assuming our model.

- The conversion parameter $\boldsymbol{R}$, which depends on the CR energy range, characterized by an unknown minimum energy $E_{\rm min}$ and maximum energy $E_{\rm max}$ for ULIRGs, and the spectral index γ of the injected CR spectrum.

  Since about 5% of the CR energy is transferred to neutrinos in pp-interactions, and IceCube observes high-energy neutrinos in the range $\sim$1 TeV to $\sim$1 PeV, we adopt $E_{\rm min} = 20$ TeV and $E_{\rm max} = 20$ PeV. For a spectral index $\gamma = 2$, this yields $R \approx 7$.

To extrapolate the contribution of these local ULIRGs, we integrate the ULIRG population up to redshift $z = 4$, consistent with previous works [150, 227]. Figure 3.10 shows that for $\gamma = 2$ and $\gamma = 3$ the corresponding factors are $\xi_z = 3.4$ and $\xi_z = 1.8$, respectively.

Assuming a CR spectral index of $\gamma = 2$, which also applies to the resulting high-energy neutrino spectrum, and adopting a maximum meson production efficiency of $f_\pi = 1$ (reasonable given the high nuclear particle densities observed in ULIRGs), we estimate the single-flavor neutrino flux from the ULIRG population, scaled by energy squared, as

$$E_{\nu_\mu}^2 \Phi_{\nu_\mu+\bar{\nu}_\mu} \approx 1 \cdot 10^{-9} \times \left(\frac{\xi_z}{3.4}\right)\left(\frac{7}{R}\right)\left(\frac{f_\pi}{1}\right)\left(\frac{\eta_{\rm tot}}{0.0018}\right)\left(\frac{\mathcal{Q}_{\rm IR}}{10^{46.11}\,\mathrm{erg\,s^{-1}\,Mpc^{-3}}}\right)\frac{\mathrm{GeV}}{\mathrm{cm^2\,s\,sr}}.$$

This flux lies well below the Waxman-Bahcall bound introduced in Section 1.5.1. Furthermore, the prediction is of the order of the 90% confidence level upper limit on high-energy neutrino emission from the ULIRG population set by the IceCube Collaboration for a spectral index $\gamma = 2$, $E_{\nu_\mu}^2 \Phi_{\nu_\mu+\bar{\nu}_\mu} \approx 4 \cdot 10^{-9}\,\mathrm{GeV\,cm^{-2}\,s^{-1}\,sr^{-1}}$ ([150], see also Figure 2.7).

If the efficiency of converting supernova kinetic energy into particle acceleration is four to five times higher ($\eta_{\rm SN} \approx 0.4{-}0.5$), which is not excluded, the predicted starburst-driven neutrino flux would well exceed IceCube's upper limit. Extending the CR energy range injected into ULIRGs, however, increases R, lowering the energy density. Furthermore, if the meson production efficiency in pp-interactions is lower

than assumed, it is also unlikely that high-energy neutrino emission would surpass the current limit. Given these uncertainties, constraining model parameters remains challenging. In any case, this prediction indicates that if the model described in this chapter is the dominant high-energy neutrino production mechanism in ULIRGs, they cannot account for the entirety of the observed IceCube flux.

LIRG population

First, we require a complete, volume-limited sub-sample of local LIRGs. However, since this is the first targeted extrapolation of the LIRG population, we cannot rely on an existing sample, as was done for the ULIRGs. Below, we outline the methodology adopted in this work to construct such a sample, following the approach used for the ULIRG population [150, 313].

- **Volume-limited sample:** GOALS is a subsample of the IRAS Revised Bright Galaxy Sample (RBGS [235]; see also Section 2.3.1) and is therefore a complete flux-limited sample of galaxies with an IRAS 60-μm flux density of $S_{60\mu\mathrm{m,IRAS}} > 5.24$ Jy. However, GOALS is not a complete volume-limited sample, as suggested by Figure 2.8.

  To define a representative sample of local LIRGs, we first estimate the distance up to which the least luminous LIRGs (i.e. $L_{\mathrm{IR}} = 10^{11} L_{\odot}$) can be detected with the RBGS sensitivity at 60 μm, i.e. $S_{60\mu\mathrm{m,IRAS}} = 5.24$ Jy. To do so, a fit is performed to the observed correlation between $S_{60\mu\mathrm{m,IRAS}}$ and the total IR flux, $F_{\mathrm{IR}} = L_{\mathrm{IR}}/4\pi D_L^2$ for all GOALS LIRGs. The fit is of the form

$$\log_{10}\left(\frac{S_{60\mu\mathrm{m,IRAS}}}{\mathrm{Jy}}\right) = a\log_{10}\left(\frac{F_{\mathrm{IR}}}{\mathrm{W\ m^{-2}}}\right) + b\,, \tag{3.41}$$

  with best-fit parameters $a = 1.00 \pm 0.01$ and $b = 13.01 \pm 0.08$. Given these parameters, the distance corresponding to $L_{\mathrm{IR}} = 10^{11} L_{\odot}$ and $S_{60\mu\mathrm{m,IRAS}} = 5.24$ Jy is found by inverting Eq. (3.41). Doing so, we find $D_L \approx 80$ Mpc. In this work, we opt for a conservative value of $D_L = 75$ Mpc which corresponds to $z = 0.0167$. As such, the 62 LIRGs within this redshift define the local sample of LIRGs used to estimate the diffuse neutrino flux from the total LIRG population.

We define the GOALS LIRGs within $z < 0.0176$ as a complete, volume-limited sub-sample consisting of 62 LIRGs. This subset is assumed to be representative of the broader LIRG population,. The total IR generation rate for this representative sample is $\mathcal{Q}_{\mathrm{IR}} \approx 6 \times 10^{47}\ \mathrm{erg\,Mpc^{-3}\,yr^{-1}}$. Assuming the same parameter values as for ULIRGs, we estimate the energy-squared scaled single-flavor neutrino flux from the LIRG population as,

$$E_{\nu_\mu}^2 \Phi_{\nu_\mu+\bar{\nu}_\mu} \approx 7 \cdot 10^{-8} \times \left(\frac{\xi_z}{3.4}\right)\left(\frac{7}{R}\right)\left(\frac{f_\pi}{1}\right)\left(\frac{\eta_{\mathrm{tot}}}{0.0018}\right)\left(\frac{\mathcal{Q}_{\mathrm{IR}}}{10^{47.77}\ \mathrm{erg\ s^{-1}\ Mpc^{-3}}}\right)\frac{\mathrm{GeV}}{\mathrm{cm^2\ s\ sr}}.$$

This prediction is of the order of the Waxman-Bahcall bound. The discrepancy grows if the kinetic energy transfer efficiency for particle acceleration is higher ($\eta_{\mathrm{SN}} > 0.1$). However, as with ULIRGs, extending the CR energy range increases R, reducing the predicted flux. Furthermore, LIRGs span a wide range of physical conditions (Section 2.1.1), and as such, their nuclear particle densities may be significantly lower.

This could significantly reduce the average pp-interaction optical depth compared to that in ULIRGs, potentially resulting in a much lower meson production efficiency f_π, and consequently, a suppressed diffuse high-energy neutrino flux.

It is concluded that if all LIRGs efficiently produce high-energy neutrinos through the framework developed in this chapter, then, under reasonable assumptions, steady starburst-driven neutrino emission in LIRGs could make a significant contribution to the high-energy neutrino flux observed by IceCube.

3.4.3 Tension with the gamma-ray sky

The pp-interactions that produce the high-energy neutrino flux expected from the LIRG and ULIRG populations simultaneously generate a corresponding gamma-ray flux via pion decay (see Section 1.2). Therefore, any diffuse neutrino flux prediction must be consistent with the extragalactic gamma-ray background (EGB) observed by *Fermi*-LAT [94]. More specifically, since blazars contribute approximately 86% of the EGB [314], their contribution should be subtracted from the total EGB, as previous analyses have (strongly) constrained the Fermi-blazar fraction of the IceCube neutrino flux [141].

After accounting for this, it has been argued that a generic CR calorimeter scenario implies a tension between the IceCube neutrino flux and the $\sim 14\%$ non-blazar EGB in the 0.05–1 TeV range ([142]; see Section 1.5.2). Since this calorimeter model is broadly applicable to any population producing high-energy neutrinos through hadronuclear interactions optically thin to gamma rays in the *Fermi*-LAT energy range, our starburst-driven diffuse neutrino flux prediction for LIRGs, which approaches the level of the observed diffuse IceCube flux, is also likely in tension with the non-blazar EGB.

Reducing this tension requires invoking spectral indices $\gamma > 2$ and/or infrared conversion efficiencies $\eta_{\rm tot} < 0.1\%$, which lower the predicted flux below the observed IceCube level. Consequently, the parameter space of the framework developed in this chapter is constrained by the non-blazar EGB limit.

It should be noted, however, that our estimate of the diffuse high-energy neutrino flux of LIRGs assumes that LIRGs are standard candle neutrino sources, a simplification unlikely to capture the diversity of physical conditions among LIRGs. Accounting for individual source variations could significantly impact neutrino flux predictions, as discussed in Section 3.3.2. Additionally, at $z \sim 0$, an IR luminosity threshold of $L_{\rm IR} > 10^{11} L_\odot$ primarily selects merger-driven starbursts. In contrast, at $z \sim 1$–2, when star formation rates were much higher, galaxies with $L_{\rm IR} > 10^{11} L_\odot$ are more frequently non-merging systems (e.g., [315]; see also Section 2.1). The evolving physical conditions with redshift may imply a redshift dependent neutrino production efficiency in starburst systems, necessitating further investigation to refine extrapolation results. A novel approach that would allow the standard candle assumption to be dropped is to embed the model developed here in cosmological hydrodynamical simulations such as SIMBA [25]. We outline this approach in Section 3.6.

Finally, we note that our extrapolation considers only starburst-driven neutrino production, despite evidence that some GOALS LIRGs host obscured AGN. Such AGN are promising neutrino sources due to their location in dense, dusty regions where significant gamma-ray attenuation is possible, as proven by NGC 1068 [16, 144]. Obscured AGNs could help reconcile the IceCube diffuse neutrino flux with the non-blazar EGB observed by *Fermi*-LAT. Particularly relevant are LIRGs with compact obscured nuclei (CONs), among the most heavily enshrouded regions known (Section 2.1.2).

Therefore, incorporating AGN-driven neutrino production into the extrapolation is essential for accurately constraining the model's parameter space and quantifying the contribution of U/LIRGs to the diffuse high-energy neutrino flux.

3.5 Lessons Learned

The extreme IR emission from U/LIRGs traces obscured star formation and AGN activity, both of which create favorable conditions for high-energy neutrino production. In this chapter, we present the first investigation of high-energy neutrino emission from GOALS, a multi-wavelength survey targeting the brightest U/LIRGs in the sky. To achieve this, we developed a starburst-driven neutrino production framework, motivated by the fact that local U/LIRGs are predominantly powered by starburst activity. This framework models high-energy neutrino emission at the level of individual galaxies within U/LIRG systems. Using AGN-corrected IR luminosities per galaxy—derived from Herschel Space Observatory data—we estimate each galaxy's CR luminosity. The total neutrino flux from a U/LIRG is then determined by modeling CR propagation and interactions within the nuclear region.

Eight source-specific parameters are identified as necessary to compute the expected starburst-driven neutrino flux per galaxy. Each parameter has been discussed in the context of local U/LIRGs. Particularly, this study qualitatively suggests that U/LIRGs are likely more efficient at converting high-energy protons into high-energy neutrinos compared to non-U/LIRG starburst galaxies.

We applied this framework to:

- Estimate the expected neutrino flux generated by the nuclear starburst region in the well-observed LIRG NGC 3690. We used source-specific electromagnetic data where possible. Our case study concluded that neutrino flux predictions are most sensitive to the CR injection spectral index and the maximum CR energy achieved through supernova acceleration. These parameters should be prioritized in future modeling and experimental studies. The model predicts that, even in the most optimistic scenarios, the starburst-driven neutrino flux for NGC 3690 is one to two orders of magnitude below IceCube's current sensitivity for a source at its declination, thus remaining consistent with IceCube observations. However, since the predictions are only one order of magnitude below current sensitivity, future observatories such as IceCube-Gen2 may probe the flux in optimistic cases.

- Estimate the diffuse starburst-driven neutrino flux from the GOALS sample across different spectral indices. These predictions are orders of magnitude smaller than the diffuse neutrino flux observed by IceCube. Given the positive redshift evolution of U/LIRGs, we also estimated the cumulative neutrino flux from the entire LIRG and ULIRG populations throughout cosmic history. Assuming GOALS LIRGs are standard-candle emitters, we find that CR spectral indices $\gamma > 2$ and/or IR conversion efficiencies $\eta_{\rm tot} < 0.1\%$ are needed to avoid conflict with the non-blazar extragalactic gamma-ray background observed by *Fermi*-LAT. However, we argued that the standard candle assumption is likely unrealistic due to the diverse physical conditions observed in LIRGs. Future efforts should focus on embedding models as the one developed in this chapter into cosmological hydrodynamical simulations, which would allow to omit the standard-candle assumptions. We elaborate on this in Section 3.6.

- Estimate the starburst-driven neutrino flux from NGC 1068. This prediction was compared to the recently reported evidence of high-energy neutrino emission from NGC 1068 by IceCube. Our model predicts a flux significantly below that reported by IceCube, suggesting that neutrino production in NGC 1068 is likely dominated by mechanisms other than supernova-driven activity discussed in this chapter.

3.6 Cosmological Hydrodynamical Simulations & Neutrinos

In Section 3.4, we presented an analytical method for extrapolating high-energy flux predictions from a local sample of candidate neutrino sources to the full cosmic population. This commonly used approach relies on the key assumption that all sources exhibit similar high-energy neutrino production characteristics, an assumption often referred to as the standard candle approximation. However, as discussed in Section 3.4.3, this assumption is unlikely to hold for U/LIRGs.

A more realistic estimate of the contribution of candidate source populations to the diffuse high-energy neutrino flux can be achieved using large-volume hydrodynamical simulations of the Universe. These simulations, which model the co-evolution of galaxies, black holes, and intergalactic gas, offer a dynamic and self-consistent framework for studying cosmic structure formation.

By embedding high-energy neutrino production models—such as the one developed in this chapter—into cosmological simulations, it becomes possible to move beyond the standard-candle assumption. These simulations provide source-specific information for galaxies across cosmic time, enabling the study of how the evolving properties of individual sources impact high-energy neutrino production, an aspect not currently accessible through analytical approaches.

In particular, integrating the model developed in this chapter with hydrodynamical simulations enables predictions based on intrinsic physical properties, such as star formation and starburst activity, rather than relying on generalized characteristics derived from astronomical classifications.

As an outlook for future work, we highlight the ongoing integration of our high-energy neutrino production framework with the cosmological hydrodynamical code SIMBA [25], marking a significant step toward a more comprehensive and physically grounded prediction of the diffuse high-energy neutrino flux.

3.6.1 Embedding high-energy neutrinos in SIMBA

Among the state-of-the-art cosmological hydrodynamical simulations, SIMBA stands out for its large volume of $(100\ \mathrm{Mpc}/h)^3$ and its sophisticated implementation of star formation-driven winds, calibrated using higher-resolution simulations.[6] This calibration enables SIMBA to successfully reproduce key observables of the galaxy population, such as the stellar mass function at $z = 0$ and the star formation main sequence over cosmic time [25].

Figure 3.11 shows the temperature profiles from SIMBA at two different redshifts, highlighting the impact of feedback processes and the simulation's dynamic evolution. These capabilities make SIMBA a powerful tool for modeling the evolution of star formation and AGN activity across the full diversity of galaxies throughout cosmic history.

[6] simba.roe.ac.uk/

SIBMA is a software package built upon the hydrodynamical code GIZMO, which solves the equations of hydrodynamics and incorporates a gravity solver derived from GADGET-3 [25]. The software includes implementations of AGN feedback and a unique star formation wind model, calibrated using high-resolution simulations that more accurately capture the energy input from stellar radiation, winds, and supernovae. These features enable the dynamic evolution of gas and dark matter *particles* across cosmic time within a cosmological-scale simulation volume. At various redshifts during this evolution, galaxies and halos are identified in post-processing using the Caesar package.[7] This procedure produces a single galaxy catalog per redshift, containing comprehensive information on galaxies and halos, with many key properties precomputed.

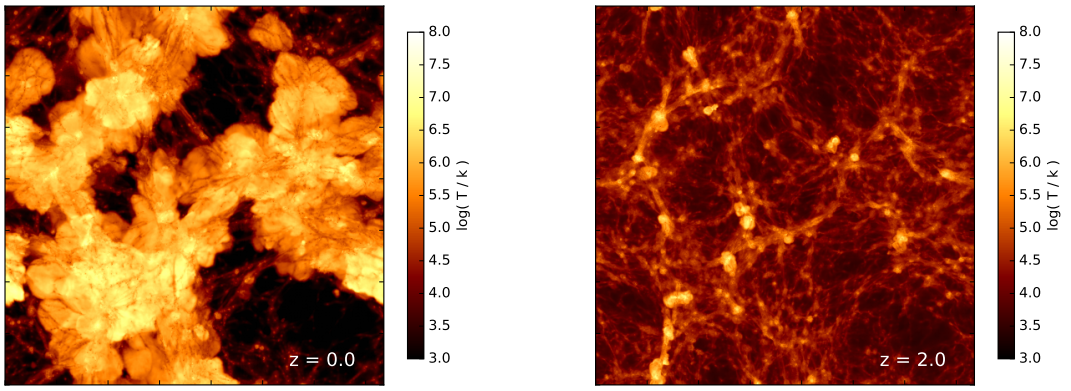

FIGURE 3.11: Temperature profiles at redshifts z=0 (left) and z=2 (right) for a random slice of 10 Mpc/h in a 50 Mpc/h SIMBA volume. At z=2 there are a few energetic bi-polar outflows visible, while at z=0 high-speed AGN outflows have shocked the intergalactic medium. Taken from [25].

For our analysis regarding high-energy neutrino production, we make use of the publicly available *Flagship Simulation Run*[8], which provides 151 snapshots spanning redshifts from $z = 20$ to $z = 0$ and as such 151 galaxy catalogs. Our primary focus thus far has been on extracting the parameters required for the high-energy neutrino production framework introduced in this chapter (see Eq. 3.25), as well as on developing the associated computational tools.

Specifically, for all galaxies at each of the 151 snapshots obtained from the *Flagship Simulation Run*, we treat the quantities required by our model as follows:

- **Supernova rate** ($\mathcal{R}_{\rm SN}$): The star-formation rate for each galaxy is directly obtained from the precomputed properties available in the galaxy catalogs. To estimate the corresponding core-collapse supernova rate, we assume that for every solar mass of stars formed, 0.01 stars with masses exceeding $8\,M_\odot$ are produced. All such massive stars are presumed to undergo core-collapse supernovae. This conversion factor is derived from a Chabrier initial mass function and is consistent with the value adopted internally in the SIMBA simulation for computing supernova rates and associated feedback processes [25, 316].

- **Advection wind speed** ($v_{\rm adv}$): Although the galaxy catalogs obtained through Caesar do not directly provide the wind speed of galactic-scale outflows, they

[7] caesar.readthedocs.io/en/latest
[8] simba.roe.ac.uk/simdata/m100n1024/s50/catalogs/

contain all the necessary properties to compute it using appropriate scaling relations. A follow-up study of this work presents a detailed discussion of the relevant scaling relations and a computational tool for calculating wind speeds [26]. Below, we provide a brief overview of the procedure used to estimate final wind speeds.

The idea is that the starburst-driven galactic wind speed scales with the galaxy's circular velocity, which is itself related to the baryonic mass via the baryonic Tully-Fisher relation [317]. However, because the wind speed and circular velocity scaling was originally derived from higher-resolution simulations, a correction must be applied to account for the resolution and physical modeling of the SIMBA simulation. This correction introduces additional dependencies on the virial radius and circular velocity of the parent halo, as well as on the stellar half-mass radius of the galaxy. Full derivations and justifications for this correction are provided in the aforementioned follow-up work [26].

In summary, SIMBA enables the estimation of galactic-scale, starburst-driven wind speeds per galaxy by combining the galaxy's baryonic mass and stellar half-mass radius with the circular velocity and virial radius of its parent halo. All of these quantities are available from the post-processed galaxy catalogs of the *Flagship Simulation Run* produced with SIMBA. It is important to note that this calculation is only applicable to star-forming galaxies, as quenched systems are not expected to host significant starburst-driven winds.

- **Volume particle density and scale height** (n & $H_{\rm SBR}$): In principle, the subatomic particle volume density in the central regions of galaxies can be derived from the raw simulation data at each redshift, and is expected to be reliable down to $\sim$ 1000 pc. Although this is larger than the $\sim$ 100 pc characteristic of starburst regions considered in our neutrino production framework, it still serves as a useful approximation. However, the technical framework to perform this extraction is still under development.

  As a workaround, we consider a set of representative cases. First, we assume fixed volume densities—e.g., $n = 100$ cm^{-3} and $n = 1000$ cm^{-3}, where the former is typical for the most nearby starburst galaxies such as M82, and the latter is more characteristic of U/LIRGs (see Figure 3.2). For these cases, we fix the vertical scale height of the nuclear disk at 150 pc, consistent with assumptions adopted throughout this work.

  In the second approach, we consider the inferred volume densities from the derivable star formation rate surface density. The star formation rate surface density, $\Sigma_{\rm SFR}$ (in $M_\odot$ yr^{-1} pc^{-2}), and the gas surface density of the same system, $\Sigma_{\rm gas}$ (in g pc^{-2}), are empirically related through a form of the Kennicutt–Schmidt law [59]: $\Sigma_{\rm SFR} \propto (\Sigma_{\rm gas})^n$. Given an assumed geometry for the nuclear region, this relation enables an estimate of the corresponding volume density in the central region (e.g. [274]).

- **Magnetic field strength** (B) The magnetic field strength in the central starburst region is currently the only structural parameter yet to be extracted, most likely also via scaling relations.

  For the model considered in this work, the magnetic field strength does not significantly affect neutrino flux predictions, provided that the nuclear volume density is sufficiently high. Assuming that cosmic rays sample the average nuclear volume density, U/LIRGs are expected to satisfy this condition (see Section

3.1.3). However, the simulations may include systems with substantially lower volume densities. Therefore, a range of magnetic field strengths should be explored.

- **Spectral index and maximum momentum** (γ & $p_{\rm max}$): The remaining source parameters pertain to the cosmic-ray injection spectrum and can be either varied or fitted to the observed diffuse high-energy neutrino flux. Notably, the spectral index of each galaxy's injection spectrum can, in principle, be freely adjusted within the simulation framework. This is usually not possible in analytic approaches, although some variation can be introduced [275].

- **Luminosity distance** (D_L): The luminosity distance for each galaxy is computed directly from its redshift using the cosmological parameters specific to the simulation, including the Hubble constant and the cosmological density parameters.

By combining the outputs of the SIMBA simulations at various redshifts with the model developed in this work, we will be able to compute the high-energy neutrino luminosity arising from supernova-driven activity across a broad range of cosmic time. This luminosity can be further converted into the corresponding diffuse high-energy neutrino flux expected at Earth. This approach is particularly promising, as it captures the diversity of physical conditions in starburst galaxies—currently a major source of uncertainty in predicting the diffuse high-energy neutrino flux from such environments. Comparing the predicted flux with the observed diffuse flux measured by IceCube allows us to constrain free parameters in the model.

Moreover, the predicted high-energy neutrino flux is accompanied by a corresponding diffuse gamma-ray flux through pion decay. This gamma-ray emission must be consistent with the non-blazar component of the extragalactic gamma-ray background (see Sections 1.5.2 and 3.4.3), providing an additional, independent constraint. The modeling of gamma-ray production at the source and its subsequent propagation will be implemented in future work.

Finally, we note that since the simulations also track the evolution of supermassive black holes, they allow the development of phenomenological models for AGN-driven high-energy neutrino production. By combining contributions from both starburst and AGN activity, hybrid predictions of the diffuse high-energy neutrino flux can be constructed, offering new insights into its still poorly understood origin. These models will also be instrumental in interpreting potential features in the observed diffuse flux that may be detected by next-generation neutrino observatories.

CHAPTER 4

The IceCube Neutrino Observatory

The idea of detecting high-energy neutrinos from extraterrestrial sources dates back to the late 1950s, shortly after the experimental confirmation of the neutrino in 1956 [318]. At the 1960 Rochester Conference, A. M. Markov proposed the groundbreaking concept of using a large volume of water or ice as Cherenkov detector to infer the properties of high-energy charged particles produced in neutrino interactions [319]. It later became evident that a cubic kilometer-scale detector would be required for meaningful high-energy neutrino astronomy due to the weakly interacting nature of neutrinos and the expected low flux (e.g. [88, 320]). This realization led to the development of several pioneering experiments, including the Antarctic Muon and Neutrino Detector Array (AMANDA) [321], which demonstrated the feasibility of using deep glacial ice as a detection medium. Building upon AMANDA's success, the first observatory to achieve the necessary scale for high-energy neutrino astronomy was the IceCube Neutrino Observatory, located at the South Pole near the Amundsen–Scott Station [116]. Instead of using a body of water, as initially envisioned, IceCube transformed a cubic kilometer of deep Antarctic ice into a Cherenkov detector by instrumenting it with an array of thousands of photodetectors.

Overview & Context Earlier, in Section 1.4, we discussed the key scientific achievements of IceCube, including the discovery of a diffuse high-energy neutrino flux in the energy range of approximately $1\ \mathrm{TeV}$ to $1\ \mathrm{PeV}$. In this chapter, we shift our focus to the detection principles (Section 4.1) and the instrumentation, data acquisition, data processing, and event characterization of the detector (Section 4.2).

Next, we examine the reconstruction of track-like signatures produced by muons in the detector (Section 4.3), a crucial concept for Section 4.4, where we introduce the up-going muon-track sample. This sample will be used in Chapters 5 and 6 to search for high-energy neutrinos from (ultra)luminous infrared galaxies in the Great Observatories All-Sky LIRG Survey, the candidate neutrino source class introduced in Chapter 2.

4.1 Detection Principle

Due to the weakly interacting nature of neutrinos, direct detection is not feasible. However, in transparent media, neutrinos can be detected indirectly through Cherenkov radiation emitted by secondary charged particles produced in weak interactions with nucleons. This detection principle is employed in operational neutrino telescopes such as IceCube. Below, we discuss the relevant neutrino interaction channels and the mechanism behind Cherenkov radiation.

4.1.1 Cross sections

For a high-energy ($\gtrsim 100\,\mathrm{GeV}$) neutrino or antineutrino of any lepton flavor (ν_ℓ or $\overline{\nu}_\ell$) propagating near or within the IceCube detector, the interaction cross section is

dominated by two types of deep-inelastic scattering (DIS) with nucleons, as described below.

- **Neutral-current (NC) interaction:** In this process, the (anti)neutrino scatters off a quark via the exchange of a neutral Z^0–boson. The interaction disrupts the nucleon, producing a relativistic hadronic cascade, denoted as X. The interaction can be schematically represented as:

$$\nu_\ell + N \xrightarrow{Z^0} \nu_\ell + X, \quad \text{and} \quad \overline{\nu}_\ell + N \xrightarrow{Z^0} \overline{\nu}_\ell + X.$$

- **Charged-current (CC) interaction:** In this process, the (anti)neutrino transforms into a charged lepton ($l^{\mp}$) of the same flavor via the exchange of a $W^{\pm}$–boson. Similar to the NC channel, this interaction disrupts the nucleon, creating a relativistic hadronic cascade X. The interaction can be schematically represented as:

$$\nu_\ell + N \xrightarrow{W^+} \ell^- + X, \quad \text{and} \quad \overline{\nu}_\ell + N \xrightarrow{W^-} \ell^+ + X.$$

In both NC and CC interactions, a fraction of the initial neutrino energy is transferred to the struck quark within the nucleon. In NC interactions, the remaining energy is carried away by the outgoing neutrino, while in CC interactions, it is transferred to the resulting charged lepton.

The fraction of energy transferred to the quark is quantified by the inelasticity parameter y, which is determined by the differential cross section [322]

$$\frac{\mathrm{d}\sigma}{\mathrm{d}y}(E, y) = a(E) + b(E) \cdot (1 - y)^2, \tag{4.1}$$

where $a(E)$ and $b(E)$ are energy-dependent coefficients. The energy of the outgoing neutrino in NC interactions and the energy of the charged lepton in CC interactions are given by $(1 - y)E_\nu$.

Figure 4.1 illustrates the mean inelasticity, $\langle y \rangle$, as a function of neutrino energy for both NC and CC interactions. At ~ 100 GeV, the mean inelasticity is approximately 0.35 for antineutrinos and 0.45 for neutrinos. Above ~ 1 PeV, the inelasticity converges to a lower value of ~ 0.25 for both NC and CC interactions. These numbers imply that in NC interactions, only a limited fraction of the energy is transferred to the detection medium, making the neutrino energy reconstruction more challenging. In CC interactions, a significant portion of the neutrino energy is carried away by the outgoing lepton, which requires proper reconstruction.

Figure 4.2 presents the cross sections for NC and CC interactions across the energy range relevant to IceCube. The ratio of CC to NC cross sections is ~ 2.4 and remains largely energy-independent. Below $E_\nu \lesssim 1$ PeV, neutrino cross sections exceed those of antineutrinos due to the valence quark composition of nucleons. However, at energies above ~ 1 PeV, neutrinos predominantly scatter off *sea* quarks—vacuum fluctuations of quark-antiquark pairs—leading to nearly identical cross sections for neutrinos and antineutrinos [322].

While CC and NC DIS dominate neutrino interactions at most energies [128], the Glashow resonance at ~ 6.3 PeV dramatically enhances the cross section for electron antineutrino interactions [324]. At this energy, the resonant process $\overline{\nu}_e + e^- \to W^- \to X$ is approximately 200 times more likely than CC or NC interactions, as illustrated in Figure 4.2. Since this resonance occurs at an energy well beyond the reach of terrestrial particle accelerators, its observation is only possible through astrophysical

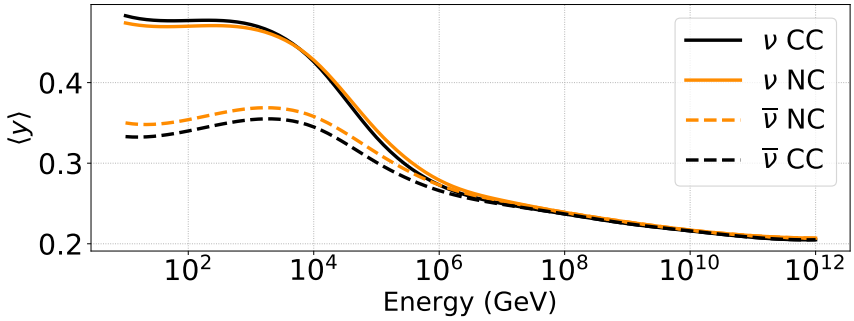

FIGURE 4.1: Mean inelasticity parameter $\langle y \rangle$, which represents the fraction of energy transferred from the (anti)neutrino to the nucleon, as a function of neutrino energy. The parametrization follows [322]. Solid and dashed lines correspond to neutrinos and antineutrinos, respectively, while black and orange indicate CC and NC interactions.

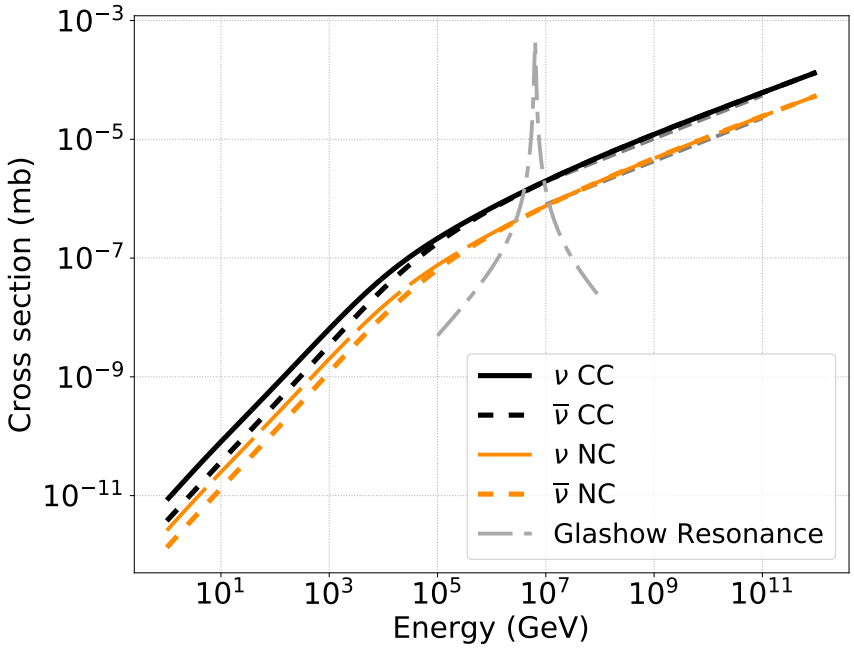

FIGURE 4.2: Cross sections for (anti)neutrino CC and NC interactions with nucleons, using the CTEQ5 parametrization [323]. Line styles and colors match those in Figure 4.1. The Glashow resonance, indicated by the grey dashed line, corresponds to the on-shell production of a W^- boson via the interaction of an electron antineutrino with an electron [324].

neutrinos. IceCube has detected an event consistent with this process [134], as was discussed in more detail in Section 1.4.2.

It is noted that the total neutrino cross sections shown in Figure 4.2 remain exceedingly small. The NC and CC interaction cross sections are approximately $10^7 - 10^8$ times smaller than those of proton-proton interactions, which are of order 10 mb at IceCube-relevant energies (see Figure 1.4). This combination of a small interaction probability and the low flux of high-energy neutrinos (see Section 1.5.1) motivated the cubic-kilometer scale design of IceCube.

4.1.2 Cherenkov radiation

One common feature of the different deep inelastic scattering interactions (and the Glashow resonance) is the production of highly relativistic charged particles. When such a particle traverses a dielectric medium, such as South Pole ice or water, it perturbs the electromagnetic field of the surrounding medium. If the particle's velocity exceeds the phase velocity of light in the medium, coherent electromagnetic radiation is emitted as a shock front along a cone centered on the particle's trajectory. This phenomenon is known as Cherenkov radiation [325].

The refractive index of the medium, $n(\lambda)$, depends on the radiation wavelength λ and determines the reduction in the speed of light in the medium (c_{medium}) relative to the speed of light in vacuum (c), such that

$$c_{\text{medium}} = \frac{c}{n(\lambda)}. \tag{4.2}$$

Cherenkov emission occurs only when $v > c_{\text{medium}}$, where v is the particle velocity. The characteristic emission angle, known as the Cherenkov angle θ_c, is given by

$$\cos\theta_c = \frac{c_{\text{medium}}}{v} = \frac{1}{\beta n(\lambda)}, \tag{4.3}$$

where $\beta = v/c$ is the normalized velocity of the particle.

For IceCube, the refractive index of Antarctic ice is approximately $n \approx 1.32$ for wavelengths in the range $300 \lesssim \lambda \lesssim 600$ nm [326, 327]. For highly relativistic particles ($\beta \approx 1$), the Cherenkov angle is then $\theta_c \sim 41°$.

The number of Cherenkov photons (N) emitted per unit track length ($\mathrm{d}x$) and per unit wavelength ($\mathrm{d}\lambda$) for a particle with charge Ze follows the Frank-Tamm formula [328]

$$\frac{\mathrm{d}N}{\mathrm{d}x\,\mathrm{d}\lambda} = \frac{2\pi\alpha Z^2}{\lambda^2}\left(1 - \frac{1}{n^2(\lambda)\cdot\beta^2}\right) = \frac{2\pi\alpha Z^2}{\lambda^2}\sin^2\theta_c, \tag{4.4}$$

where $\alpha \approx 1/137$ is the fine-structure constant. As such,the Cherenkov radiation forms a continuous spectrum, with the number of emitted photons increasing as the wavelength decreases, typically peaking in the ultraviolet regime. At sufficiently short wavelengths, a critical threshold is reached where the refractive index falls below unity, suppressing further Cherenkov emission.

Integrating Eq. (4.4) over the wavelength range $300{-}600$ nm, while assuming a constant refractive index ($n = 1.32$) and Cherenkov angle ($\theta_c = 41°$), yields an expected production of approximately 3.3×10^4 photons per meter of track length. By measuring the charge deposited by these photons and recording their arrival times (Section 4.2.3), it is possible to reconstruct key properties of the initial neutrino, such as its direction and energy (section 4.3).

4.2 Detector Instrumentation, Operation & Simulation

In the previous section, we discussed the detection principle of IceCube, which relies on the deep-inelastic scatterings of high-energy neutrinos and the subsequent production of Cherenkov photons. In this section, we describe the instrumentation, algorithms, and software of IceCube designed to detect these Cherenkov signatures and reconstruct them into physics events suitable for further analyses, such as point-source

searches presented in Chapters 5 and 6. This section primarily follows the comprehensive overview of IceCube's instrumentation and online system presented in [116, 329, 330]. For further details, the reader is referred to these references.

4.2.1 Configuration

Deep in the Antarctic ice, between depths of about 1450 m and 2450 m, 86 vertical **strings** are deployed in boreholes drilled using a high-pressure hot-water drill [331]. Each **string** is equipped with 60 **digital optical modules** (DOMs)—the primary data acquisition units of IceCube (further details discussed in Section 4.2.2)—resulting in a total of 5160 in-ice DOMs. This configuration is illustrated in Figure 4.3. Deploying the detector at these depths minimizes the presence of air bubbles, which are a major source of light scattering at shallower depths and the ice above provides some level of shielding from cosmic rays.

Of the 86 strings, 78 form the primary **In-Ice Array**, arranged in a hexagonal grid with an inter-string spacing of 125 m. On each of these strings, the DOMs are vertically spaced by 17 m. This configuration optimizes the detection of high-energy neutrinos, covering an energy range of $\gtrsim 100$ GeV to several PeV, which is expected for astrophysical neutrinos. The total instrumented volume of the In-Ice Array is approximately 1 km^3 [116].

Near the center of the In-Ice Array, eight additional strings form the **DeepCore** sub-array [332] are positioned between the seven central strings of the hexagonal layout. These strings have a denser inter-string spacing of approximately 72 m. Each DeepCore string hosts 50 DOMs deployed at depths between 2100 m and 2450 m, with a vertical spacing of 7 m. Additionally, 10 DOMs are placed at shallower depths above 2000 m with a 10 m vertical spacing, forming a veto layer to help reject down-going atmospheric muons. The denser configuration, combined with the higher quantum efficiency[1] of DeepCore DOMs compared to those in the primary In-Ice Array, and the exceptionally clear ice at these depths, enables DeepCore to achieve a reduced energy threshold of ~ 10 GeV.

The **IceTop** surface array [32], located directly above the In-Ice Array, consists of 81 stations, each equipped with two Cherenkov tanks located next to an in-ice string position, covering an area of 1 km^2. IceTop detects cosmic-ray air showers, with each tank containing two DOMs (one high-gain and one low-gain) to extend its dynamic range. It is sensitive to cosmic-ray air showers in the PeV to EeV range (see also Figure 1.1). In addition to cosmic-ray studies, IceTop serves as a veto for atmospheric muon backgrounds in the in-ice detector.

All data collected by both the in-ice and IceTop DOMs are transmitted via cables to the **IceCube Lab** (ICL), located at the surface, in the center of IceTop. The ICL hosts the online systems for **data acquisition** (DAQ) and data **processing and filtering** (PnF) (see Section 4.2.3). The data that survives the filtering is transmitted to computing centers in the Northern Hemisphere via satellite for further analysis.

4.2.2 Digital optical modules

DOMs, illustrated in Figure 4.4, are IceCube's primary data collection units. Each unit houses a downward-facing photomultiplier tube (PMT) in the lower half for light detection and a Main Board in the upper half for waveform digitization, communication, and calibration. Encased in a 1.3 cm-thick glass sphere of about 30 cm diameter, DOMs withstand long-term ice pressure of about 250 bar and temporary overpressure up to

[1] The ratio of detected photoelectrons to the number of incident photons.

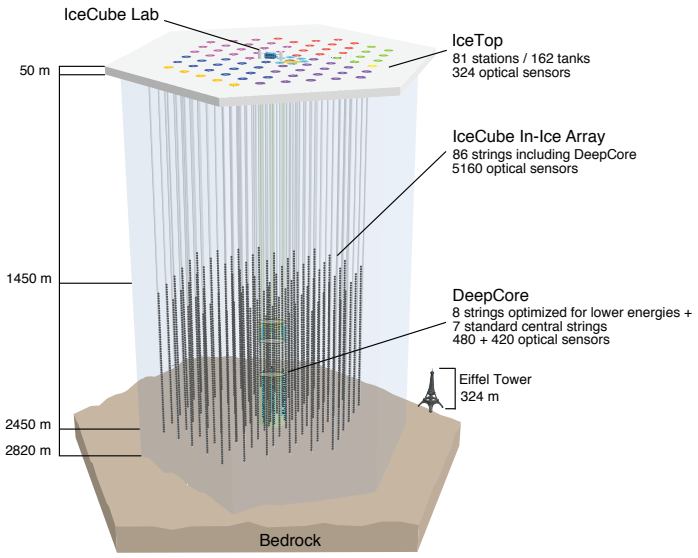

FIGURE 4.3: Illustration of the IceCube Neutrino Observatory layout. The In-Ice Array and DeepCore are shown below the surface, with the Eiffel Tower for scale. On the surface, IceTop and the IceCube Lab are indicated. Taken from [116].

about 690 bar during refreezing [116]. An optical gel couples the PMT to the glass, enhancing photon acceptance and provides mechanical support.

IceCube PMTs are used to detect single photoelectrons over a $300-650$ nm wavelength range with a peak quantum efficiency of 25% at 390 nm for standard DOMs and 34% for DeepCore DOMs [330].

When a photon strikes the PMT, it generates a photoelectron (PE) via the photoelectric effect. A high-voltage (HV) gain amplifies the PE to 10^7 electrons, producing an analog signal detectable by conventional electronics. The signal from a single photon is referred to as a single PE (SPE). When multiple photons arrive simultaneously at a DOM, the output signal is a linear combination of SPEs.

To mitigate interference from the South Pole's magnetic field, and as such improve the collection efficiency, a mu-metal cage surrounds each PMT.

A so-called **hit** is recorded in an in-ice DOM when the observed voltage reaches 25% of the average SPE amplitude, triggering the recording of a timestamp and digitization of the waveform. The latter is performed by two systems: a high-speed Analog Transient Waveform Digitizer (ATWD) and a fast analog-to-digital converter (fADC) [116]. To ensure waveform capture from before the threshold crossing, the PMT signal is first routed through a delay board, which is essentially a 10 m coiled copper wire, introducing a delay of about 75 ns. The ATWD samples[2] at 3×10^8 samples per second over 427 ns, sufficient to capture Cherenkov photons produced near the DOM (within tens of meters), while the fADC records a 6.4 μs window at 4×10^7 samples per second, capturing delayed and scattered light. This dual-digitization system enhances event reconstruction for energy and directional analysis at a later stage of the data processing.

In addition to waveform digitization, the Main Board powers the DOM, facilitates communication with neighboring DOMs and the DAQ system at the ICL, and handles calibration. DOM calibration is performed annually (monthly for IceTop DOMs due to

[2]To reduce dead time, two ATWD chips are used in each PMT.

temperature fluctuations) using `DOMcal` software [116]. Global time synchronization across all DOMs is achieved via Reciprocal Active Pulsing Calibration (`RAPcal`) [329], continuously aligning timestamps with the ICL clock. LED flashes from the Flasher Board further assist in verifying synchronization, as well as measuring local ice absorption and scattering properties.

The reliability of IceCube DOMs is exceptional, a necessity given that they cannot be maintained after deployment and refreezing in the ice. Each unit has undergone extensive testing across a wide temperature range before deployment. While approximately 1% of the DOMs failed during deployment or freeze-in, the failure rate has remained remarkably low, with fewer than one DOM per year failing since. As of 13 years into full-detector operation, 98.3% of the original 5484 modules remain operational [331].

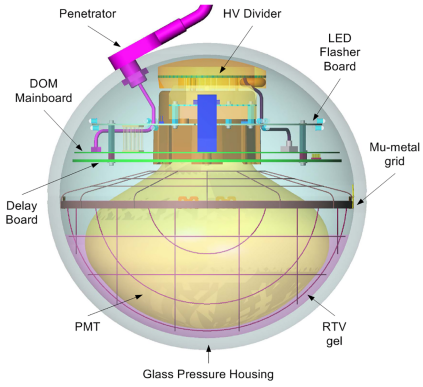

FIGURE 4.4: Illustration of a Digital Optical Module (DOM), the primary detector unit of IceCube. The various components of the DOM are described in detail in the text. Taken from [333]

4.2.3 Data acquisition, triggering & filtering

The amount of hit information transmitted to the surface depends on whether a hit occurs in **hard local coincidence** (HLC), meaning that at least one of the nearest or next-to-nearest neighboring DOMs registers a hit within a ± 1 μs time window. If this condition is met, the complete waveform is sent to the DAQ. In contrast, DOMs registering **soft local coincidence** (SLC) hits—those that do not satisfy the HLC criterion—transmit only a timestamp and coarse information about the fADC waveform around its peak voltage [116, 329]. While SLC hits are more likely associated with dark noise, HLC hits are expected to have a causal connection, characteristic of Cherenkov photons. The primary sources of dark noise include radioactive decays, electronic noise, and luminescence within the glass sphere of the DOM [116]. This local coincidence system effectively reduces the data volume transmitted to the ICL, ensuring efficient data management.

The hit information and corresponding waveforms from all DOMs are transmitted to DAQ computers at the ICL, where the data is buffered. Approximately every second [329], the central DAQ triggering computer requests timestamps of all newly recorded hits. If at least one predefined trigger algorithm is satisfied, the buffered data is used to construct a so-called event. The following discussion covers the relevant triggers and filters for the work presented here.

Online triggers

The primary trigger of IceCube is the **simple multiplicity trigger** (SMT), which requires a minimum number, N, of HLC hits within a fixed time window to identify causally connected signals. For the In-Ice Array, at least 8 HLC hits within 5 μs (SMT-8) are required.[3] To ensure a conservative data readout, each SMT-8 occurrence includes a 10 μs time window, starting 4 μs before and ending 6 μs after the trigger condition is met. Additional triggers, based on similar hit-multiplicity criteria, may introduce topological constraints, such as requiring hits to be confined within a defined cylindrical volume. See [116] for an overview of the different triggers in IceCube.

Since multiple triggers can be satisfied simultaneously, all trigger windows are merged into a Global Trigger to ensure that events do not overlap and contain duplicate hits. A readout of Global Trigger data is referred to as a DAQ **event**, which is then stored and prepared for further processing.

The DAQ event readout rate is primarily driven by atmospheric muons penetrating the detector from the Southern Hemisphere, which is directly overhead for IceCube. This rate shows seasonal variations due to changes in atmospheric conditions, which affect particle production in air showers. It fluctuates between approximately 2.5 kHz and 2.9 kHz, with a median rate of 2.7 kHz [32]. This corresponds to a data storage consumption of about 1 TB per day [116]. Once a year, these storage disks are physically transported to Madison, Wisconsin, for long-term archiving.

Online filters

In this work, only events passing the SMT-8 trigger are considered. These events are processed at the ICL by a local computer cluster running the processing and filtering (PnF) system. The first step in the event processing pipeline is waveform calibration, where digitized signals are corrected for known detector response characteristics. The calibrated waveforms are then deconvolved using the known single-photon response of each DOM, extracting discrete charge deposits at specific times, referred to as *pulse maps*. These pulse maps serve as the foundation for event reconstruction and characterization, as discussed in Section 4.3.

Subsequently, software filters are applied *in situ* at the South Pole to perform an initial selection of events relevant to specific physics analyses. The event selection used in this work (Section 4.4) targets track-like signatures characteristic of astrophysical and atmospheric muon neutrinos, as well as atmospheric muons. The topology of these events is particularly well-suited for point-source searches of high-energy neutrinos (see Section 4.2.4). Accordingly, the primary filter of interest in this study is the **muon filter**, designed to identify promising high-energy track-like events.[4] Rather than prioritizing a highly pure selection, these filters aim to maximize the retention of potentially interesting events.

Beyond event selection for physics analyses, these filters serve a critical role in reducing the data volume before transmission via satellite to the Northern Hemisphere, where more detailed analyses are conducted. Due to bandwidth limitations, only approximately 15% of the DAQ event rate can be transmitted.

Once the data reach the Northern Hemisphere, the initial filtering procedures from the South Pole are reprocessed offline with slightly refined parameters. Additionally,

[3] The time window varies for the In-Ice Array, IceTop, and DeepCore due to differences in time required for a particle to cross the array. For DeepCore, at least 3 HLC hits (SMT-3) within 2.5 μs are required.

[4] Other online filters include the high-charge filter, which selects events with a total photoelectron count exceeding 10^3, and the shower filter, which identifies cascade-like events [116].

further filtering stages are applied to enhance event selection for various physics analyses.

4.2.4 Event signatures

An IceCube **event** refers to a collection of DOMs that registered photon hits, along with their associated waveform data and timestamps, after passing a series of cleaning and processing steps. The waveform information allows for the extraction of the deposited charge as a function of time, serving as a proxy for local energy deposition. The total energy deposited during an event is then estimated by summing the contributions from all participating DOMs. Moreover, the nanosecond-scale timing resolution of the In-Ice Array allows for precise separation of DOM timestamps. Combined with the known geometry of the detector, this enables the reconstruction of time-dependent light propagation patterns within the array.

Using these capabilities, IceCube classifies events into three distinct topologies: *cascades*, *tracks*, and *double-bangs*. Each topology exhibits characteristic energy deposition profiles and offers unique insights into the underlying physical processes, as discussed below.

Reminder: In general, IceCube cannot distinguish between neutrinos and antineutrinos, except in the specific case of the Glashow resonance (Section 1.4.2). Throughout the discussion of different event signatures, we will refer explicitly to both neutrinos and antineutrinos. However, in subsequent sections, the term "neutrino" will be used to denote both neutrinos and antineutrinos, unless otherwise specified.

Cascades

A neutral-current (NC) interaction involving any neutrino flavor produces a hadronic shower (Section 4.1). Such a shower develops over roughly 10 m [118], which is smaller than both the vertical (17 m) and horizontal (125 m) DOM spacing in the In-Ice Array and is therefore not resolvable. Due to the scattering of Cherenkov photons as they propagate, the resulting light distribution thus appears approximately spherical, referred to as a *cascade*.

In charged-current (CC) interactions involving electron (anti)neutrinos, both electromagnetic and hadronic showers are produced (Section 4.2). Since these showers develop over comparable length scales, their Cherenkov emissions overlap, resulting in a cascade-like event within the detector.

CC interactions of tau (anti)neutrinos similarly often lead to cascade-like events. This occurs when the produced (anti)tau decays hadronically or into an electron (or positron), with branching ratios of 65% and 18%, respectively [29]. In such cases, there are effectively two energy depositions: the first from the initial CC interaction, and the second from the decay of the (anti)tau. However, the secondary energy deposition typically occurs close to the interaction vertex and is not distinguishable from the primary. As discussed later in this section, the two energy depositions can only be spatially separated at the highest energies, where the (anti)tau propagation length becomes significant.

The remaining 17% of (anti)tau decays produce a (anti)muon, resulting in a more extended energy deposition with a track-like topology. These events are categorized separately in the following discussion.

Due to the roughly spherical Cherenkov signature, cascade events are typically well-contained within the detector, allowing for precise shower energy reconstruction.

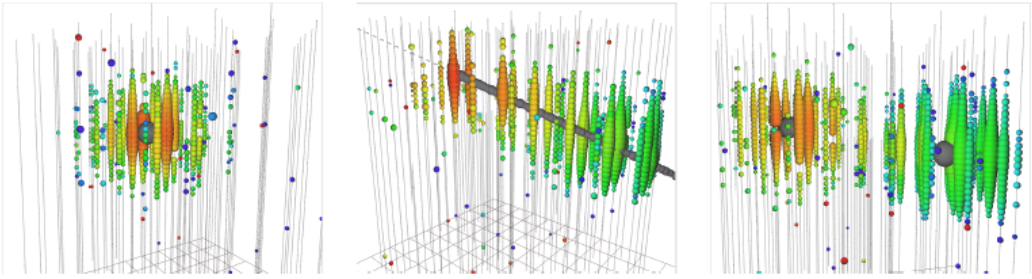

(a) Cascade (b) Track (c) Double bang

FIGURE 4.5: Different event topologies in the IceCube detector. (a) The cascade topology as a result of ν_e in a CC interaction or any of the neutrino flavors in a NC interaction. (b) A muon track from ν_μ in a CC interaction. (c) Double-bang signature from ν_τ in a CC interaction. It is noted that these are all simulated events, adapted from [334].

Cascades thus provide excellent energy resolution, with average uncertainties of about 15% above 10 TeV [118], but have relatively poor directional resolution, on the order of $7°$ [13, 119] for a typical signal event. A simulated cascade event is shown in Figure 4.5 (a).

Tracks

Track events, as shown in Figure 4.5 (b), predominantly arise from CC interactions of muon (anti)neutrinos.[5] Unlike electrons (positrons), the resulting (anti)muon deposits energy more gradually due to its larger mass. High-energy (anti)muon $\gtrsim 100$ GeV can travel several kilometers through ice, often escaping the IceCube detector before coming to a stop. This extends IceCube's effective area, as neutrino interactions can occur outside the instrumented volume and still provide a detectable signal. Furthermore, the extended path length enables precise directional reconstruction of the initial (anti)muon, in contrast to the more spherical topology of cascade-like events.

For neutrino energies exceeding 1 TeV, the direction of the (anti)muon closely aligns with that of the original (anti)neutrino, achieving an angular resolution better than $1°$ [117]. However, at energies of $\lesssim 1$ TeV, the kinematic angle between the (anti)muon and (anti)neutrino becomes important.

Because most tracks are only partially contained within the detector, only a lower bound can be placed on the energy of the (anti)muon. By extension, only a lower bound can be placed on the energy of the original (anti)neutrino. As a result, track events have relatively poor energy resolution. Nonetheless, their superior directional accuracy makes them well-suited for point-source searches of high-energy neutrinos (e.g., [16]). As such a search is the focus of Chapters 5 and 6 of this work, the track-like signatures are of primary interest for this work.

Double bang

The *double-bang* topology is one of the most distinctive signatures. This occurs when a tau (anti)neutrino interacts via a CC interaction. The first high-energy deposition (the first "bang") arises from the hadronic shower produced in the initial CC neutrino interaction. This interaction is accompanied by the creation of a (anti)tau, which then

[5] A small fraction of track events originates from CC interactions of tau (anti)neutrinos, as approximately 17% of (anti)tau decays produce an (anti)muon [29].

propagates a distance of approximately 50 m per PeV of energy before decaying [132, 133]. If the (anti)tau decays hadronically or into an electron—processes that occur in about 83% of cases ([29]; see also the cascade section)—a second localized energy deposition (the second "bang") is produced. A simulated reconstruction of a double-bang event is shown in Figure 4.5 (c).

Due to the value of the inelasticity parameter (Figure 4.1), the energy of the "second bang" is in general larger than that of the first one. This provides an additional handle in identifying tau neutrino events.

However, IceCube can only resolve these two distinct energy depositions if the (anti)tau has a sufficiently long lifetime in the detector frame. Otherwise, the event appears as a single cascade. For a tau (anti)neutrino with energy $\gtrsim 1\ \mathrm{PeV}$, the (anti)tau's propagation length exceeds the vertical inter-DOM spacing in the IceCube In-Ice Array, allowing for an observable displacement between the two cascades.

At intermediate energies, where the (anti)tau propagation length is shorter and the two cascades are not clearly separable, energy losses may still produce two distinguishable pulses in a single DOM. As discussed in Section 1.4, IceCube rules out the absence of astrophysical tau (anti)neutrinos at the 5σ significance level [133].

4.2.5 Atmospheric background

Cosmic rays can interact inelastically with atmospheric nuclei through hadronic processes, as described in Section 1.2.1. These interactions lead to the production of atmospheric neutrinos, primarily originating from the decay of charged pions and kaons. This component forms the so-called *conventional* atmospheric neutrino flux.

Modeling of cosmic-ray air showers indicates that, above energies of approximately $\sim 1\ \mathrm{TeV}$, the atmospheric neutrino spectrum follows a power law of $E^{-3.7}$ [120, 335], significantly softer than the primary cosmic-ray spectrum of roughly $E^{-2.7}$ (see Section 1.4.1). This steepening arises because, at these energies, pions and kaons are more likely to interact with atmospheric nuclei before decaying, thus reducing the energy transferred to neutrinos.

At energies of $\sim 10{-}100\ \mathrm{TeV}$, an additional (and eventually dominant) contribution is expected from *prompt* neutrinos, produced in the decay of short-lived charmed mesons. Unlike conventional atmospheric neutrinos, prompt neutrinos are expected to follow the harder $E^{-2.7}$ spectrum of primary cosmic rays, since their parent particles decay before undergoing significant energy loss. However, the prompt atmospheric neutrino flux has not yet been experimentally observed (e.g. [7]).

The primary background in searches for astrophysical neutrinos in IceCube arises from hadronuclear interactions of cosmic rays in the atmosphere. The development of particle air showers is described by coupled differential equations that track particle populations as a function of energy and interaction depth. These are typically solved numerically due to their complexity. Such calculations show that the dominant lepton fluxes reaching the IceCube detector are composed of **atmospheric muons** and **atmospheric neutrinos** [336]. Both muons and muon neutrinos can produce track-like Cherenkov signatures that resemble those of astrophysical neutrinos. However, their significantly higher flux complicates the identification of astrophysical sources.

Atmospheric muons trigger the IceCube data acquisition (DAQ) system (see Section 4.2.3) at a rate of approximately 2.7 kHz [116]. This background can be almost entirely suppressed in analyses focused on the Northern Hemisphere, where for declinations $\delta \gtrsim -5^\circ$, the Earth's interior and the overlying Antarctic ice act as an effective shield [170] (see also Figure 2.9). Atmospheric neutrinos [335], however, constitute

an irreducible background, as they can traverse the Earth and reach the detector from any direction. They are observed at a rate of $\mathcal{O}(\text{mHz})$ [337], which remains several orders of magnitude higher than the flux of astrophysical neutrinos, estimated at $\mathcal{O}(\mu\text{Hz})$ (see Section 1.4.1).

In addition to focusing on the Northern Hemisphere, analyses exploit spectral differences between atmospheric and astrophysical neutrinos to aid in their discrimination. One example of a high-energy selection is the High-Energy Starting Event (HESE) sample, which requires a minimum total deposited charge of 6000 photoelectrons in the detector [6]. Additionally, the outer layers of the detector act as a veto, effectively rejecting atmospheric muons, which cannot produce tracks originating within the instrumented volume. Notably, the HESE analysis led to the discovery of the diffuse high-energy neutrino flux in 2013 [4, 5].

A final effective method for reducing the atmospheric background, when the analysis permits, is focusing on cascade-like events instead of tracks. Since atmospheric muons, the primary background in IceCube, primarily produce track-like signatures, cascade selections significantly suppress this background. This strategy was successfully employed in the analysis that provided evidence of neutrino emission from the Galactic plane ([13]; see Section 1.6.2).

4.2.6 Event simulations

Monte Carlo (MC) simulations are essential tools for evaluating the performance of reconstruction algorithms, event selection criteria, and IceCube analyses more broadly. They provide a controlled environment to study detector responses and validate theoretical models. Below, we outline a the different steps in event simulations and highlight the relevant algorithms and software components for the MC simulations used in this work.

Neutrinos are first generated uniformly over the full surface of the Earth, usually with a spectral index between E^{-1} and E^{-2}, ensuring sufficient statistical coverage across a wide energy range. Each neutrino is then propagated through the Earth, where it may interact via deep-inelastic scattering, as discussed in Section 4.1. These interactions result in either energy loss or full absorption. Energy loss occurs primarily through neutral-current (NC) interactions of all flavors, or through charged-current (CC) interactions of tau neutrinos, where the produced tau subsequently decays leptonically. In contrast, absorption is predominantly due to CC interactions of electron and muon neutrinos.

The transmission probability of neutrinos as a function of zenith angle and neutrino energy is shown in Figure 4.6. Notably, the Earth becomes increasingly opaque to neutrinos with energies above $E_\nu \gtrsim 100\ \text{TeV}$.

Upon reaching the IceCube detection volume, neutrinos are forced to interact within the detector simulation. The resulting events are recorded with weights proportional to their interaction probabilities, which depend on both the neutrino-nucleon cross-section and the energy-dependent transmission probability through the Earth. Additionally, the final event weights include a scaling factor that allows reweighting from the neutrino generation spectrum to any desired spectrum (see e.g. [338]).

The underlying physics processes are modeled by the All Neutrino Interaction Generator (`ANIS`) [339]. An IceCube-specific extension of `ANIS`, known as `NuGen`, was used to generate the MC datasets employed in this analysis.

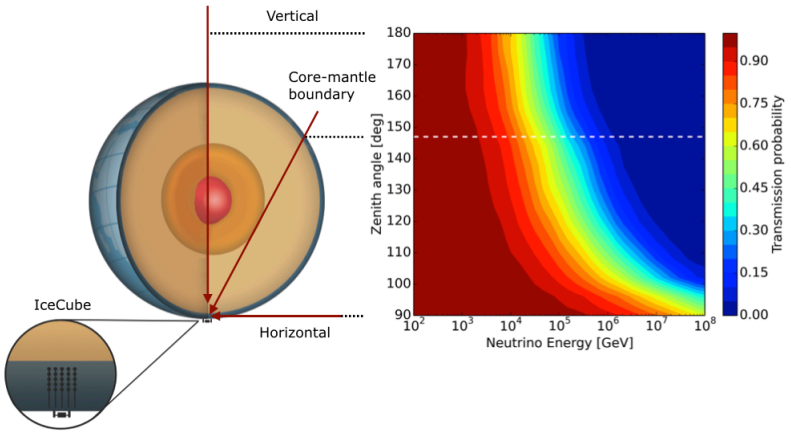

FIGURE 4.6: Transmission probability of high-energy neutrinos through the Earth as a function of the zenith angle and neutrino energy. Figure taken from [343].

The final step involves simulating the propagation and energy loss of secondary charged particles produced near or within the detector volume as a result of deep-inelastic scattering events [340, 341]. As these particles traverse the ice, they emit Cherenkov photons, whose subsequent propagation is simulated using a predefined model of the optical properties of the ice. For the MC datasets referenced here, the *Spice3.2.1* ice model is employed [342].

When these photons reach a digital optical module (DOM; see Section 4.2.2), IceCube-specific software simulates the detector's response. The resulting pulse maps are processed through the data acquisition (DAQ) and PnF software pipelines (see Section 4.2.3).

This simulation chain enables direct comparison between experimental event selections and their corresponding MC-simulated samples. Ensuring strong agreement between simulation and data is crucial for the reliability of the analyses presented in Chapters 5 and 6.

4.3 Muon-Track Reconstruction

At the South Pole, filtering techniques are employed to reduce the data volume for satellite transmission by selecting physics-relevant events. The primary filter relevant to this work is the *muon filter*. This filter selects high-energy, track-like events based on a minimum detected charge and track quality criteria. Events that satisfy any of the filter conditions are transmitted to the Northern Hemisphere, where more computationally intensive reconstructions are performed.

Accurate energy reconstruction is essential for distinguishing astrophysical from atmospheric neutrinos, the latter of which exhibit a softer energy spectrum (see Section 4.2.5). In addition, good energy resolution enables detailed studies of astrophysical sources. Precise directional reconstruction, along with robust estimates of angular

uncertainty, is critical for identifying spatial clustering of events, a key signature of potential high-energy neutrino sources.

The following sections introduce offline algorithms for reconstructing track-like events, including the determination of direction, estimation of angular uncertainty, and computation of reconstructed energy. The selection of muon-track events is described in detail in Section 4.4.

4.3.1 Directional reconstruction

This work uses an algorithm known as the *SplineMPE fit* to determine the angular direction of events. This algorithm builds upon a sequence of three preliminary fit methods—*LineFit*, *SPE Fit*, and *MPE Fit* (discussed in this section)—each serving as a seed for the next step in the reconstruction chain:

$$\text{LineFit} \xrightarrow{\text{seed}} \text{SPE Fit} \xrightarrow{\text{seed}} \text{MPE Fit} \xrightarrow{\text{seed}} \text{SplineMPE Fit} .$$

Before discussing each of the fit methods in this chain in more detail below, we note:

- **Coordinates**: Track reconstruction is performed in detector coordinates, defined by the zenith angle θ and the azimuth angle ϕ, which are later converted into equatorial coordinates, namely declination δ and right ascension α. Due to IceCube's location at the South Pole, the relationship between these coordinate systems is given by $\theta = \delta + \pi/2$. Note that $\theta = 0^\circ$ corresponds to a vertically down-going muon (see Figure 2.9).

- **Kinematic angle:** The directional reconstruction algorithms presented in this section estimate the muon track direction. However, in the case of a muon neutrino undergoing a CC interaction, the reconstructed muon direction is not perfectly aligned with the initial neutrino direction. This offset is quantified by the median kinematic angle ψ, which is energy-dependent and approximates to [344]:

$$\psi \approx 0.7^\circ \cdot \left(\frac{E_\nu}{1\ \text{TeV}} \right)^{-0.7} . \tag{4.5}$$

  The effect of the kinematic angle becomes significant at energies below a few TeV. Conversely, at higher energies, the reconstructed muon direction provides an increasingly accurate estimate of the original neutrino direction.

LineFit

The simplest directional reconstruction method assumes a muon traveling in a straight line at a constant velocity with velocity vector $\boldsymbol{v}$, accompanied by a plane wave of light propagating perpendicular to its direction. The muon track is parameterized as

$$\boldsymbol{r}(t_i) = \boldsymbol{r}_0 + \boldsymbol{v} \cdot (t_i - t_0), \tag{4.6}$$

where $\boldsymbol{r}_0$ is the track position at t_0, and $\boldsymbol{x}_i$ is the position of the i^{th} DOM that recorded a hit at time t_i, with $i \in \{1, 2, \ldots, N\}$. The LineFit method [345] minimizes the function

$$\underset{(t_0, \boldsymbol{r}_0, \boldsymbol{v})}{\arg\min} \sum_{i=1}^{N} \varphi \left(|\boldsymbol{r}(t_i) - \boldsymbol{x}_i| \right) , \tag{4.7}$$

where φ is the Huber cost function [346], defined as

$$\varphi(\Delta x) = \begin{cases} (\Delta x)^2, & \text{for } \Delta x < \mu, \\ \mu(2\Delta x - \mu), & \text{for } \Delta x \geq \mu. \end{cases} \tag{4.8}$$

For small DOM-track distances ($\Delta x < \mu$), the LineFit method reduces to a χ^2-minimization problem, assigning quadratic weights to hits that are assumed to be strongly correlated with the track. For larger distances ($\Delta x \geq \mu$), the Huber cost function assigns a linear weight to the hits, reducing the influence of outliers likely caused by noise. The parameter μ is optimized based on IceCube calibration data.

A key advantage of LineFit is that its minimization problem can be solved analytically, providing a first estimate of track parameters without requiring computationally expensive numerical optimization. However, it ignores Cherenkov effects, which are crucial for accurate event reconstruction. Consequently, LineFit is used as the initial step in the directional-reconstruction chain, providing a seed for the subsequent, more sophisticated reconstruction algorithms.

SPE fit

The next step in the reconstruction chain is the single photoelectron (SPE) fit, which models Cherenkov radiation emitted by a relativistic muon. This radiation forms a cone with an opening angle of $\theta_c \approx 41°$, known as the Cherenkov cone (see Section 4.1.2). Based on the geometry shown in Figure 4.7, the expected arrival time of Cherenkov light at the i^{th} DOM is given by

$$t_{\text{geo},i} = t_0 + \frac{1}{c}\left[\boldsymbol{e_v} \cdot (\boldsymbol{x}_i - \boldsymbol{r}_0) + d \cdot \tan\theta_c\right], \tag{4.9}$$

where d is the perpendicular distance from the DOM to the track and $\boldsymbol{e_v}$ is the unit velocity vector.

Now we define the time residual, t_{res}, which is defined as the difference between the observed hit time, t_{hit}, and the expected arrival time, t_{geo}, such that

$$t_{\text{res},i} \equiv t_{\text{hit},i} - t_{\text{geo},i}. \tag{4.10}$$

Let $\mathcal{P}_1(t_{\text{res}})$ be the probability density function (PDF) of time residuals associated with the detection of a single photon. This PDF depends on the track parameters $\boldsymbol{\theta} = (\theta, \phi, \boldsymbol{r}_0)$ through $t_{\text{geo},i}$. The SPE likelihood function is then defined as

$$\mathcal{L}_{\text{SPE}}(\boldsymbol{\theta}) = \prod_{i=1}^{N_{\text{DOM}}} \mathcal{P}_1(t_{\text{res},i}|\boldsymbol{\theta}), \tag{4.11}$$

with the best-fit track parameters obtained by maximizing the likelihood,

$$\hat{\boldsymbol{\theta}} = \arg\max_{\boldsymbol{\theta}} \mathcal{L}_{\text{SPE}}(\boldsymbol{\theta}). \tag{4.12}$$

The parameters $\hat{\boldsymbol{\theta}}$ are called the maximum-likelihood estimators (See Chapter 5 for more details on the maximum-likelihood method in general). Below, we derive the explicit forms of the PDFs appearing in the SPE likelihood in Eq. (4.11).

The likelihood maximization in Eq. (4.12) is initialized using the LineFit result and employs a modified gamma distribution, known as the Pandel function, to describe the time-residual distribution of photons propagating through South Pole ice (P_{res}),

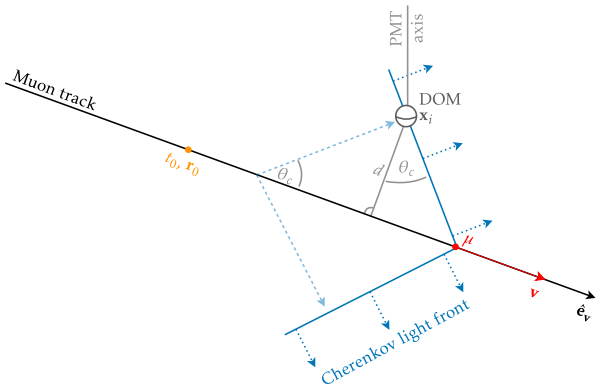

FIGURE 4.7: Geometry used in the SPE track reconstruction algorithm. A relativistic muon moving with velocity $\boldsymbol{v}$ emits Cherenkov radiation at an angle θ_c. At time t_0, the muon is located at $\boldsymbol{r}_0$. The Cherenkov light reaches DOM i at position $\boldsymbol{x}_i$, which is at a perpendicular distance d from the track. Taken from [348].

$$P(t_{\text{res}}) \propto \frac{\tau^{-d/\lambda} t_{\text{res}}^{d/\lambda - 1}}{\Gamma(d/\lambda)} \exp\left[-t_{\text{res}}\left(\frac{1}{\tau} + \frac{c_n}{\lambda_a}\right) - \frac{d}{\lambda_a}\right] . \tag{4.13}$$

The λ_a and c_n parameters represent the photon absorption length and the speed of light in ice, respectively, while λ and τ are empirically determined parameters obtained by fitting the Pandel function to a South Pole ice model [326].

However, the Pandel function is only defined for positive t_{res}, which is physically intuitive from a geometric standpoint. Nonetheless, negative time residuals can occur due to factors such as noise hits surviving pulse cleaning and the finite timing resolution of photon hit recordings. To account for this, the Pandel function in IceCube is convolved with a Gaussian PDF [347] of width σ_t, yielding the modified PDF

$$\mathcal{P}_1(t_{\text{res}}) = \int_0^\infty \frac{P(t')}{\sqrt{2\pi}\sigma_t} \exp\left[-\frac{(t_{\text{res}} - t')^2}{2\sigma_t^2}\right] \mathrm{d}t' . \tag{4.14}$$

This is the PDF that enters the likelihood function in Eq. (4.11).

The Gaussian-convolved Pandel PDF enables efficient evaluation of the SPE likelihood, providing more accurate track reconstructions than LineFit while maintaining computational efficiency. However, the SPE likelihood only considers the earliest hit in each DOM. This becomes a problem for muons with energies in excess of ~ 1 TeV. For such muons, the probability of detecting multiple hits in a single DOM increases significantly.

MPE fit

To improve on the SPE fit, a modified likelihood function is introduced, incorporating the fact that out of a total of n_i hits recorded in DOM i, $n_i - 1$ hits will have residual times larger than that of the first hit. This formulation leads to the multiple photoelectron (MPE) likelihood [326],

$$\mathcal{L}_{\text{MPE}}(\boldsymbol{\theta}) = \prod_{i=1}^{N_{\text{DOM}}} \left[n_i \mathcal{P}_1(t_{\text{res},i}) \left(\int_{t_{\text{res},i}}^\infty \mathcal{P}_1(t') \mathrm{d}t' \right)^{n_i - 1} \right] . \tag{4.15}$$

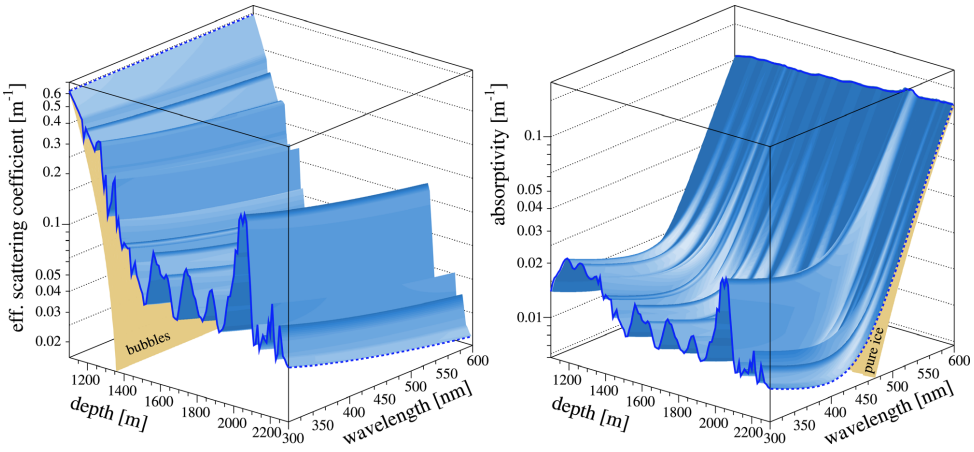

FIGURE 4.8: Effective scattering length (left) and absorption length (right) of light in South Pole ice as a function of depth and radiation wavelength, taken from [350]. The left panel illustrates that air bubbles become negligible below approximately 1300 m depth. The right panel compares the absorption length in South Pole ice to that of pure ice, highlighting deviations primarily caused by dust and ash impurities. A particularly prominent impurity layer around 2000 m depth is known as the dust layer.

Notably, for $n_i = 1$, the MPE likelihood ($\mathcal{L}_{\mathrm{MPE}}$) reduces to the SPE likelihood ($\mathcal{L}_{\mathrm{SPE}}$).

Since the integral in the likelihood expression can be solved analytically, the computational cost of the MPE-likelihood maximization remains comparable to that of the SPE fit. The MPE fit is initialized using the results of the SPE fit, ensuring a refined and more accurate track reconstruction.

SplineMPE fit

Finally, the last step is the SplineMPE fit, which improves upon the MPE fit by replacing the analytical time-residual PDF, $\mathcal{P}_1(t_{\mathrm{res}})$, with numerically computed PDFs. This approach eliminates the assumption of a homogeneous ice model used in the Pandel function, allowing for depth-dependent absorption and scattering effects, as illustrated in Figure 4.8.

Furthermore, the simulations also account for light sources at various positions and orientations within the detector. The resulting PDFs are stored in numerical tables and interpolated using penalized B-splines [349], providing the highest reconstruction accuracy in this chain.

4.3.2 Angular uncertainty

When associating the direction of reconstructed track events—such as those obtained using the SplineMPE algorithm discussed in Section 4.3—with potential source locations in the sky, it is essential to estimate the uncertainty in the angular reconstruction. In this section, we outline a multivariate method based on a boosted decision tree (BDT) [16, 338], which is used to determine the per-event angular uncertainty for the final track selection introduced in Section 4.4 and employed in Chapters 5 and 6.

To provide context for the BDT approach, we first briefly introduce the paraboloid method, a technique commonly used in point-source searches to estimate angular uncertainty.

Paraboloid

One approach to estimating the angular uncertainty of a reconstructed track direction is by constructing a confidence ellipse for the directional parameters in the likelihood space [351]. In this approach, the MPE likelihood, given in Eq. (4.15), can be approximated by a five-dimensional Gaussian distribution around the best-fit parameters obtained via maximum-likelihood estimation, provided that a sufficient number of DOMs have recorded hits. However, since the initial position vector $\boldsymbol{r}_0$ is not of interest here, the likelihood space can be projected onto the two-dimensional (θ, ϕ)-plane. In this 2D plane, the likelihood function is well described by a paraboloid (i.e., a 2D Gaussian) centered at the best-fit parameters $(\hat{\theta}, \hat{\phi})$, with uncertainties $(\sigma_\theta, \sigma_\phi)$. Consequently, this leads to the condition[6]

$$\log \mathcal{L}_{\mathrm{MPE}} \left(\hat{\theta} \pm \sigma_\theta, \hat{\phi} \pm \sigma_\phi \right) = \log \mathcal{L}_{\mathrm{MPE}} \left(\hat{\theta}, \hat{\phi} \right) - \frac{1}{2} \,, \tag{4.16}$$

which allows to define an elliptical confidence region in the (θ, ϕ)-plane [267]. The circular angular uncertainty is then obtained by taking the root-mean square of the paraboloid axes σ_θ and σ_ϕ.

The paraboloid approach provides an uncertainty on the reconstructed muon direction. As such, this uncertainty underestimates the separation between the original neutrino and the muon direction due to the energy-dependent kinematic angle (See Eq. 4.5). Furthermore, other unmodelled systematic effects worsen this effect. To mitigate this, the average mismatch can be partially corrected with an energy-dependent correction function, known as the pull correction (see e.g. [267]).

However, the pull-corrected angular uncertainty still presents several challenges. It fails to fully describe the distribution of kinematic angles for a given reconstructed muon energy, does not entirely account for the declination dependence at lower energies, and cannot handle failed fits. The latter occurs when the Gaussian approximation breaks down—mainly driven by the kinematic angle for muons with energies below about $1\ \mathrm{TeV}$—which depends on both energy and the assumed neutrino spectrum. This failure rate is estimated to be between 2% and 10% [16]. To address these limitations, a novel multivariate approach based on a boosted decision tree was developed within the IceCube collaboration.

[6] In one dimension, a Gaussian probability density function with mean μ and standard deviation σ has the functional form $f(x) = C \exp\left[-(x-\mu)^2/2\sigma^2\right]$, where $C = (2\pi\sigma^2)^{-1/2}$. Consequently, $\log f(\mu \pm \sigma) = \log C - \frac{1}{2}$. In two dimensions, this generalizes to Eq. (4.16).

Boosted decision tree

An alternative estimator for the median angular separation between the reconstructed and true muon direction is based on a BDT that takes 17 features as input [16, 338]. In addition to various energy estimators and the paraboloid uncertainty[7], the feature set includes parameters such as the location of the largest energy deposition within the event, a measure of the stochasticity in the energy loss pattern, the estimated track declination from SplineMPE (see Section 4.3.1), and angular separations between different track reconstruction methods. The broad feature set enables the BDT to exploit a wide range of event characteristics.

As a result, the declination dependence of the point-spread function—a central quantity in Chapter 5 that partially models a point source of astrophysical neutrinos—is mitigated, and the issues related to failed fits in the traditional paraboloid approach are resolved [16, 338].

The BDT is applied to the up-going muon-track sample introduced in Section 4.4 and used in Chapters 5 and 6. It is important to note, however, that the BDT was trained to estimate the median angular separation between the reconstructed and true muon directions. Consequently, to determine the total angular uncertainty, one must also account for the kinematic angle ψ—which quantifies the deviation between the true muon and its parent neutrino direction (Eq. 4.5). The total angular uncertainty is thus given by

$$\sigma = \sqrt{\sigma_{\mathrm{BDT}}^2 + \psi^2}\,, \tag{4.17}$$

where σ_{BDT} represents the BDT-estimated angular resolution. This additional contribution is incorporated into the point-spread function introduced in Chapter 5.

4.3.3 Energy reconstruction

The average energy loss of a muon per unit length as it propagates through ice can be approximated using the Bethe-Bloch formula [29]

$$\left\langle \frac{\mathrm{d}E_\mu}{\mathrm{d}x} \right\rangle = -(a + bE_\mu), \tag{4.18}$$

where both $a(E)$ and $b(E)$ are energy-dependent coefficients.

A muon with an initial energy of $E_\mu \gtrsim 300$ GeV—near IceCube's In-Ice Array lower sensitivity limit—is likely to propagate approximately 1 km in ice before stopping [352]. This poses a challenge for track reconstruction in IceCube, as the muon's energy cannot be directly inferred from its track alone.

Muon energy loss occurs primarily through two mechanisms: ionization, represented by parameter a in Eq. (4.18), and radiative processes, described by parameter b. Below approximately 1 TeV, energy loss is dominated by continuous ionization, whereas at higher energies, radiative losses—such as bremsstrahlung, pair production, and photonuclear interactions—become the dominant contribution. Due to the stochastic nature of these high-energy losses, energy deposition varies significantly among muons with the same initial energy, introducing additional challenges for energy reconstruction at $E_\mu \gtrsim 1$ TeV.

The following discusses two algorithms that estimate a muon's energy when it enters the detector volume. Each algorithm handles stochastic energy losses differently.

[7] In the rare case that the paraboloid fit fails, the corresponding parameter is treated as missing in the BDT input.

One algorithm is the truncated-energy algorithm ([352]) and the other is a deep neural network-based approach ([16, 338]). The latter is used for the final energy estimates for the event sample introduced in Section 4.4 and analyzed in Chapters 5 and 6, while the former—commonly used in high-level analyses—is presented here to illustrate the improvements achieved with the deep neural network.

Truncated Energy Reconstruction

To mitigate the influence of stochastic energy losses, the truncation strategy described in [352] and presented below can be used.

Given a reconstructed track direction, the algorithm estimates the local energy loss ($\mathrm{d}E/\mathrm{d}x$) in track-aligned segments, or bins, perpendicular to the track. In each segment, the number of detected photoelectrons (charge) is compared to the expected charge from a muon undergoing a constant energy loss of $1\ \mathrm{GeV\ m^{-1}}$ along the track direction. Various bin sizes have been investigated; in the configuration of interest here, each DOM serves as an individual bin. In this case, since photon yield and energy loss are linearly related,

$$\frac{\mathrm{d}E}{\mathrm{d}x} = \frac{q_{\mathrm{obs}}}{q_{1\mathrm{GeV}}}\ \mathrm{GeV\ m^{-1}}, \tag{4.19}$$

where q_{obs} is the observed charge at the DOM, and $q_{1\mathrm{GeV}}$ is the tabulated charge for a muon losing energy at a rate of $1\ \mathrm{GeV\ m^{-1}}$ along the reconstructed track. To ensure reliability, only DOMs within a 60 m-diameter cylindrical region centered on the track are considered by the algorithm.

To obtain a stable estimate of the muon's energy loss, the truncated mean energy loss $\langle \mathrm{d}E/\mathrm{d}x \rangle$ is computed by averaging the lowest 50% of the $\mathrm{d}E/\mathrm{d}x$ values across all DOMs. This truncation reduces the impact of large stochastic losses, which would otherwise skew the estimate and increase variance. Assuming the muon's energy remains approximately constant along the track, this truncated energy loss serves as an estimator for the muon's energy upon entering the detector via Eq. (4.18). See [352] for further details on this truncated method.

As illustrated in Figure 4.9, the truncated-energy approach leads to a degenerate energy reconstruction below approximately $1\ \mathrm{TeV}$ [16], reducing the discrimination power for events in this energy range. This behavior is not un-expected, as the truncation algorithm primarily stabilizes against stochastic energy losses, which are subdominant below $1\ \mathrm{TeV}$. In this regime, ionization energy loss dominates, resulting in continuously stopping tracks with relatively few recorded hits. Consequently, truncating information in this low-energy range introduces instabilities in the reconstruction.

Energy reconstruction using a deep neural network

An alternative approach for reconstructing the energy of up-going muons upon entering the detector is based on a deep neural network. Unlike the truncated-energy algorithm, a deep neural network can leverage the full event information. The network is trained on approximately 6 million up-going muon tracks. This method enhances the energy resolution by up to 50% across the entire energy range and effectively resolves the degeneracy below $1\ \mathrm{TeV}$ observed in the truncated-energy algorithm [16, 338], as shown in Figure 4.9.

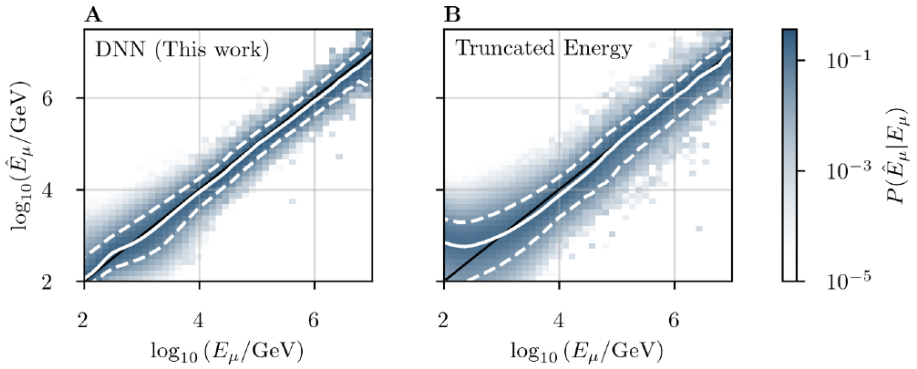

FIGURE 4.9: Comparison between the estimated and true muon energy from simulations using (A) the deep neural network–based approach and (B) the truncated energy approach. The solid white line indicates the median, while the dashed white lines represent the central 90% quantile. The black solid line denotes an ideal unbiased estimator. Figure taken from [16].

This deep neural network is used to estimate the final reconstructed energies of the event selection used for the point-source search of high-energy neutrinos presented in Chapters 5 and 6. As this event sample is dominated by lower-energy atmospheric events, a large fraction of the sample is affected by the improvement. Furthermore, the unbiased energy estimation allows to improve the kinematic angle correction, which is more prominent for lower energy neutrinos.

4.4 Event Selection: Up-Going Tracks

Given their excellent angular resolution, track-like events are frequently used in point-source searches of high-energy neutrinos. However, in IceCube, this signature is predominantly produced by atmospheric muons originating from the Southern Hemisphere, but also by atmospheric muon neutrinos from all over the sky (See Section 4.2.5).

To mitigate this background, we consider in this work only up-going muon tracks, relying on the Earth's core and the ice overburden as passive shields (see also Figure 2.9). While this effectively suppresses the atmospheric muon background from the Northern Hemisphere, the all-sky atmospheric neutrino background remains.

The up-going muon track event selection used in this work was originally developed for diffuse astrophysical neutrino searches [16, 170] and was later employed in the point-source search that led to the identification of NGC 1068 as a highly promising neutrino source [16]. In contrast to the latter, and following the seminal work of [144, 353], the final sample of tracks used for the point-source analysis in this work includes three additional data-taking seasons. These incorporate the full IceCube array, referred to as **IC86**, as well as about 1 year of data collected using an earlier, incomplete configuration with 79 strings, known as **IC79**. This results in a total of about 13 years of experimental data, with 4 additional years over the point-source search in [16].

The following provides a short overview of the various steps between trigger level at the South Pole and the final up-going muon-track sample that will be used as input for the point-source searches outlined in Chapters 5 and 6:

- **Level 1**: The event selection process in this work starts with events that pass the SMT-8 trigger and pass the online muon filter (Section 4.2.3). The online muon filter is designed to identify well-reconstructed, high-energy track-like events at the South Pole. This is achieved by applying cuts based on combinations of zenith-angle thresholds—determined using computationally inexpensive directional reconstruction algorithms such as LineFit and SPE fit (Section 4.3)—the number of DOMs that recorded a hit, and the total detected charge, which serves as a proxy for the muon energy. This filtering process reduces the data rate from approximately 2.1 kHz at the SMT-8 level, dominated by atmospheric muons from the Southern Hemisphere, to about 34 Hz [354]. This data stream is still dominated by atmospheric muons. Events that pass this initial filtering stage, referred to as level 1, are transmitted to the Northern Hemisphere for further offline processing.

- **Level 2**: Due to limited computational resources at the South Pole, most online computations are discarded and reprocessed offline using more powerful computing systems. This also involves slightly more sophisticated reconstruction algorithms as less constraints apply. However, the number of events is still large thus the most complex algorithms cannot be me applied yet. This is referred to as level 2 processing.

- **Level 3**: It is computationally not feasible to reconstruct all events from offline level 2 using the most advanced reconstruction algorithms available in IceCube. Therefore, muon level 3 efficiently reduces the atmospheric muon background while retaining the majority of muon neutrino events [354].

  The level 3 processing consists of several steps. First, a pre-selection is applied to suppress mis-reconstructed low-energy events. This includes a cut on the total charge of an event or the average DOM distance from the track weighted by the total charge of each DOM.

  Next, the detector readout window is analyzed and split into individual physics events, as multiple unrelated primary particles could have been recorded within the same readout. Since most reconstruction algorithms assume a single primary particle per event, this step is essential. However, imperfections in the splitting process could mistakenly separate hits from a single particle into multiple events, an effect that is accounted for at this level. Then, directional reconstruction is performed on the individual events. Finally, the muon level 3 cut [354] is applied to further reduce the data rate while maintaining a high selection efficiency for neutrino-induced tracks. This leaves a rate of a few Hz. At this stage, computationally expensive reconstructions can be applied such as the SpineMPE fit.

  To suppress the overwhelming muon background, we only consider up-going events, i.e. a zenith angle with $\theta \geq 85^\circ$ ($\delta \geq -5^\circ$), as for this region muons pass through a significant ice overburden, exceeding 12 km water equivalent, which efficiently stops atmospheric muons [7].

- **Level 4 & 5** The atmospheric muons that remain at this stage are down-going muons mis-reconstructed as up-going. The astrophysical neutrino event candidates are separated from the muon background by reconstruction quality. To

do so, boosted decision trees are used: one that identifies cascade-like events mis-reconstructed as high-energy muon tracks and a second one that separates muon-neutrino induced signal from atmospheric muon tracks [354].

Note: to ensure stability, only data-taking runs are considered with no more than 100 non-operational DOMs.

After levels 4 and 5, the boosted decision tree from Section 4.3.3 is applied to obtain an uncertainty on the reconstructed direction per event, where the direction is determined via the SplineMPE (Section 4.3). Furthermore, the deep neural network outlined in Section 4.3.3 is applied to obtain an energy reconstruction of each event. Events with reconstructed energies below 100 GeV are discarded and the minimum angular uncertainty per event is set to 0.1° to provide a floor value.

In the final selection 991499 high-energy neutrino events remain, over a livetime of about 4767.31 days, which corresponds to a rate of 207.98 per day or 2.41 mHz. From simulations, the expected atmospheric neutrino rate is 2.39 mHz and the astrophysical neutrino rate is 9.8 μHz [144].

Number of Events	Livetime [days]	Time Period
991499	4767.31	IC79 2010 and IC86 2011–2022 season

TABLE 4.1: Properties of the up-going muon-track event selection used in the IceCube source searches in Chapters 5 and 6. The total of 13 years for this dataset is comprised of about 0.8 years of IC79 data and 12.2 years of IC86 data.

4.4.1 Detector simulations

The up-going muon-track sample used in this work includes experimental data from both the IC86 configuration and the earlier, incomplete IC79 detector configuration. Below, we provide an overview of the Monte Carlo (MC) simulations corresponding to each configuration, which will be used in our calculations in Chapters 5 and 6.

IC86

Following [144, 353], the MC simulations used in this work double the statistics opposed to the analysis that identified NGC 1068 (IC86 2011-2019) [16, 338]. Moreover, the MC data now includes tau neutrinos, which are of interest as they improve the detection efficiency for high declinations. This is explained by a *regeneration* mechanism:

- **Regeneration mechanism:** The Earth becomes increasingly opaque to high-energy neutrinos due to the energy-dependent interaction cross section (see also Figure 4.6). When a muon neutrino undergoes a charged-current (CC) interaction, the resulting muon loses energy gradually through further interactions while traversing the Earth. In contrast, a tau neutrino interacting via a CC interaction produces a tau that decays rapidly, owing to its larger mass and shorter lifetime, regenerating a secondary, lower-energy tau neutrino [355]. This so-called *regeneration* mechanism enhances the detector's sensitivity to tau neutrinos at high energies and high declinations. It is important to note, however, that the initial tau neutrino may also lose energy during propagation due to neutral-current (NC) interactions within the regeneration chain.

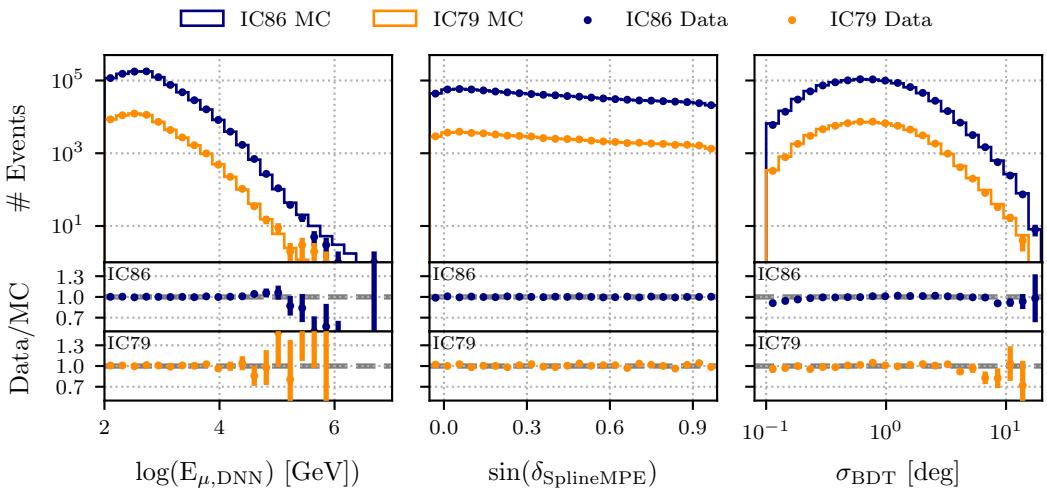

FIGURE 4.10: Comparison of data and Monte Carlo (MC) simulations for the IC86 (navy blue) and IC79 (dark orange) configurations. The observables shown are the DNN-based muon energy reconstruction ($E_{\mu,\mathrm{DNN}}$), the angular uncertainty from the SplineMPE reconstruction algorithm ($\delta_{\mathrm{SplineMPE}}$), and the angular uncertainty per event from a boosted decision tree (σ_{BDT}). The upper panels show the distributions for data and MC, while the lower panels display the corresponding Data-to-MC ratios. Figure adapted from [144].

Approximately 28 million MC events, simulated using the IC86 detector configuration, are used in this analysis. Figure 4.10 compares experimental data with MC simulations for both the IC86 and IC79 configurations, the latter of which is discussed in detail later. The observables relevant for track reconstruction, as described in Section 4.3, are shown. These include the muon energy reconstructed using a deep neural network ($E_{\mu,\mathrm{DNN}}$), the angular uncertainty from the SplineMPE directional reconstruction algorithm ($\delta_{\mathrm{SplineMPE}}$), and the per-event angular uncertainty estimated using a boosted decision tree (BDT) method (σ_{BDT}). As shown in Figure 4.10, the agreement between data and simulation is generally excellent, with discrepancies limited to the percent level in the highest energy bins.

Additional details about the simulation datasets and their properties are provided in the appendix of [144].

IC79

The IC79 configuration differs from IC86 in the In-Ice Array due to the absence of 5 strings.[8] However, the MC data from IC86 does not match the experimental data from IC79. To address this discrepancy, a MC dataset for IC79 was constructed in a separate analysis by applying the processing pipeline described in Section 4.4, starting from level 2, while removing all pulses recorded by the strings added between IC79 and IC86 [144, 353].[9] As shown in Figure 4.10, this approach results in good agreement between MC and experimental data for IC79 [144, 353].

[8] Two additional strings correspond to the DeepCore array.

[9] A large-scale MC dataset does not exist for this older configuration, and generating one would be computationally expensive.

4.4.2 Effective area

Consider a neutrino point source located at $\boldsymbol{r}_{\rm src} = (\alpha_{\rm src}, \delta_{\rm src})$, where $\alpha_{\rm src}$ and $\delta_{\rm src}$ denote the right ascension and declination of the source, respectively. Assuming that this source emits a neutrino flux described by the energy-dependent spectrum $\Phi_\nu(E_\nu)$, the expected number of detected high-energy neutrinos over an observation time T is given by

$$N_\nu = T \int_0^\infty A_{\rm eff}(E_\nu|\alpha_{\rm src}, \delta_{\rm src})\Phi_\nu(E_\nu)\,{\rm d}E_\nu, \tag{4.20}$$

where $A_{\rm eff}(E_\nu|\alpha_{\rm src}, \delta_{\rm src})$ is the so-called **effective area**. This quantity accounts for several physical and detector-related factors, including: the scattering probability of the neutrino near or within the detection volume—based on the deep-inelastic scattering cross section (Figure 4.2)—the energy-dependent transmission probability of high-energy neutrinos propagating through the Earth (Figure 4.6), and the detector's response to neutrinos of different flavors, energies, and declinations. Note that the effective area accounts for both neutrinos and antineutrinos as usually the distinction cannot be made with IceCube.

Since the event selection criteria affect the detector's sensitivity, different final event samples result in distinct effective areas. The left panel of Figure 4.11 presents the effective area derived from a dedicated MC simulation tailored to the up-going muon-track sample introduced in Section 4.4, assuming the IC86 detector configuration. The effective area is shown for three declination ranges. At the highest energies, the effective area decreases with increasing declination, as expected due to the reduced transmission probability of high-energy neutrinos traversing larger lengths through the Earth (see Figure 4.6).

The right panel of Figure 4.11 displays the ratio of the effective areas of IC86 and IC79, integrated over the Northern Sky ($-5° < \delta < 90°$). The additional strings in IC86 lead to an increased detection volume and, consequently, an approximately 10% larger effective area. Note that the highest energies corresponds to a low-statistics region.

Finally, Figure 4.12 illustrates the impact of including tau neutrinos. As previously discussed, at the highest energies, the effective area increases with declination when tau neutrinos are accounted for due to the regeneration process.

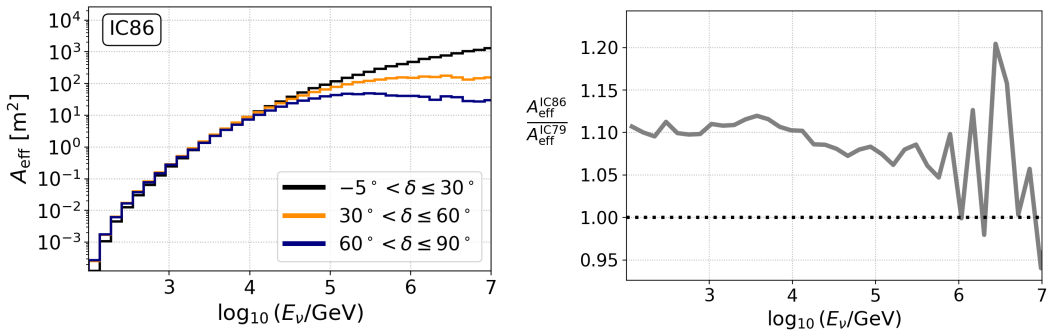

FIGURE 4.11: Left panel: Effective area as a function of neutrino energy for the IC86 configuration constructed from Monte Carlo (MC) simulations for three declinations. Right panel: Effective area fraction of IC86 over IC79 integrated over all declinations as a function of energy.

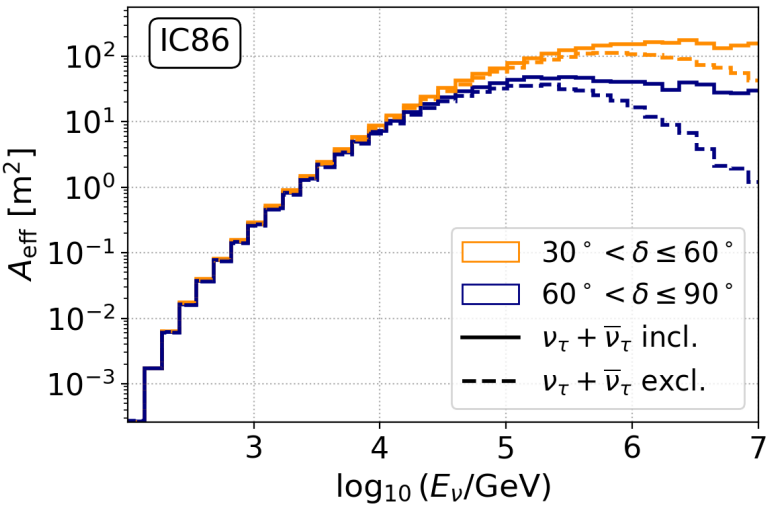

FIGURE 4.12: Effective area for the IC86 configuration for the declination ranges $30° < \delta \leq 60°$ (orange) and $60° < \delta \leq 90°$ (blue). The solid line represents the inclusion of tau (anti)neutrinos, while the dashed lines indicate their exclusion.

4.5 IceCube Realtime System

Multi-messenger astronomy uses different types of cosmic messengers—such as electromagnetic radiation, gravitational waves, and neutrinos—to extract information from a common astrophysical source. The temporal and/or spatial coincidence of two or more messengers can help identify the source through directional correlation. To support this effort, the IceCube Collaboration has developed a low-latency, real-time neutrino alert system [159]. This system facilitates rapid follow-up observations by other observatories, thereby enhancing the likelihood of detecting astrophysical counterparts to high-energy neutrinos.

Since the system update in 2019 [160], through-going track events have been classified based on their *signalness*, i.e., the probability that a high-energy neutrino is of astrophysical origin, defined as

$$\text{Signalness}(\delta, E) = \frac{N_{\text{signal}}(\delta, E)}{N_{\text{signal}}(\delta, E) + N_{\text{background}}(\delta, E)} \,. \tag{4.21}$$

N_{signal} and $N_{\text{background}}$ represent the number of signal and background neutrino events for declination (δ) above a selection-specific energy proxy. Depending on the signalness of an event, it is classified into one of two categories: **bronze alerts**, with a signalness between 30% and 50%, and **gold alerts**, with a signalness above 50%.

For each alert, a General Coordinates Network (GCN) Notice[10] is issued. This is a computer-readable message containing key information such as the reconstructed direction and angular uncertainty of the neutrino, estimated via the SplineMPE method (see Section 4.3). After a few hours, a GCN Circular[11] is released, providing results from more sophisticated reconstruction algorithms.

Alerts have facilitated follow-up campaigns, including searches for electromagnetic or gravitational sources. Particularly, the IceCube alert IC170922A resulted in

[10] https://gcn.nasa.gov/notices
[11] https://gcn.nasa.gov/circulars

the identification of the blazar TXS 0506+056 as the first possible high-energy neutrino source ([14]; also Section 1.6).

Of particular interest to our study is the fact that the IceCube real-time system identified two high-energy neutrino alerts—one bronze (IC230416A) and one gold (IC220424A)—that are spatially coincident with the most significant source identified in the IceCube point-source search presented in Chapters 5 and 6. The connection between these alerts and the source, along with their implications, is discussed in detail in Chapter 6.

4.6 IceCube Upgrade & Gen2

At present, the **IceCube Upgrade** is under construction. A total of 7 strings will be deployed within the existing IceCube array, specifically within the DeepCore array. These new strings will host 750 novel photosensors at depths ranging from 2150 m to 2425 m, with a horizontal spacing of 20 m and a vertical spacing of 3 m. Figure 4.13 shows how IceCube upgrade will be embeded in the current IceCube array.

The newly deployed photosensors include the multi-PMT Digital Optical Module (mDOM; [356]) and the Dual optical sensors in an Ellipsoid Glass for Gen2 (D-Egg; [357]). These novel designs aim to enhance photon detection efficiency and improve the detector's calibration capabilities. The IceCube Upgrade is designed to extend IceCube's sensitivity down to the GeV scale while enabling detailed calibrations of the ice properties.

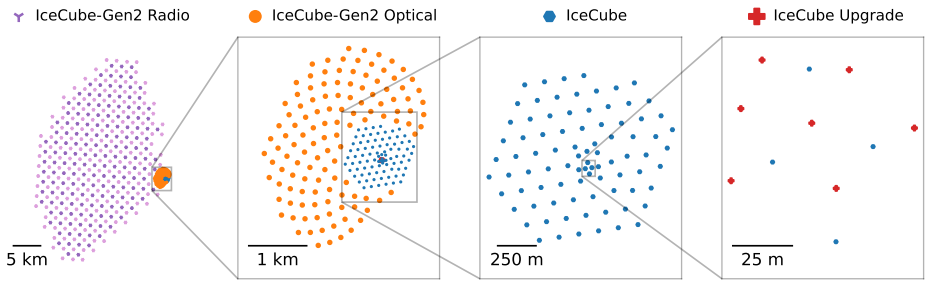

FIGURE 4.13: Surface geometry of IceCube upgrade, IceCube, IceCube-Gen2 optical, and IceCube-Gen2 radio. Taken from [113].

The IceCube Upgrade lays the groundwork for **IceCube-Gen2** [113], the next-generation expansion of the IceCube Neutrino Observatory. The preliminary baseline design of the optical component includes 120 new strings, instrumenting an 8 km^3 volume that will encompass the existing detector, as illustrated in the top view shown in Figure 4.13. The strings are planned to be spaced approximately 240 m apart, each equipped with 80 advanced DOMs deployed between depths of 1325 m and 2575 m, with a vertical spacing of 16 m. This expansion will increase the total number of optical sensors to 9600 DOMs, significantly improving IceCube's capability to detect and reconstruct high-energy neutrino interactions. The larger instrumented volume is expected to enhance sensitivity by at least a factor of five.

As discussed in Section 3.3, the enhanced sensitivity expected from the IceCube-Gen2 configuration would make it possible to test optimistic scenarios for high-energy neutrino emission driven by starburst activity in nearby (ultra)luminous infrared galaxies, as described by the model introduced in Chapter 3. In addition, the improved sensitivity would allow for a more precise characterization of the diffuse astrophysical

neutrino spectrum, enabling more accurate modeling of high-energy neutrino production from cosmologically distributed source populations. As outlined in Section 3.6, such modeling can be pursued by coupling cosmological hydrodynamical simulations with phenomenological neutrino emission models, such as the one presented in Chapter 3.

IceCube-Gen2 also plans a radio detection array designed to probe neutrino energies in the PeV to EeV energy range. The preliminary baseline design consists of 200 radio detection stations, illustrated in Figure 4.13, deployed both at the surface and about 200 m deep, covering an area of approximately 500 km^2. This component will significantly extend IceCube's reach to the highest-energy neutrinos, complementing the optical array and enabling a multi-component detection strategy spanning from GeV to EeV energies.

CHAPTER 5

IceCube Search for Neutrino Emission from GOALS Galaxies

A key scientific objective of IceCube, and neutrino telescopes more broadly, is the identification of point sources of high-energy neutrinos. Early searches relied on binned Poisson statistics to identify excess high-energy neutrino counts from a specific source direction [358]. However, subsequent analyses predominantly adopted an unbinned likelihood formalism [359], which enhances sensitivity and enables the estimation of the source spectral index. This likelihood-based approach has since become the standard within the IceCube Collaboration.

Initially, the implementation of this method included a suboptimal treatment of probability density functions (PDFs) within the likelihood function, leading to biases in inferred parameters. To address this, the IceCube Collaboration refined the approach by constructing PDFs directly from Monte Carlo (MC) simulations using kernel density estimation [16, 338]. This method relies on excellent data-MC agreement, achieved through recent advancements in reconstructing key observables and increased statistics. These improvements, detailed in [16, 338], significantly reduce biases, lower parameter variance, and enhance the discovery potential of point-source searches.

We will investigate (ultra)luminous infrared galaxies (U/LIRGs) from the Great Observatories All-sky LIRG Survey (GOALS) as potential sources of high-energy neutrinos. To do so, we apply in this work the improved likelihood formalism to the up-going muon-track sample introduced in Section 4.4. The scientific motivation for studying GOALS U/LIRGs is discussed in detail in Chapters 2 and 3.

We perform several types of time-integrated point-source searches:

- **Catalog search & binomial test**: We search for individual high-energy neutrino emission from the directions of 113 GOALS U/LIRGs with declinations $\delta > -3^\circ$ (see Section 2.3.3 for more details on the source selection).

  Additionally, we apply a binomial test to determine whether a subset of these sources forms a population of high-energy neutrino emitters.

- **Stacking search**: We test for an aggregated neutrino signal from 10 GOALS U/LIRGs with vibrationally excited hydrogen cyanide emission (HCN-vib; Section 2.1.2) and $\delta > -3^\circ$. See Section 2.1.2 for the scientific motivation of investigating these sources and Section 2.3.3 for the source selection.

The qualitative differences between these search strategies were discussed in Section 1.6.1. In this chapter, we introduce the corresponding mathematical formalisms.

Overview & Context Section 5.1 provides an overview of the statistical formalism employed in the time-integrated point-source searches presented in this work. In Section 5.2, we evaluate the performance of the statistical analysis using MC simulations.

5.1 Statistical Formalism

Consider the up-going muon-track sample introduced in Section 4.4.[1] Each event $i \in \{1, \ldots, N\}$ in this dataset is characterized by several measured properties, including the incoming direction of the initial particle, the uncertainty in its angular direction, and the deposited energy within the detector (Section 4.3). These measured quantities provide the basis for inferring the parameters that describe the underlying physical processes generating the events observed in the detector.

Let $\boldsymbol{x} = (x^1, \ldots, x^p)$ represent the p measurable physical quantities of an event, and let $\boldsymbol{x}_i = (x_i^1, \ldots, x_i^p)$ denote these quantities for event i. The probability of obtaining an event with these measured properties is described by the PDF, $\mathcal{P}(\boldsymbol{x}_i|\boldsymbol{\theta})$, which depends on a set of parameters $\boldsymbol{\theta} = (\theta^1, \ldots, \theta^q)$ that characterize the underlying physics governing the observed data.

To infer the parameters describing the underlying physics, we introduce the likelihood function $\mathcal{L}(\boldsymbol{\theta})$, defined as

$$\mathcal{L}(\boldsymbol{\theta}|\{\boldsymbol{x}_i\}) = \prod_{i=1}^{N} \mathcal{P}\left(\boldsymbol{x}_i|\boldsymbol{\theta}\right) \ . \tag{5.1}$$

The likelihood function then allows to estimate the probability of obtaining the observed data $\{\boldsymbol{x}_i\}$ for particular model parameters $\boldsymbol{\theta}$.[2] The parameters that best fit the data, known as the maximum-likelihood estimators (MLEs), are those that maximize the likelihood function over the full parameter space $\boldsymbol{\Theta}$. The MLEs are thus defined as,

$$\hat{\boldsymbol{\theta}} \equiv \arg\max_{\boldsymbol{\theta} \in \Theta} \mathcal{L}(\boldsymbol{\theta}). \tag{5.2}$$

If the likelihood function $\mathcal{L}$ is differentiable, the MLEs can be found by solving the likelihood equations,

$$\frac{\partial \mathcal{L}}{\partial \theta^i} = 0, \quad \text{for } i = 1, \ldots, q \ , \tag{5.3}$$

where $\boldsymbol{\theta} = \{\theta^1, \ldots, \theta^q\}$ denotes the set of underlying physics parameters.

Since the likelihood function is a product of PDFs, solving these equations directly can be challenging. Therefore, it is common practice to work with the *log-likelihood* function, which simplifies computations,

$$\ln \mathcal{L}(\boldsymbol{\theta}|\{\boldsymbol{x}_i\}) = \sum_{i=1}^{N} \ln \mathcal{P}(\boldsymbol{x}_i|\boldsymbol{\theta}). \tag{5.4}$$

The MLEs possess several convenient properties:

- **Consistency**: An estimator $\hat{\theta}$ is consistent if it converges to the true parameter θ_t as the sample size increases indefinitely:

$$\hat{\theta} \to \theta_t \quad \text{as} \quad N \to \infty. \tag{5.5}$$

[1] The discussion can be generalized to any event selection, but the focus in the remainder of this work will be on the up-going muon-track sample (Section 4.4).

[2] This assumes that all PDFs are identical and that the events are independent.

- **Asymptotic Normality**: In the asymptotic limit ($N \to \infty$), the estimator $\hat{\theta}$ follows a normal distribution centered around the true value θ_t with variance σ_t^2:

$$\sqrt{N}(\hat{\theta} - \theta_t) \to \mathcal{N}(0, \sigma_t^2). \tag{5.6}$$

In order to asses the statistical significance of the obtained MLEs, a statistical hypothesis test must be performed. The framework of statistical hypothesis testing is discussed in next section.

5.1.1 Hypothesis test

The maximum likelihood framework provides a robust method for statistical hypothesis testing, assessing whether observed data support a given hypothesis. Typically, a null hypothesis and an alternative (signal) hypothesis are defined, and the data are used to either reject or retain the null hypothesis. In the context of this work:

- **Null hypothesis** ($\mathcal{H}_0$): The observed data consists solely of atmospheric background and a contribution from the diffuse high-energy neutrino flux. The null hypothesis will also be referred to as the background-only hypothesis.
- **Alternative (signal) hypothesis** ($\mathcal{H}_1$): In addition to atmospheric background and diffuse astrophysical neutrinos, the dataset includes signal neutrinos from one or more steady[3] neutrino sources. The signal hypothesis will also be referred to as the signal-plus-background hypothesis.

  This work focuses on two types of signal searches, each introducing a different signal hypothesis test:

  - **Single-source search:** the signal neutrinos originate from a point source at $\boldsymbol{r}_{\mathrm{src}} = (\alpha_{\mathrm{src}}, \delta_{\mathrm{src}})$, where α_{src} and δ_{src} denote the source's right ascension and declination.
  - **Stacking search:** the signal neutrinos are an aggregated signal from multiple neutrino-emitting point sources across the sky.

  In both cases, the signal hypothesis assumes that the source(s) contribute an additional high-energy neutrino flux,

$$\Phi_\nu = \Phi_0 \left(\frac{E_\nu}{E_0} \right)^{-\gamma},$$

  with E_ν the neutrino energy, Φ_0 the flux normalization at the energy E_0, and γ the spectral index. This flux results in a number of signal neutrinos observed by the detector.

  We note that, while the neutrino spectrum is not necessarily limited to a power-law form, this model is assumed throughout the analysis.

Test Statistic

To distinguish between the signal and null hypotheses, we employ a so-called test statistic (TS) based on the likelihood-ratio test originally introduced by Neyman and Pearson [360]. In IceCube point-source analyses, the TS is typically defined as

[3] Similar hypothesis tests for time-dependent searches also exist (e.g. [153]; also Section 1.6.1), but are not covered in this work.

$$\mathrm{TS} = 2\ln\left[\frac{\sup_{\boldsymbol{\theta}\in\boldsymbol{\Theta}}\mathcal{L}(\boldsymbol{\theta})}{\sup_{\boldsymbol{\theta}\in\boldsymbol{\Theta}_b}\mathcal{L}(\boldsymbol{\theta})}\right] = 2\ln\left[\frac{\mathcal{L}(\hat{\boldsymbol{\theta}})}{\mathcal{L}(\boldsymbol{\theta}_b)}\right], \tag{5.7}$$

where $\hat{\boldsymbol{\theta}}$ and $\boldsymbol{\theta}_b$ denote the maximum likelihood estimates (MLEs) under the signal ($\mathcal{H}_1$) and null ($\mathcal{H}_0$) hypotheses, respectively. Under the null hypothesis $\mathcal{H}_0$, representing a background-only scenario, the parameter vector $\boldsymbol{\theta}_b$ is fixed and contains no free parameters. In contrast, under the alternative hypothesis $\mathcal{H}_1$, and assuming known source location(s), the free parameters include the number of signal events n_s (linked to the flux normalization Φ_0) and the spectral index γ, such that $\hat{\boldsymbol{\theta}} = (n_s^{\mathrm{fit}}, \gamma_{\mathrm{fit}})$.

In the fitting procedure, we impose the physical bound[4] $\hat{n}_s \geq 0$ and restrict the spectral index to $\gamma \in [0.5, 4.4]$. Although this latter bound is somewhat arbitrary, it is well motivated: theoretical considerations suggest $\gamma \sim 2$ (see Section 1.1.3), and diffuse high-energy neutrino observations indicate $2 < \gamma < 3$ (see Section 1.4).

Since the null hypothesis is nested within the alternative (with $n_s = 0$, or equivalently $\Phi_0 \to 0$), Wilks' theorem implies that, in the asymptotic limit of large sample size N, the TS distribution under $\mathcal{H}_0$, denoted $\mathcal{T}_b$, approaches a chi-square distribution [361]:

$$\mathcal{T}_b \to \chi^2_\nu \,. \tag{5.8}$$

The degrees of freedom ν correspond to the difference in dimensionality between the full and null parameter spaces: $\nu = \dim(\boldsymbol{\Theta}) - \dim(\boldsymbol{\Theta}_b)$. For the current analysis, since the null hypothesis has no free parameters, we expect $\nu = 2$.

The TS distributions under both the background-only ($\mathcal{T}_b$) and signal ($\mathcal{T}_s$) hypotheses are obtained through repeated pseudo-experiments. These are generated either by scrambling the experimental data or via Monte Carlo simulations tuned to reflect the observed conditions. The detailed procedure is outlined in Section 5.2.

p-value, significance, and power

For $\hat{\boldsymbol{\theta}} = \boldsymbol{\theta}_b$, the data are most consistent with background, yielding $\mathrm{TS} = 0$. Any deviation ($\hat{\boldsymbol{\theta}} \neq \boldsymbol{\theta}_b$) results in $\mathrm{TS} > 0$, potentially indicating point-source neutrinos. The significance of this deviation is assessed using the **p-value** defined as,

$$\mathrm{p} = \int_{\mathrm{TS}_{\mathrm{obs}}}^{\infty} \mathcal{T}_b(\mathrm{TS}')\,\mathrm{dTS}', \tag{5.9}$$

where $\mathrm{TS}_{\mathrm{obs}}$ is computed from the observed data. The p-value represents the probability of obtaining $\mathrm{TS} \geq \mathrm{TS}_{\mathrm{obs}}$ under $\mathcal{H}_0$, measuring the consistency of the observed TS with background expectations. A smaller p-value indicates lower compatibility with $\mathcal{H}_0$.

In fact, before testing the hypothesis is conducted, a **significance** level α is chosen which is defined as,

$$\alpha = \int_{\mathrm{TS}_{\mathrm{thr}}}^{\infty} \mathcal{T}_b(\mathrm{TS}')\,\mathrm{dTS}'. \tag{5.10}$$

[4]While negative values of $\hat{n}_s$ are computationally feasible—corresponding to underfluctuations in the data—we choose to enforce the physical constraint $\hat{n}_s \geq 0$, consistent with the fact that a negative number of signal events is unphysical.

	$\mathcal{H}_0$ **True**	$\mathcal{H}_0$ **False**
$\mathcal{H}_0$ **is not rejected**	Correct Decision	Type II Error (False Negative)
$\mathcal{H}_0$ **is rejected**	Type I Error (False Positive)	Correct Decision

TABLE 5.1: Type I and Type II errors in hypothesis testing.

The threshold $\mathrm{TS}_{\mathrm{thr}}$ is set by the chosen significance level. If $\mathrm{p} \leq \alpha$, $\mathcal{H}_0$ is rejected in favor of $\mathcal{H}_1$, suggesting the presence of a neutrino point source(s) in the tested direction(s). In (astro)particle physics, common significance levels are:

- **Evidence**: $\geq 3\sigma$ significance, corresponding to $\alpha = 1.35 \times 10^{-3}$.
- **Discovery**: $\geq 5\sigma$ significance, corresponding to $\alpha = 2.87 \times 10^{-7}$.

The significance level α represents the probability of a Type I error (false positive), as shown in Table 5.1. Under the alternative hypothesis $\mathcal{H}_s$, the probability of a Type II error (false negative) is given by

$$\beta = \int_0^{\mathrm{TS}_{\mathrm{thr}}} \mathcal{T}_s(\mathrm{TS}')\,\mathrm{dTS}' \,. \tag{5.11}$$

The **power** of the analysis is defined as the complementary probability $1-\beta$. Since power depends on the signal hypothesis, the goal of the analysis is to maximize it, ensuring the highest sensitivity to potential signals.

In conclusion, given a signal hypothesis involving one or more neutrino point sources located in specific directions and expected to contribute to a dataset, a test statistic (TS) is computed. This TS is designed to quantify the deviation from the null hypothesis, which assumes that no point sources contribute to the data. The computed TS is then compared to the distribution of TS values expected under the background-only hypothesis to estimate a p-value. The p-value quantifies the compatibility of the observed data with the null hypothesis; that is, the null hypothesis is rejected in favor of the signal hypothesis only if the p-value is less than or equal to a predefined significance threshold required to claim evidence.

To carry out such an analysis, however, an explicit form of the likelihood function must be constructed, followed by the definition of a procedure to derive the background-only TS distribution. As discussed in the following sections, the specific form of the likelihood depends on the nature of the source search under consideration. Moreover, before applying the analysis to experimental data, a series of validation steps must be carried out using simulated datasets that accurately reproduce the characteristics of the observed data. These procedures are detailed in the subsequent sections.

5.1.2 Single-source search

As outlined in the previous section, the TS—defined in Eq. (5.7)—is a central quantity in neutrino-source searches as it enables hypothesis testing. The exact form of the TS, which is essentially determined by the likelihood function, depends on the specific type of search under consideration.

In this section, we focus on the form of the TS corresponding to the hypothesis where a single neutrino source contributes to the observed data. In addition, we introduce the concept of a catalog search, which can be understood as a single-source search for each source within a predefined catalog, with an additional statistical penalty for investigating multiple locations for a possible signal. It is important to distinguish a catalog search from a stacking search, where the cumulative signal from multiple sources is analyzed together. A technical discussion on the stacking search is given in Section 5.1.4.

Single-source likelihood function

For searches involving a single source, the likelihood function is typically modeled as a combination of a signal PDF, $\mathcal{P}_s(\boldsymbol{x}_i|\boldsymbol{\theta}_s)$, and a background PDF, $\mathcal{P}_b(\boldsymbol{x}_i|\boldsymbol{\theta}_b)$, weighted by the expected number of signal (n_s) and background (n_b) events, normalized by the total event count, $n_s + n_b$.

Given that the total number of observed events, N, follows a Poisson distribution, $N \sim \text{Poisson}(n_s + n_b)$, this must be explicitly accounted for in the likelihood. The complete likelihood function for a single point source is therefore,

$$\mathcal{L}(\boldsymbol{\theta} \mid N, \{\boldsymbol{x}_i\}) = \frac{(n_b + n_s)^N}{N!} e^{-(n_s+n_b)} \times \prod_{i=1}^{N} \left[\frac{n_s}{n_b + n_s} \mathcal{P}_s(\boldsymbol{x}_i \mid \boldsymbol{\theta}_s) + \frac{n_b}{n_s + n_b} \mathcal{P}_b(\boldsymbol{x}_i \mid \boldsymbol{\theta}_b) \right]. \tag{5.12}$$

By obtaining the maximum-likelihood estimators, $\hat{\boldsymbol{\theta}} = (n_s^{\text{fit}}, \gamma_{\text{fit}})$, using the experimental data $\{\boldsymbol{x}_i\}$, and substituting Eq. (5.12) into Eq. (5.7), the TS is expressed as

$$\text{TS} = 2 \sum_{i=1}^{N} \ln \left[\frac{n_s^{\text{fit}}}{N} \left(\frac{\mathcal{P}_s(\boldsymbol{x}_i|\boldsymbol{r}_{\text{src}}, \gamma_{\text{fit}})}{\mathcal{P}_b(\boldsymbol{x}_i|\boldsymbol{\theta}_b)} - 1 \right) + 1 \right], \tag{5.13}$$

The ratio of PDFs, $\mathcal{P}_s/\mathcal{P}_b$, is referred to as the signal-over-background ratio.

To obtain Eq. (5.13), we used the fact that the dataset is strongly dominated by the atmospheric background, i.e., $N \sim n_b$. Consequently, the fraction of the Poisson terms is approximately unity.

Since the analysis in this work uses two datasets, IC79 and IC86 (see Section 4.4), each with different distributions of the observables due to instrumental differences—the absence of five strings for the In-Ice array in the IC79 configuration [144]—this must be accounted for in the TS. The modified TS is given by

$$\text{TS} = 2 \sum_{j}^{D} \sum_{i=1}^{N} \ln \left[\frac{n_s^{\text{fit},j}}{N} \left(\frac{\mathcal{P}_s^j(\boldsymbol{x}_i|\boldsymbol{r}_{\text{src}}, \gamma_{\text{fit}})}{\mathcal{P}_b^j(\boldsymbol{x}_i|\boldsymbol{\theta}_b)} - 1 \right) + 1 \right], \tag{5.14}$$

where $j \in D = \{\text{IC79, IC86}\}$, and the fitted number of signal neutrinos per dataset is,

$$n_s^{\text{fit},j} = n_s^{\text{fit}} \times \frac{T^j \int_0^\infty A_{\text{eff}}^j(E_\nu|\delta_{\text{src}}) \Phi_\nu(E_\nu, \gamma_{\text{fit}}) \mathrm{d}E_\nu}{\sum_j^D T^j \int_0^\infty A_{\text{eff}}^j(E_\nu|\delta_{\text{src}}) \Phi_\nu(E_\nu, \gamma_{\text{fit}}) \mathrm{d}E_\nu}. \tag{5.15}$$

Here A_{eff}^j and T^j are the effective area (Section 4.4.2) and the integrated livetime of the corresponding datasets, respectively. Importantly, this fraction depends only on

the source declination and spectral index, ensuring that no additional parameters are introduced compared to Eq. (5.13).

In the following, we derive an explicit form of the PDFs that make up the likelihood function for a single point-source search. The derivation mainly follows the theoretical framework outlined in [92, 338].

PDF derivation

To explicitly define the PDFs, we first identify the relevant reconstructed variables for each event in the up-going muon-track sample. As detailed in Section 4.3, the primary observables for a track-like event i are the reconstructed muon energy E_{μ_i}, muon direction $\boldsymbol{r}_{\mu_i}$, and the total angular uncertainty σ_i (defined in Eq. 4.17). Thus, we define the event vector as,

$$\boldsymbol{x}_i = \{E_{\mu_i}, \boldsymbol{r}_{\mu_i}, \sigma_i\}, \tag{5.16}$$

where $\boldsymbol{r}_{\mu_i} = (\alpha_{\mu_i}, \delta_{\mu_i})$ is the direction on the celestial sphere, expressed in coordinates $(\sin\delta, \alpha)$ for proper normalization. Given these observables, we now derive the background and signal PDFs.

- **Background PDF:** The background distribution $\mathcal{P}_b(\boldsymbol{x}_i|\boldsymbol{\theta}_b)$ is fully determined by an atmospheric background model and a diffuse high-energy neutrino model. Due to IceCube's location at the South Pole and the time-integrated nature of the data, the background PDF is expressed as:

$$\begin{aligned}\mathcal{P}_b(\boldsymbol{x}_i|\boldsymbol{\theta}_b) &= \frac{1}{2\pi}\mathcal{P}_b(E_{\mu_i}, \sin\delta_{\mu_i}, \sigma_i|\boldsymbol{\theta}_b) \\ &= \frac{1}{2\pi}\mathcal{P}_b(\sigma_i|E_{\mu_i}, \sin\delta_{\mu_i}, \boldsymbol{\theta}_b) \cdot \mathcal{P}_b(E_{\mu_i}, \sin\delta_{\mu_i}|\boldsymbol{\theta}_b)\ ,\end{aligned} \tag{5.17}$$

  where we used the law of total probability in the second equality.

- **Signal PDF:** In contrast to the null hypothesis, the signal hypothesis introduces a dependence on the source location $\boldsymbol{r}_{\mathrm{src}}$, the source flux normalization Φ_0, and the spectral index γ. The flux normalization results in a number of expected signal neutrinos n_s in the detector. However, this is not explicitly taken into account in the PDF but as weighting factor in the likelihood function, as shown in Eq. (5.12).

  Since high-energy neutrinos cluster around a source, the relevant observable is the angular separation ψ_i between the source ($\boldsymbol{r}_{\mathrm{src}}$) and the reconstructed muon direction of event i ($\boldsymbol{r}_{\mu_i}$). This allows to absorb the dependence on the right ascension of the source. Therefore the signal PDF can be expressed as:

$$\begin{aligned}\mathcal{P}_s(E_{\mu_i}, \boldsymbol{r}_{\mu_i}, \sigma_i|\boldsymbol{r}_{\mathrm{src}}, \gamma) &= \mathcal{P}_s(E_{\mu_i}, \psi_i, \sigma_i|\delta_{\mathrm{src}}, \gamma) \\ &= \frac{1}{2\pi\sin\psi_i}\mathcal{P}_s(\psi_i|E_{\mu_i}, \sigma_i, \gamma) \cdot \mathcal{P}_s(E_{\mu_i}, \sigma_i|\delta_{\mathrm{src}}, \gamma) \\ &= \frac{1}{2\pi\sin\psi_i}\mathcal{P}_s(\psi_i|E_{\mu_i}, \sigma_i, \gamma) \cdot \mathcal{P}_s(\sigma_i|E_{\mu_i}, \delta_{\mathrm{src}}, \gamma) \\ &\quad \cdot \mathcal{P}_s(E_{\mu_i}|\delta_{\mathrm{src}}, \gamma)\end{aligned} \tag{5.18}$$

Note that in the second equality the law of total probability is used and the source declination ($\delta_{\rm src}$) is absorbed in the angular uncertainty. The latter is due to the construction of the boosted decision tree used to estimate the angular uncertainty ([16, 338]; see also Section 4.3.2). In the final equality the law of total probability is once again employed, which will allow to simplify the final form of the TS as discussed later.

It was shown in an independent analysis that the angular uncertainty PDF in Eq. (5.18) only depends weakly on the spectral index and that this PDF changes minimally if the source declination is interchanged with the reconstructed muon declination [144]. As such, the angular uncertainty PDF in the signal and background PDFs effectively cancel when entering the TS, as can be seen from Eq. (5.7). As such, we express the final forms of the signal and background PDF, in terms of the surviving PDFs, as:

- **Final signal PDF:**

$$\begin{aligned}\mathcal{P}_s(\boldsymbol{x}_i|\boldsymbol{\theta}_s) &= \frac{1}{2\pi \sin\psi_i}\mathcal{P}_s(\psi_i|E_{\mu_i},\sigma_i,\gamma)\cdot\mathcal{P}_s(E_{\mu_i}|\delta_{\rm src},\gamma).\\ &\equiv \mathcal{S}(\psi_i|E_{\mu_i},\sigma_i,\gamma)\cdot\mathcal{E}(E_{\mu_i}|\delta_{\rm src},\gamma)\end{aligned} \tag{5.19}$$

- **Final background PDF:**

$$\mathcal{P}_b(\boldsymbol{x}_i|\boldsymbol{\theta_b}) = \frac{1}{2\pi}\mathcal{P}_b(E_{\mu_i},\sin\delta_{\mu_i}|\boldsymbol{\theta_b}). \tag{5.20}$$

The large majority of the point-source analyses that make use of a likelihood approach (e.g. [117, 359]), made the simplifying assumption that the signal PDF can be analytically modeled by two-dimensional Gaussian centered on the source. Then, the signal PDF is expressed as,

$$\mathcal{S}(\psi_i|E_{\mu_i},\sigma_i,\gamma) \sim \mathcal{S}(\psi_i|\sigma_i) = \frac{1}{\sigma_i\sqrt{2\pi}}\exp\left(-\frac{\psi_i^2}{2\pi\sigma_i^2}\right). \tag{5.21}$$

This analytic approximation disregards the dependence on the reconstructed energy of the events. Such energy dependence arises from the kinematic angle between the neutrino and the produced muon, as well as the variation in the angular uncertainty with energy. Additionally, the approximation neglects the spectral index dependence. While the approximation works well for hard spectral indices and high-energy events, it does not hold for lower-energy events, where the kinematic angle becomes more significant.

One way to avoid the need for analytic approximations is to construct the required PDFs using kernel density estimation (KDE), a non-parametric method for inferring an unknown PDF from observed data [362]. In this work, we use PDFs derived from MC data using KDEs, taking advantage of the excellent agreement between the MC simulations and the data in the up-going muon-track sample (Figure 4.10). As a result, separate KDEs are employed for the IC79 and IC86 configurations.

This non-parametric approach enables the construction of multidimensional PDFs required for the signal component of the likelihood function across a range of spectral indices. The background-only PDF is similarly modeled using a KDE. For each spectral

index, the point-source likelihood requires 4 KDEs for the signal component, as defined in Eq. (5.19), and one KDE for the background, as defined in Eq. (5.20). These KDEs were constructed in a dedicated preprocessing step in a seperate analysis, where they were first evaluated on a fine grid of spectral index values and subsequently stored as penalized B-splines. For further details on the KDE pipeline and its performance compared to previous implementations, we refer the reader to [144, 338].

From singe-source search to catalog search

In this work we perform a single-source search on each object in a pre-defined catalog, known as a catalog search. The catalog investigated in this work consists of 113 GOALS U/LIRGs, all with a declination (δ) exceeding $\delta > -3°$. The catalog of targeted U/LIRGs was introduced in Section 2.3.3.

The catalog search yields a total of 113 p-values, one for each of the source locations. This allows to either reject or accept the background-only hypothesis for each source location. The smallest p-value among the 113 obtained from the catalog search, denoted $\mathrm{p}_{\mathrm{best}}$, corresponds by definition to the most promising high-energy neutrino source in the catalog. However, when interpreting this result using experimental data, it is essential to consider the possibility that this most-significant p-value arises from a background fluctuation. This chance is additionally increased if the search is conduced over multiple locations (113 in our case). This effect is known as the *look-elsewhere effect*, and requires an additional correction.

Once the analysis results are obtained, the fraction of background-only trials in which $\mathrm{p}_{\mathrm{best}}$ is less than or equal to the observed $\mathrm{p}_{\mathrm{best}}$ must be computed. The resulting p-value is commonly referred to as the **global** p-value or the **post-trial** p-value for the most significant source in the analysis. A result is considered statistically significant only if the global p-value falls below the threshold required for evidence.

5.1.3 Binomial test

The catalog search outlined above results in $\mathcal{N} = 113$ p-values, one for each investigated GOALS U/LIRGs with a declination of $\delta > -3°$. To determine whether a subset of these p-values is more significant than expected under the null hypothesis, a binomial test is performed. For this purpose, we introduce the binomial p-value, $\mathrm{p}_{\mathrm{binom}}(k)$, which represents the probability of obtaining k or more p-values less than or equal to p_k, where $k \in \{1, \ldots, \mathcal{N}\}$. Here, p_1 is the smallest p-value, p_2 the second smallest, and so on. The binomial p-value is given by:

$$\mathrm{p}_{\mathrm{binom}}(k) = \sum_{m=k}^{\mathcal{N}} \binom{\mathcal{N}}{m} \mathrm{p}_k^m (1 - \mathrm{p}_k)^{\mathcal{N}-m} \,. \tag{5.22}$$

To identify the most sensitive subset, k is iteratively varied between 1 and $\mathcal{N}$. The most significant binomial p-value, $\mathrm{p}_{\mathrm{binom,best}}$, is then trial-corrected if necessary, similarly to the most significant p-value from the catalog search.

5.1.4 Stacking search

Thus far, we have considered single-source emission. However, it is also possible to search for an aggregated signal from multiple sources, a method known as a stacking search. In this work, we test for an aggregated signal of 10 U/LIRGs with with detected

vibrationally excited hydrogen cyanide (HCN-vib) emission. The source selection was introduced in Section 2.3.3.

For a set of sources indexed by $k \in \{1, \ldots, M\}$, with $M = 10$ in our case, the point-source likelihood extends to a stacking likelihood as,

$$\begin{aligned}\mathcal{L}(\boldsymbol{\theta} \mid N, \{\boldsymbol{x}_i\}) =& \frac{(n_b + n_s)^N}{N!} e^{-(n_s+n_b)} \times \\ & \prod_{i=1}^{N} \left[\frac{n_s}{n_b + n_s} \sum_{k=1}^{M} w_k \mathcal{P}_s^k(\boldsymbol{x}_i \mid \boldsymbol{\theta}_s) + \frac{n_b}{n_s + n_b} \mathcal{P}_b(\boldsymbol{x}_i \mid \boldsymbol{\theta}_b) \right] .\end{aligned} \tag{5.23}$$

In this formulation, stacking occurs within the signal term of the likelihood, where the individual signal PDFs of the sources are combined in a weighted sum. Ideally, each source would be modeled with an independent spectral index. However, due to computational constraints, a single spectral index is typically assumed for all sources.

The weights (w_k) are defined as:

$$w_k = \frac{t_k \mathcal{Y}_k}{\sum_{k=1}^{M} t_k \mathcal{Y}_k} , \tag{5.24}$$

where:

- The **theoretical** weight w_k of source k is determined based on theoretical considerations of the neutrino emission properties of the selected source class.
- The **detector** response $\mathcal{Y}_k$ of source k accounts for the effective area of the detector for a source at δ_{src} given the chosen spectral index γ of the source spectrum.

The remainder of the statistical formalism follows a similar approach to the single-source search. However, in the case of the stacking search, the hypothesis test considers as the alternative hypothesis ($\mathcal{H}_1$) the presence of an aggregated signal from a set of sources, rather than a single source.

The TS for a stacking search remains a likelihood ratio as defined in Eq. (5.7). Substituting the stacking likelihood given in Eq. (5.23) into the TS expression in Eq. (5.7), we obtain,

$$\mathrm{TS} = 2 \sum_{i=1}^{N} \ln \left[\frac{\hat{n}_s}{N} \left(\sum_{k=1}^{M} w_k \frac{\mathcal{P}_s^k(\boldsymbol{x_i} | \boldsymbol{r}_{\mathrm{src}}, \gamma_{\mathrm{fit}})}{\mathcal{P}_b(\boldsymbol{x_i} | \boldsymbol{\theta_b})} - 1 \right) + 1 \right] . \tag{5.25}$$

Similar to the single-source case, it is important to note that when using two datasets with differently distributed observables, their effects must be properly accounted for in the analysis.

Note that, although multiple sources are investigated, only a single p-value is obtained from a stacking search, as the test is performed for an aggregated signal. As such, no trial correction is needed to obtained the final p-value.

5.2 Analysis Performance

Before applying the statistical framework outlined in Section 5.1 to the up-going muon-track sample introduced in Section 4.4, we first evaluate the performance of the analysis through a series of validation steps. This stage of the analysis is conducted in a **blind** manner. In a **blind analysis**, Monte Carlo (MC) simulations or scrambled data are used in place of actual observations to prevent bias during the development of the analysis. Although previous studies have employed data scrambling (e.g., [150]), in this work we exclusively utilize MC data in the blind stage of the analysis.

The analysis is only **unblinded** once its methodology has been finalized, at which point the experimental data replaces the simulations.

A central concept in performance evaluation is the notion of a **trial**. A trial involves applying the log-likelihood ratio defined in Eq. (5.7) to a MC dataset that emulates the up-going muon-track sample, yielding a TS value. Depending on the objective, simulated signal neutrinos may be injected into the dataset.

The MC datasets used for the trial calculations are constructed via weighted sampling from a larger ensemble of MC simulations. The weights are determined based on MC-derived event properties and the expected contributions from atmospheric flux, diffuse astrophysical flux, and potential point sources, as detailed in Section 4.2.6.

By performing a large number of these so-called trials, TS distributions can be constructed under both the background-only hypothesis—which includes only contributions from atmospheric and diffuse astrophysical neutrinos—and the signal-plus-background hypothesis, which additionally includes one or more point-source contributions. From these distributions, various key performance metrics can be derived to assess the sensitivity and robustness of the analysis.

To conduct trials, we use a private IceCube software package, `i3SkyLLH`, which includes pre-defined source searches commonly used in IceCube, such as the single-source search and the stacking search introduced in Section 5.1. This package also incorporates kernel density estimators (KDEs) to model the likelihood probability density functions (PDFs). The private package is built upon `SkyLLH` [27, 28], an open-source `Python`-based framework that enables the definition of custom likelihood functions and the application of log-likelihood ratio hypothesis tests.

5.2.1 Bias tests, sensitivity & discovery potential

Below we outline the various tests we perform and the metrics we calculate to quantify the consistency and performance of the analysis, respectively.

Bias tests

We perform **bias tests** to evaluate how accurately the analysis recovers artificially injected signal neutrinos (pseudosignal). These tests assess the reconstructed number of injected signal events and the spectral index of the source, ensuring that the analysis does not introduce systematic biases that could affect result interpretation. Ideally, if the underlying PDFs in the likelihood model the physical system well, the best-fit parameters should converge to their true values as the sample size increases, ensuring consistency (Section 5.1). Deviations from this behavior may indicate mismodeling in the PDFs.

Sensitivity & discovery potential

We quantify how sensitive the analysis is to astrophysical neutrinos from the point sources using two key metrics:

- **Sensitivity**: The minimum pseudosignal required so that in 90% of signal-plus-background trials the TS value exceeds the median of the background-only TS distribution (Figure 5.1). In terms of statistical significance (α) and power ($1-\beta$), as defined in Eqs. (5.10) and (5.11), this corresponds to $\alpha = 0.5$ and $1-\beta = 0.9$, respectively.

  As further explained in Chapter 6, IceCube has a policy that the strictest upper limit on the high-energy neutrino flux from a source direction in the case of non-detection is the sensitivity.

- **Discovery potential**: The minimum pseudosignal required such that, in 50% of signal-plus-background trials, the TS value exceeds the $n\sigma$ significance threshold of the background-only TS distribution. Commonly used thresholds are the 3σ and 5σ discovery potentials, corresponding to significance levels of $\alpha = 1.35 \times 10^{-3}$ and $\alpha = 2.87 \times 10^{-7}$, respectively. The latter is the standard threshold for claiming a discovery in (astro)particle physics and illustrated in Figure 5.1. In both cases, the corresponding power is $1-\beta = 0.5$.

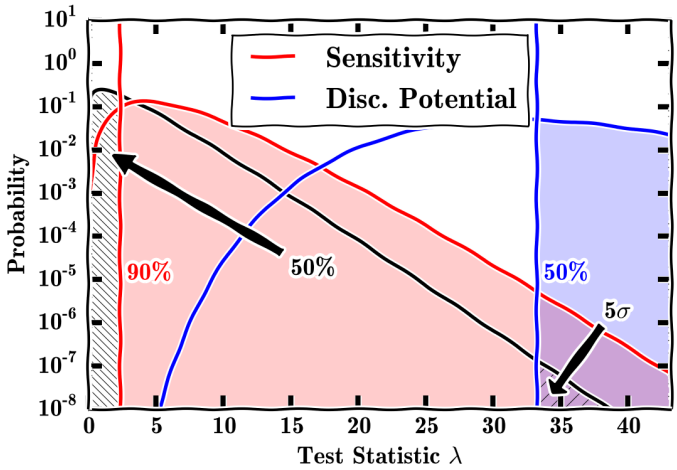

FIGURE 5.1: Illustration of the concepts sensitivity and discovery potential as introduced in the text [313].

Background-only test-statistic distribution

Both the sensitivity and $n\sigma$ discovery potential rely on the TS distribution under the background-only hypothesis. To obtain this distribution, we repeatedly generate trials under the background-only assumption (i.e., no contribution from neutrino point sources). The obtained TS from each of these trials is typically zero, as seen from Eq. (5.7), consistent with the background-only hypothesis, but random fluctuations may produce nonzero values. The resulting **background-only distribution** can then be used for the calculation of the sensitivity, discovery potential, and p-value.

As discussed in Section 5.1.1, in the asymptotic limit (i.e., for an infinitely large sample size), the background-only distribution converges to a chi-square distribution,

χ^2_ν, with $\nu = 2$ degrees of freedom. However, previous studies (e.g., [338]) have shown that Wilks' theorem does not always hold in point-source searches with IceCube. Accurately modeling the background-only distribution is, however, essential for reducing the number of trials, as this modeling directly impacts computational efficiency. For instance, calculating the 5σ discovery potential requires sampling the background-only hypothesis beyond this significance threshold, which is computationally demanding.

To characterize the background-only TS distribution, we fit in this work a truncated Gamma distribution (Γ) to the tail of the background-only distribution. This choice is motivated by the fact that the chi-square distribution is a special case of the Gamma distribution. The truncated Gamma distribution used in this work is of the form,

$$\Gamma(\mathrm{TS}|a, b, \eta) = \frac{\xi}{C_0}\Gamma(\mathrm{TS}|a, b). \,, \tag{5.26}$$

where a and b are the shape and scale parameters of the distribution, while ξ represents the fraction of TS values exceeding a chosen threshold η. Finally, C_0 is a normalization constant, given by

$$C_0 = \int_\eta^\infty \Gamma(\mathrm{TS}|a, b)\,\mathrm{d}(\mathrm{TS}) \,. \tag{5.27}$$

In the following sections we discuss, for both the catalog and stacking search, the bias tests, background characterization, sensitivity, and discovery potential.

5.2.2 Catalog search & binomial test performance

We discuss the analysis performance tests for the catalog search and the corresponding population study through a binomial test, targeting 113 GOALS U/LIRGs with a declination of $\delta > -3°$. This catalog was introduced in Section 2.3.3.

We note that the up-going muon-track sample (Section 4.4) includes events with $\delta > -5°$. In the GOALS sample, 4 sources fall within the declination range $-5° < \delta < -3°$. However, in this specific range, we observed relatively strong biases and reduced sensitivity compared to the rest of the sky. To minimize the statistical penalty associated with including additional sources in the analysis and to maintain consistency with previous studies [16, 144], we opted to exclude these sources.

Background-only test-statistic distribution

We obtained 500.000 trials under the background-only hypothesis for each of the 113 sources in the catalog.[5] In Figure 5.2 we show the background-only TS distributions for a selection of sources in the catalog, spanning a wide range of declinations. Each of the background distributions are fitted with a function of the form given in Eq. (5.26).

The distributions in Figure 5.2 show that, although the TS value is zero in most trials, as expected, the background can still produce significant deviations from the background-only hypothesis, resulting in relatively large TS values.

Once the unblinded data is available, a final TS value is computed for each source location in the catalog. These TS values will be compared to the corresponding background distributions to obtain p-values, which quantify the significance of the observed TS values.

In Figure 5.3 we also show, for all 113 sources, the fraction of TS values larger than zero, and the corresponding median TS value of the distribution, as a function of

[5] 5000 trials for a single source take about 30 minutes of CPU time.

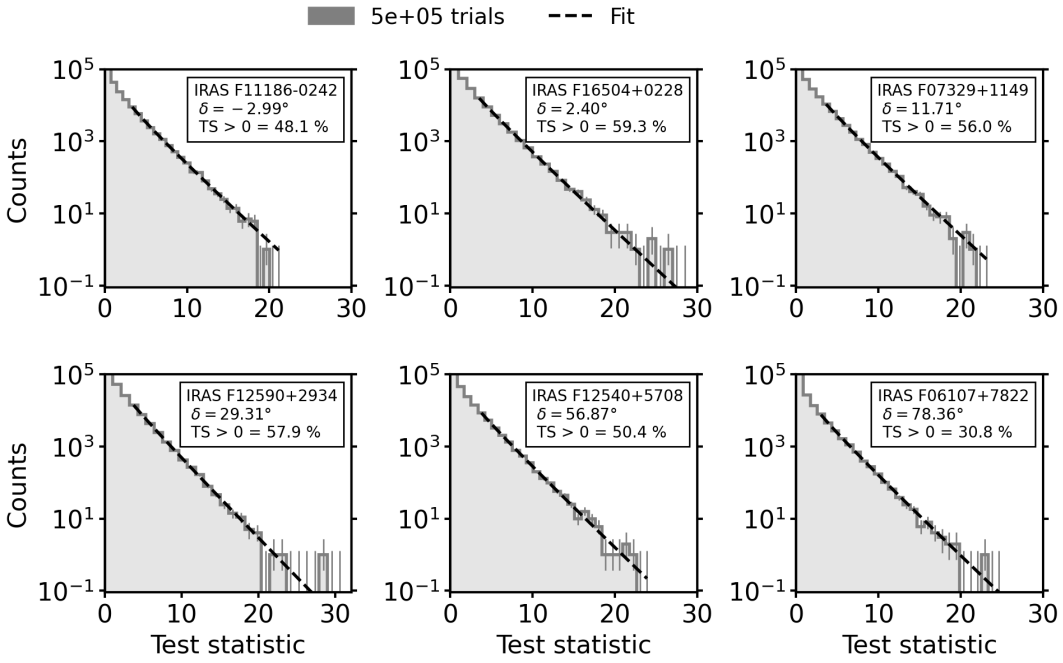

FIGURE 5.2: Background-only TS distributions obtained from 500.000 trials for various sources in the catalog, covering a wide range of declinations (δ) along the Northern Sky. The fit follows the form given in Eq. (5.26).

the sine of the declination (δ) of that source. Based on theoretical considerations, we expect, on average, that 50% of the trials will have a TS value greater than zero.

Close to the pole, the fraction of TS values larger than zero is smaller than observed for the rest of the sky. This behavior was also observed in previous analyses [338]. At very high declinations ($\sim 81°$) the events rates and reconstruction quality significantly drops. Due to the low statistics, the KDEs also do not behave as good as for the rest of the Northern Sky. As such, deviations are expected close to the pole.

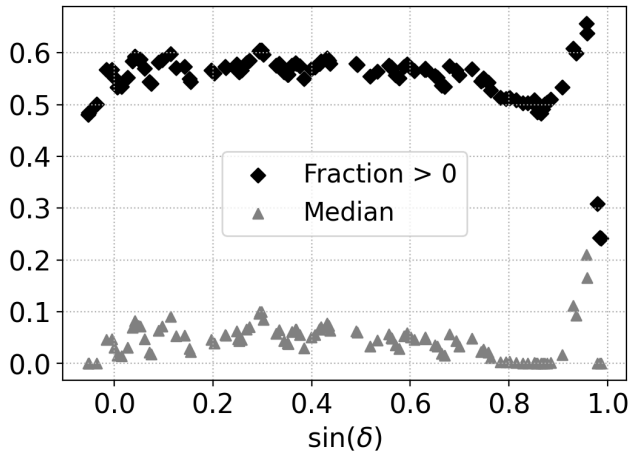

FIGURE 5.3: Fraction of TS values greater than zero (black diamonds) and the median (gray triangles) of the background-only TS distribution for all 113 targeted GOALS sources, plotted as a function of the sine of each source's declination (δ).

Fit parameter bias tests

We assess potential biases in the fitted parameters: the number of signal neutrinos (n_s^{fit}) and the spectral index (γ_{fit}) of a high-energy neutrino source assumed to follow a power-law energy spectrum. To this end, we inject pseudosignal events in the range of 1–100 (1–50) in steps of 1 for spectral indices $\gamma \in \{2.5, 3.0\}$ ($\gamma = 2.0$), performing 2000 trials per injection level.

From these trials, we compute the median values of the fitted parameters, n_s^{fit} and γ_{fit}, and compare them to the corresponding injected values, n_s^{inj}. Figures 5.4 and 5.5 show the median fitted number of signal neutrinos and the spectral index, respectively, as functions of the injected pseudosignal count for a fixed spectral index of $\gamma = 2.5$. The 68% and 95% containment intervals are also shown. The black dashed line represents the unbiased case for reference.

Rather than showing these bias plots for all sources in the catalog, we include results for a subset of the catalog spanning a wide range of Northern Hemisphere declinations. These are the same declinations as used for the background-only distributions in Figure 5.2. Similar bias plots for $\gamma \in \{2.0, 3.0\}$ are available in Appendix E.[6] We conclude:

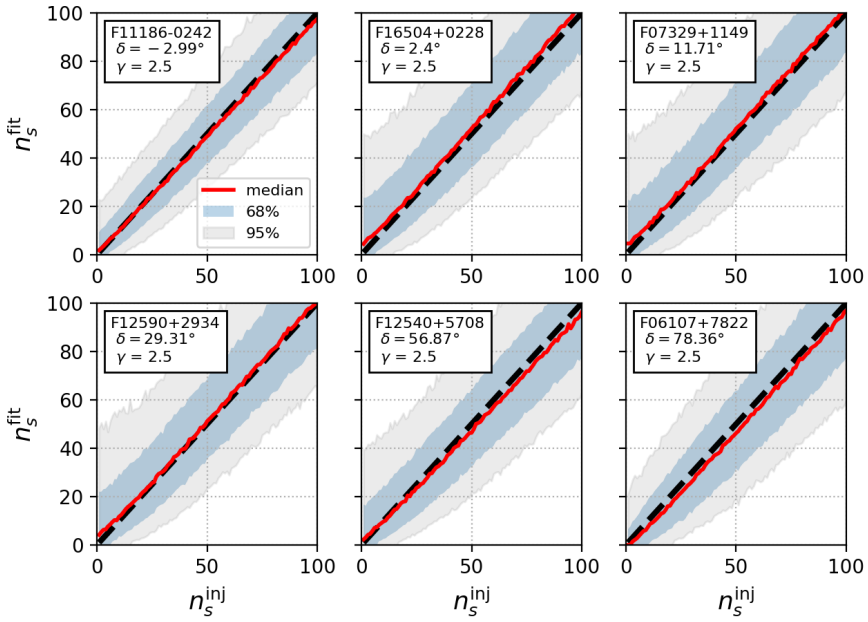

FIGURE 5.4: Median number of fitted signal neutrinos (n_s^{fit}) as a function of the injected signal neutrinos (n_s^{inj}). The black dashed line represents the unbiased case. The shaded regions correspond to the 68% and 95% containment intervals. A fixed spectral index of $\gamma = 2.5$ is used. Six out of the 113 sources are selected to ensure coverage across a wide range of declinations.

- **Signal neutrinos**: On average the number of injected signal neutrinos are well recovered at all declinations for all spectral indices. However, for a soft spectral index (e.g., $\gamma = 3$) close to the pole, the analysis performs relatively worse,

[6] For each spectral index, all 113 sources were visually inspected. This led to the identification of a previously unknown problem with the minimizer. This was resolved by the maintainers of `SkyLLH` and `i3SkyLLH`.

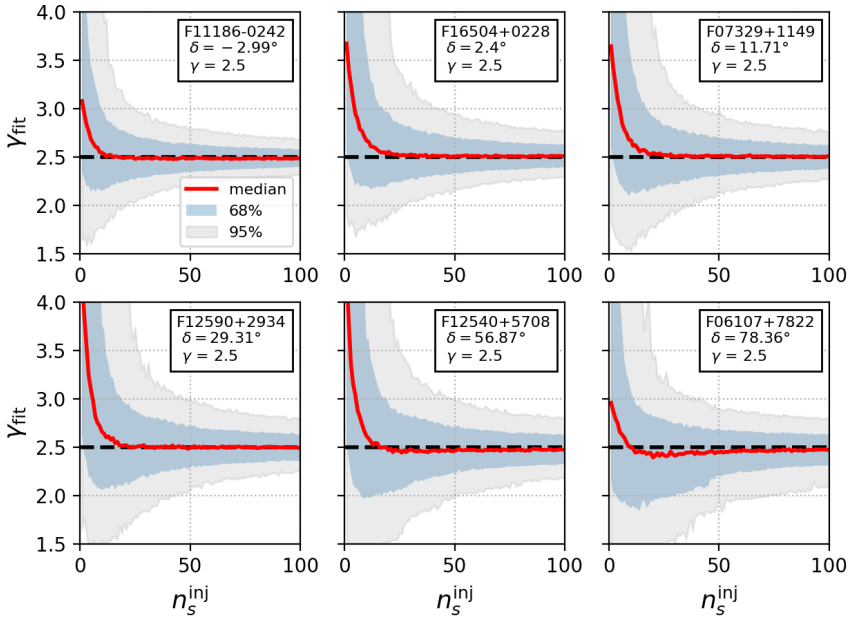

FIGURE 5.5: Median number of fitted spectral indices (γ_{fit}) as a function of the injected signal neutrinos (n_s^{inj}). The black dashed line represents the unbiased case. The shaded regions correspond to the 68% and 95% containment intervals. A fixed spectral index of $\gamma = 2.5$ is used. Six out of the 113 sources are selected to ensure coverage across a wide range of declinations.

meaning that some bias remains. This could be the result of mismodelling in the PDF, such as the angular uncertainty term in the likelihood that was discarded (Section 5.1.2).

- **Spectral index**: The general trend observed for the fitted spectral index is that, as the number of injected signal neutrinos increases, the fitted spectral index progressively converges to the true spectral index of the injected signal. Moreover, the spread of the fitted parameter decreases with an increasing number of injected signal neutrinos, as expected, since the signal features become more pronounced. We also note that, for only a few injected signal neutrinos, the best-fit spectral index tends to fit a very soft spectral index similar to the spectral index observed for the atmospheric background, $\gamma \approx 3.7$ (Section 4.2.5). This is expected as the dataset is largely background dominated.

Sensitivity & discovery potential

Two key metrics used to assess the performance of the analysis are the sensitivity and the 5σ discovery potential, introduced in Section 5.2.1 and illustrated in Figure 5.1. Below, we outline the technical procedures used to compute these metrics.

Let f_{thresh} denote the fraction of trials with $\text{TS} > \text{TS}_{\text{thresh}}$, where the threshold corresponds to either the median value ($\text{TS}_{\text{median}}$) or the 5σ value ($\text{TS}_{5\sigma}$) of the background-only TS distribution at a given source location. By definition of sensitivity and 5σ discovery potential, our goal is to determine, for each source in the catalog, the injected signal strength n_s^{inj} required to satisfy either of the following conditions:

- $f_{\text{thresh}} = 0.9$, with $\text{TS}_{\text{thresh}} = \text{TS}_{\text{median}}$, corresponding to the sensitivity;
- $f_{\text{thresh}} = 0.5$, with $\text{TS}_{\text{thresh}} = \text{TS}_{5\sigma}$, corresponding to the 5σ discovery potential.

This analysis is performed for three spectral indices: $\gamma = 2.0$, 2.5, and 3.0.

To determine the required injected signal strength, we conduct 2000 trials for each value of n_s^{inj}, with the range of injected signals chosen to suit each spectral index. A spline interpolation is then applied using the `photospline`[7] library to accurately estimate the signal strength that satisfies the desired threshold condition.

As an example, Figure 5.6 illustrates the interpolation obtained from the trials performed for the source F07329+1149 at a declination of $\delta = 11.71°$, assuming a power-law energy spectrum of neutrinos with a spectral index $\gamma = 2.5$. As expected, the required number of signal neutrinos is higher for the 5σ discovery potential compared to the sensitivity. The obtained number of signal neutrinos can be converted into the high-energy neutrino flux necessary to achieve sensitivity and the 5σ discovery potential using Eq. (4.20).

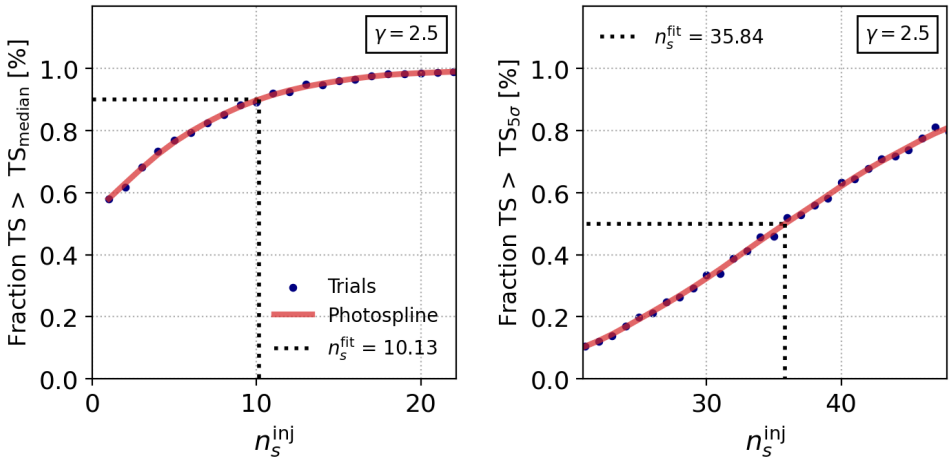

FIGURE 5.6: Fraction of signal-plus-background trials in which the test statistic (TS) exceeds either the median of the background-only TS distribution ($\text{TS}_{\text{median}}$, left) or the 5σ significance threshold ($\text{TS}_{5\sigma}$, right), plotted as a function of the number of injected signal events (n_s^{inj}). Results correspond to the GOALS galaxy F07329+1149, located at a declination of $\delta = 11.71°$, assuming a fixed spectral index of $\gamma = 2.5$.

By obtaining interpolation splines for each of the 113 investigated sources in the catalog across all spectral indices, we determine the final values for the muon-neutrino flux at 1 TeV ($\Phi^{1\ \text{TeV}}_{\nu_\mu+\bar{\nu}_\mu}$) to reach sensitivity and 5σ discovery potential. The sensitivity and discovery potential calculations for all spectral indices are presented in Figure 5.7. Both the sensitivity and 5σ discovery potential improve up to $20-25\%$ as opposed to the previous point-source search in which NGC 1068 was identified as a high-energy neutrino source [16]. This improvement is due to the increased exposure time of the dataset (a total of 4 years; see Section 4.4).

We note that, even with enhanced sensitivity, the high-energy flux predictions for starburst-driven neutrino production—based on the model described in Chapter 3 (see the table in Appendix D)—remain well below the current sensitivity threshold of IceCube. Nevertheless, the statistical formalism employed in our IceCube analysis does

[7] Available at: https://github.com/icecube/photospline

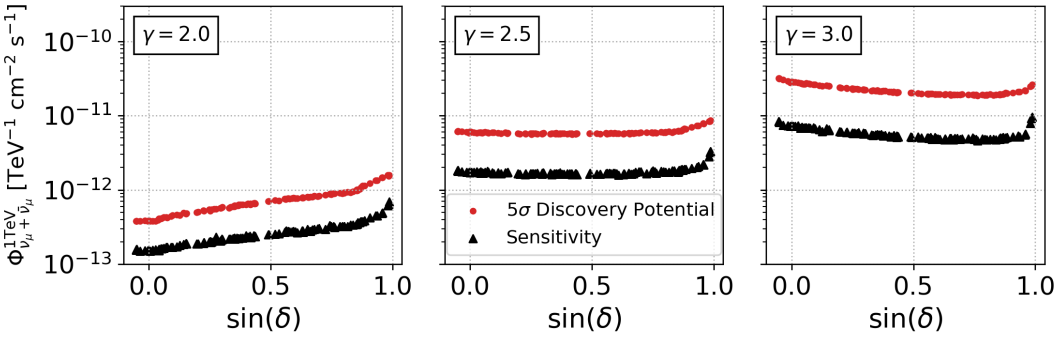

FIGURE 5.7: Sensitivity (black triangles) and 5σ discovery potential (red dots) for all 113 sources in the catalog search as a function of of the declinations of those sources. The sensitivity and discovery potential are shown for three fixed spectral indices: $\gamma = 2.0$, 2.5, and 3.0

not assume a specific model of high-energy neutrino production. Therefore, alternative mechanisms may still enable the detection of GOALS U/LIRGs as steady sources of high-energy neutrinos. The results are presented in Chapter 6.

Best p-value distribution

The catalog search yields a total of 113 p-values, one for each source investigated. As discussed in Section 5.1.2, the most significant p-value must be corrected for the *look-elsewhere effect*. This correction is achieved by constructing the distribution of the most significant p-value under the background-only hypothesis in the following way:

1. Use a Monte-Carlo (MC) dataset generated under the background-only assumption (i.e., no additional signal).
2. For each of the 113 catalog source locations, perform a single trial using this MC dataset and calculate the corresponding 113 TS values.
3. For each source, compute a p-value by evaluating the calculated TS value against its corresponding pre-computed background-only TS distribution. This yields 113 p-values.
4. Identify and record the smallest (most significant) p-value across all 113 sources. This value is denoted as $\mathrm{p_{best}}$.
5. Repeat steps 1–4 multiple times to build a distribution of $\mathrm{p_{best}}$ values under the background-only hypothesis.

The left panel of Figure 5.8 presents the distribution of -$\log_{10}(\mathrm{p_{best}})$ obtained from 50.000 trials.[8] The right panel displays the corresponding best-fit parameters for the most significant p-values. This shows that most significant p-values generated under the background-only distribution seem to arise mostly from a soft fitted spectral index with a large number of fitted pseudosignal, but also from a (unusually) hard spectral index with only a few number of fitted pseudosignal.

[8]Under the background-only hypothesis, the distribution of $\mathrm{p_{best}}$-values tends to rise toward larger values. This behavior contrasts with that of the TS distribution under the same hypothesis, from which the p-value is traditionally computed. To maintain a meaningful connection to the p-value, we instead consider the distribution of -$\log_{10}(\mathrm{p_{best}})$.

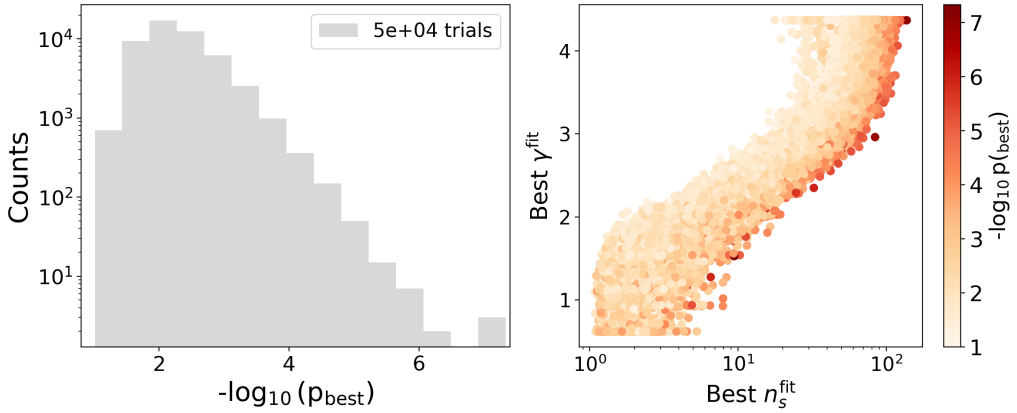

FIGURE 5.8: Distribution of 50.000 best p-value calculations as outlined in the text (left) and the corresponding fit parameters $(\gamma_{\text{fit}}, n_s^{\text{fit}})$ (right).

Binomial test

Using the $\mathcal{N} = 113$ p-values obtained from the catalog search, we will perform a population study via a binomial test. This involves computing the binomial p-value introduced in Eq. (5.22), which represents the probability of obtaining k or more p-values less than or equal to p_k, where $k \in \{1, \ldots, 113\}$. Here, p_1 denotes the most significant p-value, p_2 the second most significant, and so on. The parameter k corresponds to the *ordered source number*. To identify the most significant subset, we compute the binomial p-value for each k and determine the minimum value.

The left panel of Figure 5.9 illustrates a mock example. To obtain this plot we:

1. Generate a MC dataset under the background-only assumption.
2. For each source in the catalog, perform one trial using the same MC simulation and compute the corresponding TS value.
3. Determine the local p-value (black circles) for each source using its pre-generated background-only TS distribution.
4. Order the sources by their local p-values and compute the binomial p-value (orange triangle) for each ordered source number k.
5. Identify the most significant binomial p-value and record the corresponding source number k.

   In this mock example, the best binomial p-value is found to be $\mathrm{p}_{\text{binom,best}} = 0.02$ at $k_{\text{best}} = 13$. These values are also indicated in Figure 5.9.

   Note: To claim evidence of a significant subset of potential high-energy neutrino sources, the value of $\mathrm{p}_{\text{binom,best}}$ computed from the unblinded data must reach at least the evidence threshold.

Repeating the above steps enables the construction of the expected distribution of best binomial p-values under the background-only hypothesis. This distribution is shown in the right panel of Figure 5.9.

To obtain the final result of the binomial test, the same procedure is applied to the unblinded data. The background distribution shown in the right panel of Figure 5.9 is then used to evaluate the global p-value corresponding to the observed $\mathrm{p}_{\text{binom,best}}$.

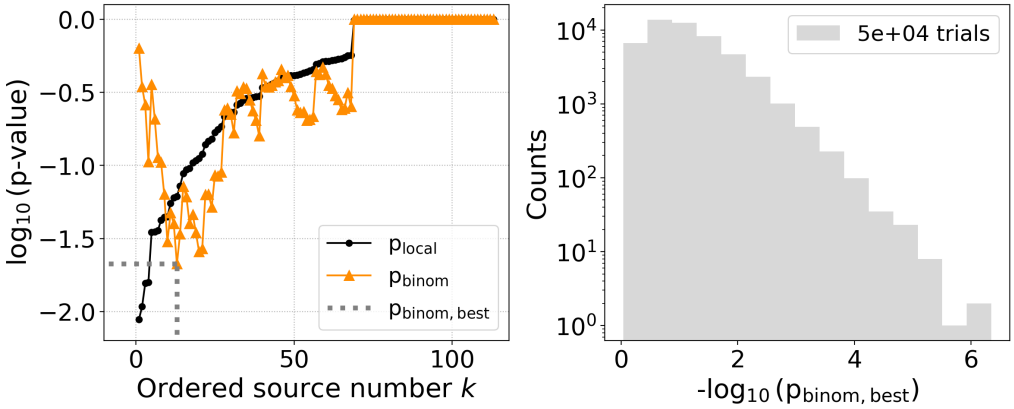

FIGURE 5.9: Left panel: A mock example illustrating the calculation of the binomial p-values ($\mathrm{p_{binom}}$) for an ordered set of local p-values ($\mathrm{p_{local}}$) obtained from a catalog search. The most significant binomial p-value, $\mathrm{p_{binom,best}} = 0.02$ at $k_{\mathrm{best}} = 13$, is indicated by the grey dotted line. Right panel: Distribution of the most significant binomial p-values obtained by applying the procedure described in the left panel to 50.000 simulations under the background-only hypothesis.

5.2.3 Stacking search performance

Below we present the analysis-performance tests for the stacking search targeting 10 GOALS U/LIRGs with vibrationally excited hydrogen cyanide (HCN-vib) emission and a declination of $\delta > -3°$. As outlined in Section 2.1.2, such emission is indicative of warm and highly obscured regions. The targeted catalog of 10 HCN-vib GOALS U/LIRGs was introduced in Section 2.3.3.

In the work presented here we only consider the inverse of the luminosity-distance squared (D_L^{-2}) as theoretical weighting scheme (see Section 5.1.4 for the statistical framework of the stacking search). This weighting is motivated by the expectation that more distant sources contribute less to the observed neutrino flux. However, this assumes that all sources have similar neutrino luminosities. While this is unlikely to be the case, we currently have no *a-priori* knowledge of high-energy neutrino production in GOALS U/LIRGs characterized by HCN-vib emission, as this is the first time a larger group has been targeted.

To relax the standard-candle assumption, one could scale the inverse squared luminosity distance with the infrared luminosity (L_{IR}). This approach is justified by the fact that infrared luminosity in U/LIRGs is driven by starburst and AGN activity, which could be linked to high-energy neutrino production (see Chapters 2 and 3). However, since this modification did not significantly improve the analysis performance, and given that this is the first study of these sources, we opted for a more general approach, using only the D_L^{-2} theoretical weighting scheme.

Background-only test-statistic distribution

We performed 500.000 trials under the background-only hypothesis to construct the corresponding background-only TS distribution for the stacking search. The resulting distribution is shown in Figure 5.10 and the distribution is fitted with a function of the form given in Eq. (5.26).

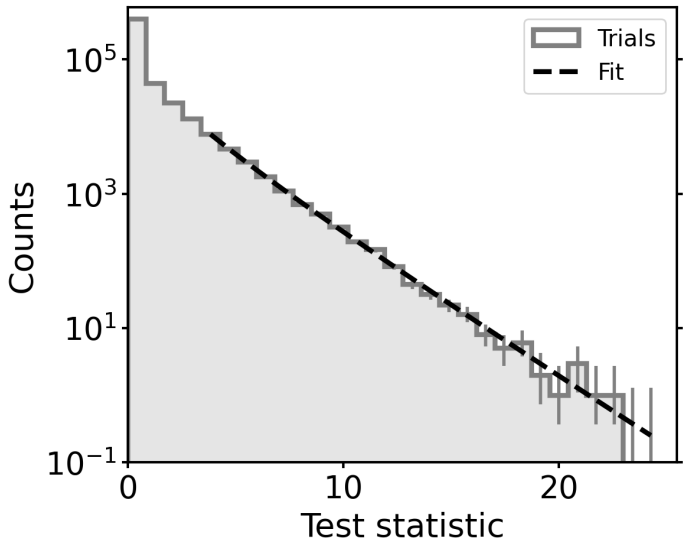

FIGURE 5.10: Background-only TS distribution obtained from 500.000 background-only trials. The black-dashed line shows the fit which follows the form given in Eq. (5.26). The TS value at 3σ and 5σ are $\mathrm{TS}_{3\sigma} = 9.9$ and $\mathrm{TS}_{5\sigma} = 27.4$, respectively.

A fraction of 50% of the TS values has a value larger than zero, which corresponds to a median TS value of zero. The TS value at 3σ and 5σ are $\mathrm{TS}_{3\sigma} = 9.9$ and $\mathrm{TS}_{5\sigma} = 27.4$, respectively.

This distribution will be used to compute the p-value for the stacking search by comparing the observed TS value with experimental data.

Fit parameter bias tests

We inject signal events (n_s^{inj}) ranging from 1 to 100 in steps of 1, performing 5000 trials for each injection and for three fixed spectral indices: $\gamma = 2.0$, 2.5, and 3.0. For each number of injected signal neutrinos, we determine the median values of the fitted spectral indices (γ_{fit}) and the fitted number of signal neutrinos (n_s^{fit}). These median values are shown in Figure 5.11 for n_s^{fit} and in Figure 5.12 for γ_{fit}, both as functions of the number of injected signal neutrinos. Additionally, the 68% and 95% containment intervals are displayed. We conclude:

- **Signal neutrinos**: On average, the number of injected pseudosignals is well recovered across all spectral indices. However, for the softest spectral indices, there is a slight bias where fewer signal neutrinos are recovered than injected. As discussed in the catalog search, this could be related to residual mismodeling in the likelihood PDFs, such as the angular uncertainty component that was discarded. Moreover, we also note that the spread in fitted values increases significantly as the the spectral index becomes softer.

- **Spectral index**: For the fitted spectral index, we observe that as the number of injected pseudosignals increases, the median γ_{fit} converges toward the injected value. Furthermore, the spread in fitted spectral indices decreases with an increasing number of injected pseudosignals, as expected, since the neutrino signal becomes more prominent.

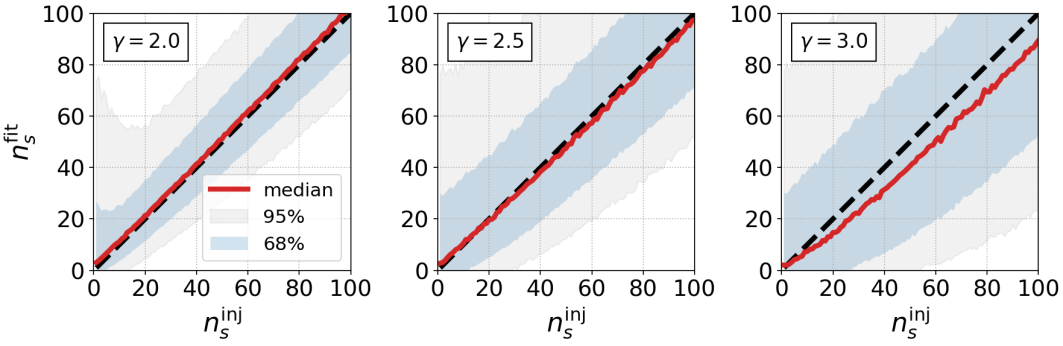

FIGURE 5.11: Median number of fitted signal neutrinos (n_s^{fit}) as a function of the number of injected signal neutrinos (n_s^{inj}). The black dashed line represents the unbiased case. The 68% and 95% containment intervals are shown. Results are presented for three fixed spectral indices: $\gamma = 2.0$, 2.5, and 3.0.

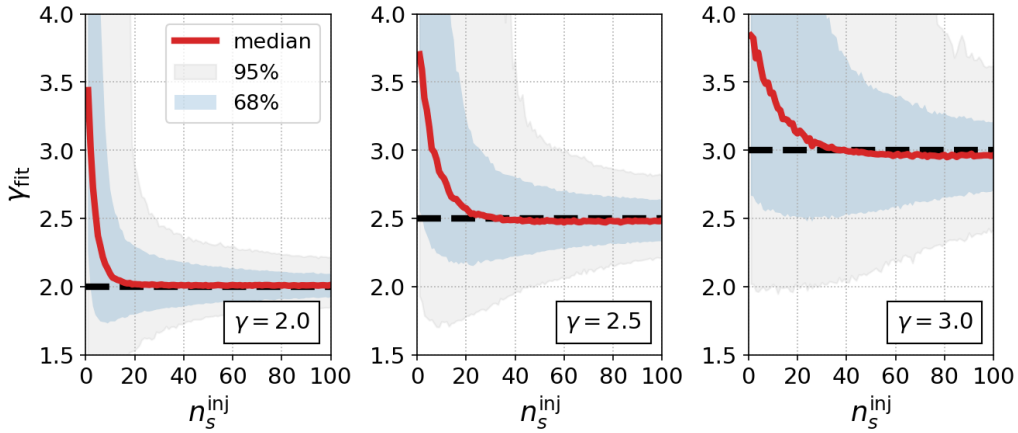

FIGURE 5.12: Median number of fitted spectral indices (γ_{fit}) as a function of the number of injected signal neutrinos (n_s^{inj}). The black dashed line represents the unbiased case. The 68% and 95% containment intervals are shown. Results are presented for three fixed spectral indices: $\gamma = 2.0$, 2.5, and 3.0.

Sensitivity & discovery potential

Two key metrics used to assess the performance of the analysis are the sensitivity and the 5σ discovery potential, introduced in Section 5.2.1 and illustrated in Figure 5.1. Below, we outline the technical procedures used to compute these metrics.

Let f_{thresh} denote the fraction of trials with $\mathrm{TS} > \mathrm{TS}_{\mathrm{thresh}}$, where the threshold corresponds to either the median value ($\mathrm{TS}_{\mathrm{median}}$) or the 5σ value ($\mathrm{TS}_{5\sigma}$) of the background-only TS distribution at a given source location. By definition of sensitivity and 5σ discovery potential, our goal is to determine the injected signal strength n_s^{inj} required to satisfy either of the following conditions:

- $f_{\mathrm{thresh}} = 0.9$, with $\mathrm{TS}_{\mathrm{thresh}} = \mathrm{TS}_{\mathrm{median}}$, corresponding to the sensitivity;
- $f_{\mathrm{thresh}} = 0.5$, with $\mathrm{TS}_{\mathrm{thresh}} = \mathrm{TS}_{5\sigma}$, corresponding to the 5σ discovery potential.

This analysis is done for three spectral indices: $\gamma = 2.0$, 2.5, and 3.0.

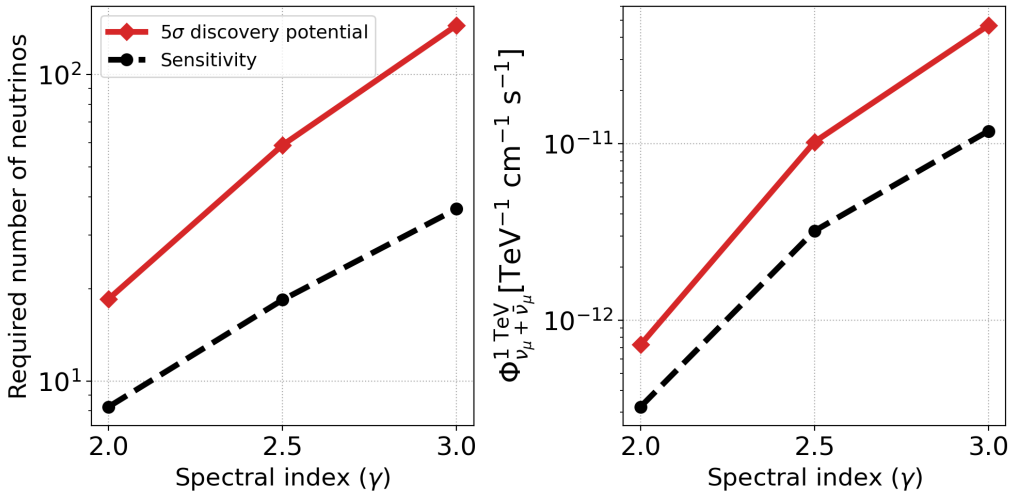

FIGURE 5.13: The number of pseudosignal events (left) required to reach sensitivity and 5σ discovery potential for the stacking search as a function of the spectral index (γ). The corresponding muon-neutrino flux (right) at 1 TeV ($\Phi^{1\ \mathrm{TeV}}_{\nu_\mu+\bar{\nu}_\mu}$) as a function of the spectral index γ.

For each spectral index, we conduct 5000 trials per n_s^{inj} and use spline interpolation, implemented via the `photospline` library, to determine the required injected signal. The resulting splines for different spectral indices are shown in Appendix E.5.

The left panel of Figure 5.13 depicts the number of injected neutrinos needed to reach sensitivity and 5σ discovery potential, while the right panel shows the corresponding muon-neutrino flux at 1 TeV ($\Phi^{1\ \mathrm{TeV}}_{\nu_\mu+\bar{\nu}_\mu}$). The conversion between the number of signal neutrinos and the high-energy neutrino flux follows Eq. (4.20). As expected, a larger injected signal is required to achieve discovery potential compared to sensitivity, and the required signal increases as the spectral index softens.

CHAPTER 6

Results & Implications for Neutrino Emission from GOALS Galaxies

Using the statistical point-source formalism presented in Chapter 5, we investigate correlations between 13 years of the up-going muon-track sample (introduced in Section 4.4) and (ultra)luminous infrared galaxies (U/LIRGs) from the Great Observatories All-Sky LIRG Survey (GOALS). The motivation for considering GOALS U/LIRGs as candidate high-energy neutrino sources is outlined in Chapters 1, 2, and 3.

Specifically, we search for high-energy neutrino emission on a per-source basis from 113 GOALS U/LIRGs located in the Northern Sky and assess the presence of interesting subpopulations using a binomial test. Additionally, we perform a stacking analysis to probe for a cumulative signal from a subset of 10 GOALS ULIRGs. The sources used in each of the searches are introduced in Section 2.3.3 and the details of the statistical methodology and performance evaluation are provided in Sections 5.1 and 5.2, respectively.

The analyses yield 113 p-values from the individual source searches, one p-value from the binomial test, and one from the stacking search. Among these, only the individual source p-values and the binomial p-value—provided they show sufficiently large pre-trial significance to suggest evidence—require correction for statistical trials. Based on the final p-values, we distinguish two outcomes:

- **Observed flux**: If the final p-value is significant enough to claim evidence or discovery, we reject the background-only hypothesis, which assumes only atmospheric backgrounds and a diffuse astrophysical neutrino flux from the investigated source location. In such cases, the corresponding high-energy neutrino flux from the implied source is inferred from the best-fit parameters obtained via the likelihood analysis outlined in Chapter 5.

- **Upper Limit**: If the observed p-value is not statistically significant, we set an upper limit on the high-energy neutrino flux from the tested source direction. This limit is determined using Neyman's frequentist approach to construct a one-sided confidence interval. For a fixed spectral index, the confidence level (CL) corresponding to an upper limit on the neutrino flux is then given by:

$$\mathrm{CL} = \int_{\mathrm{TS}_{\mathrm{obs}}}^{\infty} \mathcal{T}_s(\mathrm{TS}' \mid \Phi_0^{\mathrm{CL}}, \gamma)\, \mathrm{d}(\mathrm{TS}') \,, \tag{6.1}$$

  where $\mathcal{T}_s$ is the test-statistic (TS) distribution under the signal-plus-background hypothesis, and $\mathrm{TS}_{\mathrm{obs}}$ is the TS value obtained from the observed data. The flux normalization Φ_0^{CL} that satisfies the specified confidence level is reported as the flux upper limit. Throughout this work, we adopt $\mathrm{CL} = 90\%$.

  The procedure for obtaining Φ_0^{CL} parallels the methods used to compute the sensitivity and $n\sigma$ discovery potential, as detailed in Section 5.2.1. For a fixed spectral index, the steps are as follows:

1. Inject a specified number of signal neutrinos into the Monte Carlo simulation, following the assumed energy spectrum.
2. Perform multiple signal-plus-background trials using the chosen number of injected signal neutrinos.
3. Repeat this procedure for a range of injected signal neutrino counts.
4. For each set of trials (corresponding to a given injected signal level), calculate the fraction of TS values that exceed the observed value, $\mathrm{TS}_{\mathrm{obs}}$.
5. Interpolate these fractions as a function of the injected signal using a spline function.
6. Determine the injected signal level for which 90% of trials yield $\mathrm{TS} > \mathrm{TS}_{\mathrm{obs}}$.
7. Convert this signal level into a flux using Eq. (4.20).

We note that the upper limit becomes more stringent when fewer signal events are fitted to the data. Within IceCube convention, the most stringent upper limit that can be reported corresponds to the analysis sensitivity. Thus, if $\mathrm{TS}_{\mathrm{obs}}$ lies below the median of the background TS distribution, we report $\Phi_0^{90\%}$ corresponding to this median.

Addressing NGC 1068

The galaxy NGC 1068 is a LIRG with a declination of $\delta > -3^\circ$ and is included in the GOALS sample. Given these criteria, it would be a natural candidate for inclusion in our analysis. However, NGC 1068 was already identified as a source of high-energy neutrinos with a significance of about 4.2σ by the IceCube Collaboration at the time this analysis was being developed ([16]; see also Section 1.6.2). As discussed in the initial source selection in Section 2.3, we chose to exclude NGC 1068 from the catalog search in order to avoid biases and enhance the chances of discovering previously unidentified sources of high-energy neutrinos.

We note that the initial evidence for NGC 1068 as a high-energy neutrino source is based on the up-going muon track sample presented in section 4.4, but uses only 9 years of data instead of the 13 years of data used in this work. Recently, an independent analysis within the IceCube Collaboration, also using 13 years of up-going muon track, re-unblinded the location of NGC 1068. The analysis resulted in a slightly lower global p-value of 4.0σ for NGC 1068 [144].

NGC 1068 is excluded from the calculation of any global p-values in this work. However, following unblinding, the catalog search and binomial test will be repeated with NGC 1068 included. This choice is motivated by the fact that NGC 1068 is a natural member of the LIRG population. In this context, only local p-values will be reported, and the results cannot be used to draw definitive conclusions. Tests performed after the unblinding of the analysis will be referred to as **post-unblinding checks**.

Preliminary results warning

The results presented here are preliminary. While no significant changes to the results or the conclusions drawn are anticipated, minor revisions may be made in the final publication.

6.1 Catalog Search Results

Having selected the sources (Section 2.3), defined the methodology (Section 5.1), and evaluated the analysis performance (Section 5.2), we now proceed to unblind the data and obtain the results for the different searches. In this section, we present and discuss the results of the catalog search and the corresponding binomial test.

The most significant source in the tested catalog of 113 GOALS U/LIRGs is NGC 7469, which exhibits a local p-value corresponding to a significance of 3.7σ. However, after accounting for the *look-elsewhere effect* (see Section 5.2.2), the global p-value translates to a reduced significance of approximately 2.3σ, which falls short of the threshold required to claim evidence for high-energy neutrino emission. Nevertheless, independent analyses have reported additional indications favoring this galaxy, as will be discussed in greater detail in Section 6.1.1.

All other investigated source locations yield TS values corresponding to significances below the threshold required to claim evidence, although not all have an observed TS of $\mathrm{TS}_{\mathrm{obs}} = 0$. The unblinding results are summarized in Table F.1 in the appendix. These results include the observed test statistic ($\mathrm{TS}_{\mathrm{obs}}$), the best-fit number of signal neutrinos (n_s^{fit}), the best-fit spectral index (γ_{fit}), the local p-value (p_{local}), the local significance (σ_{local}), and the global significance for the most significant source (σ_{global}).

The non-detection of high energy neutrinos allows the setting of 90% CL upper limits on the high-energy neutrino emission from the investigated source locations. These upper limits are calculated using Eq. (6.1). Figure 6.1 shows the 90% CL upper limits for all objects categorized by the sine of their declination for three assumed spectral indices: $\gamma = 2.0$, 2.5 and 3.0. Note that the largest upper limits are associated with the highest observed TS values. For sources with $\mathrm{TS}_{\mathrm{obs}} = 0$, the upper limit corresponds to the sensitivity flux, as shown in Figure 5.7.

In Table F.1 of the Appendix, we also report the 90% CL upper bounds on the high-energy muon-neutrino flux at 1 TeV, assuming spectral indices of $\gamma = 2.0$ and $\gamma = 2.5$.

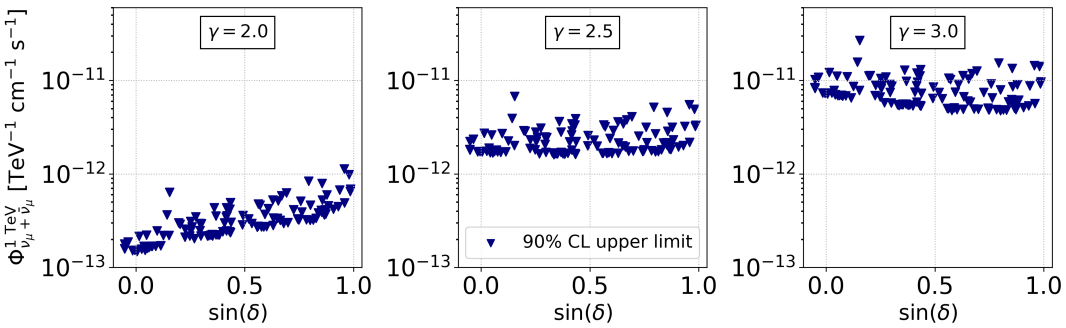

FIGURE 6.1: 90% confidence level (CL) upper limits on the high-energy muon-neutrino flux for the 113 investigated GOALS U/LIRGs. The upper limits are shown for $\gamma = 2.0, 2.5$, and 3.0.

.

As post-unblinding check, we also investigate the source location of NGC 1068. We find a a local p-value with a corresponding significance of 5.0σ. This local p-value is not trial corrected as this galaxy was excluded from the initial source selection. Therefore this significance cannot be used to make any claims.

For the best-fit parameters of NGC 1068 we obtain a soft spectral index of $\gamma_{\rm fit} = 3.4$ and a number of signal neutrinos equal to $n_s^{\rm fit} = 102.2$. These fit results, along with the local significance, are consistent with those obtained in a parallel analysis that computed the global significance of NGC 1068 using 13 years of up-going muon-track data [144]. The reader is referred to the analysis for further discussion of the evolution of the best-fit parameters versus the initial identification of NGC 1068 with only 9 years of data [16].

6.1.1 NGC 7469

The most significant source in the catalog search presented in this work is NGC 7469 (IRASF23007+0836). An image of this galaxy in electromagnetic wavelengths is shown in Figure 6.2 and Table 6.1 shows the unblinding results for this source.

NGC 7469 has a local p-value of $\mathrm{p}_{\rm local} = 9.4 \times 10^{-5}$, which corresponds to a significance of 3.7σ. However, after correcting for the look-elsewhere effect (see Section 5.2.2) a global p-value of $\mathrm{p}_{\rm global} = 1.0 \times 10^{-2}$ is obtained, which corresponds to a significance of 2.3σ. Therefore, we conclude a soft excess from the direction of NGC 7469, but cannot claim evidence for high-energy neutrino emission.

We note that the best-fit spectral index of the assumed power-law spectrum is hard, with $\gamma_{\rm fit} = 1.9^{+0.4}_{-0.5}$. The uncertainties correspond to the 1σ interval derived from the one-dimensional likelihood profile. Notably, the best-fit spectral index of NGC 7469 is significantly harder than that of NGC 1068, for which $\gamma_{\rm fit} = 3.4^{+0.2}_{-0.2}$ [144].

The right panel of Figure 6.2 shows the background-only TS distribution for the location of NGC 7469 as defined in the GOALS catalog. This distribution is obtained from 500.000 background-only trials. The trials are indicated in gray and the black dashed line shows the best fit of the form given in Eq. (5.26). In addition, we show the TS values required to reach the 3σ and 5σ discovery potential, respectively, as well as the observed TS value.

Characteristics & comparison to NGC 1068

NGC 7469 is a bright LIRG with $\log_{10}(L_{\rm IR}/L_\odot) = 11.65$ at a luminosity distance of about 70 Mpc [234, 244]. Its central region hosts an actively accreting supermassive black hole with a mass of $\sim 10^7\ M_\odot$ [363], classified as a Seyfert I active galactic nucleus (AGN; see section 1.1.4). This AGN is surrounded by a compact circumnuclear starburst region with a radius of about 580 pc (e.g. [252, 254]). NGC 7469 is the closest known example of a galaxy system that has both a rapidly accreting supermassive black hole and a compact nuclear starburst ring.

NGC 7469 forms an interacting pair with the nearby galaxy IC 5283, classified as an early-stage merger [184]. This pair is part of a system collectively called Arp 298. The companion galaxy shows no sign of nuclear activity.

Both NGC 1068 and NGC 7469 are classified as LIRGs and Seyfert galaxies. However, they differ significantly in orientation, distance, and spatial distribution of starburst activity. NGC 1068 is observed at a higher tilt angle, presenting its galactic disk more edge-on, leading to partial obscuration by the dusty torus (e.g. [163]). This geometry results in significant line-of-sight obscuration toward the nucleus, with a corresponding column density of $N_{\rm H} \approx 10^{25}\ {\rm cm}^{-2}$ [364], making direct observations challenging. In contrast, NGC 7469 is viewed almost face-on, with a column density of $N_{\rm H} \approx 10^{20.53}\ {\rm cm}^{-2}$ [364], offering a comparatively unobstructed view of its central region.

TABLE 6.1: Unblinding results for NGC 7469. The table lists the source coordinates in right ascension ($\alpha_{\rm src}$) and declination ($\delta_{\rm src}$), both in degrees (°), along with the observed test statistic ($\mathrm{TS}_{\rm obs}$), the local p-value ($\mathrm{p}_{\rm local}$), and the global p-value ($\mathrm{p}_{\rm global}$). Additionally, the best-fit number of signal neutrinos ($n_s^{\rm fit}$) and spectral index ($\gamma_{\rm fit}$) are provided.

$(\alpha_{\rm src}, \delta_{\rm src})$	$\mathrm{TS}_{\rm obs}$	$\mathrm{p}_{\rm local}$	$\mathrm{p}_{\rm global}$	$(n_s^{\rm fit}, \gamma_{\rm fit})$
$(345.82°, 8.88°)$	15.5	9.4×10^{-5} (3.7σ)	1.0×10^{-2} (2.3σ)	$(5.5, 1.9)$

In terms of distance, NGC 1068 is approximately five times closer than NGC 7469 [19]. At first glance, it is striking that their hard X-ray fluxes appear comparable despite this distance disparity. However, this apparent similarity arises from obscuration effects. After correcting for absorption, the intrinsic $14 - 195$ keV flux of NGC 1068 is found to be about three times higher than that of NGC 7469 [364]. Furthermore, we note that while NGC 1068 has been detected in gamma rays [165], there is currently no confirmed gamma-ray detection of NGC 7469.

Although both NGC 1068 and NGC 7469 host actively accreting supermassive black holes and circumnuclear star formation, the spatial extent of their starburst regions differs significantly. In NGC 7469 the starburst ring is relatively compact, with a radius of about 580 pc [288, 365], whereas in NGC 1068 it extends to about 1300 pc [311].

We conclude that significant differences in source properties exist that may be associated with high-energy neutrino production. In addition to the distinctions outlined above, we note a discrepancy in the best-fit spectral indices of NGC 1068 and NGC 7469. If the excess observed for NGC 7469 develops into a statistically significant detection while maintaining its current spectral index, this disparity could point to the existence of at least two distinct classes of high-energy neutrino sources.

Spatial coincidence with two IceCube alerts

Most interestingly, closer inspection reveals that the observed excess for NGC 7469 is entirely due to the spatial coincidence with two high-energy neutrinos ($\gtrsim 100$ TeV), which were flagged by IceCube's realtime alert system. As discussed in Section 4.5, this alert system was put in place to identify and communicate high-energy neutrinos which have a high probability of being of astrophysical origin.

Particularly, two events identified by the alert system and that drive the significance of NGC 7469 are:

- **IC220424A**[1]: gold alert with a signalness of 50% and an estimated energy of 184 TeV. See Eq. (4.21) for the definition of gold and bronze events.
- **IC230416A**[2]: bronze alert with a signalness of 34% of 127 TeV.

Unfortunately, both events occurred in close proximity to the Sun and Moon at the time of detection, as indicated in the corresponding alerts, which impeded follow-up observations in other messengers. Nevertheless, once flagged, the neutrino events proceed through the standard sequence of filtering and processing steps in IceCube (see Chapter 4). Provided they satisfy the relevant selection criteria, they may ultimately be included in high-level datasets employed in point-source searches, such

[1]GCN Notice IC220424A: gcn.gsfc.nasa.gov/notices_amon_g_b/136565_2186969.amon
[2]GCN Notice IC230416A: gcn.gsfc.nasa.gov/notices_amon_g_b/137840_57034692.amon

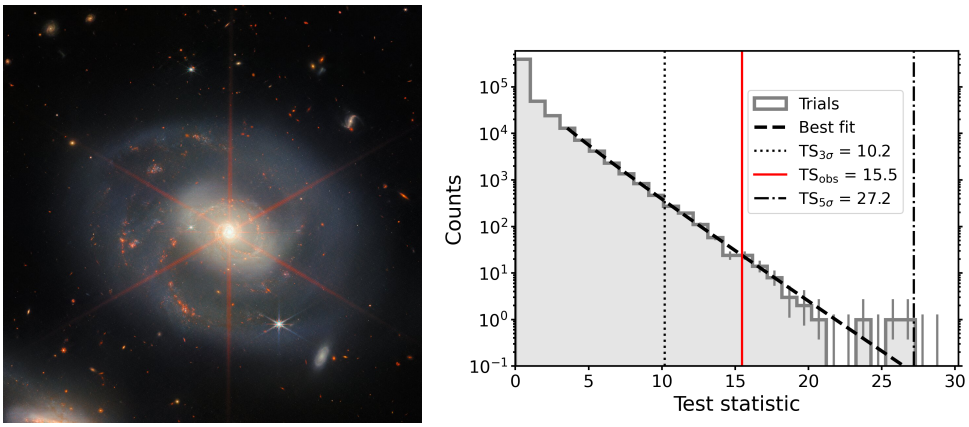

FIGURE 6.2: Left: NGC 7469 observed as part of the Great Observatories All-sky LIRG Survey (GOALS) Early Release Science program with the NASA/ESA/CSA James Webb Space Telescope. The center of the galaxy hosts a bright active galactic nucleus, surrounded by intense starburst activity, indicated by the orange regions. The prominent star-shaped feature is an artifact of the telescope, known as a diffraction spike. *Credit: ESA/Webb, NASA & CSA, L. Armus, A. S. Evans*. Right panel: Background-only test-statistic (TS) distribution at the location of NGC 7469, as defined in the GOALS catalog. The distribution is obtained from 500.000 background-only trials (shown in gray) as described in Section 5.2. The dashed black line represents the best-fit curve as described by Eq. (5.26). Vertical lines indicate the TS values corresponding to the 3σ ($\mathrm{TS}_{3\sigma}$) and 5σ ($\mathrm{TS}_{5\sigma}$) discovery potentials, as well as the observed TS value ($\mathrm{TS}_{\mathrm{obs}}$).

as the up-going muon-track sample introduced in Section 4.4. These events, possibly with different reconstructed variables, could then contribute to the TS values of a source, as is the case here.

Figure 6.3 shows how the TS value for NGC 7469 changes as the top-contributing events in its direction are gradually removed from the up-going muon-track sample.

We find that, after removing the top two contributing events in the direction of NGC 7469—corresponding to the two alert events—the significance drops to zero. For comparison, we perform the same analysis for NGC 1068, which shows a more gradual decrease in the TS value. This behavior is primarily due to the fact that the events contributing to the significance of NGC 1068 are more numerous but individually less energetic ($\sim 1{-}10$ TeV) [144]. As a result, the signal-to-background ratio per event (see Eq. (5.12)) is lower, and each event contributes less to the overall significance.

Figure 6.4 presents the significance map around the location of NGC 7469, indicated by the red dot, based on electromagnetic observations. To obtain this figure, a grid of pixels with dimensions of approximately $0.3^\circ \times 0.3^\circ$ is defined, and the TS value, given in Eq. (5.7), is computed at the center of each pixel. These TS values are then used to derive the corresponding significance levels via their associated p-values. Figure 6.4 displays the resulting p-value map, with the most significant location marked by a white cross. Interestingly, the angular separation between the best-fit position and the electromagnetic counterpart is only about 0.07°. The 68% and 95% confidence regions corresponding to the most significant location (white cross) are also shown, along with the coordinates of IC220424A and IC230416A.

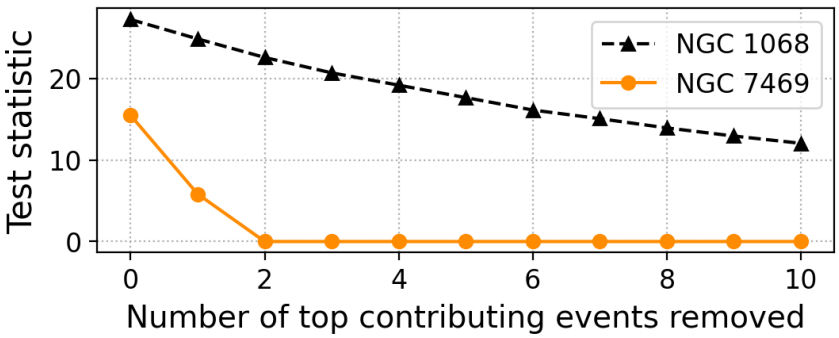

FIGURE 6.3: Test statistic (TS) value as a function of the number of top contributing events that are removed. This is shown for both NGC 1068 (black triangles) and NGC 7469 (yellow circles).

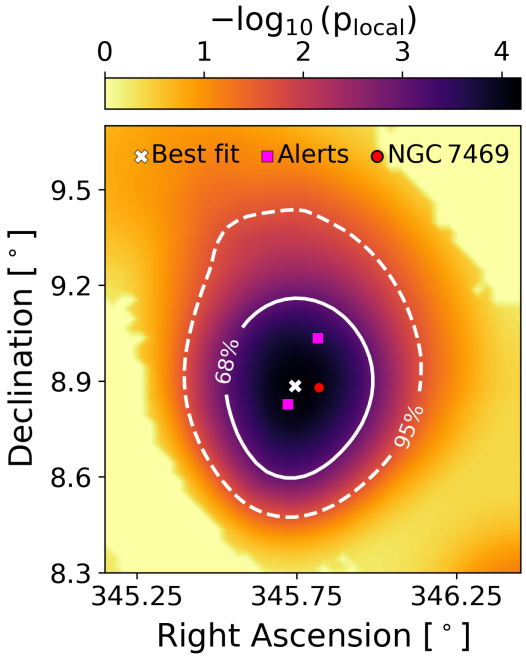

FIGURE 6.4: A scan of the local p-value (p_{local}) in the vicinity of the optical position of NGC 7469 (red dot), shown in the coordinates plane. The location of the most significant excess is marked by a white cross, with the 68% and 95% containment regions indicated by white solid and dashed lines, respectively. The positions of the two IceCube alerts, IC220424A and IC230416A, are also marked (purple rectangles).

Independent hints for NGC 7469 as candidate high-energy neutrino source

Two independent analyses have found indications of high-energy neutrino emission from the direction of NGC 7469:

- An a-posteriori analysis was conducted using four years of IceCube data, focusing exclusively on IceCube alert events. The study found that the spatial coincidence of two alerts—IC220424A and IC230416A—with the location of NGC 7469 is unlikely to be due to background fluctuations alone, with a reported significance of 3.2σ [366]. This result supports the possibility that one or both alert events may have originated from NGC 7469.

- A separate IceCube point-source search investigated high-energy neutrino emission from a catalog of 47 Seyfert galaxies. The analysis followed the statistical formalism outlined in Chapter 5 and used the same dataset as described in Section 4.4.[3] This Seyfert-focused study identified NGC 7469 as the most significant source in the catalog [353], with a global p-value corresponding to 2.4σ significance, comparable to the global significance 2.3σ identified in this work. We stress that the Seyfert analysis employed a different source catalog and investigated multiple emission models, resulting in different hypothesis tests and as such a unique trial correction specific to that study.

Both of these analyses were conducted after the methodology and source catalog described in Chapters 2, 5 and 6 had already been finalized. Consequently, the observed excess of high-energy neutrino emission from NGC 7469 was not known at the time of finalizing the methodology.

These different identifications, in combination with the fact that NGC 7469 is a nearby and luminous AGN with a compact starburst region, make this a particularly promising high-energy neutrino source.

6.1.2 Binomial test

Figure 6.5 shows the binomial test (see Section 5.2.2 for an outline of the methodology) using the p-values obtained from the unblinded data. The left panel shows the binomial test for the 113 catalog sources, excluding NGC 1068. We conclude that the most significant subset of sources corresponds to the $k_{\mathrm{best}} = 58$ most significant p-values. The best-binomial p-value corresponding to $k_{\mathrm{best}} = 58$ is $\mathrm{p}_{\mathrm{binom,best}} = 6.5 \times 10^{-3}$, which corresponds to a significance level of 2.5σ. Correcting for the look-elsewhere effect (see Section 5.2.2) lowers the significance to about 1.4σ. As this significance is well below the threshold to require evidence ($> 3\sigma$), it is concluded that no statistically significant subset of p-values is identified for the 113 investigated GOALS objects through the binomial test.

As post-unblinding check we investigate the effect of including the LIRG NGC 1068 in the binomial test. The test is shown in the right panel of Figure 6.5. Doing so, we conclude that the most significant subset out of the 114 GOALS U/LIRGs now consists of one galaxy only, i.e. $k_{\mathrm{best}} = 1$, which is NGC 1068. This translates to a local best-binomial p-value of $\mathrm{p}_{\mathrm{binom,best}} = 4.0 \times 10^{-5}$, corresponding to a 3.9σ significance level. We calculate no global p-value as NGC 1068 was not included in the initial selection of galaxies.

[3] The overlap of sources between our work and the Seyfert analysis is: MCG +4-48-2, NGC 7469, NGC 7682, NGC 6240.

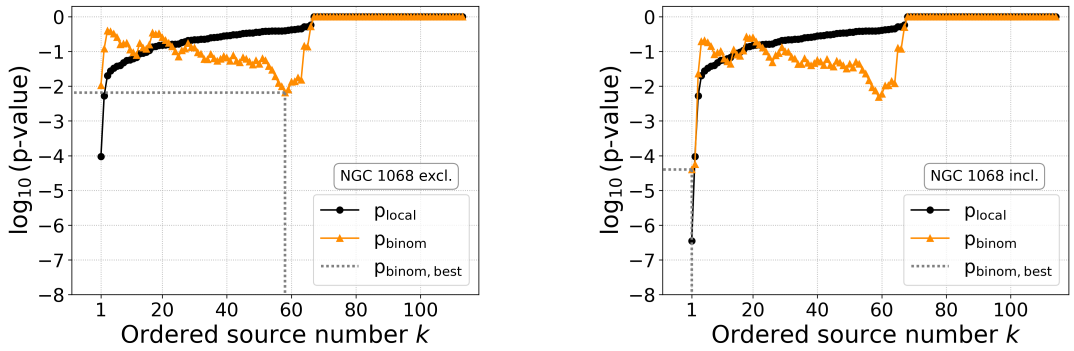

FIGURE 6.5: Binomial p-values (orange triangles) as a function of the ordered source number $k \in \{1, \ldots, 113\}$, where p_k is the k-th most significant local p-value (black circle). The binomial p-value represents the probability of observing k or more local p-values less than or equal to p_k. The most significant binomial p-value and its corresponding source number are highlighted. The left panel excludes NGC 1068, while the right panel includes it.

Finally, we note that in the right panel of Figure 6.5, the binomial p-values corresponding to $k = 1$ and $k = 2$ are nearly identical. In the $k = 2$ case, the two contributing sources are NGC 1068 and NGC 7469.

6.1.3 Interpretation

The GOALS sample encompasses a diverse range of galaxy types, including Seyfert I and II AGN, LINERs, and starburst galaxies (Chapter 2). Consequently, the non-detections from our IceCube search provide the most stringent per-source constraints to date on steady high-energy neutrino emission across a broad spectrum of physical conditions present in these systems. In the following, we interpret the results of the catalog search in the context of the electromagnetic properties revealed by GOALS.

The interpretation presented in this section was developed in collaboration with a select group of GOALS members. The sharing of unblinded IceCube results prior to publication was made possible by formal associate memberships granted to these GOALS members by the IceCube Collaboration.

AGN vs staburst-driven point sources

As outlined in Chapter 2, although the GOALS catalog encompasses a broad range of galaxy types, it is dominated by starburst galaxies. The lack of high-energy neutrino detections from the surveyed GOALS U/LIRGs therefore implies a non-detection from a substantial population of starburst-dominated U/LIRGs within a distance range of approximately 10 to 400 Mpc. This result contrasts with previous evidence of high-energy neutrino emission from the direction of the nearby AGN-dominated LIRG NGC 1068 [16, 144] at about 16 Mpc [234].

One interpretation of these findings is that nearby, luminous AGN may be detectable by IceCube as steady sources of high-energy neutrinos, whereas starburst-driven systems within the same distance range remain undetectable.

Under this assumption, the observed excess of high-energy neutrinos associated with NGC 7469 is not unexpected. Following NGC 1068, NGC 7469 is the next-nearest GOALS LIRG in the Northern Sky that hosts a luminous AGN. It is also worth noting

that the total infrared luminosity of NGC 7469 lies on the higher end of the distribution for LIRGs, indicative of a powerful energy source.

A closer examination of the GOALS sample shows that five Northern-Sky galaxies exhibit higher infrared fluxes, factoring in both intrinsic luminosity and distance, than NGC 7469. However, all but one of these lack clear signs of AGN activity. The exception, UGC 8058, does host an AGN, but the galaxy resides at approximately twice to three times the distance. These galaxies in this context are discussed in more detail later in this section.

The non-detectability of individual starburst-driven U/LIRGs as steady sources of high-energy neutrinos is also consistent with the findings presented in Chapter 3. There, we demonstrated that the expected steady-state high-energy neutrino flux from local, starburst-dominated U/LIRGs remains well below IceCube's point-source sensitivity. It is important to emphasize, however, that this interpretation does not exclude a potentially significant cumulative contribution from the entire population of such sources. As discussed in Section 3.4, diffuse high-energy neutrino emission from LIRGs in particular could plausibly account for the observed diffuse flux level under reasonably motivated assumptions.

Finally, we note that the hypothesis suggesting nearby AGN-driven systems as persistent high-energy neutrino sources is further supported by independent observations beyond NGC 1068. Notably, the nearby Seyfert galaxy NGC 4151, located at a distance of ~ 16 Mpc and classified as neither a LIRG nor a ULIRG, was investigated in a separate IceCube analysis [145], where it exhibited a 2.9σ deviation from the background-only hypothesis. Moreover, a recent analysis has identified a binomial excess at the evidence level across 11 Seyfert galaxies [144].

Highlighting individual U/LIRGs

Below, we highlight the sources in the GOALS sample that exhibit higher IR flux than NGC 7469. These galaxies are presented in descending order of brightness. Although NGC 1068 is the brightest IR source in the GOALS sample, it is excluded from this discussion, as it has already been covered extensively earlier in this work.

Each of the highlighted systems is of interest in the context of multi-messenger astronomy. However, our primary goal here is to use their properties to motivate broader conclusions regarding starburst- versus AGN-driven high-energy neutrino emission, as explored earlier in this section. These discussions also underscore the value of the extensive electromagnetic data available from GOALS, which, when combined with the high-energy neutrino observations, provide a powerful framework for interpreting the high-energy environments in GOALS U/LIRGs.

- **NGC 2146** (LIRG): NGC 2146 is one of the nearest galaxies in the GOALS catalog, classified as a starburst galaxy with a luminosity distance of approximately 17 Mpc and an infrared luminosity of $\log_{10}(L_{\rm IR}/L_{\odot}) = 11.14$ [234, 244]. Its intense star-forming activity is likely triggered by a past tidal interaction or a minor merger [367]. A prominent galactic superwind is observed along the minor axis, driven by the combined effects of stellar winds and supernovae [368, 369], making NGC 2146 an important local laboratory for investigating feedback mechanisms in starburst environments. Both the supernova-driven activity and the resulting galactic superwind are potential sites for the production of high-energy radiation, including gamma rays and high-energy neutrinos (see Chapter 3). Indeed, GeV gamma-ray emission has been detected from the direction of

NGC 2146 [370]. However, due to its high declination of $\delta = 78.36°$ [244], the galaxy lies in a region of reduced sensitivity for IceCube (see Figure 5.7). The lack of a corresponding high-energy neutrino detection may thus be attributed to the limited detectability of steady starburst-driven processes and/or the reduced instrumental sensitivity in this region of the sky.

- **NGC 3690 or Arp 299** (LIRG): As discussed in Section 3.2, Arp 299 is the most IR-luminous system within 50 Mpc, with $\log_{10}(L_{\rm IR}/L_\odot) = 11.93$, and is located at a declination of $\delta = 58.56°$ [234, 244]. This mid-stage merger between two galaxies hosts intense starburst activity, a Compton-thick AGN, and a known tidal disruption event—all plausible high-energy neutrino sources. Although the predicted neutrino flux from the starburst alone lies below IceCube's current sensitivity (Figure 3.6), models incorporating contributions from the buried AGN(s) could be tested against the currently most stringent upper limits presented here.

- **Arp 220** (ULIRG): At a distance of about 88 Mpc, Arp 220 is the nearest known ULIRG, with an infrared luminosity of $\log_{10}(L_{\rm IR}/L_\odot) = 12.38$ and a favorable declination of $\delta = 23.50°$ [234, 244]. As an advanced-stage merger of two gas-rich galaxies, Arp 220 exhibits two distinct nuclear regions, with 97 compact radio sources identified as supernovae or remnants [200]. The western nucleus hosts an extremely obscured component, with column densities up to $N_{\rm H} \sim 10^{26}$ cm^{-2} [217]. Recent JWST spectra reveal no unambiguous evidence for AGN and instead favoring a deeply buried nuclear starburst [371].

  Given its extreme luminosity, distance, gamma-ray detection [95, 96], and obscured nature, Arp 220 has long been considered a prime candidate for high-energy neutrino emission. The non-detection of high-energy neutrinos provides the best constraints on the high-energy neutrino flux from this galaxy.

- **NGC 4418** (LIRG): At a luminosity distance of approximately 34 Mpc and declination $\delta = -0.88°$, NGC 4418 falls within a region of excellent IceCube sensitivity across various spectral indices [234, 244]. With $\log_{10}(L_{\rm IR}/L_\odot) = 11.06$ [234], it lies at the lower end of the LIRG class but is notable for its extremely compact, heavily obscured nucleus. The central energy source, confined to a region < 20 pc, is enshrouded in dust with column densities exceeding $N_{\rm H} \sim 10^{25-26}$ cm^{-2} [218]. Its nature, either a deeply buried AGN or compact starburst, remains debated. NGC 4418 is a prototypical compact obscured nucleus (CON), as identified by strong emission from vibrationally excited hydrogen cyanide (HCN-vib; see Section 2.1.2). NGC 4418 was an appealing candidate given powerful obscured nucleus, proximity, and favorable sky location making.

  Future identification of the central power source may provide insights into the absence of detectable high-energy neutrino emission. The highly compact nature of the source, or even a more definitive classification as a starburst galaxy versus an AGN, could play a significant role in this context. This argument also applies to the highly compact and energetic nature of western nucleus in Arp 220. We further explore this idea in Section 6.2.

- **UGC 08058** (ULIRG): Also known as Mrk 231, this galaxy is one of the most luminous ULIRGs in GOALS, with $\log_{10}(L_{\rm IR}/L_\odot) = 12.50$ [234] and a luminosity distance of 192 Mpc, located at a declination of $\delta = 56.87°$. Mrk 231 hosts a quasar, making it a unique hybrid object that combines features of powerful AGN activity and extreme star formation. The AGN is embedded within a dense molecular disk, and powerful outflows have been observed [372]. Although this

an extremely powerful source, it is located much farther away than the other sources discussed here, thereby potentially significantly suppressing a potential high-energy neutrino luminosity.

Motivated follow-up searches

The results of the catalog search and binomial test motivate the following searches:

- A catalog search targeting starburst galaxies closer than the nearest sources in GOALS, NGC 1068 and NGC 2146, both in the Northern and Southern Sky. This would help to further distinguish between the detectability of predominantly starburst and AGN-dominated systems.
- Time-integrated point-source searches targeting nearby GOALS U/LIRGs with both a luminous AGN and (circum)nuclear starburst activity in the Southern Sky specifically. This recommendation is based on the independent evidence for high energy neutrino emission from NGC 1068 [16, 144] and the excess observed from the direction of NGC 7469 in our work, both nearby, luminous AGN with strong (circum)nuclear starbursts.

  Particularly noteworthy examples include the nearby LIRGs NGC 5135 and NGC 7130, located between about 60 and 70 Mpc (see Table D), respectively. Both are classified as type-2 Seyfert galaxies with a Compton-thick AGN and exhibit clear signatures of starburst activity.

These searches should be done not only by IceCube, but by any telescope on the global scale that sees fit.

6.2 Stacking Search Results

We conducted a stacking search to identify a cumulative signal from a sample of 10 U/LIRGs in GOALS with detected vibrationally excited hydrogen cyanide (HCN-vib) emission. The sources included in this analysis are listed in Table F.2.

HCN-vib emission traces compact, highly dust-obscured, and energetic regions, typically powered by a buried AGN and/or nuclear starburst. These conditions represent a common characteristic among the selected galaxies (see Section 2.1.2). Such environments provide favorable conditions for high-energy neutrino production, assuming cosmic-ray acceleration occurs, while simultaneously attenuating gamma-ray emission through interactions with the dense amounts of dust and gas [85, 227]. As discussed in Section 1.5.2, gamma-ray-opaque, high-energy neutrino sources are supported by both individual source detections and diffuse observations.

The observed test statistic (TS) value for the stacking analysis is $\mathrm{TS}_{\mathrm{obs}} = 0$, corresponding to a p-value of unity. This indicates that the result is fully consistent with the background-only hypothesis.

Since the median of the background-only TS distribution for the stacking search is very close to zero (see section 5.2.3), the 90% confidence level (CL) upper limit for the cumulative neutrino flux from the 10 investigated sources corresponds to the sensitivity. Figure 5.13 shows the sensitivity at $1\ \mathrm{TeV}$ for the stacked signal.

6.2.1 Interpretation

We conclude that 10 of the most dust-enshrouded systems in GOALS detected via significant HCN-vib emission show no statistically significant evidence of high-energy neutrino emission—neither individually (catalog search; see Section 6.1) nor collectively (stacking analysis).

AGN vs starburst & phase-dependent emission

Interpreting the non-detection of high-energy neutrinos from these extremely obscured and energetic HCN-vib U/LIRGs remains challenging, primarily due to the uncertain nature of their central power sources (see Section 2.1.2). Nevertheless, future efforts aimed at identifying the dominant central engine, combined with continued neutrino searches, may offer valuable insights. If HCN-vib bright U/LIRGs are ultimately found to be primarily powered by deeply embedded starbursts, the persistent non-detection could lend support to the hypothesis outlined in Section 6.1. This hypothesis posits that AGN-dominated systems are more likely to produce detectable high-energy neutrino emission, whereas starburst-driven sources may fall below current detection thresholds. Notably, a recent in-depth study of Arp 220—a prototypical HCN-vib ULIRG—conducted with the James Webb Space Telescope (JWST) reports no unambiguous evidence for AGN activity in its western nucleus [371].

Given that HCN-vib U/LIRGs likely represent a distinct phase in galaxy evolution, the persistent non-detection of high-energy neutrinos from GOALS U/LIRGs may also reflect a phase-dependent efficiency in particle acceleration—and, by extension, in high-energy neutrino production. Notably, both NGC 1068 and NGC 7469—sources that exhibit tentative signs of high-energy neutrino emission (see Section 6.1)—show energetic electromagnetic activity on spatial scales that are considerably larger than those of the extremely compact and heavily obscured HCN-vib bright U/LIRGs such as NGC 4418 and Arp 220.

This contrast in spatial extent can be quantified by comparing the half-light radius at 70 μm ($R_{70\,\mu\mathrm{m}}$).[4] For prototypical HCN-vib sources such as NGC 4418, IC 860, and Arp 220, $R_{70\,\mu\mathrm{m}}$ is smaller—indicating greater compactness—by factors of approximately 10, 6, and 2, respectively, relative to NGC 7469, which has $R_{70\,\mu\mathrm{m}} \sim 577$ pc [234].

Motivated follow-up searches

As discussed in Chapter 2, U/LIRGs are observed both as isolated systems and as galaxies in various stages of interaction along the merger sequence. From a theoretical standpoint, it is well motivated to search for high-energy neutrino emission across these evolutionary stages to better understand the efficiency of neutrino production. In particular, advanced mergers are expected to be efficient emitters due to intensified nuclear activity and elevated densities of dust, gas, and radiation, which enhance the probability of hadronic interactions. However, this picture may be more complex: certain phases of extreme obscuration could prevent particle acceleration, thereby suppressing high-energy neutrino emission.

U/LIRGs with strong HCN-vib emission exhibit highly compact and obscured nuclear regions, possibly indicating a shared evolutionary phase. Yet, these HCN-vib-bright systems do not show significant high-energy neutrino emission, either individually or in aggregate. In contrast, tentative neutrino signals have been reported from

[4] The radius encompassing half of the galaxy's light measured at 70 μm.

galaxies such as NGC 1068 and NGC 7469, which lack strong HCN-vib signatures and exhibit more extended nuclear structures. This contrast suggests that high-energy neutrino production may depend on a galaxy's evolutionary phase, reinforcing the theoretical motivation to study neutrino emission across the full spectrum of U/LIRG evolution.

A promising strategy is to examine galaxies spanning a broad range of interaction stages and secularly evolving systems. To construct representative samples for IceCube source searches, it is advantageous to extend beyond the GOALS sample and include interacting and merging systems across the full sky. Relevant source catalogs include the Atlas of Peculiar Galaxies [373] and merger candidates identified in the Sloan Digital Sky Survey (SDSS) [374]. Although these catalogs lack the multiwavelength depth of GOALS, their significantly larger sizes offer substantial statistical power for stacking analyses [143].

We note that constructing a representative local sample—as opposed to stacking exclusively on known HCN-vib sources in the Northern Hemisphere, as done in this work—can facilitate robust extrapolation of the contribution of such systems to the diffuse high-energy neutrino flux observed by IceCube (e.g., [150]). This can be pursued using either analytic models of galaxy evolution or cosmological hydrodynamical simulations, as introduced in Section 3.6.

An alternative approach to probing specific evolutionary phases in the cores of galaxies—rather than focusing solely on merger stages—is to classify galaxies based on physical parameters such as the Eddington ratio ($\lambda_{\rm edd}$), which compares the actual luminosity of a supermassive black hole to its theoretical maximum, and the column density ($N_{\rm H}$), which have been shown to be correlated [375]. This classification enables an investigation into whether specific regions within the $N_{\rm H}$–$\lambda_{\rm edd}$ parameter space, reflecting distinct nuclear conditions, are associated with enhanced high-energy neutrino production. Note that the focus here would be on the AGN activity.

Regardless of the tested source samples, we recommend enhancing stacking analyses by incorporating the most recent hemisphere-specific IceCube datasets and exploring more sophisticated weighting schemes. As demonstrated throughout this thesis, hybrid systems such as U/LIRGs exhibit substantial variation in both physical conditions and likely neutrino production mechanisms. In particular, AGN activity tends to increase with merger progression (Chapter 2). We therefore advocate for hybrid stacking weights that incorporate contributions from both AGN- and starburst-driven emission scenarios, such as the approach developed in Chapter 3. More complex descriptions of the emission mechanisms would also allow for constraints of the model parameters.

CHAPTER 7

Conclusions & Outlook

The IceCube Neutrino Observatory detects a diffuse flux of high-energy (TeV-PeV) neutrinos [4–11]. Evidence for neutrino emission has been reported from the Galactic plane [13] and two active galaxies, NGC 1068 [16] and TXS 0506+056 [14, 15], though none have reached the statistical significance to claim a discovery. Even if confirmed, the contributions from these active galaxies would remain at the percent level, while the Galactic plane would account for about ten percent of the observed flux. Thus, despite this observational breakthrough, the origins of the astrophysical neutrino flux remain largely unknown.

In this work, we explore a potential class of sources that may contribute to IceCube's high-energy neutrino flux. Identifying such sources is of fundamental importance, as it will help to resolve the long-standing mystery surrounding the origin of cosmic particle accelerators [1].

In Chapter 1, we explored the high-energy Universe via subatomic particles, highlighting high-energy neutrinos as key cosmic messengers due to their neutral, weakly interacting nature and hadronic origins. We highlight that diffuse and targeted observations of high-energy neutrinos indicate a lack of corresponding gamma-ray emission, suggesting the presence of gamma-ray dim neutrino sources [17, 18, 142].

Chapter 2 introduced luminous and ultraluminous infrared galaxies (LIRGs and ULIRGs, respectively) as promising candidate neutrino sources. LIRGs are defined by extreme infrared luminosities in the range $10^{11} L_\odot \leq L_{\rm IR} \equiv L_{\rm IR[8–1000\,\mu m]} < 10^{12} L_\odot$, while ULIRGs have even larger IR luminosities, $L_{\rm IR} \geq 10^{12} L_\odot$. Nearby U/LIRGs are typically interacting or merging galaxy systems, characterized by intense, dust-obscured star formation ($\sim 10{-}100\ M_\odot\ {\rm yr}^{-1}$) and, at higher luminosities, an increasing contribution from active galactic nuclei (AGN) (e.g. [19, 184, 234, 244]). LIRGs are observed across all stages of a galaxy merger, as well as secularly evolving galaxies, whereas ULIRGs are almost exclusively found in advanced merger stages [182–184].

As discussed in Chapter 2, the starburst and AGN environments in U/LIRGs could support hadronic particle acceleration, producing high-energy neutrinos and gamma rays via interactions with dense gas and radiation. Strong potential for gamma-ray attenuation through interaction within this source environment makes U/LIRGs promising gamma-ray dim, neutrino-bright sources.

While the ULIRG population as a whole has been the focus of several studies in this context [150, 227, 232, 233], LIRGs—and per-source analyses of ULIRGs—remain comparatively underexplored. This thesis addresses that gap by conducting a comprehensive investigation of local U/LIRGs, using the multi-wavelength dataset from the Great Observatories All-Sky LIRG Survey (GOALS). This survey includes 180 LIRGs and 22 ULIRGs at redshifts $z < 0.09$ [19]. Notably, NGC 1068—a nearby, luminous LIRG and archetypal obscured AGN included in GOALS—has recently been identified as the first compelling candidate for high-energy neutrino emission at the evidence level [16]. This further highlights the astrophysical significance of LIRGs.

In this work, the investigation of GOALS U/LIRGs as candidate neutrino sources is divided into two parts. In what follows we conclude the main results of each part.

Framework for starburst-driven high-energy neutrino emission

In Chapter 3, we introduced a novel framework for steady-state high-energy neutrino production in the starburst regions of U/LIRGs, developed in collaboration with the GOALS project [22, 23]. This model estimates a galaxy's high-energy neutrino flux based on its infrared luminosity, with parameters constrained by data from the GOALS survey. The focus on starburst-driven emission is consistent with the starburst-dominated nature of most GOALS sources [234]. We made the following conclusions and computations using our framework:

- We applied the framework to a detailed **case study** focused on NGC 3690. We showed that the dominant sources of uncertainty in the predicted fluxes stem from the spectral index of the injection spectrum, the maximum attainable energy of cosmic-ray particles in the source environment, and the calorimetric conditions. These findings underscore key areas for future refinement.

- We extended the framework to the **GOALS sample**, providing the first starburst-driven neutrino flux predictions for a statistically significant population of local U/LIRGs. A comparison with current and projected detector sensitivities shows that, while IceCube is unlikely to detect such emission from individual sources, IceCube-Gen2 may be capable of probing optimistic emission scenarios.

- Our estimate for **NGC 1068** falls significantly below the recently reported neutrino signal from this source [16]. This implies the presence of additional, dominant contributions—most likely from its AGN component (see also [376]).

Given the strong positive redshift evolution in the number density of LIRGs and ULIRGs [179, 222], their cumulative emission may represent a significant component of the diffuse astrophysical neutrino flux. To explore this possibility, we analytically extrapolated the local neutrino fluxes predicted by our model across cosmic time, employing an established framework [17, 18]. Our findings suggest that:

- **LIRGs** could constitute a non-negligible contribution to the diffuse astrophysical neutrino flux. However, this contribution is constrained by the extragalactic gamma-ray background [98] and the calorimeter conditions across the diverse LIRG population. This constitutes the first observation-driven estimate of the LIRG contribution to the diffuse high-energy neutrino flux.

- For **ULIRGs**, we find that their contribution via the starburst channel is likely subdominant. This is consistent with existing upper limits for this source class reported by the IceCube Collaboration, which are of the same order as our prediction [150].

These projections assume approximately uniform neutrino production conditions across the populations, likely oversimplifying the environmental diversity revealed by GOALs [19] and by high-redshift observations of U/LIRGs [190]. To overcome this limitation, we have begun integrating our model into SIMBA, a cosmological hydrodynamic simulation spanning a comoving volume of $100\ \mathrm{Mpc}/h$ [25]. This integration enables a more detailed analysis of starburst regions relevant to high-energy neutrino production through cosmic history. Doing so, we move beyond the projection of local

fluxes using analytic methods, assuming that the neutrino production properties are uniform over cosmic history. Once complete, this framework will enable robust predictions and tighter constraints on model parameters. Notably, the implementation is not limited to starburst scenarios as `SIMBA` also traces AGN activity in the simulations.

IceCube search for high-energy neutrinos from northern GOALS U/LIRGs

We conducted a correlation analysis comparing 13 years of up-going muon-track data from IceCube (see Chapter 4) and 113 northern GOALS U/LIRGs with declinations greater than -3°. Informed by our modeling framework and the current lack of definitive knowledge regarding the emission mechanisms in neutrino sources, the analysis adopts a model-independent approach by assuming a generic power-law energy spectrum. This avoids constraining the interpretation to any specific emission scenario, thereby accommodating a broad range of possible neutrino emission mechanisms.

Our analysis encompasses individual source searches of the 113 U/LIRGs, a binomial test to identify potentially interesting subgroups within this sample of 113 U/LIRGs, and a focused analysis targetting a cumulative signal of 10 highly compact, warm, and obscured galaxies exhibiting vibrationally excited hydrogen cyanide (HCN-vib). The statistical formalism underlying these tests, as well as their performance, was discussed in detail in Chapter 5.

Results and interpretation of our correlation studies are presented and discussed in Chapter 6. While no statistically significant excess was observed for any of the searches, we provide various important insights:

- We set the most **stringent upper limits** to date on steady high-energy neutrino emission from a broad range of nearby ($z < 0.09$), powerful systems. This includes starburst-dominated, AGN-dominated, and hybrid galaxies. Combined with the rich electromagnetic data from GOALS[1], these high-energy neutrino constraints (Table F.1) provide a foundation for modeling high-energy processes in the local Universe.

- The **lack of detection from the many starburst-dominated sources** in our sample—reflecting some of the strongest starburst activity in the nearby Universe ($z < 0.09$)—supports important context for the mounting evidence for high-energy neutrino emission from AGN-dominated systems at comparable distance [16, 144, 145].

- Although not statistically significant, we observed an excess toward the LIRG **NGC 7469** with a global significance of 2.3σ. This excess spatially coincides with two ~ 100 TeV neutrinos detected by IceCube's real-time alert system [159, 160, 366]. Intriguingly, NGC 7469 was also identified in two independent analyses at the $2-3\sigma$ level [144, 366]. Given its proximity ($D_L \approx 71$ Mpc) and high IR luminosity ($\log_{10}(L_{\rm IR}/L_\odot) = 11.58$) [234], driven by a circumnuclear starburst region [252] and an AGN [254], it emerges as a novel candidate neutrino source.

These findings also offer valuable direction for future multi-messenger studies:

- We recommend extending the search for per-source neutrino emission from starburst-driven systems to the Southern Hemisphere, as well as to starburst galaxies closer than the nearest GOALS LIRG (NGC 1068) in the Northern Hemisphere. These efforts can be pursued by any neutrino observatory with appropriate sensitivity. Broadening the search will help clarify the detectability of

[1] goals.ipac.caltech.edu/

high-energy neutrino emission from both AGN- and starburst-powered galaxies, building on the the insights established in this work.

- The observed excesses from NGC 1068 and NGC 7469 motivate targeted studies of similar sources. Therefore we highlight NGC 7130 and NGC 5135 as promising candidate neutrino sources. Both are luminous Southern-hemisphere galaxies that host powerful AGN and starburst activity [377].

- While late-stage mergers show increased obscuration and nuclear activity [184], potentially favoring neutrino production, our analysis of 10 highly compact, HCN-vib bright sources—tracers of extreme obscuration—shows no significant neutrino excess. This may indicate that highly compact nuclear activity suppresses particle acceleration and thus high-energy neutrino production.

  In contrast, galaxies with tentative neutrino emission—such as NGC 1068 [16], NGC 4151 [145], and NGC 7469 (this work)—exhibit more extended nuclear morphologies, suggesting that central structural properties may influence neutrino production. To explore this, stacking analyses could be applied to galaxy samples across various merger stages as well as to secularly evolving galaxies. Future searches may extend beyond the GOALS sample to broader merger catalogs, such as the Arp Atlas [373] and SDSS-based candidates [374], improving statistical power and constraints on the diffuse neutrino flux, especially when combined with simulations (see Section 3.6). Additionally, classifying galaxies by nuclear properties like Eddington ratio ($\lambda_{\rm edd}$) and column density ($N_{\rm H}$)—which are correlated [375]—could help identify regions of parameter space relevant to neutrino emission.

  Across all approaches, we recommend using updated hemisphere-specific IceCube datasets and hybrid weighting schemes based on phenomenological models (such as in Chapter 3) to improve stacking sensitivity and better constrain the physical conditions enabling high-energy neutrino production.

Final remarks

Our modeling and correlation analyses using IceCube and GOALS data suggest that nearby starburst-dominated galaxies are unlikely to be detectable point sources of steady, high-energy neutrino emission. Instead, active hybrid galaxies exhibiting both starburst and AGN activity emerge as more plausible sources, consistent with growing observational evidence implicating local AGN-dominated systems.

We caution that the classification of detected sources as Seyfert galaxies (e.g., NGC 1068 and NGC 4151) does not necessarily imply Seyfert-type galaxies dominate the diffuse neutrino flux. Detection may be influenced by proximity and favorable emission conditions. Our results indicate that starburst activity in dense environments, integrated over cosmic time, could contribute significantly to the diffuse flux. These findings motivate further study of the cosmological roles of both starburst and AGN-driven activity and call for efforts to better understand local hybrid sources as potential high-energy neutrino emitters.

APPENDIX A

Notations & conventions

Astroparticle physics is an interdisciplinary field that combines insights from particle physics and classical astronomy. This overlap often leads to different notations being used to express the same or related quantities. Below, we outline how relevant quantities used in this work from classical astronomy translate to those used in (astro)particle physics. The focus will be on the expression of fluxes and energy densities.

A.1 Classical Astronomy

The electromagnetic **differential energy flux** from an astrophysical source is defined as the energy per unit time, $\mathrm{d}E/\mathrm{d}t$, passing through a unit area at Earth, $\mathrm{d}A$, per unit frequency

$$f_\nu = \frac{\mathrm{d}E}{\mathrm{d}\nu\,\mathrm{d}A\,\mathrm{d}t}\ . \tag{A.1}$$

The usual unit of measurement is the Jansky (Jy), where $1\ \mathrm{Jy} = 10^{-26}\ \mathrm{W\ m^{-2}\ Hz^{-1}}$.

Historically, parts of the electromagnetic spectrum have been characterized based on wavelength (λ) rather than frequency (ν). For example, the far-infrared portion of the electromagnetic spectrum, which is of particular interest in this work, spans wavelengths between [$\lambda_1 = 1000\ \mu\mathrm{m}$, $\lambda_2 = 8\ \mu\mathrm{m}$]. Using the relationship $\lambda = c/\nu$, where c is the speed of light, this corresponds to frequencies in the range $[\nu_1 = 3.0 \times 10^2\ \mathrm{GHz}, \nu_2 = 3.7 \times 10^4\ \mathrm{GHz}]$.

The **total energy flux**, F, can be obtained by integrating f_ν over a waveband bounded by the minimum (ν_1) and maximum (ν_2) frequencies such that

$$F \equiv \frac{\mathrm{d}E}{\mathrm{d}A\,\mathrm{d}t} = \int_{\nu_1}^{\nu_2} f_\nu\,\mathrm{d}\nu\ , \tag{A.2}$$

typically given in units of W m^{-2}. Note that the frequency range $[\nu_1, \nu_2]$ is obtained from the observed spectrum at Earth.

If the source emits isotropically, the *differential intrinsic luminosity*, L_ν, and the *intrinsic luminosity*, L, of the source are related to the observed fluxes as

$$f_\nu = \frac{L_{\nu_s}}{4\pi D_L^2} \quad \text{and} \quad F = \frac{L}{4\pi D_L^2}, \tag{A.3}$$

where D_L is the luminosity distance to the source. We take into account that, if the source is sufficiently far away, the expansion of the Universe must be considered. In such cases, the frequency emitted in the rest frame of the source, ν_s, is redshifted to an observed frequency,

$$\nu = \frac{\nu_s}{1+z}. \tag{A.4}$$

The intrinsic **(bolometric) luminosity**, L, is then given by

$$L = \int_{(1+z)\nu_1}^{(1+z)\nu_2} L_\nu \, \mathrm{d}\nu, \tag{A.5}$$

and is often expressed in terms of the bolometric solar luminosity, $L_\odot = 3.828 \times 10^{26}$ W.

A.2 Astroparticle Physics

The **differential particle flux** is defined as the particle rate, $\mathrm{d}N/\mathrm{d}t$, passing through a unit area at Earth, $\mathrm{d}A$, per unit particle energy, $\mathrm{d}E$

$$\Phi(E) \equiv \frac{\mathrm{d}N}{\mathrm{d}E \, \mathrm{d}A \, \mathrm{d}t} \, , \tag{A.6}$$

typically expressed in units of $\mathrm{GeV}^{-1} \, \mathrm{cm}^{-2} \, \mathrm{s}^{-1}$. Particle fluxes of interest in this work (cosmic rays, neutrinos, and gamma rays) are often well-described by a power-law spectrum, $\Phi \propto E^{-\gamma}$, where γ is the spectral index.

Physically relevant quantities can be derived from $\Phi(E)$ by incorporating factors of energy:

- **Differential energy flux**:

$$E\Phi(E) = E\frac{\mathrm{d}N}{\mathrm{d}E \, \mathrm{d}A \, \mathrm{d}t} \, , \tag{A.7}$$

  analogous to f_ν introduced in Eq. (A.1). The *total energy flux*, F, can then be expressed as

$$F = \int_{E_1}^{E_2} E\Phi(E) \, \mathrm{d}E = \begin{cases} \frac{\mathcal{A}}{\gamma-2} \left(E_1^{-\gamma+2} - E_2^{-\gamma+2} \right) & (\gamma \neq 2) \\ \\ \mathcal{A} \left(\ln E_2 - \ln E_1 \right) & (\gamma = 2) \, , \end{cases} \tag{A.8}$$

  with $\mathcal{A}$ is the normalization constant such that $\Phi(E) = \mathcal{A}E^{-\gamma}$.

  The differential energy flux is related to the *differential luminosity* of the source by

$$E\Phi(E) = \frac{L_\epsilon}{4\pi D_L^2}, \tag{A.9}$$

  where $\epsilon = (1+z)E$ is the energy in the source frame, and the total luminosity is obtained via

$$L = \int_{\epsilon_1}^{\epsilon_2} L_E \, \mathrm{d}E. \tag{A.10}$$

- **Differential energy flux per logarithmic energy interval**:

$$E^2\Phi(E) = E\frac{\mathrm{d}N}{\mathrm{d}\ln E \, \mathrm{d}A \, \mathrm{d}t}, \tag{A.11}$$

  with typical units of $\mathrm{GeV} \, \mathrm{cm}^{-2} \, \mathrm{s}^{-1}$. Notably, for a power-law spectrum $\Phi(E) = \mathcal{A}E^{-\gamma}$, the quantity $E^2\Phi(E)$ becomes energy-independent when $\gamma = 2$, yielding $E^2\Phi(E) = \mathcal{A}$.

Using the concepts introduced above, we also introduce the concept of a diffuse flux. Consider a solid angle on the sky, $\mathrm{d}\Omega$, from which a particle flux is observed that cannot be attributed to a specific source. This **diffuse flux** arises from unresolved sources and secondary contributions from particle interactions during propagation. It is defined as

$$\Phi^{\mathrm{diffuse}} \equiv \frac{\mathrm{d}N}{\mathrm{d}E\,\mathrm{d}A\,\mathrm{d}t\,\mathrm{d}\Omega}, \tag{A.12}$$

with typical units of $\mathrm{GeV}^{-1}\ \mathrm{cm}^{-2}\ \mathrm{s}^{-1}\ \mathrm{sr}^{-1}$.

An important related quantity is the energy budget required to account for the observed diffuse flux. To evaluate this, we introduce the **differential energy generation rate** of a particle species X, defined as the differential luminosity produced per unit comoving volume $\mathrm{d}V$,

$$E\mathcal{Q}_{E_X} \equiv E\frac{\mathrm{d}L_E}{\mathrm{d}V}, \tag{A.13}$$

related to the **total energy generation rate**

$$\mathcal{Q}_X \equiv \frac{\mathrm{d}L}{\mathrm{d}V} = \int_{\epsilon_1}^{\epsilon_2} \mathcal{Q}_{E_X}\,\mathrm{d}E\ . \tag{A.14}$$

Both $E\mathcal{Q}_E$ and $\mathcal{Q}$ are typically expressed in units of $\mathrm{erg\,Mpc}^{-3}\,\mathrm{yr}^{-1}$.

Assuming that the diffuse flux of particles moving at the speed of light c is isotropic over the full sky, multiplying the diffuse flux by a factor $4\pi/c$ gives the overall energy density. Dividing this energy density by a characteristic production timescale τ (e.g., the Hubble time $t_{\mathrm{H}} = H_0^{-1}$ for extragalactic sources) yields the differential energy generation rate expressed as

$$E\mathcal{Q}_{E_X} = \left(\frac{4\pi}{c\tau}\right) E^2\Phi^{\mathrm{diffuse}}, \tag{A.15}$$

which represents the rate required to produce the observed diffuse flux.

Finally, the differential and total energy generation rates are related as:

$$R(E,\gamma,E_1,E_2) \equiv \frac{\mathcal{Q}_X}{E\mathcal{Q}_{E_X}} = \begin{cases} \left(\frac{E_1^{-\gamma+2}-E_2^{-\gamma+2}}{\gamma-2}\right) E^{\gamma-2} & \text{if } \gamma \neq 2 \\ \ln E_2 - \ln E_1 & \text{if } \gamma = 2\ . \end{cases} \tag{A.16}$$

APPENDIX B

Effective Optical Depth & Calorimeter Condition

To quantify the calorimetric conditions in starburst regions, we introduced in Section 3.1.3 the parameter

$$\mathcal{C}_{\rm pp} \equiv \frac{\tau}{\tau_{\rm pp}} \,, \tag{B.1}$$

where $\mathcal{C}_{\rm pp}$ represents the ratio of the total timescale τ to the timescale for proton-proton (pp) interactions, $\tau_{\rm pp}$. By definition, pp-interactions dominate over particle escape when $\mathcal{C}_{\rm pp} \to 1$, whereas particle escape dominates for $\mathcal{C}_{\rm pp} \ll 1$. Between these extremes, we define the transition point as $\mathcal{C}_{\rm pp} = 0.5$. For this value of $\mathcal{C}_{\rm pp}$, the following conditions hold:

$$\begin{cases} \tau_{\rm pp} < \tau_{\rm diff}, \quad \tau_{\rm pp} < \tau_{\rm gwind} & \text{if} \quad \tau_{\rm diff}^{-1} \neq 0, \quad \tau_{\rm gwind}^{-1} \neq 0, \\ \tau_{\rm pp} = \tau_{\rm diff} & \text{if} \quad \tau_{\rm gwind}^{-1} \to 0, \\ \tau_{\rm pp} = \tau_{\rm gwind} & \text{if} \quad \tau_{\rm diff}^{-1} \to 0. \end{cases} \tag{B.2}$$

For $\mathcal{C}_{\rm pp} > 0.5$, the pp-interaction timescale is the shortest, ensuring a regime where most of the cosmic-ray energy is dissipated through hadronic interactions.

In the literature [17], the meson production efficiency f_π for pp-interactions is defined as:

$$f_\pi = \frac{\tau_{\rm esc}}{\tau_{\rm pp}} \,, \tag{B.3}$$

where $\tau_{\rm esc}$ is the effective escape timescale of particles. In the nuclear starburst regions of U/LIRGs, this timescale accounts for both diffusive and advective processes, and is given by:

$$\tau_{\rm esc} = \left(\tau_{\rm diff}^{-1} + \tau_{\rm adv}^{-1}\right)^{-1} . \tag{B.4}$$

The relationship between the parameter $\mathcal{C}_{\rm pp}$ and f_π is

$$\mathcal{C}_{\rm pp} = \frac{f_\pi}{f_\pi + 1}. \tag{B.5}$$

This can be seen by noting that:

$$\begin{aligned}\mathcal{C}_{\rm pp} &= \frac{\tau}{\tau_{\rm pp}} = \frac{\tau_{\rm esc}\tau_{\rm pp}}{\tau_{\rm esc}+\tau_{\rm pp}} \cdot \frac{1}{\tau_{\rm pp}} \\ &= \frac{\tau_{\rm adv}\tau_{\rm diff}\tau_{\rm pp}}{\tau_{\rm adv}\tau_{\rm diff}+\tau_{\rm adv}\tau_{\rm pp}+\tau_{\rm diff}\tau_{\rm pp}} \\ &= \left(\tau_{\rm pp}^{-1}+\tau_{\rm adv}^{-1}+\tau_{\rm diff}^{-1}\right)^{-1} \iff \mathcal{C}_{\rm pp} = \frac{f_\pi}{f_\pi+1}.\end{aligned}$$

The parameter $\mathcal{C}_{\rm pp}$ naturally emerges in the context of the proton momentum distribution, defined in Eq. (3.20),

$$\mathcal{F}_{\rm p} = Q_{\rm p}\cdot\tau = Q_{\rm p}\cdot\tau_{\rm pp}\cdot\frac{\tau}{\tau_{\rm pp}} = Q_{\rm p}\cdot\tau_{\rm pp}\cdot\mathcal{C}_{\rm pp}, \tag{B.6}$$

where $Q_{\rm p}$, defined in Eq. (3.6) represents the cosmic-ray production rate. This formulation highlights how $\mathcal{C}_{\rm pp}$ influences the cosmic-ray energy distribution in starburst regions.

APPENDIX C

Energy Distributions of Leptons Produced in Hadronic Interactions

In [87], the authors provide analytical fits to the energy distributions of electrons and neutrinos produced in pp-interactions

$$\begin{cases} \pi^+ \to \mu^+ + \nu_\mu^{(1)} \to e^+ + \nu_e + \bar{\nu}_\mu^{(2)} + \nu_\mu^{(1)} \\ \pi^- \to \mu^- + \bar{\nu}_\mu^{(1)} \to e^- + \bar{\nu}_e + \nu_\mu^{(2)} + \bar{\nu}_\mu^{(1)} \end{cases} . \tag{C.1}$$

These distributions were obtained by first simulating the meson spectra produced in pp-interactions using Monte Carlo generators SIBYLL [300] and QGSJET [301], then analytically calculating the decay to electrons, positrons, and (anti)neutrinos, and finally fitting the distributions of the decay products.

Below we present the fits to these distributions, which are used in Section 3.1.4 as part of the mathematical framework for starburst-driven neutrino production in starburst galaxies.

First define $x = E_e/E_\pi$ and $L = \ln(E_p/1\,\mathrm{TeV})$. Then the energy distribution of electrons and positrons (e) obtained from muon decay is well described by

$$F_e(x,\, E_p) = B_e \, \frac{(1 + k_e(\ln x)^2)^3}{x\,(1 + \frac{0.3}{x^{\beta_e}})} \, (-\ln x)^5 \,, \tag{C.2}$$

where

$$B_e = \frac{1}{69.5 + 2.65\,L + 0.3\,L^2} \,, \tag{C.3}$$

$$\beta_e = \frac{1}{(0.201 + 0.062\,L + 0.00042\,L^2)^{1/4}} \,, \tag{C.4}$$

$$k_e = \frac{0.279 + 0.141\,L + 0.0172\,L^2}{0.3 + (2.3 + L)^2} \,. \tag{C.5}$$

The spectrum of muon neutrinos $\nu_\mu^{(2)}$ obtained in that same decay, $F_{\nu_\mu}^{(2)}(x,\, E_p)$, is described by the same function given in Eq. C.5, but with $x = E_{\nu_\mu}/E_p$.

The spectrum of muon neutrinos $\nu_\mu^{(1)}$ produced through the direct decay of the pion, $F_{\nu_\mu}^{(1)}$, can be described by

$$F_{\nu_\mu}^{(1)}(x,\, E_p) = B' \, \frac{\ln(y)}{y} \left(\frac{1 - y^{\beta'}}{1 + k' y^{\beta'} (1 - y^{\beta'})} \right)^4 \times$$

$$\left[\frac{1}{\ln(y)} - \frac{4\beta' y^{\beta'}}{1 - y^{\beta'}} - \frac{4k'\beta' y^{\beta'} (1 - 2y^{\beta'})}{1 + k' y^{\beta'} (1 - y^{\beta'})} \right] , \tag{C.6}$$

where $x = E_{\nu_\mu}/E_p$, $y = x/0.427$,

$$B' = 1.75 + 0.204\,L + 0.010\,L^2\,, \tag{C.7}$$

$$\beta' = \frac{1}{1.67 + 0.111\,L + 0.0038L^2}\,, \tag{C.8}$$

$$k' = 1.07 - 0.086\,L + 0.002\,L^2\,. \tag{C.9}$$

Note that the spectrum of $F^{(1)}_{\nu_\mu}$ has a sharp cutoff at $x = 0.427$, which originates from the fact that

$$E_{\nu,\mathrm{max}} = (1 - m_\pi^2/m_\mu^2)E_\pi$$

derived from four-vector kinematics. The total spectrum of muonic neutrinos is thus $F_{\nu_\mu} = F^{(1)}_{\nu_\mu} + F^{(2)}_{\nu_\mu}$.

Finally, for the distribution of electron neutrinos (F_e), we have that $F_{\nu_e} \approx F_e$ within 5%.

APPENDIX D

GOALS Galaxy Parameters & Predicted Neutrino Emissions

TABLE D.1: A total of 229 galaxies from the Great Observatories All-Sky LIRG Survey (GOALS) are investigated in Chapter 3 as potential high-energy neutrino sources. For each galaxy, the dataset includes the source name, right ascension ($\alpha_{\rm src}$) and declination ($\delta_{\rm src}$) in degrees (°), luminosity distance (D_L) in megaparsecs (Mpc), infrared luminosity ($L_{\rm IR}/L_\odot$) in solar units, and the average AGN contribution to the bolometric luminosity ($\langle\alpha_{\rm AGN}\rangle$) [234]. Also listed are the supernova rate ($\mathcal{R}_{\rm SN}$), given in events per year (yr^{-1}) and calculated using Eq. (3.5), and the muon-neutrino flux at 1 TeV ($\Phi_{\nu_\mu+\bar{\nu}_\mu}$), computed via Eq. (3.24) assuming a spectral index of $\gamma = 2$, with units of $\mathrm{TeV}^{-1}\ \mathrm{cm}^{-2}\ \mathrm{s}^{-1}$.

Name	$\alpha_{\rm src}$	$\delta_{\rm src}$	D_L	$\log_{10}(L_{\rm IR}/L_\odot)$	$\langle\alpha_{\rm AGN}\rangle$	$\mathcal{R}_{\rm SN}$	$\Phi_{\nu_\mu+\bar{\nu}_\mu} \times 10^{14}$
NGC0023	2.47	25.92	65.2	11.11	0.09	0.12	0.31
NGC0034a	2.78	−12.11	84.1	11.50	0.04	0.32	0.49
MCG-02-01-051a	4.71	−10.38	117.5	11.67	0.07	0.45	0.36
ESO350-IG038	9.22	−33.56	89.0	11.28	0.23	0.15	0.21
NGC0232a	10.69	−23.56	95.2	11.48	0.09	0.29	0.34
NGC0232b	10.72	−23.54	95.2	10.64	0.47	0.02	0.03
MCG+12-02-001	13.51	73.08	69.8	11.49	0.06	0.30	0.68
NGC0317B	14.42	43.79	77.8	11.23	0.05	0.17	0.30
IC1623AB	16.95	−17.51	85.5	11.73	0.12	0.49	0.73
MCG-03-04-014	17.54	−16.85	144.0	11.62	0.07	0.40	0.21

Name	$\alpha_{\rm src}$	$\delta_{\rm src}$	D_L	$\log_{10}(L_{\rm IR}/L_\odot)$	$\langle\alpha_{\rm AGN}\rangle$	$\mathcal{R}_{\rm SN}$	$\Phi_{\nu_\mu+\bar{\nu}_\mu}\times 10^{14}$
ESO244-G012a	19.53	−44.46	91.5	11.40	0.06	0.25	0.32
CGCG436-030	20.01	14.36	134.0	11.69	0.09	0.46	0.28
ESO353-G020	23.71	−36.14	68.8	11.16	0.08	0.14	0.32
ESO297-G011b	24.10	−37.32	74.6	10.84	0.11	0.06	0.13
ESO297-G011a	24.10	−37.34	74.6	10.71	0.07	0.05	0.10
IRASF01364-1042	24.72	−10.45	210.0	11.83	0.05	0.67	0.17
IRASF01417+1651	26.13	17.10	119.0	11.61	0.00	0.42	0.33
NGC0695	27.81	22.58	139.0	11.70	0.09	0.47	0.27
UGC01385	28.72	36.92	79.8	11.09	0.08	0.12	0.20
NGC0838c	32.35	−10.14	53.8	10.71	0.17	0.04	0.17
NGC0838a	32.41	−10.15	53.8	11.06	0.05	0.11	0.43
NGC0838b	32.43	−10.18	53.8	11.05	0.09	0.11	0.40
NGC0828	32.54	39.19	76.3	11.34	0.12	0.20	0.38
IC0214	33.52	5.17	129.0	11.40	0.08	0.24	0.16
NGC0877b	34.47	14.52	54.6	10.12	0.10	0.01	0.05
NGC0877a	34.50	14.54	54.6	10.80	0.14	0.06	0.21
MCG+05-06-36b	35.83	32.19	145.0	11.02	0.12	0.10	0.05
MCG+05-06-36a	35.84	32.20	145.0	11.50	0.13	0.29	0.15
UGC01845	36.03	47.97	67.0	11.15	0.07	0.14	0.33
NGC0958	37.68	−2.93	80.6	10.88	0.20	0.06	0.11
NGC0992	39.36	21.10	58.0	11.06	0.08	0.11	0.36
NGC1068	40.67	−0.01	15.9	11.39	1.00	0.00	0.00
UGC02238	41.57	13.10	92.4	11.37	0.10	0.22	0.28
IRASF02437+2122	41.66	21.59	98.8	11.26	0.14	0.16	0.18
UGC02369a	43.51	14.97	136.0	11.69	0.09	0.46	0.27
UGC02608	48.76	42.04	100.0	11.41	0.50	0.13	0.15
NGC1275	49.95	41.51	75.0	10.96	0.44	0.05	0.10
IRASF03217+4022	51.27	40.56	100.0	11.37	0.06	0.23	0.25

Name	$\alpha_{\rm src}$	$\delta_{\rm src}$	D_L	$\log_{10}(L_{\rm IR}/L_\odot)$	$\langle\alpha_{\rm AGN}\rangle$	$\mathcal{R}_{\rm SN}$	$\Phi_{\nu_\mu+\bar{\nu}_\mu}\times 10^{14}$
NGC1365	53.40	−36.14	17.9	10.95	0.38	0.06	1.96
IRASF03359+1523	54.69	15.55	152.0	11.52	0.00	0.34	0.16
CGCG465-012b	58.53	15.99	94.3	10.75	0.13	0.05	0.06
CGCG465-012a	58.57	15.93	94.3	11.15	0.08	0.14	0.17
IRAS03582+6012	60.64	60.34	131.0	11.38	0.44	0.14	0.09
UGC02982	63.09	5.55	74.9	11.21	0.11	0.15	0.29
ESO420-G013	63.46	−32.01	51.0	11.11	0.25	0.10	0.42
NGC1572	65.68	−40.60	88.6	11.31	0.10	0.19	0.27
IRAS04271+3849	67.64	38.93	80.8	11.16	0.06	0.14	0.24
NGC1614	68.50	−8.58	67.8	11.67	0.12	0.43	1.02
UGC03094	68.89	19.17	106.0	11.38	0.19	0.20	0.20
ESO203-IG001	71.71	−48.56	235.0	11.88	0.37	0.50	0.10
MCG-05-12-006	73.02	−32.99	81.3	11.10	0.08	0.12	0.20
NGC1797	76.94	−8.02	63.4	11.01	0.06	0.10	0.27
CGCG468-002b	77.08	17.36	77.9	10.51	0.49	0.02	0.03
CGCG468-002a	77.09	17.37	77.9	11.17	0.03	0.15	0.27
IRAS05083+2441	77.86	24.76	99.2	11.21	0.06	0.16	0.18
IRASF05081+7936	79.19	79.67	240.0	12.03	0.08	1.02	0.19
IRAS05129+5128	79.23	51.53	120.0	11.38	0.06	0.23	0.18
IRASF05189-2524	80.26	−25.36	187.0	12.15	0.60	0.59	0.18
IRASF05187-1017	80.28	−10.25	122.0	11.34	0.04	0.22	0.16
IRAS05223+1908	81.32	19.18	128.0	11.54	0.92	0.03	0.02
MCG+08-11-002	85.18	49.70	83.7	11.58	0.04	0.38	0.59
NGC1961	85.52	69.38	59.0	10.63	0.25	0.03	0.10
UGC03351	86.45	58.70	65.8	11.35	0.09	0.21	0.53
IRAS05442+1732	86.80	17.56	80.5	11.27	0.06	0.18	0.31
IRASF06076-2139a	92.44	−21.67	165.0	11.68	0.11	0.44	0.18
UGC03410b	93.49	80.48	59.7	10.28	0.16	0.02	0.05

Name	$\alpha_{\rm src}$	$\delta_{\rm src}$	D_L	$\log_{10}(L_{\rm IR}/L_\odot)$	$\langle\alpha_{\rm AGN}\rangle$	$\mathcal{R}_{\rm SN}$	$\Phi_{\nu_\mu+\bar{\nu}_\mu}\times 10^{14}$
UGC03410a	93.62	80.45	59.7	10.96	0.11	0.08	0.26
NGC2146	94.66	78.36	17.5	11.14	0.01	0.14	5.06
ESO255-IG007a	96.84	−47.18	173.0	11.78	0.05	0.59	0.22
ESO255-IG007b	96.85	−47.18	173.0	10.70	0.07	0.05	0.02
ESO557-G002b	97.94	−17.65	93.6	10.49	0.09	0.03	0.04
ESO557-G002a	97.95	−17.62	93.6	11.21	0.02	0.17	0.21
UGC03608	104.39	46.40	94.3	11.37	0.06	0.23	0.28
IRASF06592-6313	104.92	−63.30	104.0	11.29	0.09	0.18	0.19
IRASF07027-6011a	105.85	−60.26	141.0	11.21	0.51	0.08	0.05
IRASF07027-6011b	105.87	−60.28	141.0	11.48	0.06	0.29	0.16
NGC2342a	107.33	20.64	78.0	11.27	0.06	0.18	0.33
NGC2369	109.16	−62.34	47.6	11.20	0.10	0.15	0.71
IRAS07251-0248	111.91	−2.91	400.0	12.35	0.14	2.00	0.14
NGC2388a	112.22	33.82	62.1	11.33	0.03	0.22	0.61
MCG+02-20-003	113.93	11.71	72.8	11.10	0.14	0.11	0.23
IRAS08355-4944	129.26	−49.91	118.0	11.66	0.18	0.39	0.31
NGC2623	129.60	25.75	84.1	11.66	0.10	0.43	0.66
ESO432-IG006b	131.11	−31.70	74.4	10.87	0.09	0.07	0.14
ESO432-IG006a	131.12	−31.69	74.4	10.84	0.12	0.06	0.12
ESO60-IG016	133.13	−69.03	210.0	11.82	0.23	0.53	0.13
IRASF08572+3915	135.11	39.07	264.0	12.05	0.47	0.62	0.10
IRAS09022-3615	136.05	−36.45	271.0	12.37	0.19	1.97	0.29
UGC04881b	138.98	44.33	178.0	11.01	0.05	0.10	0.03
UGC04881a	138.98	44.33	178.0	11.57	0.05	0.37	0.13
UGC05101	143.97	61.35	177.0	12.02	0.25	0.82	0.28
MCG+08-18-013	144.15	48.47	117.0	11.38	0.20	0.20	0.16
IC0563	146.58	3.05	92.9	10.94	0.09	0.08	0.10
IRASF09437+0317	146.59	3.07	92.9	10.84	0.14	0.06	0.08

Name	$\alpha_{\rm src}$	$\delta_{\rm src}$	D_L	$\log_{10}(L_{\rm IR}/L_\odot)$	$\langle\alpha_{\rm AGN}\rangle$	$\mathcal{R}_{\rm SN}$	$\Phi_{\nu_\mu+\bar{\nu}_\mu}\times 10^{14}$
NGC3110a	151.01	−6.48	79.5	11.34	0.10	0.20	0.35
IC2545	151.52	−33.89	156.0	11.80	0.22	0.51	0.23
IRASF10173+0828	155.00	8.23	224.0	11.93	0.04	0.85	0.18
NGC3221	155.58	21.57	65.7	10.93	0.09	0.08	0.20
NGC3256	156.96	−43.90	38.9	11.64	0.05	0.43	3.11
ESO264-G036	160.78	−46.21	100.0	11.26	0.14	0.16	0.18
ESO264-G057	164.76	−43.44	83.3	11.20	0.07	0.15	0.24
IRASF10565+2448	164.83	24.54	197.0	12.14	0.04	1.38	0.39
MCG+07-23-019	165.97	40.85	158.0	11.72	0.03	0.53	0.23
CGCG011-076	170.30	−2.98	117.0	11.31	0.18	0.17	0.14
IC2810a	171.44	14.68	157.0	11.52	0.05	0.33	0.14
ESO319-G022	171.98	−41.61	80.0	11.08	0.04	0.12	0.20
NGC3690W	172.13	58.56	50.7	11.09	0.27	0.09	0.40
NGC3690E	172.14	58.56	50.7	11.37	0.04	0.23	0.99
ESO320-G030	178.30	−39.13	41.2	11.18	0.03	0.15	0.98
ESO440-IG058a	181.72	−31.95	112.0	11.42	0.06	0.26	0.22
IRASF12112+0305	183.44	2.81	340.0	12.33	0.06	2.09	0.20
ESO267-G030b	183.47	−47.27	97.1	11.18	0.06	0.15	0.17
NGC4194	183.54	54.53	43.0	11.10	0.09	0.12	0.70
ESO267-G030a	183.55	−47.23	97.1	11.31	0.18	0.17	0.20
IRAS12116-5615	183.59	−56.54	128.0	11.72	0.10	0.49	0.33
IRASF12224-0624	186.27	−6.68	125.0	11.43	0.20	0.22	0.16
NGC4418	186.73	−0.88	36.5	11.06	0.48	0.06	0.51
Mrk231	194.06	56.87	192.0	12.50	0.53	1.54	0.46
NGC4922	195.36	29.31	111.0	11.39	0.17	0.21	0.19
CGCG043-099	195.46	4.33	175.0	11.70	0.05	0.49	0.18
MCG-02-33-098a	195.58	−15.77	78.7	10.94	0.11	0.08	0.14
MCG-02-33-098b	195.59	−15.77	78.7	10.47	0.04	0.03	0.05

Name	$\alpha_{\rm src}$	$\delta_{\rm src}$	D_L	$\log_{10}(L_{\rm IR}/L_\odot)$	$\langle\alpha_{\rm AGN}\rangle$	$\mathcal{R}_{\rm SN}$	$\Phi_{\nu_\mu+\bar{\nu}_\mu}\times 10^{14}$
ESO507-G070	195.72	−23.92	106.0	11.63	0.03	0.43	0.42
IRAS13052-5711	197.08	−57.46	106.0	11.38	0.02	0.24	0.24
IC0860	198.76	24.62	56.8	11.16	0.06	0.14	0.48
IRAS13120-5453	198.78	−55.16	144.0	12.35	0.04	2.23	1.18
VV250b	198.88	62.13	142.0	10.92	0.05	0.08	0.04
VV250a	198.90	62.12	142.0	11.75	0.05	0.56	0.30
UGC08387	200.15	34.14	110.0	11.80	0.03	0.64	0.57
NGC5104	200.35	0.34	90.8	11.29	0.10	0.18	0.24
MCG-03-34-064	200.60	−16.73	82.2	11.15	0.88	0.02	0.03
NGC5135	201.43	−29.83	60.9	11.34	0.24	0.17	0.51
ESO173-G015	201.85	−57.49	34.0	11.41	0.03	0.26	2.45
IC4280	203.22	−24.21	82.4	11.15	0.12	0.13	0.21
NGC5256	204.57	48.28	129.0	11.50	0.23	0.25	0.17
NGC5257a	204.97	0.84	108.5	11.42	0.07	0.25	0.24
NGC5257b	204.99	0.83	108.5	11.40	0.11	0.23	0.22
Mrk273	206.18	55.89	173.0	12.21	0.31	1.16	0.42
UGC08739	207.31	35.26	81.4	11.16	0.10	0.14	0.22
ESO221-IG010	207.74	−49.06	62.9	11.22	0.07	0.16	0.44
NGC5331a	208.07	2.10	155.0	11.57	0.07	0.36	0.16
NGC5331b	208.07	2.11	155.0	10.77	0.12	0.05	0.02
NGC5394	209.64	37.45	58.7	10.97	0.08	0.09	0.28
CGCG247-020	214.93	49.24	120.0	11.40	0.06	0.25	0.19
IRASF14348-1447	219.41	−15.01	387.0	12.53	0.09	3.20	0.23
IRASF14378-3651	220.25	−37.08	315.0	12.23	0.05	1.68	0.18
NGC5734a	221.29	−20.87	67.1	11.03	0.14	0.10	0.23
NGC5734b	221.30	−20.91	67.1	10.83	0.17	0.06	0.14
VV340b	224.25	24.61	157.0	10.91	0.13	0.07	0.03
VV340a	224.25	24.62	157.0	11.59	0.16	0.34	0.15

Name	$\alpha_{\rm src}$	$\delta_{\rm src}$	D_L	$\log_{10}(L_{\rm IR}/L_\odot)$	$\langle\alpha_{\rm AGN}\rangle$	$\mathcal{R}_{\rm SN}$	$\Phi_{\nu_\mu+\bar{\nu}_\mu}\times 10^{14}$
CGCG049-057	228.30	7.22	65.4	11.39	0.04	0.24	0.63
ESO099-G004	231.24	−63.13	137.0	11.78	0.07	0.58	0.34
IRASF15250+3609	231.75	35.98	254.0	12.09	0.18	1.05	0.18
NGC5936	232.50	12.99	67.1	11.17	0.08	0.14	0.34
Arp220	233.74	23.50	87.9	12.38	0.09	2.27	3.21
NGC5990	236.57	2.42	64.4	11.21	0.31	0.12	0.31
NGC6052	241.30	20.54	77.6	10.98	0.10	0.09	0.16
NGC6090	242.92	52.46	137.0	11.54	0.05	0.34	0.20
IRASF16164-0746	244.80	−7.90	128.0	11.71	0.05	0.51	0.34
CGCG052-037	247.74	4.08	116.0	11.55	0.07	0.34	0.28
NGC6156	248.72	−60.62	48.0	11.05	0.16	0.10	0.46
ESO069-IG006	249.55	−68.44	212.0	12.10	0.06	1.23	0.30
IRASF16399-0937	250.67	−9.72	128.0	11.56	0.08	0.35	0.23
ESO453-G005	251.88	−29.36	100.0	11.45	0.05	0.28	0.30
NGC6240	253.25	2.40	116.0	11.97	0.11	0.86	0.70
IRASF16516-0948	253.60	−9.89	107.0	11.26	0.07	0.18	0.17
NGC6286b	254.60	58.96	85.7	10.86	0.08	0.07	0.10
NGC6286a	254.63	58.94	85.7	11.32	0.11	0.19	0.29
IRASF17132+5313	258.58	53.18	232.0	11.90	0.02	0.81	0.16
IRASF17138-1017	259.15	−10.35	84.0	11.53	0.07	0.33	0.51
IRASF17207-0014	260.84	−0.28	198.0	12.54	0.05	3.42	0.95
ESO138-G027	261.68	−59.93	98.3	11.44	0.07	0.27	0.30
UGC11041	268.72	34.78	77.5	11.15	0.12	0.13	0.23
CGCG141-034	269.24	24.02	93.4	11.25	0.08	0.17	0.21
IRAS17578-0400	270.13	−4.01	68.5	11.51	0.03	0.33	0.76
IRAS18090+0130b	272.89	1.53	134.0	11.06	0.09	0.11	0.07
IRAS18090+0130a	272.91	1.53	134.0	11.53	0.08	0.32	0.20
NGC6621	273.23	68.36	94.3	11.31	0.10	0.19	0.23

Name	$\alpha_{\rm src}$	$\delta_{\rm src}$	D_L	$\log_{10}(L_{\rm IR}/L_\odot)$	$\langle\alpha_{\rm AGN}\rangle$	$\mathcal{R}_{\rm SN}$	$\Phi_{\nu_\mu+\bar{\nu}_\mu}\times 10^{14}$
IC4687a	273.41	−57.73	81.9	11.36	0.08	0.22	0.36
CGCG142-034b	274.14	22.11	88.1	10.28	0.18	0.02	0.02
CGCG142-034a	274.17	22.11	88.1	11.04	0.09	0.10	0.15
IRASF18293-3413	278.17	−34.19	86.0	11.94	0.05	0.86	1.27
NGC6670Ab	278.39	59.89	129.5	11.39	0.05	0.24	0.16
NGC6670Aa	278.41	59.89	129.5	11.34	0.05	0.22	0.14
IC4734	279.61	−57.49	73.4	11.42	0.07	0.25	0.52
NGC6701	280.80	60.65	62.4	11.05	0.08	0.11	0.30
NGC6786b	287.72	73.41	113.0	11.20	0.07	0.15	0.13
NGC6786a	287.77	73.43	113.0	10.97	0.16	0.08	0.07
ESO593-IG008	288.63	−21.32	222.0	11.92	0.05	0.82	0.18
IRASF19297-0406	293.09	−4.00	395.0	12.45	0.05	2.78	0.19
IRAS19542+1110	299.15	11.32	295.0	11.76	0.08	0.55	0.07
ESO339-G011	299.41	−37.94	88.6	11.27	0.41	0.11	0.16
NGC6907a	306.28	−24.81	50.1	10.91	0.09	0.08	0.33
MCG+04-48-002a	307.15	25.73	64.2	11.08	0.17	0.10	0.27
NGC6926a	308.28	−2.03	89.1	10.89	0.29	0.06	0.08
IRAS20351+2521	309.32	25.53	151.0	11.57	0.07	0.36	0.17
CGCG448-020a	314.35	17.13	161.0	11.86	0.05	0.72	0.30
ESO286-IG019	314.61	−42.65	193.0	12.10	0.24	0.99	0.29
ESO286-G035	316.05	−43.59	79.1	11.13	0.06	0.13	0.23
IRAS21101+5810	317.87	58.39	174.0	11.69	0.03	0.49	0.18
ESO343-IG013b	324.04	38.54	85.8	10.64	0.04	0.04	0.06
ESO343-IG013a	324.05	−38.54	85.8	10.92	0.09	0.08	0.12
NGC7130	327.08	−34.95	72.7	11.40	0.22	0.20	0.42
ESO467-G027	333.67	−27.46	77.3	11.02	0.11	0.10	0.18
IC5179	334.04	−36.84	51.4	11.17	0.10	0.14	0.57
ESO602-G025	337.86	−19.03	110.0	11.43	0.14	0.24	0.22

Name	$\alpha_{\rm src}$	$\delta_{\rm src}$	D_L	$\log_{10}(L_{\rm IR}/L_\odot)$	$\langle\alpha_{\rm AGN}\rangle$	$\mathcal{R}_{\rm SN}$	$\Phi_{\nu_\mu+\bar{\nu}_\mu}\times 10^{14}$
UGC12150	340.30	34.25	93.5	11.43	0.07	0.26	0.32
ESO239-IG002	342.42	−48.85	191.0	11.84	0.03	0.70	0.21
IRASF22491-1808	342.96	−17.87	351.0	12.22	0.02	1.69	0.15
NGC7469	345.82	8.87	70.8	11.58	0.24	0.30	0.65
CGCG453-062	346.24	19.55	109.0	11.38	0.08	0.23	0.21
ESO148-IG002	348.94	−59.05	199.0	12.08	0.19	1.01	0.28
IC5298	349.00	25.56	119.0	11.63	0.33	0.30	0.23
NGC7552	349.04	−42.58	23.5	11.13	0.08	0.13	2.55
NGC7591	349.57	6.59	71.4	11.13	0.09	0.13	0.27
NGC7592a	349.59	−4.42	106.0	10.87	0.20	0.06	0.06
NGC7592b	349.59	−4.42	106.0	11.09	0.05	0.12	0.12
ESO077-IG014a	350.27	−69.22	186.0	11.06	0.02	0.12	0.04
ESO077-IG014b	350.27	−69.21	186.0	11.63	0.05	0.42	0.13
NGC7674	351.99	8.78	125.0	11.42	0.74	0.07	0.05
NGC7679a	352.19	3.51	73.8	11.04	0.17	0.09	0.19
IRASF23365+3604	354.76	36.35	287.0	12.23	0.05	1.68	0.22
MCG-01-60-022	355.50	−3.61	100.0	11.17	0.08	0.14	0.15
IRAS23436+5257	356.52	53.23	149.0	11.59	0.12	0.36	0.18
NGC7752b	356.74	29.46	73.6	10.75	0.08	0.05	0.11
NGC7752a	356.77	29.48	73.6	10.08	0.16	0.01	0.02
NGC7771c	357.77	20.15	61.2	10.84	0.16	0.06	0.18
NGC7771a	357.85	20.11	61.2	11.39	0.06	0.24	0.70
Mrk331	357.86	20.59	79.3	11.54	0.03	0.35	0.61

APPENDIX E

IceCube Analysis performance

E.1 Catalog search

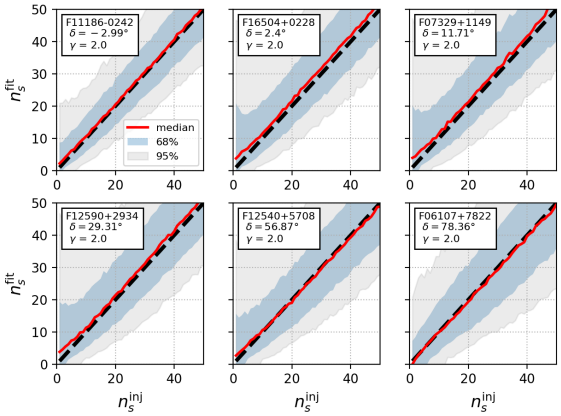

FIGURE E.1: Median number of fitted signal neutrinos (n_s^{fit}) as a function of the injected signal neutrinos (n_s^{inj}). The black dashed line represents the unbiased case. The shaded regions correspond to the 68% and 95% containment intervals. A fixed spectral index of $\gamma = 2.0$ is used. Six out of the 113 sources are selected to ensure coverage across a wide range of declinations.

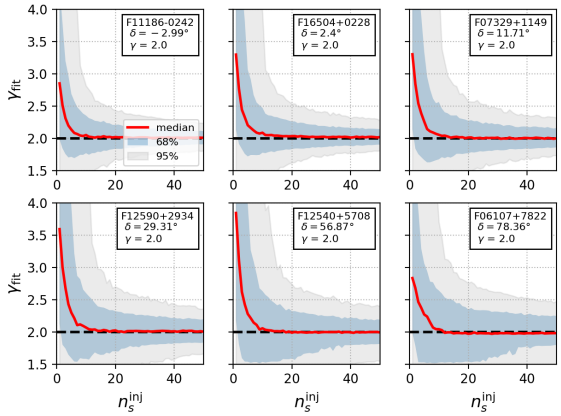

FIGURE E.2: Median number of fitted spectral indices (γ_{fit}) as a function of the injected signal neutrinos (n_s^{inj}). The black dashed line represents the unbiased case. The shaded regions correspond to the 68% and 95% containment intervals. A fixed spectral index of $\gamma = 2.0$ is used. Six out of the 113 sources are selected to ensure coverage across a wide range of declinations.

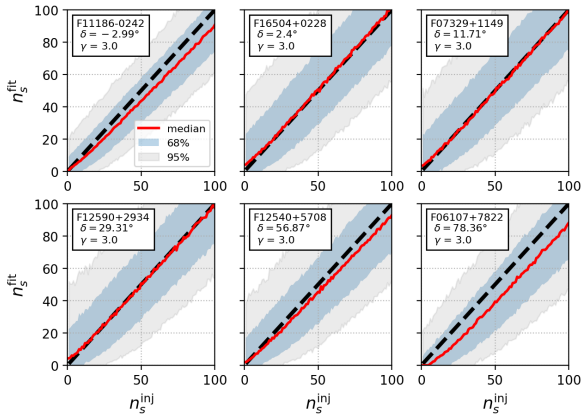

FIGURE E.3: Median number of fitted signal neutrinos (n_s^{fit}) as a function of the injected signal neutrinos (n_s^{inj}). The black dashed line represents the unbiased case. The shaded regions correspond to the 68% and 95% containment intervals. A fixed spectral index of $\gamma = 3.0$ is used. Six out of the 113 sources are selected to ensure coverage across a wide range of declinations.

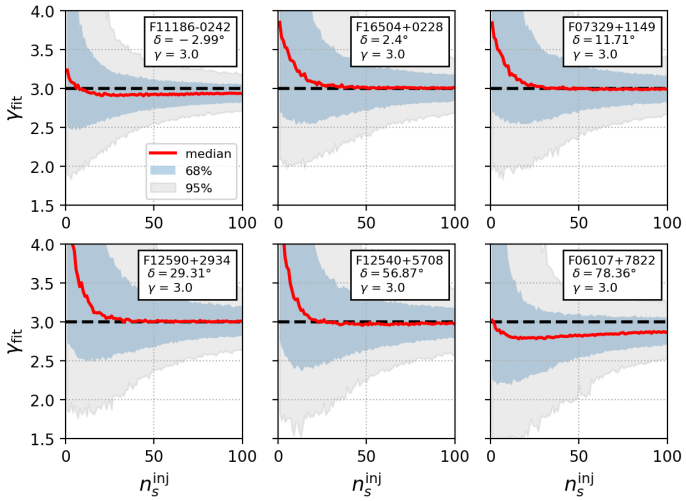

FIGURE E.4: Median number of fitted spectral indices (γ_{fit}) as a function of the injected signal neutrinos (n_s^{inj}). The black dashed line represents the unbiased case. The shaded regions correspond to the 68% and 95% containment intervals. A fixed spectral index of $\gamma = 3.0$ is used. Six out of the 113 sources are selected to ensure coverage across a wide range of declinations.

E.2 Stacking search

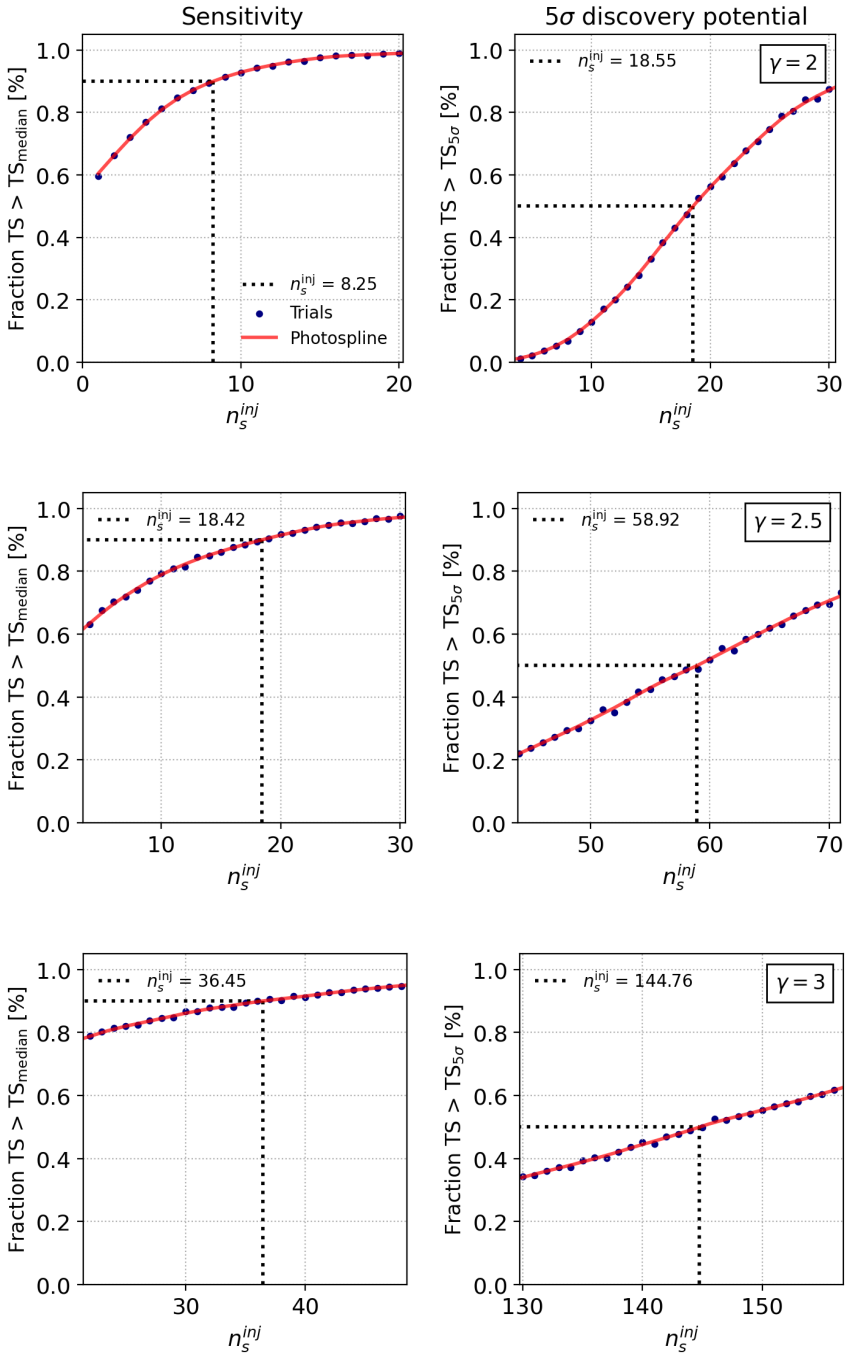

FIGURE E.5: Fraction of signal-plus-background trials in which the test statistic (TS) exceeds the TS value corresponding to the background-only median (left) and the 5σ significance threshold (right), plotted as a function of the injected pseudosignal (n_s^{inj}). Each row corresponds to a fixed spectral index: from top to bottom, $\gamma = 2.0$, 2.5, and 3.0.

APPENDIX F

IceCube Analysis Results

TABLE F.1: Unblinding results for the catalog search of 113 GOALS U/LIRGs, as presented in Chapters 5 and 6. The table lists the source positions in right ascension ($\alpha_{\rm src}$) and declination ($\delta_{\rm src}$) both in degrees (°), the observed test statistic ($\mathrm{TS}_{\rm obs}$), the best-fit spectral index ($\gamma_{\rm fit}$), the best-fit number of signal neutrinos ($n_s^{\rm fit}$), the local p-value ($\mathrm{p}_{\rm local}$), the local significance ($\sigma_{\rm local}$), the global significance ($\sigma_{\rm global}$) for the most significant source, and the upper limit on the muon-neutrino flux at 1 TeV ($\Phi_0^{90\%}$) for spectral indices of $\gamma = 2.0$ and 2.5. The flux is parametrized as $\Phi_{\nu_\mu+\bar{\nu}_\mu} = \Phi_0^{90\%}\,(E_\nu/1\ \mathrm{TeV})^{-\gamma} \times 10^{-14}\ \mathrm{TeV}^{-1}\ \mathrm{cm}^{-2}\ \mathrm{s}^{-1}$.

IRAS name	$\alpha_{\rm src}$	$\delta_{\rm src}$	$\mathrm{TS}_{\rm obs}$	$\gamma_{\rm fit}$	$n_s^{\rm fit}$	$\mathrm{p}_{\rm local}$	$\sigma_{\rm local}$	$\sigma_{\rm global}$	$\Phi_0^{90\%}$ ($\gamma = 2.0$)	$\Phi_0^{90\%}$ ($\gamma = 2.5$)
F23007+0836	345.82	8.88	15.5	1.9	5.5	9.4×10^{-5}	3.7	2.3	63.5	675.0
F16104+5235	242.92	52.46	7.4	2.3	12.8	5.3×10^{-3}	2.6	/	83.6	515.5
F05414+5840	86.45	58.70	4.8	3.9	47.2	2.0×10^{-2}	2.1	/	79.2	453.6
F00506+7248	13.52	73.08	5.5	4.2	61.3	2.8×10^{-2}	1.9	/	11.3	549.9
F00548+4331	14.42	43.80	4.4	2.2	7.9	3.3×10^{-2}	1.8	/	62.8	410.2
20264+2533	307.13	25.73	4.2	3.2	37.0	3.8×10^{-2}	1.8	/	49.5	388.4
F10173+0828	155.00	8.23	4.0	3.0	34.2	3.9×10^{-2}	1.8	/	36.5	393.2
F03117+4151	48.76	42.04	3.5	2.6	12.3	4.7×10^{-2}	1.7	/	58.3	379.2
F06107+7822	94.66	78.36	2.0	0.6	1.6	5.5×10^{-2}	1.6	/	98.2	491.2
F02345+2053	39.36	21.10	3.4	2.6	13.4	5.7×10^{-2}	1.6	/	43.5	364.2

04271+3849	67.64	38.93	3.2	3.8	37.3	6.2×10^{-2}	1.5	/	52.7	359.8
F14547+2449	224.25	24.61	3.1	3.8	42.2	6.7×10^{-2}	1.5	/	43.5	342.7
F11011+4107	165.97	40.85	2.5	2.0	5.4	8.6×10^{-2}	1.4	/	51.6	343.7
F23135+2517	349.00	25.56	2.7	4.4	43.4	8.9×10^{-2}	1.3	/	42.1	333.2
F22389+3359	340.30	34.25	2.5	3.9	34.9	9.5×10^{-2}	1.3	/	47.7	333.6
F17530+3447	268.72	34.78	2.2	2.6	10.9	1.1×10^{-1}	1.2	/	46.4	319.1
F14179+4927	214.93	49.24	1.7	3.9	27.5	1.3×10^{-1}	1.1	/	51.3	316.1
F03514+1546	58.57	15.93	1.8	2.8	17.0	1.4×10^{-1}	1.1	/	34.7	308.3
19542+1110	299.15	11.32	1.7	3.4	26.4	1.5×10^{-1}	1.0	/	29.9	289.5
F07329+1149	113.93	11.71	1.6	2.6	7.0	1.5×10^{-1}	1.0	/	28.9	286.6
F13564+3741	209.65	37.44	1.6	2.6	6.2	1.5×10^{-1}	1.0	/	42.5	291.4
05083+2441	77.86	24.76	1.6	2.9	14.1	1.6×10^{-1}	1.0	/	35.8	287.9
F09320+6134	143.96	61.35	1.2	3.5	16.6	1.6×10^{-1}	1.0	/	59.5	314.8
F02152+1418	34.49	14.53	1.5	3.6	27.7	1.6×10^{-1}	1.0	/	31.1	279.9
F02437+2122	41.66	21.59	1.6	2.0	2.7	1.6×10^{-1}	1.0	/	35.5	280.7
F16577+5900	254.62	58.95	1.0	3.6	20.9	1.8×10^{-1}	0.9	/	52.5	285.6
F13373+0105	204.98	0.84	1.1	2.4	4.9	1.9×10^{-1}	0.9	/	21.6	272.3
F10565+2448	164.83	24.54	1.2	3.6	22.7	2.1×10^{-1}	0.8	/	34.4	261.3
F04097+0525	63.09	5.55	1.2	4.4	29.2	2.1×10^{-1}	0.8	/	24.6	269.9
23436+5257	356.52	53.23	0.9	4.3	22.0	2.2×10^{-1}	0.8	/	46.2	269.3
F05365+6921	85.52	69.38	1.2	4.0	25.2	2.2×10^{-1}	0.8	/	67.3	323.4
F23444+2911	356.76	29.47	1.1	4.4	25.5	2.2×10^{-1}	0.8	/	35.9	258.1
F12112+0305	183.44	2.81	1.1	4.4	26.8	2.3×10^{-1}	0.8	/	22.1	260.4
F01417+1651	26.13	17.10	1.1	4.2	28.3	2.3×10^{-1}	0.7	/	29.5	248.4
F02512+1446	43.51	14.97	0.8	3.1	10.2	2.5×10^{-1}	0.7	/	27.2	246.7
F06538+4628	104.39	46.40	0.9	4.4	22.7	2.5×10^{-1}	0.7	/	41.4	253.9
05442+1732	86.79	17.56	0.9	3.9	23.7	2.6×10^{-1}	0.7	/	29.3	245.9
F23365+3604	354.76	36.35	0.8	2.6	3.9	2.7×10^{-1}	0.6	/	37.0	239.5
F02435+1253	41.57	13.10	0.7	3.1	14.2	2.8×10^{-1}	0.6	/	25.7	231.7

F20304-0211	308.28	−2.03	0.4	3.5	10.8	2.9×10^{-1}	0.6	/	18.7	235.8
F14280+3126	217.54	31.22	0.6	3.8	16.1	2.9×10^{-1}	0.6	/	33.1	229.9
F00073+2538	2.47	25.92	0.6	2.3	2.1	3.1×10^{-1}	0.5	/	30.4	221.8
F11231+1456	171.45	14.67	0.6	3.7	17.8	3.1×10^{-1}	0.5	/	24.8	222.7
F17548+2401	269.24	24.02	0.6	4.4	19.0	3.1×10^{-1}	0.5	/	30.0	220.2
05368+4940	85.18	49.69	0.4	3.4	9.9	3.3×10^{-1}	0.4	/	39.2	216.2
F02070+3857	32.54	39.19	0.5	4.4	16.6	3.3×10^{-1}	0.4	/	33.7	214.5
F15107+0724	228.30	7.23	0.4	3.0	8.7	3.4×10^{-1}	0.4	/	22.0	225.5
F02281-0309	37.68	−2.94	0.2	4.4	5.7	3.4×10^{-1}	0.4	/	17.9	222.7
21101+5810	317.87	58.39	0.2	4.4	11.1	3.6×10^{-1}	0.4	/	40.7	215.5
F20550+1655	314.35	17.13	0.5	4.4	17.9	3.6×10^{-1}	0.4	/	24.9	207.4
F13136+6223	198.89	62.13	0.2	2.6	2.4	3.8×10^{-1}	0.3	/	45.7	231.1
F12540+5708	194.06	56.87	0.1	4.4	8.9	3.8×10^{-1}	0.3	/	38.3	214.0
F02203+3158	35.84	32.19	0.3	4.4	12.9	3.8×10^{-1}	0.3	/	29.6	198.0
F23254+0830	351.99	8.78	0.2	4.4	13.0	3.9×10^{-1}	0.3	/	22.0	200.8
F12590+2934	195.35	29.31	0.3	4.4	13.1	3.9×10^{-1}	0.3	/	28.4	199.2
F03217+4022	51.27	40.56	0.3	3.7	9.8	3.9×10^{-1}	0.3	/	33.4	199.2
F03164+4119	49.95	41.51	0.2	3.2	7.1	3.9×10^{-1}	0.3	/	32.0	193.9
F11257+5850	172.13	58.56	0.1	4.4	8.9	3.9×10^{-1}	0.3	/	39.0	204.0
03582+6012	60.64	60.34	0.1	4.4	6.8	4.1×10^{-1}	0.2	/	41.3	211.9
F15276+1309	232.50	12.99	0.2	3.4	8.3	4.2×10^{-1}	0.2	/	21.1	187.4
F13497+0220	208.07	2.10	0.2	3.2	7.5	4.3×10^{-1}	0.2	/	16.8	189.6
F01173+1405	20.01	14.36	0.2	2.6	2.6	4.5×10^{-1}	0.1	/	21.7	180.6
F13126+2453	198.76	24.62	0.1	3.9	9.2	4.5×10^{-1}	0.1	/	24.6	180.4
F13470+3530	207.31	35.26	0.0	4.4	3.3	5.1×10^{-1}	/	/	27.2	165.0
F16030+2040	241.30	20.54	0.0	3.5	3.0	5.2×10^{-1}	/	/	22.4	164.1
F15437+0234	236.57	2.42	0.0	3.9	1.1	5.8×10^{-1}	/	/	15.2	168.9
F10196+2149	155.58	21.57	0.0	4.4	0.0	1.0×10^{0}	/	/	22.3	169.7
F05081+7936	79.19	79.67	0.0	2.5	0.0	1.0×10^{0}	/	/	64.7	323.2

F06052+8027	93.56	80.46	0.0	4.2	0.0	1.0×10^0	/	/	68.9	332.1
23262+0314	352.19	3.51	0.0	4.4	0.0	1.0×10^0	/	/	16.3	173.6
07063+2043	107.31	20.62	0.0	2.8	0.0	1.0×10^0	/	/	21.6	164.8
F07256+3355	112.19	33.84	0.0	4.4	0.0	1.0×10^0	/	/	26.9	166.2
F09126+4432	138.98	44.33	0.0	4.4	0.0	1.0×10^0	/	/	30.2	175.8
F18131+6820	273.24	68.36	0.0	4.3	0.0	1.0×10^0	/	/	44.7	201.2
F01484+2220	27.81	22.58	0.0	4.4	0.0	1.0×10^0	/	/	22.4	162.8
F23488+1949	357.81	20.13	0.0	4.4	0.0	1.0×10^0	/	/	22.1	164.8
F12592+0436	195.46	4.33	0.0	4.4	0.0	1.0×10^0	/	/	16.8	172.0
F23024+1916	346.24	19.55	0.0	1.9	0.0	1.0×10^0	/	/	21.8	160.7
F15250+3608	231.75	35.98	0.0	4.4	0.0	1.0×10^0	/	/	27.2	168.7
F15163+4255	229.53	42.74	0.0	3.0	0.0	1.0×10^0	/	/	29.5	174.6
F23488+2018	357.84	20.58	0.0	4.4	0.0	1.0×10^0	/	/	22.5	164.9
07251-0248	111.91	−2.92	0.0	2.6	0.0	1.0×10^0	/	/	15.9	179.4
F12116+5448	183.54	54.53	0.0	4.4	0.0	1.0×10^0	/	/	32.2	173.5
F17207-0014	260.84	−0.28	0.0	2.5	0.0	1.0×10^0	/	/	15.3	174.1
F13428+5608	206.18	55.89	0.0	4.4	0.0	1.0×10^0	/	/	33.5	181.4
F18425+6036	280.80	60.65	0.0	4.4	0.0	1.0×10^0	/	/	37.2	182.7
F19120+7320	287.75	73.42	0.0	4.4	0.0	1.0×10^0	/	/	49.1	216.9
F18329+5950	278.40	59.89	0.0	4.4	0.0	1.0×10^0	/	/	36.4	185.5
F02208+4744	36.03	47.97	0.0	4.4	0.0	1.0×10^0	/	/	33.1	173.7
F13188+0036	200.35	0.34	0.0	4.4	0.0	1.0×10^0	/	/	14.8	172.7
F04326+1904	68.89	19.17	0.0	4.4	0.0	1.0×10^0	/	/	21.7	168.1
F18145+2205	274.16	22.11	0.0	4.4	0.0	1.0×10^0	/	/	22.4	164.4
F23157+0618	349.56	6.57	0.0	4.4	0.0	1.0×10^0	/	/	17.1	171.9
F05054+1718	77.09	17.37	0.0	3.1	0.0	1.0×10^0	/	/	21.6	170.4
F16284+0411	247.73	4.08	0.0	2.5	0.0	1.0×10^0	/	/	16.9	179.7
F08572+3915	135.11	39.06	0.0	4.4	0.0	1.0×10^0	/	/	28.2	166.5
F12243-0036	186.75	−0.89	0.0	4.4	0.0	1.0×10^0	/	/	15.1	172.7

F08339+6517	129.60	65.12	0.0	4.4	0.0	1.0×10^0	/	/	42.1	194.8
F16504+0228	253.25	2.40	0.0	4.4	0.0	1.0×10^0	/	/	15.9	175.1
F02114+0456	33.50	5.17	0.0	4.4	0.0	1.0×10^0	/	/	16.8	170.2
18090+0130	272.90	1.53	0.0	4.4	0.0	1.0×10^0	/	/	15.7	175.5
F03359+1523	54.70	15.55	0.0	2.5	0.0	1.0×10^0	/	/	20.4	164.7
F09437+0317	146.59	3.06	0.0	4.4	0.0	1.0×10^0	/	/	16.0	167.9
F08354+2555	129.60	25.75	0.0	4.4	0.0	1.0×10^0	/	/	23.6	161.8
05129+5128	79.23	51.53	0.0	4.4	0.0	1.0×10^0	/	/	32.3	177.1
F09333+4841	144.14	48.47	0.0	4.4	0.0	1.0×10^0	/	/	32.3	181.1
F13362+4831	204.57	48.28	0.0	0.6	0.0	1.0×10^0	/	/	32.4	175.7
F15327+2340	233.74	23.50	0.0	4.4	0.0	1.0×10^0	/	/	24.0	166.1
F11186-0242	170.29	-2.99	0.0	4.4	0.0	1.0×10^0	/	/	15.8	182.5
F13182+3424	200.15	34.14	0.0	3.2	0.0	1.0×10^0	/	/	27.6	167.0
20351+2521	309.32	25.53	0.0	4.4	0.0	1.0×10^0	/	/	24.1	165.7
F17132+5313	258.59	53.18	0.0	2.9	0.0	1.0×10^0	/	/	32.0	172.7
F01519+3640	28.74	36.92	0.0	4.4	0.0	1.0×10^0	/	/	27.3	165.7

TABLE F.2: The table provides the optical and IRAS source names, the source positions in right ascension ($\alpha_{\rm src}$) and declination ($\delta_{\rm src}$), both in degrees (°), as well as the luminosity distance in megaparsecs (Mpc). The stacking analysis performed on these sources is fully consistent with the background-only hypothesis, as discussed in Chapter 6.

IRAS name	Optical name	$\alpha_{\rm src}$	$\delta_{\rm src}$	D_L
F12243-0036	NGC 4418	186.75	−0.89	36.50
F17207-0014	/	260.84	−0.28	198.00
F12112+0305	/	183.44	2.81	340.00
F15107+0724	CGCG049-057	228.30	7.23	65.40
F15327+2340	Arp 220	233.74	23.50	87.90
F13126+2453	IC0860	198.76	24.62	56.80
F15250+3608	/	231.75	35.98	254.00
F12540+5708	UGC08058	194.06	56.87	192.00
F11257+5850	NGC3690 (Arp 299)	172.13	58.56	50.70
F09320+6134	UGC05101	143.96	61.35	177.00

Bibliography

[1] V. Hess. “On the Observations of the Penetrating Radiation during Seven Balloon Flights”. In: *arXiv e-prints*, arXiv:1808.02927 (2018), arXiv:1808.02927. DOI: 10.48550/arXiv.1808.02927. arXiv: 1808.02927 [physics.hist-ph].

[2] B. P. Abbott et al. “Observation of Gravitational Waves from a Binary Black Hole Merger”. In: *Physical Review Letters* 116.6, 061102 (2016), p. 061102. DOI: 10.1103/PhysRevLett.116.061102. arXiv: 1602.03837 [gr-qc].

[3] B. P. Abbott et al. “GW170817: Observation of Gravitational Waves from a Binary Neutron Star Inspiral”. In: *Physical Review Letters* 119.16, 161101 (2017), p. 161101. DOI: 10.1103/PhysRevLett.119.161101. arXiv: 1710.05832 [gr-qc].

[4] M. G. Aartsen et al. “Evidence for High-Energy Extraterrestrial Neutrinos at the IceCube Detector”. In: *Science* 342.6161, 1242856 (2013), p. 1242856. DOI: 10.1126/science.1242856. arXiv: 1311.5238 [astro-ph.HE].

[5] M. G. Aartsen et al. “Observation of High-Energy Astrophysical Neutrinos in Three Years of IceCube Data”. In: *Physical Review Letters* 113.10, 101101 (2014), p. 101101. DOI: 10.1103/PhysRevLett.113.101101. arXiv: 1405.5303 [astro-ph.HE].

[6] R. Abbasi et al. “The IceCube high-energy starting event sample: Description and flux characterization with 7.5 years of data”. In: *Physical Review D* 104 (2021), p. 022002. DOI: 10.1103/PhysRevD.104.022002. arXiv: 2011.03545 [astro-ph.HE].

[7] R. Abbasi et al. “Improved Characterization of the Astrophysical Muon-neutrino Flux with 9.5 Years of IceCube Data”. In: *Astrophysical Journal* 928.1, 50 (2022), p. 50. DOI: 10.3847/1538-4357/ac4d29. arXiv: 2111.10299 [astro-ph.HE].

[8] M. G. Aartsen et al. “Characteristics of the diffuse astrophysical electron and tau neutrino flux with six years of IceCube high energy cascade data”. In: *Physical Review Letters* 125.12 (2020), p. 121104. DOI: 10.1103/PhysRevLett.125.121104. arXiv: 2001.09520 [astro-ph.HE].

[9] M. G. Aartsen et al. “Measurements using the inelasticity distribution of multi-TeV neutrino interactions in IceCube”. In: *Physical Review D* 99.3 (2019). DOI: 10.1103/PhysRevD.99.032004. arXiv: 1808.07629 [hep-ex].

[10] R. Abbasi et al. “Characterization of the astrophysical diffuse neutrino flux using starting track events in IceCube”. In: *Physical Review D* 110.2, 022001 (2024), p. 022001. DOI: 10.1103/PhysRevD.110.022001. arXiv: 2402.18026 [astro-ph.HE].

[11] M. G. Aartsen et al. “A Combined Maximum-likelihood Analysis of the High-energy Astrophysical Neutrino Flux Measured with IceCube”. In: *Astrophysical Journal* 809.1, 98 (2015), p. 98. DOI: 10.1088/0004-637X/809/1/98. arXiv: 1507.03991 [astro-ph.HE].

[12] R. Abbasi et al. “The IceCube Collaboration – Contributions to the 38th International Cosmic Ray Conference (ICRC2023)”. In: *arXiv e-prints*, arXiv:2307.13047 (2023), arXiv:2307.13047. DOI: 10.48550/arXiv.2307.13047. arXiv: 2307.13047 [astro-ph.HE].

[13] R. Abbasi et al. “Observation of high-energy neutrinos from the Galactic plane”. In: *Science* 380.6652 (2023), pp. 1338–1343. DOI: 10.1126/science.adc9818. arXiv: 2307.04427 [astro-ph.HE].

[14] M. G. Aartsen et al. “Multimessenger observations of a flaring blazar coincident with high-energy neutrino IceCube-170922A”. In: *Science* 361.6398, eaat1378 (2018), eaat1378. DOI: 10.1126/science.aat1378. arXiv: 1807.08816 [astro-ph.HE].

[15] M. G. Aartsen et al. “Neutrino emission from the direction of the blazar TXS 0506+056 prior to the IceCube-170922A alert”. In: *Science* 361.6398 (2018), pp. 147–151. DOI: 10.1126/science.aat2890. arXiv: 1807.08794 [astro-ph.HE].

[16] R. Abbasi et al. “Evidence for neutrino emission from the nearby active galaxy NGC 1068”. In: *Science* 378.6619 (2022), pp. 538–543. DOI: 10.1126/science.abg3395. arXiv: 2211.09972 [astro-ph.HE].

[17] K. Murase, M. Ahlers, and B. C. Lacki. “Testing the hadronuclear origin of PeV neutrinos observed with IceCube”. In: *Physical Review D* 88.12, 121301 (2013), p. 121301. DOI: 10.1103/PhysRevD.88.121301. arXiv: 1306.3417 [astro-ph.HE].

[18] K. Murase, D. Guetta, and M. Ahlers. “Hidden Cosmic-Ray Accelerators as an Origin of TeV-PeV Cosmic Neutrinos”. In: *Physical Review Letters* 116.7, 071101 (2016), p. 071101. DOI: 10.1103/PhysRevLett.116.071101. arXiv: 1509.00805 [astro-ph.HE].

[19] L. Armus et al. “GOALS: The Great Observatories All-Sky LIRG Survey”. In: *Publications of the Astronomical Society of the Pacific* 121.880 (2009), p. 559. DOI: 10.1086/600092. arXiv: 0904.4498 [astro-ph.CO].

[20] A. Debot. “Investigation of possible astrophysical source classes responsible for the observed IceCube alert avents”. Bachelor thesis. Vrije Universiteit Brussel, 2023. URL: https://drive.google.com/file/d/1N2MfWfgROZ3ifPBrO_lFidPjUNwJAtTS/view?usp=sharing.

[21] L. Jacops. “Investigation of high-energy neutrino production in cosmic accelerators due to photohadronic interactions”. Bachelor thesis. Vrije Universiteit Brussel, 2023. URL: https://drive.google.com/file/d/17ND87UdFgkOmco33ZWovqmabbnMoBjkN/view?usp=sharing.

[22] Y. Merckx et al. “Investigating starburst-driven neutrino emission from galaxies in the Great Observatories All-Sky LIRG Survey”. In: *Physical Review D* 108.2, 023015 (2023), p. 023015. DOI: 10.1103/PhysRevD.108.023015. arXiv: 2304.01020 [astro-ph.HE].

[23] Y. Merckx et al. “Investigating starburst-driven neutrino emission from GOALS galaxies”. In: *Proceedings of Science* ICRC2023 (2023), p. 972. DOI: 10.22323/1.444.0972.

[24] Y. Vekemans. "Investigating the Supernova Rate in (Ultra) Luminous Infrared Galaxies in View of Foreseen Neutrino Studies With the IceCube Neutrino Observatory". Bachelor thesis. Vrije Universiteit Brussel, 2022. URL: drive.google.com/file/d/1bUfTkQQ-5-YG1D_-honWaem4EXPfXjhS/view?usp=sharing.

[25] R. Davé et al. "Simba: Cosmological Simulations with Black Hole Growth and Feedback". In: *Monthly Notices of the Royal Astronomical Society* 486.2 (2019), pp. 2827–2849. DOI: 10.1093/mnras/stz937. arXiv: 1901.10203 [astro-ph.GA].

[26] A. Debot. "Modeling of High-Energy Neutrino Emission from Star-Forming Activity Using the SIMBA Cosmological Simulation". Master thesis. Vrije Universiteit Brussel, 2025.

[27] M. Wolf. "SkyLLH - A generalized Python-based tool for log-likelihood analyses in multi-messenger astronomy". In: *Proceedings of Science* ICRC2019 (2021), p. 1035. DOI: 10.22323/1.358.1035. arXiv: 1908.05181 [astro-ph.IM].

[28] R. Abbasi et al. "The SkyLLH framework for IceCube point-source search". In: *Proceedings of Science* ICRC2021 (2021), p. 1073. DOI: 10.22323/1.395.1073. arXiv: 2107.08934 [astro-ph.IM].

[29] S. Navas et al. "Review of Particle Physics". In: *Physical Review D* 110 (3 2024), p. 030001. DOI: 10.1103/PhysRevD.110.030001. URL: https://link.aps.org/doi/10.1103/PhysRevD.110.030001.

[30] S. Ting. "The Alpha Magnetic Spectrometer on the International Space Station". In: *Nuclear Physics B - Proceedings Supplements* 243-244 (2013). Proceedings of the IV International Conference on Particle and Fundamental Physics in Space, pp. 12–24. ISSN: 0920-5632. DOI: https://doi.org/10.1016/j.nuclphysbps.2013.09.028. URL: https://www.sciencedirect.com/science/article/pii/S0920563213005525.

[31] J. Chang et al. "The DArk Matter Particle Explorer mission". In: *Astroparticle Physics* 95 (2017), pp. 6–24. ISSN: 0927-6505. DOI: https://doi.org/10.1016/j.astropartphys.2017.08.005. URL: https://www.sciencedirect.com/science/article/pii/S0927650517300841.

[32] R. Abbasi et al. "IceTop: The surface component of IceCube. The IceCube Collaboration". In: *Nuclear Instruments and Methods in Physics Research A* 700 (2013), pp. 188–220. DOI: 10.1016/j.nima.2012.10.067. arXiv: 1207.6326 [astro-ph.IM].

[33] "The Pierre Auger Cosmic Ray Observatory". In: *Nuclear Instruments and Methods in Physics Research Section A: Accelerators, Spectrometers, Detectors and Associated Equipment* 798 (2015), pp. 172–213. ISSN: 0168-9002. DOI: https://doi.org/10.1016/j.nima.2015.06.058. URL: https://www.sciencedirect.com/science/article/pii/S0168900215008086.

[34] T. Abu-Zayyad et al. "The surface detector array of the Telescope Array experiment". In: *Nuclear Instruments and Methods in Physics Research A* 689 (2012), pp. 87–97. DOI: 10.1016/j.nima.2012.05.079. arXiv: 1201.4964 [astro-ph.IM].

[35] M. Malacari et al. "The first full-scale prototypes of the fluorescence detector array of single-pixel telescopes". In: *Astroparticle Physics* 119, 102430 (2020), p. 102430. DOI: 10.1016/j.astropartphys.2020.102430. arXiv: 1911.05285 [astro-ph.HE].

[36] T. Winchen et al. “Cosmic Ray Physics with the LOFAR Radio Telescope”. In: *Journal of Physics Conference Series*. Vol. 1181. Journal of Physics Conference Series. IOP, 2019, 012020, p. 012020. DOI: 10.1088/1742-6596/1181/1/012020. arXiv: 1903.08474 [astro-ph.HE].

[37] D. J. Bird et al. “Detection of a Cosmic Ray with Measured Energy Well beyond the Expected Spectral Cutoff due to Cosmic Microwave Radiation”. In: *Astrophysical Journal* 441 (1995), p. 144. DOI: 10.1086/175344. arXiv: astro-ph/9410067 [astro-ph].

[38] C. J. Cesarsky. “Cosmic-ray confinement in the galaxy”. In: *Annual Review of Astronomy and Astrophysics* 18 (1980), pp. 289–319. DOI: 10.1146/annurev.aa.18.090180.001445.

[39] M. Kachelrieß. “Transition from Galactic to Extragalactic Cosmic Rays”. In: *European Physical Journal Web of Conferences*. Vol. 210. European Physical Journal Web of Conferences. 2019, 04003, p. 04003. DOI: 10.1051/epjconf/201921004003.

[40] M. G. Aartsen et al. “Cosmic ray spectrum and composition from PeV to EeV using 3 years of data from IceTop and IceCube”. In: *Physical Review D* 100.8, 082002 (2019), p. 082002. DOI: 10.1103/PhysRevD.100.082002. arXiv: 1906.04317 [astro-ph.HE].

[41] A. M. Bykov et al. “Cosmic Ray Production in Supernovae”. In: *Space Science Reviews* 214.1, 41 (2018), p. 41. DOI: 10.1007/s11214-018-0479-4. arXiv: 1801.08890 [astro-ph.HE].

[42] I. A. Grenier, J. H. Black, and A. W. Strong. “The Nine Lives of Cosmic Rays in Galaxies”. In: *Annual Review of Astronomy and Astrophysics* 53 (2015), pp. 199–246. DOI: 10.1146/annurev-astro-082214-122457.

[43] D. Caprioli and A. Spitkovsky. “Simulations of Ion Acceleration at Non-relativistic Shocks. I. Acceleration Efficiency”. In: *Astrophysical Journal* 783.2, 91 (2014), p. 91. DOI: 10.1088/0004-637X/783/2/91. arXiv: 1310.2943 [astro-ph.HE].

[44] V. Ptuskin, V. Zirakashvili, and E.-S. Seo. “Spectrum of Galactic Cosmic Rays Accelerated in Supernova Remnants”. In: *Astrophysical Journal* 718.1 (2010), pp. 31–36. DOI: 10.1088/0004-637X/718/1/31. arXiv: 1006.0034 [astro-ph.CO].

[45] S. Thoudam et al. “Cosmic-ray energy spectrum and composition up to the ankle: the case for a second Galactic component”. In: *Astronomy & Astrophysics* 595, A33 (2016), A33. DOI: 10.1051/0004-6361/201628894. arXiv: 1605.03111 [astro-ph.HE].

[46] K. Greisen. “End to the Cosmic-Ray Spectrum?” In: *Physical Review Letters* 16.17 (1966), pp. 748–750. DOI: 10.1103/PhysRevLett.16.748.

[47] G. T. Zatsepin and V. A. Kuz’min. “Upper Limit of the Spectrum of Cosmic Rays”. In: *Soviet Journal of Experimental and Theoretical Physics Letters* 4 (1966), p. 78.

[48] A. Coleman et al. “Ultra high energy cosmic rays The intersection of the Cosmic and Energy Frontiers”. In: *Astroparticle Physics* 147, 102794 (2023), p. 102794. DOI: 10.1016/j.astropartphys.2022.102794. arXiv: 2205.05845 [astro-ph.HE].

[49] E. Fermi. "Galactic Magnetic Fields and the Origin of Cosmic Radiation." In: *Astrophysical Journal* 119 (1954), p. 1. DOI: 10.1086/145789.

[50] A. R. Bell. "The acceleration of cosmic rays in shock fronts - I." In: *Monthly Notices of the Royal Astronomical Society* 182 (1978), pp. 147–156. DOI: 10.1093/mnras/182.2.147.

[51] R. D. Blandford and J. P. Ostriker. "Particle acceleration by astrophysical shocks." In: *Astrophysical Journal Letters* 221 (1978), pp. L29–L32. DOI: 10.1086/182658.

[52] M. Newman. "Power laws, Pareto distributions and Zipf's law". In: *Contemporary Physics* 46.5 (2005), pp. 323–351. DOI: 10.1080/00107510500052444. eprint: https://doi.org/10.1080/00107510500052444. URL: https://doi.org/10.1080/00107510500052444.

[53] R. A. Treumann. "Fundamentals of collisionless shocks for astrophysical application, 1. Non-relativistic shocks". In: *The Astronomy and Astrophysics Review* 17.4 (2009), pp. 409–535. DOI: 10.1007/s00159-009-0024-2.

[54] P. Blasi and E. Amato. "Diffusive propagation of cosmic rays from supernova remnants in the Galaxy. I: spectrum and chemical composition". In: *Journal of Cosmology and Astroparticle Physics* 2012.1, 010 (2012), p. 010. DOI: 10.1088/1475-7516/2012/01/010. arXiv: 1105.4521 [astro-ph.HE].

[55] A. M. Hillas. "The Origin of Ultra-High-Energy Cosmic Rays". In: *Annual Review of Astronomy and Astrophysics* 22 (1984), pp. 425–444. DOI: 10.1146/annurev.aa.22.090184.002233.

[56] R. Alves Batista et al. "Open Questions in Cosmic-Ray Research at Ultrahigh Energies". In: *Frontiers in Astronomy and Space Sciences* 6, 23 (2019), p. 23. DOI: 10.3389/fspas.2019.00023. arXiv: 1903.06714 [astro-ph.HE].

[57] A. Levan et al. "Gamma-Ray Burst Progenitors". In: *Space Science Reviews* 202.1-4 (2016), pp. 33–78. DOI: 10.1007/s11214-016-0312-x. arXiv: 1611.03091 [astro-ph.HE].

[58] E. Waxman. "Cosmological Gamma-Ray Bursts and the Highest Energy Cosmic Rays". In: *Physical Review Letters* 75.3 (1995), pp. 386–389. DOI: 10.1103/PhysRevLett.75.386. arXiv: astro-ph/9505082 [astro-ph].

[59] J. Kennicutt Robert C. "The Global Schmidt Law in Star-forming Galaxies". In: *Astrophysical Journal* 498.2 (1998), pp. 541–552. DOI: 10.1086/305588. arXiv: astro-ph/9712213 [astro-ph].

[60] K. Rozwadowska, F. Vissani, and E. Cappellaro. "On the rate of core collapse supernovae in the milky way". In: *New Astronomy* 83, 101498 (2021), p. 101498. DOI: 10.1016/j.newast.2020.101498. arXiv: 2009.03438 [astro-ph.HE].

[61] A. Marcowith et al. "Core-collapse supernovae as cosmic ray sources". In: *Monthly Notices of the Royal Astronomical Society* 479.4 (2018), pp. 4470–4485. ISSN: 0035-8711. DOI: 10.1093/mnras/sty1743. eprint: https://academic.oup.com/mnras/article-pdf/479/4/4470/25180551/sty1743.pdf. URL: https://doi.org/10.1093/mnras/sty1743.

[62] P. Cristofari. "The Hunt for Pevatrons: The Case of Supernova Remnants". In: *Universe* 7.9 (2021), p. 324. DOI: 10.3390/universe7090324. arXiv: 2110.07956 [astro-ph.HE].

[63] P. L. Biermann et al. “The Origin of the Most Energetic Galactic Cosmic Rays: Supernova Explosions into Massive Star Plasma Winds”. In: *Galaxies* 7.2 (2019), p. 48. DOI: 10.3390/galaxies7020048.

[64] M. Cardillo, E. Amato, and P. Blasi. “On the cosmic ray spectrum from type II supernovae expanding in their red giant presupernova wind”. In: *Astroparticle Physics* 69 (2015), pp. 1–10. DOI: 10.1016/j.astropartphys.2015.03.002. arXiv: 1503.03001 [astro-ph.HE].

[65] K. Fang et al. “Testing the newborn pulsar origin of ultrahigh energy cosmic rays with EeV neutrinos”. In: *Physical Review D* 90.10, 103005 (2014), p. 103005. DOI: 10.1103/PhysRevD.90.103005. arXiv: 1311.2044 [astro-ph.HE].

[66] H. Athar, C. S. Kim, and J. Lee. “Intrinsic and Oscillated Astrophysical Neutrino Flavor Ratios Revisited”. In: *Modern Physics Letters A* 21.13 (2006), pp. 1049–1065. DOI: 10.1142/S021773230602038X. arXiv: hep-ph/0505017 [hep-ph].

[67] S. Veilleux et al. “Cool outflows in galaxies and their implications”. In: *Astronomy and Astrophysics Review* 28.1, 2 (2020), p. 2. DOI: 10.1007/s00159-019-0121-9. arXiv: 2002.07765 [astro-ph.GA].

[68] L. A. Anchordoqui, G. E. Romero, and J. A. Combi. “Heavy nuclei at the end of the cosmic-ray spectrum?” In: *Physical Review D* 60.10, 103001 (1999), p. 103001. DOI: 10.1103/PhysRevD.60.103001. arXiv: astro-ph/9903145 [astro-ph].

[69] L. Ferrarese and D. Merritt. “A Fundamental Relation between Supermassive Black Holes and Their Host Galaxies”. In: *Astrophysical Journal Letters* 539.1 (2000), pp. L9–L12. DOI: 10.1086/312838. arXiv: astro-ph/0006053 [astro-ph].

[70] H. Netzer. “Revisiting the Unified Model of Active Galactic Nuclei”. In: *Annual Review of Astronomy and Astrophysics* 53 (2015), pp. 365–408. DOI: 10.1146/annurev-astro-082214-122302. arXiv: 1505.00811 [astro-ph.GA].

[71] P. Padovani et al. “Active galactic nuclei: what’s in a name?” In: *Astronomy and Astrophysics Review* 25.1, 2 (2017), p. 2. DOI: 10.1007/s00159-017-0102-9. arXiv: 1707.07134 [astro-ph.GA].

[72] P. Padovani. “On the two main classes of active galactic nuclei”. In: *Nature Astronomy* 1, 0194 (2017), p. 0194. DOI: 10.1038/s41550-017-0194. arXiv: 1707.08069 [astro-ph.GA].

[73] P. Padovani. “The microjansky and nanojansky radio sky: source population and multiwavelength properties”. In: *Monthly Notices of the Royal Astronomical Society* 411.3 (2011), pp. 1547–1561. DOI: 10.1111/j.1365-2966.2010.17789.x. arXiv: 1009.6116 [astro-ph.CO].

[74] F. M. Rieger. “Active Galactic Nuclei as Potential Sources of Ultra-High Energy Cosmic Rays”. In: *Universe* 8.11 (2022), p. 607. DOI: 10.3390/universe8110607. arXiv: 2211.12202 [astro-ph.HE].

[75] E. Y. Khachikian and D. W. Weedman. “An atlas of Seyfert galaxies.” In: *Astrophysical Journal* 192 (1974), pp. 581–589. DOI: 10.1086/153093.

[76] A. Comastri. “Compton-Thick AGN: The Dark Side of the X-Ray Background”. In: *Supermassive Black Holes in the Distant Universe*. Ed. by A. J. Barger. Vol. 308. Astrophysics and Space Science Library. 2004, p. 245. DOI: 10.1007/978-1-4020-2471-9_8. arXiv: astro-ph/0403693 [astro-ph].

[77] S. Gezari. "Tidal Disruption Events". In: *Annual Review of Astronomy and Astrophysics* 59 (2021), pp. 21–58. DOI: 10.1146/annurev-astro-111720-030029. arXiv: 2104.14580 [astro-ph.HE].

[78] C. Guépin et al. "Ultra-high-energy cosmic rays and neutrinos from tidal disruptions by massive black holes". In: *Astronomy & Astrophysics* 616, A179 (2018), A179. DOI: 10.1051/0004-6361/201732392. arXiv: 1711.11274 [astro-ph.HE].

[79] D. Biehl et al. "Tidally disrupted stars as a possible origin of both cosmic rays and neutrinos at the highest energies". In: *Scientific Reports* 8, 10828 (2018), p. 10828. DOI: 10.1038/s41598-018-29022-4. arXiv: 1711.03555 [astro-ph.HE].

[80] S. van Velzen. "On the Mass and Luminosity Functions of Tidal Disruption Flares: Rate Suppression due to Black Hole Event Horizons". In: *Astrophysical Journal* 852.2, 72 (2018), p. 72. DOI: 10.3847/1538-4357/aa998e. arXiv: 1707.03458 [astro-ph.HE].

[81] T. Matsumoto and B. D. Metzger. "Synchrotron afterglow model for AT 2022cmc: jetted tidal disruption event or engine-powered supernova?" In: *Monthly Notices of the Royal Astronomical Society* 522.3 (2023), pp. 4028–4037. DOI: 10.1093/mnras/stad1182. arXiv: 2301.11939 [astro-ph.HE].

[82] C. A. G. Canal, S. J. Sciutto, and T. Tarutina. "Testing hadronic-interaction packages at cosmic-ray energies". In: *Physical Review D* 79 (5 2009), p. 054006. DOI: 10.1103/PhysRevD.79.054006. URL: https://link.aps.org/doi/10.1103/PhysRevD.79.054006.

[83] S. Hümmer et al. "Simplified Models for Photohadronic Interactions in Cosmic Accelerators". In: *Astrophysical Journal* 721.1 (2010), pp. 630–652. DOI: 10.1088/0004-637X/721/1/630. arXiv: 1002.1310 [astro-ph.HE].

[84] S. R. Kelner and F. A. Aharonian. "Energy spectra of gamma rays, electrons, and neutrinos produced at interactions of relativistic protons with low energy radiation". In: *Physical Review D* 78.3, 034013 (2008), p. 034013. DOI: 10.1103/PhysRevD.78.034013. arXiv: 0803.0688 [astro-ph].

[85] M. Vereecken. "Aspects of astrophysical particle production and beyond the Standard Model phenomenology". In: *arXiv e-prints*, arXiv:1911.12244 (2019), arXiv:1911.12244. DOI: 10.48550/arXiv.1911.12244. arXiv: 1911.12244 [hep-ph].

[86] K. Mannheim and R. Schlickeiser. "Interactions of cosmic ray nuclei". In: *Astronomy & Astrophysics* 286 (1994), pp. 983–996. DOI: 10.48550/arXiv.astro-ph/9402042. arXiv: astro-ph/9402042 [astro-ph].

[87] S. R. Kelner, F. A. Aharonian, and V. V. Bugayov. "Energy spectra of gamma rays, electrons, and neutrinos produced at proton-proton interactions in the very high energy regime". In: *Physical Review D* 74.3, 034018 (2006), p. 034018. DOI: 10.1103/PhysRevD.74.034018. arXiv: astro-ph/0606058 [astro-ph].

[88] E. Waxman and J. Bahcall. "High energy neutrinos from astrophysical sources: An upper bound". In: *Physical Review D* 59.2, 023002 (1998), p. 023002. DOI: 10.1103/PhysRevD.59.023002. arXiv: hep-ph/9807282 [hep-ph].

[89] M. Ahlers and F. Halzen. "Pinpointing extragalactic neutrino sources in light of recent IceCube observations". In: *Physical Review D* 90.4, 043005 (2014), p. 043005. DOI: 10.1103/PhysRevD.90.043005. arXiv: 1406.2160 [astro-ph.HE].

[90] M. Ahlers and F. Halzen. "Opening a New Window onto the Universe with IceCube". In: *Progress in Particle and Nuclear Physics* 102 (2018), pp. 73–88. DOI: 10.1016/j.ppnp.2018.05.001. arXiv: 1805.11112 [astro-ph.HE].

[91] D. Hooper and K. Plant. "Leptonic Model for Neutrino Emission from Active Galactic Nuclei". In: *Physical Review Letters* 131.23, 231001 (2023), p. 231001. DOI: 10.1103/PhysRevLett.131.231001. arXiv: 2305.06375 [astro-ph.HE].

[92] A. Das, B. T. Zhang, and K. Murase. "Revealing the Production Mechanism of High-energy Neutrinos from NGC 1068". In: *Astrophysical Journal* 972.1, 44 (2024), p. 44. DOI: 10.3847/1538-4357/ad5a04. arXiv: 2405.09332 [astro-ph.HE].

[93] M. Ajello et al. "3FHL: The Third Catalog of Hard Fermi-LAT Sources". In: *The Astrophysical Journal Supplement Series* 232.2, 18 (2017), p. 18. DOI: 10.3847/1538-4365/aa8221. arXiv: 1702.00664 [astro-ph.HE].

[94] M. Ackermann et al. "The Spectrum of Isotropic Diffuse Gamma-Ray Emission between 100 MeV and 820 GeV". In: *Astrophysical Journal* 799.1, 86 (2015), p. 86. DOI: 10.1088/0004-637X/799/1/86. arXiv: 1410.3696 [astro-ph.HE].

[95] M. Ajello et al. "The γ-Ray Emission of Star-forming Galaxies". In: *Astrophysical Journal* 894.2, 88 (2020), p. 88. DOI: 10.3847/1538-4357/ab86a6. arXiv: 2003.05493 [astro-ph.GA].

[96] A. Ambrosone, M. Chianese, and A. Marinelli. "Constraining the hadronic properties of star-forming galaxies above 1 GeV with 15-years Fermi-LAT data". In: *Journal of Cosmology and Astroparticle Physics* 2024.8, 040 (2024), p. 040. DOI: 10.1088/1475-7516/2024/08/040. arXiv: 2402.18638 [astro-ph.HE].

[97] I. Bartos and M. Kowalski. *Multimessenger Astronomy*. 2399-2891. IOP Publishing, 2017. ISBN: 978-0-7503-1369-8. DOI: 10.1088/978-0-7503-1369-8. URL: https://dx.doi.org/10.1088/978-0-7503-1369-8.

[98] P. Lipari. "The origin of the power-law form of the extragalactic gamma-ray flux". In: *Astroparticle Physics* 125, 102507 (2021), p. 102507. DOI: 10.1016/j.astropartphys.2020.102507. arXiv: 2001.00982 [astro-ph.HE].

[99] A. U. Abeysekara et al. "The High-Altitude Water Cherenkov (HAWC) observatory in México: The primary detector". In: *Nuclear Instruments and Methods in Physics Research A* 1052, 168253 (2023), p. 168253. DOI: 10.1016/j.nima.2023.168253. arXiv: 2304.00730 [astro-ph.HE].

[100] Z. Cao et al. "The Large High Altitude Air Shower Observatory (LHAASO) Science Book (2021 Edition)". In: *arXiv e-prints*, arXiv:1905.02773 (2019), arXiv:1905.02773. DOI: 10.48550/arXiv.1905.02773. arXiv: 1905.02773 [astro-ph.HE].

[101] S. Funk et al. "The trigger system of the H.E.S.S. telescope array". In: *Astroparticle Physics* 22.3-4 (2004), pp. 285–296. DOI: 10.1016/j.astropartphys.2004.08.001. arXiv: astro-ph/0408375 [astro-ph].

[102] E. Lorenz and MAGIC Collaboration. "Status of the 17 m ∅ MAGIC telescope". In: *New Astronomy Reviews* 48.5-6 (2004), pp. 339–344. DOI: 10.1016/j.newar.2003.12.059.

[103] J. Holder et al. "The first VERITAS telescope". In: *Astroparticle Physics* 25.6 (2006), pp. 391–401. DOI: 10.1016/j.astropartphys.2006.04.002. arXiv: astro-ph/0604119 [astro-ph].

[104] M. Amenomori et al. "First Detection of Photons with Energy Beyond 100 TeV from an Astrophysical Source". In: *Physical Review Letters* 123.5 (2019), p. 051101. DOI: 10.1103/PhysRevLett.123.051101. arXiv: 1906.05521 [astro-ph.HE].

[105] Z. Cao et al. "Ultrahigh-energy photons up to 1.4 petaelectronvolts from 12 γ-ray Galactic sources". In: *Nature* 594.7861 (2021), pp. 33–36. DOI: 10.1038/s41586-021-03498-z.

[106] Lhaaso Collaboration. "An ultrahigh-energy γ -ray bubble powered by a super PeVatron". In: *Science Bulletin* 69.4 (2024), pp. 449–457. DOI: 10.1016/j.scib.2023.12.040. arXiv: 2310.10100 [astro-ph.HE].

[107] J. N. Bahcall and R. Davis. "Solar Neutrinos - a Scientific Puzzle". In: *Science* 191 (1976), pp. 264–267. DOI: 10.1126/science.191.4224.264.

[108] K. Hirata et al. "Observation of a neutrino burst from the supernova SN1987A". In: *Physical Review Letters* 58.14 (1987), pp. 1490–1493. DOI: 10.1103/PhysRevLett.58.1490.

[109] R. M. Bionta et al. "Observation of a neutrino burst in coincidence with supernova 1987A in the Large Magellanic Cloud". In: *Physical Review Letters* 58.14 (1987), pp. 1494–1496. DOI: 10.1103/PhysRevLett.58.1494.

[110] S. Adrián-Martínez et al. "Letter of intent for KM3NeT 2.0". In: *Journal of Physics G* 43.8, 084001 (2016), p. 084001. DOI: 10.1088/0954-3899/43/8/084001. arXiv: 1601.07459 [astro-ph.IM].

[111] Avrorin, A.D. et al. "Baikal-GVD". In: *EPJ Web Conf.* 136 (2017), p. 04007. DOI: 10.1051/epjconf/201713604007. URL: https://doi.org/10.1051/epjconf/201713604007.

[112] M. Agostini et al. "The Pacific Ocean Neutrino Experiment". In: *Nature Astronomy* 4 (2020), pp. 913–915. DOI: 10.1038/s41550-020-1182-4. arXiv: 2005.09493 [astro-ph.HE].

[113] M. G. Aartsen et al. "IceCube-Gen2: the window to the extreme Universe". In: *Journal of Physics G* 48.6, 060501 (2021), p. 060501. DOI: 10.1088/1361-6471/abbd48. arXiv: 2008.04323 [astro-ph.HE].

[114] J. A. Aguilar et al. "Design and sensitivity of the Radio Neutrino Observatory in Greenland (RNO-G)". In: *Journal of Instrumentation* 16.3, P03025 (2021), P03025. DOI: 10.1088/1748-0221/16/03/P03025. arXiv: 2010.12279 [astro-ph.IM].

[115] K. de Vries et al. "The Radar Echo Telescope for Neutrinos". In: *Proceedings of Science* ICRC2021 (2021), p. 1195. DOI: 10.22323/1.395.1195.

[116] M. G. Aartsen et al. "The IceCube Neutrino Observatory: instrumentation and online systems". In: *Journal of Instrumentation* 12.3 (2017), P03012. DOI: 10.1088/1748-0221/12/03/P03012. arXiv: 1612.05093 [astro-ph.IM].

[117] M. G. Aartsen et al. “Time-Integrated Neutrino Source Searches with 10 Years of IceCube Data”. In: 124.5, 051103 (2020), p. 051103. DOI: 10.1103/PhysRevLett.124.051103. arXiv: 1910.08488 [astro-ph.HE].

[118] M. G. Aartsen et al. “Energy reconstruction methods in the IceCube neutrino telescope”. In: *Journal of Instrumentation* 9.3, P03009 (2014), P03009. DOI: 10.1088/1748-0221/9/03/P03009. arXiv: 1311.4767 [physics.ins-det].

[119] M. G. Aartsen et al. “Search for Sources of Astrophysical Neutrinos Using Seven Years of IceCube Cascade Events”. In: *Astrophysical Journal* 886.1, 12 (2019), p. 12. DOI: 10.3847/1538-4357/ab4ae2. arXiv: 1907.06714 [astro-ph.HE].

[120] M. G. Aartsen et al. “Characterization of the atmospheric muon flux in IceCube”. In: *Astroparticle Physics* 78 (2016), pp. 1–27. DOI: 10.1016/j.astropartphys.2016.01.006. arXiv: 1506.07981 [astro-ph.HE].

[121] R. Naab, E. Ganster, and Z. Zhang. “Measurement of the astrophysical diffuse neutrino flux in a combined fit of IceCube’s high energy neutrino data”. In: *38th International Cosmic Ray Conference*. 2023. arXiv: 2308.00191 [astro-ph.HE].

[122] J. P. Kneller and G. C. McLaughlin. “Three flavor neutrino oscillations in matter: Flavor diagonal potentials, the adiabatic basis, and the CP phase”. In: *Physica Review D* 80.5, 053002 (2009), p. 053002. DOI: 10.1103/PhysRevD.80.053002. arXiv: 0904.3823 [hep-ph].

[123] E. Catano-Mur. “Recent results from NOvA”. In: *arXiv e-prints*, arXiv:2206.03542 (2022), arXiv:2206.03542. DOI: 10.48550/arXiv.2206.03542. arXiv: 2206.03542 [hep-ex].

[124] K. J. Kelly et al. “Back to (Mass-)Square(d) One: The Neutrino Mass Ordering in Light of Recent Data”. In: *arXiv e-prints*, arXiv:2007.08526 (2020), arXiv:2007.08526. DOI: 10.48550/arXiv.2007.08526. arXiv: 2007.08526 [hep-ph].

[125] I. Esteban et al. “The fate of hints: updated global analysis of three-flavor neutrino oscillations”. In: *Journal of High Energy Physics* 2020.9, 178 (2020), p. 178. DOI: 10.1007/JHEP09(2020)178. arXiv: 2007.14792 [hep-ph].

[126] The Katrin Collaboration et al. “Direct neutrino-mass measurement with sub-electronvolt sensitivity”. In: *Nature Physics* 18.2 (2022), pp. 160–166. DOI: 10.1038/s41567-021-01463-1. arXiv: 2105.08533 [hep-ex].

[127] Planck Collaboration et al. “Planck 2018 results. VI. Cosmological parameters”. In: *Astronomy & Astrophysics* 641, A6 (2020), A6. DOI: 10.1051/0004-6361/201833910. arXiv: 1807.06209 [astro-ph.CO].

[128] J. F. Beacom et al. “Measuring flavor ratios of high-energy astrophysical neutrinos”. In: *Physical Review D* 68.9, 093005 (2003), p. 093005. DOI: 10.1103/PhysRevD.68.093005. arXiv: hep-ph/0307025 [hep-ph].

[129] T. Kashti and E. Waxman. “Astrophysical Neutrinos: Flavor Ratios Depend on Energy”. In: *Physical Review Letters* 95.18, 181101 (2005), p. 181101. DOI: 10.1103/PhysRevLett.95.181101. arXiv: astro-ph/0507599 [astro-ph].

[130] L. A. Anchordoqui et al. “Galactic point sources of TeV antineutrinos”. In: *Physics Letters B* 593.1-4 (2004), pp. 42–47. DOI: 10.1016/j.physletb.2004.04.054. arXiv: astro-ph/0311002 [astro-ph].

[131] E. Waxman and J. Bahcall. "High Energy Neutrinos from Cosmological Gamma-Ray Burst Fireballs". In: *Physical Review Letters* 78 (12 1997), pp. 2292–2295. DOI: 10.1103/PhysRevLett.78.2292. URL: https://link.aps.org/doi/10.1103/PhysRevLett.78.2292.

[132] IceCube Collaboration et al. "Detection of astrophysical tau neutrino candidates in IceCube". In: *The European Physical Journal C* 82.11, 1031 (2022), p. 1031. DOI: 10.1140/epjc/s10052-022-10795-y. arXiv: 2011.03561 [hep-ex].

[133] R. Abbasi et al. "Observation of Seven Astrophysical Tau Neutrino Candidates with IceCube". In: *Physical Review Letters* 132.15, 151001 (2024), p. 151001. DOI: 10.1103/PhysRevLett.132.151001. arXiv: 2403.02516 [astro-ph.HE].

[134] M. G. IceCube Collaboration Aartsen et al. "Detection of a particle shower at the Glashow resonance with IceCube". In: *Nature* 591.7849 (2021), pp. 220–224. DOI: 10.1038/s41586-021-03256-1. arXiv: 2110.15051 [hep-ex].

[135] S. Aiello et al. "Observation of an ultra-high-energy cosmic neutrino with KM3NeT". In: *Nature* 638.8050 (2025). [Erratum: Nature 640, E3 (2025)], pp. 376–382. DOI: 10.1038/s41586-024-08543-1.

[136] KM3NeT Collaboration et al. "Characterising Candidate Blazar Counterparts of the Ultra-High-Energy Event KM3-230213A". In: *arXiv e-prints*, arXiv:2502.08484 (2025), arXiv:2502.08484. DOI: 10.48550/arXiv.2502.08484. arXiv: 2502.08484 [astro-ph.HE].

[137] O. Adriani et al. "On the Potential Cosmogenic Origin of the Ultra-high-energy Event KM3-230213A". In: *Astrophysical Journal Letters* 984.2, L41 (2025), p. L41. DOI: 10.3847/2041-8213/adcc29. arXiv: 2502.08508 [astro-ph.HE].

[138] O. Adriani et al. "On the Potential Galactic Origin of the Ultra-High-Energy Event KM3-230213A". In: *arXiv e-prints*, arXiv:2502.08387 (2025), arXiv:2502.08387. DOI: 10.48550/arXiv.2502.08387. arXiv: 2502.08387 [astro-ph.HE].

[139] M. Ackermann et al. "High-energy and ultra-high-energy neutrinos: A Snowmass white paper". In: *Journal of High Energy Astrophysics* 36 (2022), pp. 55–110. DOI: 10.1016/j.jheap.2022.08.001. arXiv: 2203.08096 [hep-ph].

[140] J. Bahcall and E. Waxman. "High energy astrophysical neutrinos: The upper bound is robust". In: *Physical Review D* 64.2, 023002 (2001), p. 023002. DOI: 10.1103/PhysRevD.64.023002. arXiv: hep-ph/9902383 [hep-ph].

[141] M. G. Aartsen et al. "The Contribution of Fermi-2LAC Blazars to Diffuse TeV-PeV Neutrino Flux". In: *Astrophysical Journal* 835.1, 45 (2017), p. 45. DOI: 10.3847/1538-4357/835/1/45. arXiv: 1611.03874 [astro-ph.HE].

[142] K. Bechtol et al. "Evidence against Star-forming Galaxies as the Dominant Source of Icecube Neutrinos". In: *Astrophysical Journal* 836.1, 47 (2017), p. 47. DOI: 10.3847/1538-4357/836/1/47. arXiv: 1511.00688 [astro-ph.HE].

[143] R. Abbasi et al. "Time-integrated Searches for Point-like Sources of Neutrinos with the 40-string IceCube Detector". In: *Astrophysical Journal* 732.1, 18 (2011), p. 18. DOI: 10.1088/0004-637X/732/1/18. arXiv: 1012.2137 [astro-ph.HE].

[144] C. Bellenghi. "The emergence of a new sky: First associations of IceCube high-energy neutrinos with Active Galactic Nuclei". PhD thesis. Munich Technical University, 2024.

[145] R. Abbasi et al. "Search for neutrino emission from hard X-ray AGN with IceCube". In: *arXiv e-prints*, arXiv:2406.06684 (2024), arXiv:2406.06684. DOI: 10.48550/arXiv.2406.06684. arXiv: 2406.06684 [astro-ph.HE].

[146] R. Abbasi et al. "Search for Astrophysical Neutrinos from 1FLE Blazars with IceCube". In: *Astrophysical Journal* 938.1, 38 (2022), p. 38. DOI: 10.3847/1538-4357/ac8de4. arXiv: 2207.04946 [astro-ph.HE].

[147] R. Abbasi et al. "Search for Correlations of High-energy Neutrinos Detected in IceCube with Radio-bright AGN and Gamma-Ray Emission from Blazars". In: *Astrophysical journal* 954.1, 75 (2023), p. 75. DOI: 10.3847/1538-4357/acdfcb. arXiv: 2304.12675 [astro-ph.HE].

[148] R. Abbasi et al. "Search for neutrino emission from cores of active galactic nuclei". In: *Physical Review D* 106.2, 022005 (2022), p. 022005. DOI: 10.1103/PhysRevD.106.022005. arXiv: 2111.10169 [astro-ph.HE].

[149] A. Loeb and E. Waxman. "The cumulative background of high energy neutrinos from starburst galaxies". In: *Journal of Cosmology and Astroparticle Physics* 2006.5, 003 (2006), p. 003. DOI: 10.1088/1475-7516/2006/05/003. arXiv: astro-ph/0601695 [astro-ph].

[150] R. Abbasi et al. "Search for High-energy Neutrinos from Ultraluminous Infrared Galaxies with IceCube". In: *Astrophysical Journal* 926.1, 59 (2022), p. 59. DOI: 10.3847/1538-4357/ac3cb6. arXiv: 2107.03149 [astro-ph.HE].

[151] R. Abbasi et al. "Search for Multi-flare Neutrino Emissions in 10 yr of IceCube Data from a Catalog of Sources". In: *Astrophysical Journal Letters* 920.2, L45 (2021), p. L45. DOI: 10.3847/2041-8213/ac2c7b. arXiv: 2109.05818 [astro-ph.HE].

[152] R. Abbasi et al. "Search for 10–1000 GeV Neutrinos from Gamma-Ray Bursts with IceCube". In: *Astrophysical Journal* 964.2, 126 (2024), p. 126. DOI: 10.3847/1538-4357/ad220b. arXiv: 2312.11515 [astro-ph.HE].

[153] R. Abbasi et al. "Searches for Neutrinos from Gamma-Ray Bursts Using the IceCube Neutrino Observatory". In: *Astrophysical Journal* 939.2, 116 (2022), p. 116. DOI: 10.3847/1538-4357/ac9785. arXiv: 2205.11410 [astro-ph.HE].

[154] R. Abbasi et al. "Limits on Neutrino Emission from GRB 221009A from MeV to PeV Using the IceCube Neutrino Observatory". In: *Astrophysical Journal Letters* 946.1, L26 (2023), p. L26. DOI: 10.3847/2041-8213/acc077. arXiv: 2302.05459 [astro-ph.HE].

[155] R. Stein et al. "A tidal disruption event coincident with a high-energy neutrino". In: *Nature Astronomy* 5 (2021), pp. 510–518. DOI: 10.1038/s41550-020-01295-8. arXiv: 2005.05340 [astro-ph.HE].

[156] S. Reusch et al. "Candidate Tidal Disruption Event AT2019fdr Coincident with a High-Energy Neutrino". In: *Physical Review Letters* 128.22, 221101 (2022), p. 221101. DOI: 10.1103/PhysRevLett.128.221101. arXiv: 2111.09390 [astro-ph.HE].

[157] S. van Velzen et al. "Establishing accretion flares from supermassive black holes as a source of high-energy neutrinos". In: *Monthly Notices of the Royal Astronomical Society* 529.3 (2024), pp. 2559–2576. DOI: 10.1093/mnras/stae610. arXiv: 2111.09391 [astro-ph.HE].

[158] J. Necker. "Search for High-Energy Neutrinos from TDE-like Flares with IceCube". In: *arXiv e-prints*, arXiv:2307.15531 (2023), arXiv:2307.15531. DOI: 10.48550/arXiv.2307.15531. arXiv: 2307.15531 [astro-ph.HE].

[159] M. G. Aartsen et al. "The IceCube realtime alert system". In: *Astroparticle Physics* 92 (2017), pp. 30–41. DOI: 10.1016/j.astropartphys.2017.05.002. arXiv: 1612.06028 [astro-ph.HE].

[160] E. Blaufuss et al. "The Next Generation of IceCube Real-time Neutrino Alerts". In: *Proceedings of Science* ICRC2019 (2020), p. 1021. DOI: 10.22323/1.358.1021. arXiv: 1908.04884 [astro-ph.HE].

[161] W. Luszczak. "TXS 0506+056 with Updated IceCube Data". In: *arXiv e-prints*, arXiv:2307.14559 (2023), arXiv:2307.14559. DOI: 10.48550/arXiv.2307.14559. arXiv: 2307.14559 [astro-ph.HE].

[162] J. F. Gallimore et al. "The Subarcsecond Radio Structure in NGC 1068. I. Observations and Results". In: *Astrophysical Journal* 458 (1996), p. 136. DOI: 10.1086/176798.

[163] S. García-Burillo et al. "ALMA images the many faces of the NGC 1068 torus and its surroundings". In: *Astronomy & Astrophysics* 632, A61 (2019), A61. DOI: 10.1051/0004-6361/201936606. arXiv: 1909.00675 [astro-ph.GA].

[164] S. García-Burillo et al. "Molecular line emission in NGC 1068 imaged with ALMA. I. An AGN-driven outflow in the dense molecular gas". In: *Astronomy & Astrophysics* 567, A125 (2014), A125. DOI: 10.1051/0004-6361/201423843. arXiv: 1405.7706 [astro-ph.GA].

[165] S. Abdollahi et al. "Fermi Large Area Telescope Fourth Source Catalog". In: *The Astrophysical Journal Supplement Series* 247.1, 33 (2020), p. 33. DOI: 10.3847/1538-4365/ab6bcb. arXiv: 1902.10045 [astro-ph.HE].

[166] C. Ricci et al. "A hard X-ray view of luminous and ultra-luminous infrared galaxies in GOALS - I. AGN obscuration along the merger sequence". In: *Monthly Notices of the Royal Astronomical Society* 506.4 (2021), pp. 5935–5950. DOI: 10.1093/mnras/stab2052. arXiv: 2107.10864 [astro-ph.GA].

[167] F. Rico-Villas et al. "Vibrationally excited HC_3N emission in NGC 1068: tracing the recent star formation in the starburst ring". In: *Monthly Notices of the Royal Astronomical Society* 502.2 (2021), pp. 3021–3034. DOI: 10.1093/mnras/stab197. arXiv: 2008.03693 [astro-ph.GA].

[168] K. Murase. "Hidden Hearts of Neutrino Active Galaxies". In: *Astrophysical Journal Letters* 941.1, L17 (2022), p. L17. DOI: 10.3847/2041-8213/aca53c. arXiv: 2211.04460 [astro-ph.HE].

[169] P. Padovani et al. "High-energy neutrinos from the vicinity of the supermassive black hole in NGC 1068". In: *Nature Astronomy* 8 (2024), pp. 1077–1087. DOI: 10.1038/s41550-024-02339-z. arXiv: 2405.20146 [astro-ph.HE].

[170] M. G. Aartsen et al. "Observation and Characterization of a Cosmic Muon Neutrino Flux from the Northern Hemisphere Using Six Years of IceCube Data". In: *Astrophysical Journal* 833.1, 3 (2016), p. 3. DOI: 10.3847/0004-637X/833/1/3. arXiv: 1607.08006 [astro-ph.HE].

[171] G. Neugebauer et al. “The Infrared Astronomical Satellite (IRAS) mission.” In: *Astrophysical Journal Letters* 278 (1984), pp. L1–L6. DOI: 10.1086/184209.

[172] S. G. Kleinmann et al. “The Properties and Environment of the Giant, Infrared-Luminous Galaxy IRAS 09104+4109”. In: *Astrophysical Journal* 328 (1988), p. 161. DOI: 10.1086/166276.

[173] M. Rowan-Robinson et al. “A high-redshift IRAS galaxy with huge luminosity—hidden quasar or protogalaxy?” In: *Nature* 351.6329 (1991), pp. 719–721. DOI: 10.1038/351719a0.

[174] S. Serjeant et al. “The K-band Hubble diagram of submillimetre galaxies and hyperluminous galaxies”. In: *Monthly Notices of the Royal Astronomical Society* 346.4 (2003), pp. L51–L56. DOI: 10.1111/j.1365-2966.2003.07305.x. arXiv: astro-ph/0310661 [astro-ph].

[175] M. W. Werner et al. “The Spitzer Space Telescope Mission”. In: *Astrophysical Journal Supplement* 154.1 (2004), pp. 1–9. DOI: 10.1086/422992. arXiv: astro-ph/0406223 [astro-ph].

[176] H. Murakami et al. “The Infrared Astronomical Mission AKARI*”. In: *Publications of the Astronomical Society of Japan* 59 (2007), S369–S376. DOI: 10.1093/pasj/59.sp2.S369. arXiv: 0708.1796 [astro-ph].

[177] G. L. Pilbratt et al. “Herschel Space Observatory. An ESA facility for far-infrared and submillimetre astronomy”. In: *Astronomy & Astrophysics* 518, L1 (2010), p. L1. DOI: 10.1051/0004-6361/201014759. arXiv: 1005.5331 [astro-ph.IM].

[178] E. L. Wright et al. “The Wide-field Infrared Survey Explorer (WISE): Mission Description and Initial On-orbit Performance”. In: *Astronomical Journal* 140.6 (2010), pp. 1868–1881. DOI: 10.1088/0004-6256/140/6/1868. arXiv: 1008.0031 [astro-ph.IM].

[179] B. Magnelli et al. “Evolution of the dusty infrared luminosity function from z = 0 to z = 2.3 using observations from Spitzer”. In: *Astronomy & Astrophysics* 528, A35 (2011), A35. DOI: 10.1051/0004-6361/200913941. arXiv: 1101.2467 [astro-ph.CO].

[180] C.-W. Tsai et al. “The Most Luminous Galaxies Discovered by WISE”. In: *Astrophysical Journal* 805.2, 90 (2015), p. 90. DOI: 10.1088/0004-637X/805/2/90. arXiv: 1410.1751 [astro-ph.GA].

[181] J. P. Gardner et al. “The James Webb Space Telescope”. In: *Space Science Reviews* 123.4 (2006), pp. 485–606. DOI: 10.1007/s11214-006-8315-7. arXiv: astro-ph/0606175 [astro-ph].

[182] J. L. Wang et al. “Luminous Infrared Galaxies in the Local Universe”. In: *Astrophysical Journal* 649.2 (2006), pp. 722–729. DOI: 10.1086/506902. arXiv: astro-ph/0603574 [astro-ph].

[183] A. Alonso-Herrero et al. “Near-Infrared and Star-forming properties of Local Luminous Infrared Galaxies”. In: *Astrophysical Journal* 650 (2006), pp. 835–849. DOI: 10.1086/506958. arXiv: astro-ph/0606186.

[184] S. Stierwalt et al. “Mid-infrared Properties of Nearby Luminous Infrared Galaxies. I. Spitzer Infrared Spectrograph Spectra for the GOALS Sample”. In: *Astrophysical Journal Supplement* 206.1, 1 (2013), p. 1. DOI: 10.1088/0067-0049/206/1/1. arXiv: 1302.4477 [astro-ph.CO].

[185] C.-L. Hung et al. "A Comparison of the Morphological Properties between Local and z ∼1 Infrared Luminous Galaxies: Are Local and High-z (U)LIRGs Different?" In: *Astrophysical Journal* 791.1, 63 (2014), p. 63. DOI: 10.1088/0004-637X/791/1/63. arXiv: 1406.4509 [astro-ph.GA].

[186] D. B. Sanders et al. "Ultraluminous Infrared Galaxies and the Origin of Quasars". In: *Astrophysical Journal* 325 (1988), p. 74. DOI: 10.1086/165983.

[187] A. Toomre and J. Toomre. "Galactic Bridges and Tails". In: *Astrophysical Journal* 178 (1972), pp. 623–666. DOI: 10.1086/151823.

[188] A. Toomre. "Theories of spiral structure." In: *Annual Review of Astronomy and Astrophysics* 15 (1977), pp. 437–478. DOI: 10.1146/annurev.aa.15.090177.002253.

[189] J. Melbourne, D. C. Koo, and E. Le Floc'h. "Optical Morphology Evolution of Infrared Luminous Galaxies in GOODS-N". In: *Astrophysical Journal Letters* 632.2 (2005), pp. L65–L68. DOI: 10.1086/498019. arXiv: astro-ph/0509037 [astro-ph].

[190] P. F. Hopkins et al. "Mergers, active galactic nuclei and 'normal' galaxies: contributions to the distribution of star formation rates and infrared luminosity functions". In: *Monthly Notices of the Royal Astronomical Society* 402.3 (2010), pp. 1693–1713. DOI: 10.1111/j.1365-2966.2009.15990.x. arXiv: 0911.1131 [astro-ph.CO].

[191] M. T. Sargent et al. "The Contribution of Starbursts and Normal Galaxies to Infrared Luminosity Functions at z < 2". In: *Astrophysical Journal Letters* 747.2, L31 (2012), p. L31. DOI: 10.1088/2041-8205/747/2/L31. arXiv: 1202.0290 [astro-ph.CO].

[192] J. E. Barnes and L. Hernquist. "Transformations of Galaxies. II. Gasdynamics in Merging Disk Galaxies". In: *Astrophysical Journal* 471 (1996), p. 115. DOI: 10.1086/177957.

[193] J. C. Mihos and L. Hernquist. "Gasdynamics and Starbursts in Major Mergers". In: *Astrophysical Journal* 464 (1996), p. 641. DOI: 10.1086/177353. arXiv: astro-ph/9512099 [astro-ph].

[194] E. J. Murphy et al. "Calibrating Extinction-free Star Formation Rate Diagnostics with 33 GHz Free-free Emission in NGC 6946". In: *Astrophysical Journal* 737.2, 67 (2011), p. 67. DOI: 10.1088/0004-637X/737/2/67. arXiv: 1105.4877 [astro-ph.CO].

[195] J. H. Howell et al. "The Great Observatories All-sky LIRG Survey: Comparison of Ultraviolet and Far-infrared Properties". In: *Astrophysical Journal* 715.1 (2010), pp. 572–588. DOI: 10.1088/0004-637X/715/1/572. arXiv: 1004.0985 [astro-ph.GA].

[196] E. J. Murphy et al. "The Star Formation in Radio Survey: GBT 33 GHz Observations of Nearby Galaxy Nuclei and Extranuclear Star-forming Regions". In: *Astrophysical Journal* 761.2, 97 (2012), p. 97. DOI: 10.1088/0004-637X/761/2/97. arXiv: 1210.3360 [astro-ph.CO].

[197] A. M. Hopkins. "The Dawes Review 8: Measuring the Stellar Initial Mass Function". In: *Publications of the Astronomical Society of Australia* 35, e039 (2018), e039. DOI: 10.1017/pasa.2018.29. arXiv: 1807.09949 [astro-ph.GA].

[198] A. Burrows and D. Vartanyan. "Core-collapse supernova explosion theory". In: *Nature* 589.7840 (2021), pp. 29–39. DOI: 10.1038/s41586-020-03059-w. arXiv: 2009.14157 [astro-ph.SR].

[199] J. K. Truelove and C. F. McKee. "Evolution of Nonradiative Supernova Remnants". In: *Astrophysical Journal Supplement* 120.2 (1999), pp. 299–326. DOI: 10.1086/313176.

[200] E. Varenius et al. "The population of SNe/SNRs in the starburst galaxy Arp 220. A self-consistent analysis of 20 years of VLBI monitoring". In: *Astronomy & Astrophysics* 623, A173 (2019), A173. DOI: 10.1051/0004-6361/201730631. arXiv: 1702.04772 [astro-ph.GA].

[201] M. Bondi et al. "The nuclear starburst in Arp 299-A: from the 5.0 GHz VLBI radio light-curves to its core-collapse supernova rate". In: *Astronomy & Astrophysics* 539, A134 (2012), A134. DOI: 10.1051/0004-6361/201118446. arXiv: 1201.3220 [astro-ph.CO].

[202] K. Iwamoto et al. "A hypernova model for the supernova associated with the γ-ray burst of 25 April 1998". In: *Nature* 395.6703 (1998), pp. 672–674. DOI: 10.1038/27155. arXiv: astro-ph/9806382 [astro-ph].

[203] S. Mattila et al. "A dust-enshrouded tidal disruption event with a resolved radio jet in a galaxy merger". In: *Science* 361.6401 (2018), pp. 482–485. DOI: 10.1126/science.aao4669. arXiv: 1806.05717 [astro-ph.GA].

[204] C. Tadhunter et al. "A tidal disruption event in the nearby ultra-luminous infrared galaxy F01004-2237". In: *Nature Astronomy* 1, 0061 (2017), p. 0061. DOI: 10.1038/s41550-017-0061. arXiv: 1702.02573 [astro-ph.GA].

[205] F. K. Liu and X. Chen. "Enhanced Off-center Stellar Tidal Disruptions by Supermassive Black Holes in Merging Galaxies". In: *Astrophysical Journal* 767.1, 18 (2013), p. 18. DOI: 10.1088/0004-637X/767/1/18. arXiv: 1302.4437 [astro-ph.CO].

[206] N. Stone and A. Loeb. "Prompt tidal disruption of stars as an electromagnetic signature of supermassive black hole coalescence". In: *Monthly Notices of the Royal Astronomical Society* 412.1 (2011), pp. 75–80. DOI: 10.1111/j.1365-2966.2010.17880.x. arXiv: 1004.4833 [astro-ph.CO].

[207] V. U. "The Role of AGN in Luminous Infrared Galaxies from the Multiwavelength Perspective". In: *Universe* 8.8, 392 (2022), p. 392. DOI: 10.3390/universe8080392. arXiv: 2207.13690 [astro-ph.GA].

[208] A. O. Petric et al. "Mid-Infrared Spectral Diagnostics of Luminous Infrared Galaxies". In: *Astrophysical Journal* 730.1, 28 (2011), p. 28. DOI: 10.1088/0004-637X/730/1/28. arXiv: 1012.1891 [astro-ph.GA].

[209] D. Farrah et al. "High-Resolution Mid-Infrared Spectroscopy of Ultraluminous Infrared Galaxies". In: *Astrophysical Journal* 667.1 (2007), pp. 149–169. DOI: 10.1086/520834. arXiv: 0706.0513 [astro-ph].

[210] T. Díaz-Santos et al. "The Spatial Extent of (U)LIRGs in the Mid-infrared. I. The Continuum Emission". In: *Astrophysical Journal* 723.2 (2010), pp. 993–1005. DOI: 10.1088/0004-637X/723/2/993. arXiv: 1009.0038 [astro-ph.CO].

[211] S. Veilleux et al. "Spitzer Quasar and Ulirg Evolution Study (QUEST). IV. Comparison of 1 Jy Ultraluminous Infrared Galaxies with Palomar-Green Quasars". In: *Astrophysical Journal Supplement* 182.2 (2009), pp. 628–666. DOI: 10.1088/0067-0049/182/2/628. arXiv: 0905.1577 [astro-ph.CO].

[212] A. Alonso-Herrero et al. "Local Luminous Infrared Galaxies. II. Active Galactic Nucleus Activity from Spitzer/Infrared Spectrograph Spectra". In: *Astrophysical Journal* 744.1, 2 (2012), p. 2. DOI: 10.1088/0004-637X/744/1/2. arXiv: 1109.1372 [astro-ph.CO].

[213] T. Kawaguchi, N. Yutani, and K. Wada. "Mass Accretion toward Black Holes in the Final Phase of Galaxy Mergers". In: *Astrophysical Journal* 890.2, 125 (2020), p. 125. DOI: 10.3847/1538-4357/ab655a. arXiv: 1912.10621 [astro-ph.GA].

[214] National Radio Astronomy Observatory (NRAO). *A Unified AGN Model*. Online, accessed 13 May 2025, URL: https://public.nrao.edu/gallery/a-unified-agn-model/.

[215] S. Aalto et al. "Probing highly obscured, self-absorbed galaxy nuclei with vibrationally excited HCN". In: *Astronomy & Astrophysics* 584, A42 (2015), A42. DOI: 10.1051/0004-6361/201526410. arXiv: 1504.06824 [astro-ph.GA].

[216] S. Aalto et al. "The hidden heart of the luminous infrared galaxy IC 860. I. A molecular inflow feeding opaque, extreme nuclear activity". In: *Astronomy & Astrophysics* 627, A147 (2019), A147. DOI: 10.1051/0004-6361/201935480. arXiv: 1905.07275 [astro-ph.GA].

[217] L. Barcos-Muñoz et al. "High-resolution Radio Continuum Measurements of the Nuclear Disks of Arp 220". In: *Astrophysical Journal* 799.1, 10 (2015), p. 10. DOI: 10.1088/0004-637X/799/1/10. arXiv: 1411.0932 [astro-ph.GA].

[218] K. Sakamoto et al. "Deeply Buried Nuclei in the Infrared-luminous Galaxies NGC 4418 and Arp 220. I. ALMA Observations at λ = 1.4-0.4 mm and Continuum Analysis". In: *Astrophysical Journal* 923.2, 206 (2021), p. 206. DOI: 10.3847/1538-4357/ac2746. arXiv: 2109.06695 [astro-ph.GA].

[219] N. Falstad et al. "CON-quest. Searching for the most obscured galaxy nuclei". In: *Astronomy & Astrophysics* 649, A105 (2021), A105. DOI: 10.1051/0004-6361/202039291. arXiv: 2102.13563 [astro-ph.GA].

[220] M. A. Johnstone et al. "Searching for Compact Obscured Nuclei in Compton Thick AGN". In: *arXiv e-prints*, arXiv:2504.15248 (2025), arXiv:2504.15248. DOI: 10.48550/arXiv.2504.15248. arXiv: 2504.15248 [astro-ph.GA].

[221] B. T. Soifer et al. "The IRAS Bright Galaxy Sample. II. The Sample and Luminosity Function". In: *Astrophysical Journal* 320 (1987), p. 238. DOI: 10.1086/165536.

[222] E. Le Floc'h et al. "Infrared Luminosity Functions from the Chandra Deep Field-South: The Spitzer View on the History of Dusty Star Formation at 0 < z < 1". In: *Astrophysical Journal* 632.1 (2005), pp. 169–190. DOI: 10.1086/432789. arXiv: astro-ph/0506462 [astro-ph].

[223] B. Magnelli et al. "The 0.4<z<1.3 star formation history of the Universe as viewed in the far-infrared". In: *Astronomy & Astrophysics* 496.1 (2009), pp. 57–75. DOI: 10.1051/0004-6361:200811443. arXiv: 0901.1543 [astro-ph.CO].

[224] J. A. Zavala et al. "The Evolution of the IR Luminosity Function and Dust-obscured Star Formation over the Past 13 Billion Years". In: *Astrophysical Journal* 909.2, 165 (2021), p. 165. DOI: 10.3847/1538-4357/abdb27. arXiv: 2101.04734 [astro-ph.GA].

[225] A. M. Hopkins and J. F. Beacom. "On the Normalization of the Cosmic Star Formation History". In: *Astrophysical Journal* 651.1 (2006), pp. 142–154. DOI: 10.1086/506610. arXiv: astro-ph/0601463 [astro-ph].

[226] H. Yüksel et al. "Revealing the High-Redshift Star Formation Rate with Gamma-Ray Bursts". In: *Astrophysical Journal Letters* 683.1 (2008), p. L5. DOI: 10.1086/591449. arXiv: 0804.4008 [astro-ph].

[227] M. Vereecken and K. D. de Vries. "Obscured pp-channel neutrino sources". In: *arXiv e-prints*, arXiv:2004.03435 (2020), arXiv:2004.03435. arXiv: 2004.03435 [astro-ph.HE].

[228] L. L. Cowie et al. "The Evolution of the Ultraluminous Infrared Galaxy Population from Redshift 0 to 1.5". In: *Astrophysical Journal Letters* 603.2 (2004), pp. L69–L72. DOI: 10.1086/383198. arXiv: astro-ph/0402235 [astro-ph].

[229] T. A. Thompson et al. "Magnetic Fields in Starburst Galaxies and the Origin of the FIR-Radio Correlation". In: *Astrophysical Journal* 645.1 (2006), pp. 186–198. DOI: 10.1086/504035. arXiv: astro-ph/0601626 [astro-ph].

[230] D. Downes and P. M. Solomon. "Rotating Nuclear Rings and Extreme Starbursts in Ultraluminous Galaxies". In: *Astrophysical Journal* 507.2 (1998), pp. 615–654. DOI: 10.1086/306339. arXiv: astro-ph/9806377 [astro-ph].

[231] K. Murase and F. W. Stecker. "High-Energy Neutrinos from Active Galactic Nuclei". In: *The Encyclopedia of Cosmology. Set 2: Frontiers in Cosmology. Volume 2: Neutrino Physics and Astrophysics*. Ed. by F. W. Stecker. 2023, pp. 483–540. DOI: 10.1142/9789811282645_0010.

[232] H.-N. He et al. "Diffuse PeV neutrino emission from ultraluminous infrared galaxies". In: *Physical Review D* 87.6, 063011 (2013), p. 063011. DOI: 10.1103/PhysRevD.87.063011. arXiv: 1303.1253 [astro-ph.HE].

[233] A. Palladino et al. "IceCube neutrinos from hadronically powered gamma-ray galaxies". In: *Journal of Cosmology and Astroparticle Physics* 2019.9, 004 (2019), p. 004. DOI: 10.1088/1475-7516/2019/09/004. arXiv: 1812.04685 [astro-ph.HE].

[234] T. Díaz-Santos et al. "A Herschel/PACS Far-infrared Line Emission Survey of Local Luminous Infrared Galaxies". In: *Astrophysical Journal* 846.1, 32 (2017), p. 32. DOI: 10.3847/1538-4357/aa81d7. arXiv: 1705.04326 [astro-ph.GA].

[235] D. B. Sanders et al. "The IRAS Revised Bright Galaxy Sample". In: *Astronomical Journal* 126.4 (2003), pp. 1607–1664. DOI: 10.1086/376841. arXiv: astro-ph/0306263 [astro-ph].

[236] S. Stierwalt et al. "Mid-infrared Properties of Luminous Infrared Galaxies. II. Probing the Dust and Gas Physics of the GOALS Sample". In: *Astrophysical Journal* 790.2, 124 (2014), p. 124. DOI: 10.1088/0004-637X/790/2/124. arXiv: 1406.3891 [astro-ph.GA].

[237] H. Inami et al. "Mid-infrared Atomic Fine-structure Emission-line Spectra of Luminous Infrared Galaxies: Spitzer/IRS Spectra of the GOALS Sample". In: *Astrophysical Journal* 777.2, 156 (2013), p. 156. DOI: 10.1088/0004-637X/777/2/156. arXiv: 1309.4788 [astro-ph.CO].

[238] T. Díaz-Santos et al. "Explaining the [C II]157.7 μm Deficit in Luminous Infrared Galaxies—First Results from a Herschel/PACS Study of the GOALS Sample". In: *Astrophysical Journal* 774.1, 68 (2013), p. 68. DOI: 10.1088/0004-637X/774/1/68. arXiv: 1307.2635 [astro-ph.CO].

[239] T. Díaz-Santos et al. "Extended [C II] Emission in Local Luminous Infrared Galaxies". In: *Astrophysical Journal Letters* 788.1, L17 (2014), p. L17. DOI: 10.1088/2041-8205/788/1/L17. arXiv: 1405.3983 [astro-ph.GA].

[240] Y. Zhao et al. "A Herschel Survey of the [N II] 205 μm Line in Local Luminous Infrared Galaxies: The [N II] 205 μm Emission as a Star Formation Rate Indicator". In: *Astrophysical Journal Letters* 765.1, L13 (2013), p. L13. DOI: 10.1088/2041-8205/765/1/L13. arXiv: 1301.7318 [astro-ph.CO].

[241] N. Lu et al. "Warm Molecular Gas in Luminous Infrared Galaxies". In: *Astrophysical Journal Letters* 787.2, L23 (2014), p. L23. DOI: 10.1088/2041-8205/787/2/L23. arXiv: 1405.0313 [astro-ph.GA].

[242] N. Lu et al. "Measuring Star Formation Rate and Far-infrared Color in High-redshift Galaxies Using the CO(7-6) and [N II] 205 μm Lines". In: *Astrophysical Journal Letters* 802.1, L11 (2015), p. L11. DOI: 10.1088/2041-8205/802/1/L11. arXiv: 1503.02052 [astro-ph.GA].

[243] Y. Zhao et al. "The [NII] 205 μm Emission in Local Luminous Infrared Galaxies". In: *Astrophysical Journal* 819.1, 69 (2016), p. 69. DOI: 10.3847/0004-637X/819/1/69. arXiv: 1601.01404 [astro-ph.GA].

[244] J. K. Chu et al. "The Great Observatories All-Sky LIRG Survey: Herschel Image Atlas and Aperture Photometry". In: *Astrophysical Journal Supplement* 229.2, 25 (2017), p. 25. DOI: 10.3847/1538-4365/aa5d15. arXiv: 1702.01756 [astro-ph.GA].

[245] S. Haan et al. "The Nuclear Structure in Nearby Luminous Infrared Galaxies: Hubble Space Telescope NICMOS Imaging of the GOALS Sample". In: *Astronomical Journal* 141.3, 100 (2011), p. 100. DOI: 10.1088/0004-6256/141/3/100. arXiv: 1012.4012 [astro-ph.CO].

[246] D. .-. Kim et al. "Hubble Space Telescope ACS Imaging of the GOALS Sample: Quantitative Structural Properties of Nearby Luminous Infrared Galaxies with L $_{IR} > 10^{11.4}$ L $_{\odot}$". In: *Astrophysical Journal* 768.2, 102 (2013), p. 102. DOI: 10.1088/0004-637X/768/2/102. arXiv: 1303.3977 [astro-ph.CO].

[247] D. C. Martin et al. "The Galaxy Evolution Explorer: A Space Ultraviolet Survey Mission". In: *Astrophysical Journal Letters* 619.1 (2005), pp. L1–L6. DOI: 10.1086/426387. arXiv: astro-ph/0411302 [astro-ph].

[248] K. Iwasawa et al. "C-GOALS: Chandra observations of a complete sample of luminous infrared galaxies from the IRAS Revised Bright Galaxy Survey". In: *Astronomy & Astrophysics* 529, A106 (2011), A106. DOI: 10.1051/0004-6361/201015264. arXiv: 1103.2755 [astro-ph.CO].

[249] N. Torres-Albà et al. "C-GOALS. II. Chandra observations of the lower luminosity sample of nearby luminous infrared galaxies in GOALS". In: *Astronomy & Astrophysics* 620, A140 (2018), A140. DOI: 10.1051/0004-6361/201834105. arXiv: 1810.02371 [astro-ph.GA].

[250] H. Inami et al. "GOALS-JWST: Unveiling Dusty Compact Sources in the Merging Galaxy IIZw096". In: *Astrophysical Journal Letters* 940.1, L6 (2022), p. L6. DOI: 10.3847/2041-8213/ac9389. arXiv: 2208.10647 [astro-ph.GA].

[251] A. S. Evans et al. "GOALS-JWST: Hidden Star Formation and Extended PAH Emission in the Luminous Infrared Galaxy VV 114". In: *Astrophysical Journal Letters* 940.1, L8 (2022), p. L8. DOI: 10.3847/2041-8213/ac9971. arXiv: 2208.14507 [astro-ph.GA].

[252] V. U et al. “GOALS-JWST: Resolving the Circumnuclear Gas Dynamics in NGC 7469 in the Mid-infrared”. In: *Astrophysical Journal Letters* 940.1, L5 (2022), p. L5. DOI: 10.3847/2041-8213/ac961c. arXiv: 2209.01210 [astro-ph.GA].

[253] T. Bohn et al. “GOALS-JWST: NIRCam and MIRI Imaging of the Circumnuclear Starburst Ring in NGC 7469”. In: *Astrophysical Journal Letters* 942.2, L36 (2023), p. L36. DOI: 10.3847/2041-8213/acab61. arXiv: 2209.04466 [astro-ph.GA].

[254] L. Armus et al. “GOALS-JWST: Mid-infrared Spectroscopy of the Nucleus of NGC 7469”. In: *Astrophysical Journal Letters* 942.2, L37 (2023), p. L37. DOI: 10.3847/2041-8213/acac66. arXiv: 2209.13125 [astro-ph.GA].

[255] T. S. .-. Lai et al. “GOALS-JWST: Tracing AGN Feedback on the Star-forming Interstellar Medium in NGC 7469”. In: *Astrophysical Journal Letters* 941.2, L36 (2022), p. L36. DOI: 10.3847/2041-8213/ac9ebf. arXiv: 2209.06741 [astro-ph.GA].

[256] S. T. Linden et al. “GOALS-JWST: Revealing the Buried Star Clusters in the Luminous Infrared Galaxy VV 114”. In: *Astrophysical Journal Letters* 944.2, L55 (2023), p. L55. DOI: 10.3847/2041-8213/acb335. arXiv: 2210.05763 [astro-ph.GA].

[257] J. Rich et al. “GOALS-JWST: Pulling Back the Curtain on the AGN and Star Formation in VV 114”. In: *Astrophysical Journal Letters* 944.2, L50 (2023), p. L50. DOI: 10.3847/2041-8213/acb2b8. arXiv: 2301.02338 [astro-ph.GA].

[258] T. S. .-. Lai et al. “GOALS-JWST: Small Neutral Grains and Enhanced 3.3 μm PAH Emission in the Seyfert Galaxy NGC 7469”. In: *Astrophysical Journal Letters* 957.2, L26 (2023), p. L26. DOI: 10.3847/2041-8213/ad0387. arXiv: 2307.15169 [astro-ph.GA].

[259] M. Bianchin et al. “GOALS-JWST: Gas Dynamics and Excitation in NGC 7469 Revealed by NIRSpec”. In: *Astrophysical Journal* 965.2, 103 (2024), p. 103. DOI: 10.3847/1538-4357/ad2a50. arXiv: 2308.00209 [astro-ph.GA].

[260] A. R. Thompson et al. “The Very Large Array.” In: *Astrophysical Journal Supplement* 44 (1980), pp. 151–167. DOI: 10.1086/190688.

[261] A. Wootten and A. R. Thompson. “The Atacama Large Millimeter/Submillimeter Array”. In: *Proceedings of the IEEE* 97.8 (2009), pp. 1463–1471. DOI: 10.1109/JPROC.2009.2020572.

[262] A. M. Medling et al. “Stellar and Gaseous Nuclear Disks Observed in Nearby (U)LIRGs”. In: *Astrophysical Journal* 784.1, 70 (2014), p. 70. DOI: 10.1088/0004-637X/784/1/70. arXiv: 1401.7338 [astro-ph.GA].

[263] A. M. Medling et al. “Following Black Hole Scaling Relations through Gas-rich Mergers”. In: *Astrophysical Journal* 803.2, 61 (2015), p. 61. DOI: 10.1088/0004-637X/803/2/61. arXiv: 1502.06617 [astro-ph.GA].

[264] V. U et al. “Keck OSIRIS AO LIRG Analysis (KOALA): Feedback in the Nuclei of Luminous Infrared Galaxies”. In: *Astrophysical Journal* 871.2, 166 (2019), p. 166. DOI: 10.3847/1538-4357/aaf1c2.

[265] *Infrared Astronomical Satellite (IRAS) Catalogs and Atlases.Volume 1: Explanatory Supplement*. Vol. 1. 1988.

[266] V. U et al. “Spectral Energy Distributions of Local Luminous and Ultraluminous Infrared Galaxies”. In: *Astrophysical Journal Supplement Series* 203.1, 9 (2012), p. 9. DOI: 10.1088/0067-0049/203/1/9. arXiv: 1209.1611 [astro-ph.CO].

[267] T. Kintscher. “Rapid Response to Extraordinary Events: Transient Neutrino Sources with the IceCube Experiment”. PhD thesis. Humboldt-Universität zu Berlin, Mathematisch-Naturwissenschaftliche Fakultät, 2020. DOI: http://dx.doi.org/10.18452/21948.

[268] M. Imanishi et al. “ALMA Sub-arcsecond-resolution 183 GHz H_2O and Dense Molecular Line Observations of Nearby Ultraluminous Infrared Galaxies”. In: *Astrophysical Journal* 926.2, 159 (2022), p. 159. DOI: 10.3847/1538-4357/ac3a68. arXiv: 2111.09338 [astro-ph.GA].

[269] R. Stein et al. “A tidal disruption event coincident with a high-energy neutrino”. In: *Nature Astronomy* 5 (2021), pp. 510–518. DOI: 10.1038/s41550-020-01295-8. arXiv: 2005.05340 [astro-ph.HE].

[270] E. Peretti et al. “Cosmic ray transport and radiative processes in nuclei of starburst galaxies”. In: *Monthly Notices of the Royal Astronomical Society* 487.1 (2019), pp. 168–180. DOI: 10.1093/mnras/stz1161. arXiv: 1812.01996 [astro-ph.HE].

[271] D. Xiao et al. “Revisiting the Contributions of Supernova and Hypernova Remnants to the Diffuse High-Energy Backgrounds: Constraints on Very High Redshift Injection”. In: *Astrophysical Journal* 826.2, 133 (2016), p. 133. DOI: 10.3847/0004-637X/826/2/133. arXiv: 1604.08131 [astro-ph.HE].

[272] N. Senno et al. “Extragalactic Star-forming Galaxies with Hypernovae and Supernovae as High-energy Neutrino and Gamma-ray Sources: the case of the 10 TeV Neutrino data”. In: *Astrophysical Journal* 806.1, 24 (2015), p. 24. DOI: 10.1088/0004-637X/806/1/24. arXiv: 1501.04934 [astro-ph.HE].

[273] I. Tamborra, S. Ando, and K. Murase. “Star-forming galaxies as the origin of diffuse high-energy backgrounds: gamma-ray and neutrino connections, and implications for starburst history”. In: *Journal of Cosmology and Astroparticle Physics* 2014.9 (2014), pp. 043–043. DOI: 10.1088/1475-7516/2014/09/043. arXiv: 1404.1189 [astro-ph.HE].

[274] A. Ambrosone et al. “Could Nearby Star-forming Galaxies Light Up the Point-like Neutrino Sky?” In: *Astrophysical Journal Letters* 919.2, L32 (2021), p. L32. DOI: 10.3847/2041-8213/ac25ff. arXiv: 2106.13248 [astro-ph.HE].

[275] A. Ambrosone et al. “Starburst galaxies strike back: a multi-messenger analysis with Fermi-LAT and IceCube data”. In: *Monthly Notices of the Royal Astronomical Society* 503.3 (2021), pp. 4032–4049. DOI: 10.1093/mnras/stab659. arXiv: 2011.02483 [astro-ph.HE].

[276] E. Kankare et al. “Discovery of Two Supernovae in the Nuclear Regions of the Luminous Infrared Galaxy IC 883”. In: *Astrophysical Journal Letters* 744.2, L19 (2012), p. L19. DOI: 10.1088/2041-8205/744/2/L19. arXiv: 1112.0777 [astro-ph.SR].

[277] C. Leitherer et al. “Starburst99: Synthesis Models for Galaxies with Active Star Formation”. In: *Astrophysical Journal Supplement* 123.1 (1999), pp. 3–40. DOI: 10.1086/313233. arXiv: astro-ph/9902334 [astro-ph].

[278] G. A. Vázquez and C. Leitherer. "Optimization of Starburst99 for Intermediate-Age and Old Stellar Populations". In: *Astrophysical Journal* 621.2 (2005), pp. 695–717. DOI: 10.1086/427866. arXiv: astro-ph/0412491 [astro-ph].

[279] C. Leitherer et al. "A Library of Theoretical Ultraviolet Spectra of Massive, Hot Stars for Evolutionary Synthesis". In: *Astrophysical Journal Supplement* 189.2 (2010), pp. 309–335. DOI: 10.1088/0067-0049/189/2/309. arXiv: 1006.5624 [astro-ph.SR].

[280] C. Leitherer et al. "The Effects of Stellar Rotation. II. A Comprehensive Set of Starburst99 Models". In: *Astrophysical Journal Supplement Series* 212.1, 14 (2014), p. 14. DOI: 10.1088/0067-0049/212/1/14. arXiv: 1403.5444 [astro-ph.GA].

[281] E. E. Salpeter. "The Luminosity Function and Stellar Evolution." In: *Astrophysical Journal* 121 (1955), p. 161. DOI: 10.1086/145971.

[282] P. Kroupa. "On the variation of the initial mass function". In: *Monthly Notices of the Royal Astronomical Society* 322.2 (2001), pp. 231–246. DOI: 10.1046/j.1365-8711.2001.04022.x. arXiv: astro-ph/0009005 [astro-ph].

[283] P. Papadopoulos et al. "Extreme cosmic ray dominated regions: a new paradigm for high star formation density events in the Universe". In: *Monthly Notices of the Royal Astronomical Society* 414.2 (2011), pp. 1705–1714. DOI: 10.1111/j.1365-2966.2011.18504.x. arXiv: 1009.2496 [astro-ph.CO].

[284] K. Sliwa et al. "Extreme CO Isotopic Abundances in the ULIRG IRAS 13120-5453: An Extremely Young Starburst or Top-heavy Initial Mass Function". In: *Astrophysical Journal Letters* 840.2, L11 (2017), p. L11. DOI: 10.3847/2041-8213/aa6ea4. arXiv: 1704.06671 [astro-ph.GA].

[285] T. Brown and C. D. Wilson. "Extreme CO Isotopologue Line Ratios in ULIRGS: Evidence for a Top-heavy IMF". In: *Astrophysical Journal* 879.1, 17 (2019), p. 17. DOI: 10.3847/1538-4357/ab2246. arXiv: 1905.06950 [astro-ph.GA].

[286] Z.-Y. Zhang et al. "Stellar populations dominated by massive stars in dusty starburst galaxies across cosmic time". In: *Nature* 558.7709 (2018), pp. 260–263. DOI: 10.1038/s41586-018-0196-x. arXiv: 1806.01280 [astro-ph.GA].

[287] R.-R. Chary. "The Stellar Initial Mass Function at the Epoch of Reionization". In: *Astrophysical Journal* 680.1 (2008), pp. 32–40. DOI: 10.1086/587737. arXiv: 0712.1498 [astro-ph].

[288] Y. Song et al. "A Comparison between Nuclear Ring Star Formation in LIRGs and in Normal Galaxies with the Very Large Array". In: *Astrophysical Journal* 916.2, 73 (2021), p. 73. DOI: 10.3847/1538-4357/ac05c2. arXiv: 2107.00412 [astro-ph.GA].

[289] L. Mayer, S. Kazantzidis, and A. Escala. "Formation of Nuclear Disks and Supermassive Black Hole Binaries in Galaxy Mergers". In: *Memorie della Società Astronomica Italiana* 79 (2008), p. 1284. arXiv: 0807.3329 [astro-ph].

[290] D. Caprioli. "Understanding hadronic gamma-ray emission from supernova remnants". In: *Journal of Cosmology and Astroparticle Physics* 2011.5, 026 (2011), p. 026. DOI: 10.1088/1475-7516/2011/05/026. arXiv: 1103.2624 [astro-ph.HE].

[291] P. Blasi. "The origin of galactic cosmic rays". In: *Astronomy and Astrophysics Review* 21, 70 (2013), p. 70. DOI: 10.1007/s00159-013-0070-7. arXiv: 1311.7346 [astro-ph.HE].

[292] R. A. Chevalier and A. W. Clegg. "Wind from a starburst galaxy nucleus". In: *Nature* 317.6032 (1985), pp. 44–45. DOI: 10.1038/317044a0.

[293] E. Peretti et al. "Particle acceleration and multimessenger emission from starburst-driven galactic winds". In: *Monthly Notices of the Royal Astronomical Society* 511.1 (2022), pp. 1336–1348. DOI: 10.1093/mnras/stac084. arXiv: 2104.10978 [astro-ph.HE].

[294] S. Veilleux et al. "Fast Molecular Outflows in Luminous Galaxy Mergers: Evidence for Quasar Feedback from Herschel". In: *Astrophysical Journal* 776.1, 27 (2013), p. 27. DOI: 10.1088/0004-637X/776/1/27. arXiv: 1308.3139 [astro-ph.CO].

[295] K. Sakamoto et al. "An Infrared-luminous Merger with Two Bipolar Molecular Outflows: ALMA and SMA Observations of NGC 3256". In: *Astrophysical Journal* 797.2, 90 (2014), p. 90. DOI: 10.1088/0004-637X/797/2/90. arXiv: 1403.7117 [astro-ph.GA].

[296] G. M. Frichter, T. K. Gaisser, and T. Stanev. "Inelasticity in p-nucleus collisions and its application to high energy cosmic-ray cascades". In: *Physical Review D* 56.5 (1997), pp. 3135–3142. DOI: 10.1103/PhysRevD.56.3135. arXiv: astro-ph/9704061 [astro-ph].

[297] A. K. Leroy et al. "ALMA Reveals the Molecular Medium Fueling the Nearest Nuclear Starburst". In: *Astrophysical Journal* 801.1, 25 (2015), p. 25. DOI: 10.1088/0004-637X/801/1/25. arXiv: 1411.2836 [astro-ph.GA].

[298] T. M. Yoast-Hull et al. "Winds, Clumps, and Interacting Cosmic Rays in M82". In: *Astrophysical Journal* 768.1, 53 (2013), p. 53. DOI: 10.1088/0004-637X/768/1/53. arXiv: 1303.4305 [astro-ph.HE].

[299] B. Eichmann and J. Becker Tjus. "The Radio-Gamma Correlation in Starburst Galaxies". In: *Astrophysical Journal* 821.2, 87 (2016), p. 87. DOI: 10.3847/0004-637X/821/2/87. arXiv: 1510.03672 [astro-ph.HE].

[300] R. S. Fletcher et al. "sibyll: An event generator for simulation of high energy cosmic ray cascades". In: *Physical Review D* 50 (9 1994), pp. 5710–5731. DOI: 10.1103/PhysRevD.50.5710. URL: https://link.aps.org/doi/10.1103/PhysRevD.50.5710.

[301] N. Kalmykov, S. Ostapchenko, and A. Pavlov. "Quark-gluon-string model and EAS simulation problems at ultra-high energies". In: *Nuclear Physics B - Proceedings Supplements* 52.3 (1997), pp. 17–28. ISSN: 0920-5632. DOI: https://doi.org/10.1016/S0920-5632(96)00846-8. URL: https://www.sciencedirect.com/science/article/pii/S0920563296008468.

[302] T. M. Heckman et al. "An X-Ray and Optical Investigation of the Starburst-driven Superwind in the Galaxy Merger ARP 299". In: *Astrophysical Journal* 517.1 (1999), pp. 130–147. DOI: 10.1086/307193. arXiv: astro-ph/9812317 [astro-ph].

[303] R. D. Gehrz, R. A. Sramek, and D. W. Weedman. "Star bursts and the extraordinary galaxy NGC 3690." In: *Astrophysical Journal* 267 (1983), pp. 551–562. DOI: 10.1086/160892.

[304] A. Ptak et al. "A Focused, Hard X-Ray Look at Arp 299 with NuSTAR". In: *Astrophysical Journal* 800.2, 104 (2015), p. 104. DOI: 10.1088/0004-637X/800/2/104. arXiv: 1412.3120 [astro-ph.GA].

[305] Chandra X-ray Observatory. *Arp 299: Galactic Goulash*. Online, accessed on 19 January 2025, URL: https://chandra.harvard.edu/photo/2017/arp299/.

[306] M. Pérez-Torres et al. "Star formation and nuclear activity in luminous infrared galaxies: an infrared through radio review". In: *Astronomy and Astrophysics Review* 29.1, 2 (2021), p. 2. DOI: 10.1007/s00159-020-00128-x. arXiv: 2010.05072 [astro-ph.GA].

[307] A. Sargent and N. Scoville. "Anatomy of a Merger: CO in ARP 299 (IC 694–NGC 3690)". In: *Astrophysical Journal Letters* 366 (1991), p. L1. DOI: 10.1086/185896.

[308] F. Bigiel et al. "The Star Formation Law in Nearby Galaxies on Sub-Kpc Scales". In: *Astronomical Journal* 136.6 (2008), pp. 2846–2871. DOI: 10.1088/0004-6256/136/6/2846. arXiv: 0810.2541 [astro-ph].

[309] N. Ramírez-Olivencia et al. "Sub-arcsecond imaging of Arp 299-A at 150 MHz with LOFAR: Evidence for a starburst-driven outflow". In: *Astronomy & Astrophysics* 610, L18 (2018), p. L18. DOI: 10.1051/0004-6361/201732543. arXiv: 1802.03226 [astro-ph.GA].

[310] N. Ramírez-Olivencia et al. "Sub-arcsecond LOFAR imaging of Arp 299 at 150 MHz. Tracing the nuclear and diffuse extended emission of a bright LIRG". In: *Astronomy & Astrophysics* 658, A4 (2022), A4. DOI: 10.1051/0004-6361/202140822. arXiv: 2108.07291 [astro-ph.GA].

[311] S. García-Burillo et al. "ALMA imaging of C_2H emission in the disk of NGC 1068". In: *Astronomy & Astrophysics* 608, A56 (2017), A56. DOI: 10.1051/0004-6361/201731862. arXiv: 1709.05895 [astro-ph.GA].

[312] J. Stettner. "Measurement of the diffuse astrophysical muon-neutrino spectrum with ten years of IceCube data". In: *Proceedings of Science* ICRC2019 (2019), p. 1017. DOI: 10.22323/1.358.1017.

[313] P. Correa. "Merging Neutrino Astronomy with the Extreme Infrared Sky". PhD thesis. Vrije Universiteit Brussel, 2022.

[314] M. Ackermann et al. "Resolving the Extragalactic γ -Ray Background above 50 GeV with the Fermi Large Area Telescope". In: *Physical Review Letters* 116.15, 151105 (2016), p. 151105. DOI: 10.1103/PhysRevLett.116.151105. arXiv: 1511.00693 [astro-ph.CO].

[315] P. Madau and M. Dickinson. "Cosmic Star-Formation History". In: *Annual Review of Astronomy and Astrophysics* 52 (2014), pp. 415–486. DOI: 10.1146/annurev-astro-081811-125615. arXiv: 1403.0007 [astro-ph.CO].

[316] R. Davé, R. Thompson, and P. F. Hopkins. "MUFASA: galaxy formation simulations with meshless hydrodynamics". In: *Monthly Notices of the Royal Astronomical Society* 462.3 (2016), pp. 3265–3284. DOI: 10.1093/mnras/stw1862. arXiv: 1604.01418 [astro-ph.GA].

[317] S. S. McGaugh et al. "The Baryonic Tully-Fisher Relation". In: *Astrophysical Journal Letters* 533.2 (2000), pp. L99–L102. DOI: 10.1086/312628. arXiv: astro-ph/0003001 [astro-ph].

[318] C. L. Cowan et al. "Detection of the free neutrino: A Confirmation". In: *Science* 124 (1956), pp. 103–104. DOI: 10.1126/science.124.3212.103.

[319] M. A. Markov. "On high energy neutrino physics". In: *10th International Conference on High Energy Physics*. 1960, pp. 578–581.

[320] A. Roberts. "The birth of high-energy neutrino astronomy: A personal history of the DUMAND project". In: *Reviews of Modern Physics* 64.1 (1992), pp. 259–312. DOI: 10.1103/RevModPhys.64.259.

[321] E. Andres et al. "The AMANDA neutrino telescope: principle of operation and first results". In: *Astroparticle Physics* 13.1 (2000), pp. 1–20. DOI: 10.1016/S0927-6505(99)00092-4. arXiv: astro-ph/9906203 [astro-ph].

[322] R. Gandhi et al. "Ultrahigh-energy neutrino interactions". In: *Astroparticle Physics* 5.2 (1996), pp. 81–110. DOI: 10.1016/0927-6505(96)00008-4. arXiv: hep-ph/9512364 [hep-ph].

[323] H. L. Lai et al. "Global QCD analysis of parton structure of the nucleon: CTEQ5 parton distributions". In: *European Physical Journal C* 12.3 (2000), pp. 375–392. DOI: 10.1007/s100529900196. arXiv: hep-ph/9903282 [hep-ph].

[324] S. L. Glashow. "Resonant Scattering of Antineutrinos". In: *Physical Review* 118.1 (1960), pp. 316–317. DOI: 10.1103/PhysRev.118.316.

[325] P. A. Čerenkov. "Visible Radiation Produced by Electrons Moving in a Medium with Velocities Exceeding that of Light". In: *Physical Review* 52.4 (1937), pp. 378–379. DOI: 10.1103/PhysRev.52.378.

[326] J. Ahrens et al. "Muon track reconstruction and data selection techniques in AMANDA". In: *Nuclear Instruments and Methods in Physics Research A* 524.1-3 (2004), pp. 169–194. DOI: 10.1016/j.nima.2004.01.065. arXiv: astro-ph/0407044 [astro-ph].

[327] P. B. Price and K. Woschnagg. "Role of group and phase velocity in high-energy neutrino observatories". In: *Astroparticle Physics* 15.1 (2001), pp. 97–100. DOI: 10.1016/S0927-6505(00)00142-0. arXiv: hep-ex/0008001 [hep-ex].

[328] I. M. Frank and I. E. Tamm. "Coherent visible radiation of fast electrons passing through matter". In: *Compt. Rend. Acad. Sci. URSS* 14.3 (1937). Ed. by V. L. Ginzburg, B. M. Bolotovsky, and I. M. Dremin, pp. 109–114. DOI: 10.3367/UFNr.0093.196710o.0388.

[329] R. Abbasi et al. "The IceCube data acquisition system: Signal capture, digitization, and timestamping". In: *Nuclear Instruments and Methods in Physics Research A* 601.3 (2009), pp. 294–316. DOI: 10.1016/j.nima.2009.01.001. arXiv: 0810.4930 [physics.ins-det].

[330] R. Abbasi et al. "Calibration and characterization of the IceCube photomultiplier tube". In: *Nuclear Instruments and Methods in Physics Research A* 618.1-3 (2010), pp. 139–152. DOI: 10.1016/j.nima.2010.03.102. arXiv: 1002.2442 [astro-ph.IM].

[331] F. Halzen and J. Kelley. "Transforming Antarctic Ice into a Cherenkov Neutrino Detector". In: *arXiv e-prints*, arXiv:2411.15329 (2024), arXiv:2411.15329. DOI: 10.48550/arXiv.2411.15329. arXiv: 2411.15329 [astro-ph.HE].

[332] R. Abbasi et al. "The design and performance of IceCube DeepCore". In: *Astroparticle Physics* 35.10 (2012), pp. 615–624. DOI: 10.1016/j.astropartphys.2012.01.004. arXiv: 1109.6096 [astro-ph.IM].

[333] IceCube Collaboration. *Diagrams*. Online, accessed 10 March 2025, URL: https://icecube.wisc.edu/gallery/diagrams/.

[334] M. G. Aartsen et al. "The IceCube Neutrino Observatory - Contributions to ICRC 2017 Part II: Properties of the Atmospheric and Astrophysical Neutrino Flux". In: (2017). arXiv: 1710.01191 [astro-ph.HE].

[335] R. Abbasi et al. “Measurement of the atmospheric neutrino energy spectrum from 100 GeV to 400 TeV with IceCube”. In: *Physical Review D* 83.1, 012001 (2011), p. 012001. DOI: 10.1103/PhysRevD.83.012001. arXiv: 1010.3980 [astro-ph.HE].

[336] T. K. Gaisser, R. Engel, and E. Resconi. *Cosmic Rays and Particle Physics*. 2nd ed. Cambridge University Press, 2016.

[337] R. Abbasi et al. “Observation of seasonal variations of the flux of high-energy atmospheric neutrinos with IceCube”. In: *European Physical Journal C* 83.9, 777 (2023), p. 777. DOI: 10.1140/epjc/s10052-023-11679-5. arXiv: 2303.04682 [astro-ph.HE].

[338] T. Glauch. “The Origin of High-Energy Cosmic Particles: IceCube Neutrinos and the Blazar Case”. PhD thesis. Munich Techical University, 2021.

[339] A. Gazizov and M. Kowalski. “ANIS: High energy neutrino generator for neutrino telescopes”. In: *Computer Physics Communications* 172.3 (2005), pp. 203–213. DOI: 10.1016/j.cpc.2005.03.113. arXiv: astro-ph/0406439 [astro-ph].

[340] D. Chirkin and W. Rhode. “Propagating leptons through matter with Muon Monte Carlo (MMC)”. In: *arXiv e-prints*, hep-ph/0407075 (2004), hep–ph/0407075. DOI: 10.48550/arXiv.hep-ph/0407075. arXiv: hep-ph/0407075 [hep-ph].

[341] J. H. Koehne et al. “PROPOSAL: A tool for propagation of charged leptons”. In: *Computer Physics Communications* 184 (2013), pp. 2070–2090. DOI: 10.1016/j.cpc.2013.04.001.

[342] M. Rongen. “Calibration of the IceCube neutrino observatory”. Veröffentlicht auf dem Publikationsserver der RWTH Aachen University; Dissertation, RWTH Aachen University, 2019. Dissertation. Aachen: RWTH Aachen University, 2019, 1 Online–Ressource (xv, 205 Seiten) : Illustrationen, Diagramme. DOI: 10.18154/RWTH-2019-09941. URL: https://publications.rwth-aachen.de/record/771097.

[343] M. G. Aartsen et al. “Measurement of the multi-TeV neutrino interaction cross-section with IceCube using Earth absorption”. In: *Nature* 551.7682 (2017), pp. 596–600. DOI: 10.1038/nature24459. arXiv: 1711.08119 [hep-ex].

[344] J. G. Learned and K. Mannheim. “High-Energy Neutrino Astrophysics”. In: *Annual Review of Nuclear and Particle Science* 50 (2000), pp. 679–749. DOI: 10.1146/annurev.nucl.50.1.679.

[345] M. G. Aartsen et al. “Improvement in fast particle track reconstruction with robust statistics”. In: *Nuclear Instruments and Methods in Physics Research A* 736 (2014), pp. 143–149. DOI: 10.1016/j.nima.2013.10.074. arXiv: 1308.5501 [astro-ph.IM].

[346] P. J. Huber. “Robust Estimation of a Location Parameter”. In: *The Annals of Mathematical Statistics* 35.1 (1964), pp. 73–101. DOI: 10.1214/aoms/1177703732. URL: https://doi.org/10.1214/aoms/1177703732.

[347] N. van Eijndhoven, O. Fadiran, and G. Japaridze. “Implementation of a Gauss convoluted Pandel PDF for track reconstruction in neutrino telescopes”. In: *Astroparticle Physics* 28.4-5 (2007), pp. 456–462. DOI: 10.1016/j.astropartphys.2007.09.001. arXiv: 0704.1706 [astro-ph].

[348] P. Coppin. "Investigation of the precursor phase of gamma-ray bursts through gamma-ray and high-energy neutrino observations". PhD thesis. Vrije Universiteit Brussel, 2022.

[349] N. Whitehorn, J. van Santen, and S. Lafebre. "Penalized splines for smooth representation of high-dimensional Monte Carlo datasets". In: *Computer Physics Communications* 184.9 (2013), pp. 2214–2220. DOI: 10.1016/j.cpc.2013.04.008. arXiv: 1301.2184 [physics.data-an].

[350] M. Ackermann et al. "Optical properties of deep glacial ice at the South Pole". In: *Journal of Geophysical Research (Atmospheres)* 111.D13, D13203 (2006), p. D13203. DOI: 10.1029/2005JD006687.

[351] T. Neunhöffer. "Estimating the angular resolution of tracks in neutrino telescopes based on a likelihood analysis". In: *Astroparticle Physics* 25.3 (2006), pp. 220–225. DOI: 10.1016/j.astropartphys.2006.01.002. arXiv: astro-ph/0403367 [astro-ph].

[352] R. Abbasi et al. "An improved method for measuring muon energy using the truncated mean of dE/dx". In: *Nuclear Instruments and Methods in Physics Research A* 703 (2013), pp. 190–198. DOI: 10.1016/j.nima.2012.11.081. arXiv: 1208.3430 [physics.data-an].

[353] C. Bellenghi et al. "Extending the IceCube search for neutrino point sources in the Northern sky with additional years of data". In: *arXiv e-prints*, arXiv:2308.12742 (2023), arXiv:2308.12742. DOI: 10.48550/arXiv.2308.12742. arXiv: 2308.12742 [astro-ph.HE].

[354] L. Rädel. "Measurement of High-Energy Muon Neutrinos with the IceCube Neutrino Observatory". PhD thesis. RWTH Aachen U., 2017. DOI: 10.18154/RWTH-2017-10054.

[355] E. Bugaev et al. "Propagation of τ-neutrinos and τ-leptons through the Earth and their detection in underwater/ice neutrino telescopes". In: *Astroparticle Physics* 21.5 (2004), pp. 491–509. DOI: 10.1016/j.astropartphys.2004.03.002. arXiv: hep-ph/0312295 [hep-ph].

[356] S. Mechbal and N. Feigl. "Characterization and testing of the IceCube Upgrade mDOM". In: *Proceedings of Science* ICRC2023 (2023), p. 1183. DOI: 10.22323/1.444.1183.

[357] R. Abbasi et al. "D-Egg: a dual PMT optical module for IceCube". In: *Journal of Instrumentation* 18.4, P04014 (2023), P04014. DOI: 10.1088/1748-0221/18/04/P04014. arXiv: 2212.14526 [astro-ph.IM].

[358] J. Ahrens et al. "Search for Extraterrestrial Point Sources of Neutrinos with AMANDA-II". In: *Physical Review Letters* 7, 071102 (2004), p. 071102. DOI: 10.1103/PhysRevLett.92.071102. arXiv: astro-ph/0309585 [astro-ph].

[359] J. Braun et al. "Methods for point source analysis in high energy neutrino telescopes". In: *Astroparticle Physics* 29.4 (2008), pp. 299–305. DOI: 10.1016/j.astropartphys.2008.02.007. arXiv: 0801.1604 [astro-ph].

[360] J. Neyman and E. S. Pearson. "On the Problem of the Most Efficient Tests of Statistical Hypotheses". In: *Breakthroughs in Statistics: Foundations and Basic Theory*. Ed. by S. Kotz and N. L. Johnson. New York, NY: Springer New York, 1992, pp. 73–108. ISBN: 978-1-4612-0919-5. DOI: 10.1007/978-1-4612-0919-5_6. URL: https://doi.org/10.1007/978-1-4612-0919-5_6.

[361] S. S. Wilks. "The Large-Sample Distribution of the Likelihood Ratio for Testing Composite Hypotheses". In: *The Annals of Mathematical Statistics* 9.1 (1938), pp. 60–62. ISSN: 00034851, 21688990. URL: http://www.jstor.org/stable/2957648 (visited on 05/01/2025).

[362] A. Poluektov. "Kernel density estimation of a multidimensional efficiency profile". In: *Journal of Instrumentation* 10.2, P02011 (2015), P02011. DOI: 10.1088/1748-0221/10/02/P02011. arXiv: 1411.5528 [physics.data-an].

[363] B. M. Peterson et al. "Reverberation Mapping of the Seyfert 1 Galaxy NGC 7469". In: *Astrophysical Journal* 795.2, 149 (2014), p. 149. DOI: 10.1088/0004-637X/795/2/149. arXiv: 1409.4448 [astro-ph.GA].

[364] C. Ricci et al. "BAT AGN Spectroscopic Survey. V. X-Ray Properties of the Swift/BAT 70-month AGN Catalog". In: *Astrophysical Journal Supplement* 233.2, 17 (2017), p. 17. DOI: 10.3847/1538-4365/aa96ad. arXiv: 1709.03989 [astro-ph.HE].

[365] R. Genzel et al. "Infrared Imaging and Spectroscopy of NGC 7469". In: *Astrophysical Journal* 444 (1995), p. 129. DOI: 10.1086/175588.

[366] G. Sommani et al. "Two 100 TeV Neutrinos Coincident with the Seyfert Galaxy NGC 7469". In: *Astrophysical Journal* 981.2, 103 (2025), p. 103. DOI: 10.3847/1538-4357/adb031. arXiv: 2403.03752 [astro-ph.HE].

[367] A. Taramopoulos, H. Payne, and F. H. Briggs. "HI observations of the starburst galaxy NGC 2146". In: *Astronomy & Astrophysics* 365 (2001), pp. 360–369. DOI: 10.1051/0004-6361:20000143. arXiv: astro-ph/0005370 [astro-ph].

[368] A. Greve et al. "NGC 2146's starburst region and extended structure". In: *Astronomy & Astrophysics* 459.2 (2006), pp. 441–451. DOI: 10.1051/0004-6361:20053693.

[369] L. Armus et al. "ROSAT Observations of NGC 2146: Evidence for a Starburst-driven Superwind". In: *Astrophysical Journal* 445 (1995), p. 666. DOI: 10.1086/175729.

[370] Q.-W. Tang, X.-Y. Wang, and P.-H. T. Tam. "Discovery of GeV Emission from the Direction of the Luminous Infrared Galaxy NGC 2146". In: *Astrophysical Journal* 794.1, 26 (2014), p. 26. DOI: 10.1088/0004-637X/794/1/26. arXiv: 1407.3391 [astro-ph.HE].

[371] V. Buiten et al. "MICONIC: JWST Unveils Shocked Hot Core Chemistry in the Western Nucleus of Arp 220". In: *arXiv e-prints*, arXiv:2502.10271 (2025), arXiv:2502.10271. DOI: 10.48550/arXiv.2502.10271. arXiv: 2502.10271 [astro-ph.GA].

[372] C. Feruglio et al. "The multi-phase winds of Markarian 231: from the hot, nuclear, ultra-fast wind to the galaxy-scale, molecular outflow". In: *Astronomy & Astrophysics* 583, A99 (2015), A99. DOI: 10.1051/0004-6361/201526020. arXiv: 1503.01481 [astro-ph.GA].

[373] H. Arp. "Atlas of Peculiar Galaxies". In: *Astrophysical Journal Supplement* 14 (1966), p. 1. DOI: 10.1086/190147.

[374] D. W. Darg et al. "Galaxy Zoo: the fraction of merging galaxies in the SDSS and their morphologies". In: *Monthly Notices of the Royal Astronomical Society* 401.2 (2010), pp. 1043–1056. DOI: 10.1111/j.1365-2966.2009.15686.x. arXiv: 0903.4937 [astro-ph.GA].

[375] C. Ricci et al. "BASS XXXVII: The Role of Radiative Feedback in the Growth and Obscuration Properties of Nearby Supermassive Black Holes". In: *Astrophysical Journal* 938.1, 67 (2022), p. 67. DOI: 10.3847/1538-4357/ac8e67. arXiv: 2209.00014 [astro-ph.GA].

[376] B. Eichmann et al. "Solving the Multimessenger Puzzle of the AGN-starburst Composite Galaxy NGC 1068". In: *Astrophysical Journal* 939.1, 43 (2022), p. 43. DOI: 10.3847/1538-4357/ac9588. arXiv: 2207.00102 [astro-ph.HE].

[377] S. Yamada et al. "Hard X-Ray to Radio Multiwavelength SED Analysis of Local U/LIRGs in the GOALS Sample with a Self-consistent AGN Model including a Polar-dust Component". In: *Astrophysical Journal Supplement* 265.2, 37 (2023), p. 37. DOI: 10.3847/1538-4365/acb349. arXiv: 2301.03613 [astro-ph.GA].